The CMB In Exact Inhomogeneous Cosmologies

Thesis submitted to the University of Cardiff for the degree of

Master of Philosophy

Lee Ashley Stokes

School of Physics and Astronomy,
University of Cardiff

June 11, 2014

Abstract

In the past, the standard method of analysing temperature and polarization anisotropies imprinted into the Cosmic Microwave Background by large-scale structure was to use approximate perturbative techniques applied to a Friedmann-Robertson-Walker model. Instead, this thesis researches models based on exact inhomogeneous solutions of the Einstein field equations, such as the Lemaître-Tolman (spherically symmetric with dust source) and Szekeres models (non-symmetric), to see whether there might be effects arising from large inhomogeneities that are missed in the standard approach.

Contents

Chapter 1

Introduction

In this chapter we discuss a number of theoretical techniques, some of which will be relevant for later work in this thesis. We give only a few technical details since a more complete approach is covered in many standard reference works. We also discuss the motivation behind using exact inhomogeneous cosmologies for modelling cosmic microwave background anisotropies and large-scale structure.

1.1 THEORETICAL OUTLINE

For the purposes of this work we assume the validity of general relativity as a description of spacetime. In particular, we assume that the relationship between curvature and the matter content of the Universe is described by the Einstein field equations,

$$G_{\mu\nu} = 8\pi G T_{\mu\nu} + \Lambda g_{\mu\nu}, \tag{1.1}$$

where $G_{\mu\nu}$ is the Einstein curvature tensor, $T_{\mu\nu}$ is the matter energy-momentum tensor, $g_{\mu\nu}$ is the metric tensor with signature $(+ - --)$ and Λ is the cosmological constant. The Friedmann-Robertson-Walker (FRW) universes, consisting of a foliation of maximally symmetric 3-spaces possessing six spacelike Killing vector fields and one timelike vector field, are now well understood. For completeness we write the FRW metric in the form

$$ds^2 = dt^2 - S^2(t)d\sigma^2, \tag{1.2}$$

where $d\sigma^2$ is the metric of a three-space of constant curvature and is independent of time. These spaces can possess positive, negative or zero curvature and, by a rescaling of the function S, one can normalize these curvatures k to be $+1, -1$ or 0 respectively. Then the metric $d\sigma^2$ can be written [1],

$$ds^2 = dt^2 - f^2(r)(d\theta^2 + \sin^2\theta d\phi^2), \tag{1.3}$$

where

$$f(r) = \begin{cases} \sin r & \text{if} \quad k = +1 \\ r & \text{if} \quad k = 0 \\ \sinh r & \text{if} \quad k = -1 \end{cases} \tag{1.4}$$

and k represents spatial curvature as being positive, flat or negative for $k = +1, 0, -1$ respectively. Here we take $c = 1$.

The FRW metric can also be written in the form

$$ds^2 = dt^2 - a^2(t)\left(\frac{1}{1 - kr^2}dr^2 + r^2(d\theta^2 + \sin^2\theta d\phi^2)\right), \tag{1.5}$$

which describes a homogeneous, isotropic and expanding universe. Substitution of (1.5) into the Einstein field equations yields the temporal component G_{tt} of the Einstein curvature tensor as

$$G^t_t = \frac{3}{a^2}(k + \dot{a}^2) = 3\left(\frac{k}{a^2} + H^2\right), \tag{1.6}$$

where

$$H = \frac{\dot{a}}{a} \tag{1.7}$$

is the Hubble parameter measuring the expansion rate of the Universe as a function of time, and the overdot represents ordinary differentiation with respect to time. The spatial components are equivalent and given as

$$G_r^r = G_\theta^\theta = G_\phi^\phi = -2\frac{\ddot{a}}{a} - \frac{k}{a^2} - H^2. \tag{1.8}$$

The stress-energy tensor T_ν^μ is that of a perfect fluid, so that

$$T_\nu^\mu = \text{diag}(\rho, P, P, P), \tag{1.9}$$

where ρ is the energy density and P is the pressure. Equations (1.6) and (1.8) can be combined with (1.9) to yield

$$3\left(\frac{k}{a^2} + H^2\right) + \Lambda = 8\pi\rho, \tag{1.10}$$

$$2\frac{\ddot{a}}{a} + \frac{k}{a^2} + H^2 + \Lambda = -8\pi P. \tag{1.11}$$

These are known as the Friedmann equations. Construction of a cosmological model within a FRW framework requires the solution of these. However, we also need to know how the density evolves with time and hence we need the fluid equation

$$\dot{\rho} = -3H\left(\rho + \frac{P}{c^2}\right). \tag{1.12}$$

These equations therefore need to be solved simultaneously.

1.1.1 CRITERIA FOR A FRW LIMIT

Whilst the necessary conditions for a given metric to have a FRW limit are not always easy to apply, they are [2]:

- The source must be a perfect fluid. Furthermore, any additional components of the energy-momentum tensor must be set to zero.

- The rotation ω must be set to zero, so that

$$\omega_{\alpha\beta} = u_{[\alpha;\beta]} - \dot{u}_{[\alpha}u_{\beta]} = 0, \tag{1.13}$$

  where u_α is the velocity field of the fluid, the semicolon represents a covariant derivative with respect to the subscript following it and square brackets around indices represent antisymmetrization. This is equivalent to the existence of simultaneously comoving and synchronous coordinates.

- The acceleration must be zero. In synchronous and comoving coordinates, this condition has the particularly simple form:

$$g_{00,i} = 0 \quad , \quad i = 1, 2, 3, \tag{1.14}$$

  where the comma represents a partial derivative with respect to the subscript following it.

- The shear σ must be zero, so that

$$\sigma_{\alpha\beta} = u_{(\alpha\beta)} - \dot{u}_{(\alpha}u_{\beta)} - \frac{1}{3}\theta(g_{\alpha\beta} - u_\alpha u_\beta) = 0, \tag{1.15}$$

  where parentheses around indices represent symmetrization and $\theta = u^\alpha_{;\alpha}$ is the expansion scalar. In synchronous and comoving coordinates, the condition $\sigma = 0$ is equivalent to:

$$u^0 g_{ij,0} = \tfrac{2}{3}\theta g_{ij} \quad , \quad i, j = 1, 2, 3. \tag{1.16}$$

- The gradients of the expansion scalar and matter-density must be collinear with velocity.

- The gradient of pressure must be collinear with the velocity field.

- The hypersurfaces orthogonal to the velocity field must have constant curvature.

- The Weyl tensor $C_{\alpha\beta\gamma\delta}$ must vanish, so that

$$C_{\alpha\beta\gamma\delta} = R_{\alpha\beta\gamma\delta} + \frac{1}{2}(g_{\alpha\delta}R_{\gamma\beta} + g_{\beta\gamma}R_{\delta\alpha} - g_{\alpha\gamma}R_{\delta\beta} - g_{\beta\delta}R_{\gamma\alpha}) + \frac{1}{6}(g_{\alpha\gamma}g_{\delta\beta} - g_{\alpha\delta}g_{\gamma\beta})R = 0, \quad (1.17)$$

where $R_{\alpha\beta\gamma\delta}$ is the Riemann tensor, $R_{\alpha\beta}$ are the appropriate components of the Ricci tensor and R is the Ricci scalar. This corresponds to a Petrov Type O classification and ensures that the spacetime is conformally flat.

1.2   COSMOLOGICAL PERTURBATION THEORY

The goal of cosmological perturbation theory is to relate the physics of the early universe (e.g. inflation) to CMB anisotropy and large-scale structure and to provide the initial conditions for numerical simulations of structure formation. The physics during the period from the end of inflation to the beginning of nonlinear gravitational collapse is complicated by relativistic effects but greatly simplified by the small amplitude of perturbations. Thus, an essentially complete and accurate treatment of relativistic perturbation evolution is possible, at least in the context of simple fluctuation models like inflation [3], [4].

The starting point for cosmological perturbation theory is the metric of a perturbed FRW spacetime,

$$ds^2 = \left(g_{\mu\nu}^{(0)} + g_{\mu\nu}^{(1)}\right)dx^\mu dx^\nu = a^2(\tau)(-d\tau^2 + \gamma_{ij}(\vec{x})dx^i dx^j + h_{\mu\nu}(\vec{x},\tau)dx^\mu dx^\nu), \quad (1.18)$$

where, in this section, we adopt the $(-+++)$ convention for the metric. Spatial coordinates take the ranges $1 \le i, j \le 3$, x^i (or $\vec{x}$ for all three) is a comoving spatial coordinate, τ is conformal time, $a(\tau)$ is the cosmic expansion scale factor, c is taken as unity and $\gamma_{ij}(\vec{x})$ is the 3-metric of a maximally symmetric constant curvature space. Conformal time is related to the proper time measured by a comoving observer, i.e. one fixed at $\vec{x}$, by $dt = a(\tau)d\tau$. For cosmological perturbation theory it is more convenient than proper time. The metric perturbations are given by $h_{\mu\nu} = g_{\mu\nu}^{(1)}/a^2$.

1.2.1   SCALAR-VECTOR-TENSOR DECOMPOSITION

In linear perturbation theory, the metric perturbations $h_{\mu\nu}$ are regarded as a tensor field residing on the background FRW spacetime. As a symmetric 4×4 matrix, $h_{\mu\nu}$ has 10 degrees of freedom. Because of the ability to make continuous deformations of the coordinates, 4 of these degrees of freedom are gauge (coordinate) dependent, leaving 6 physical degrees of freedom. A proper treatment of cosmological perturbation theory requires clear separation between physical and gauge degrees of freedom.

The metric degrees of freedom in linear perturbation theory were presented by [5]. He presented the scalar-vector-tensor decomposition of the metric. It is based on a $3 + 1$ split of the components, which we write as follows:

$$h_{00} \equiv -2\psi \quad , \quad h_{0i} \equiv w_i \quad , \quad h_{ij} = 2(\phi\gamma_{ij} + S_{ij}) \quad , \quad \gamma^{ij}S_{ij} = 0. \quad (1.19)$$

Here, γ^{ij} is the inverse matrix of γ_{ij}. The trace part of h_{ij} has been absorbed into ϕ so that S_{ij} has only 5 independent components.

With the space-time $(3 + 1)$ split, we use γ_{ij} (or γ^{ij}) to lower (or raise) indices of spatial 3-vectors and tensors. For convenience, spatial derivatives will be written using the 3-dimensional covariant derivative ∇_i defined with respect to the 3-metric γ_{ij}; it is a three-dimensional version of the full 4-dimensional covariant derivative presented in general relativity textbooks. For example, if $k = 0$, we can choose Cartesian coordinates such that $\gamma_{ij} = \delta_{ij}$ and $\nabla_i = \partial/\partial x^i$.

The scalar-tensor-vector split is based on the decomposition of a vector into longitudinal and transverse parts. For any three-vector field $w_i(\vec{x})$, we may write

$$w_i = w_i^{\parallel} + w_i^{\perp}, \tag{1.20}$$

where

$$\vec{\nabla} \times \vec{w}^{\parallel} = \vec{\nabla} \cdot \vec{w}^{\perp} = 0. \tag{1.21}$$

The curl and divergence are defined using the spatial covariant derivative, e.g. $\vec{\nabla} \cdot \vec{w} = \gamma^{ij} \nabla_i w_j$.

The longitudinal/transverse decomposition is not unique (e.g. one may always add a constant to $w_i^{\parallel}$) but it always exists. The terminology arises because in the Fourier domain $w_i^{\parallel}$ is parallel to the wavevector while $w_i^{\perp}$ is transverse (perpendicular to the wavevector). Note that $w_i^{\parallel} = \nabla_i \phi_w$ for some scalar field ϕ_w. Thus, the longitudinal/transverse decomposition allows us to write a vector field in terms of a scalar (the longitudinal or irrotational part) and a part that cannot be obtained from a scalar (the transverse or rotational part).

A similar decomposition holds for a two-index tensor, but now each index can be either longitudinal or transverse. For a symmetric tensor, there are three possibilities: both indices are longitudinal, one is transverse, or two are transverse. These are written as follows:

$$S_{ij} = S_{ij}^{\parallel} + S_{ij}^{\perp} + S_{ij}^{T}, \tag{1.22}$$

where

$$\gamma^{jk} \nabla_k S_{ij} = \gamma^{jk} \nabla_k S_{ij}^{\parallel} + \gamma^{jk} \nabla_k S_{ij}^{\perp}. \tag{1.23}$$

The first term in equation (1.20) is a longitudinal vector while the second term is a transverse vector. The divergence of the doubly-transverse part, S_{ij}^{T}, is zero. For a traceless symmetric tensor, the doubly and singly longitudinal parts can be obtained from the gradients of a scalar and a transverse vector, respectively:

$$S_{ij}^{\parallel} = \left(\nabla_i \nabla_j - \tfrac{1}{3} \gamma_{ij} \nabla^2 \right) \phi_s \quad , \quad S_{ij}^{\perp} = \nabla_i S_j^{\perp} + \nabla_j S_i^{\perp}. \tag{1.24}$$

Now we have the mathematical background needed to perform the scalar-tensor-vector split of the physical degrees of freedom of the metric. The 'tensor mode' represents the part of h_{ij} that cannot be obtained from the gradients of a scalar or vector, namely S_{ij}^{T}. The tensor mode is gauge-invariant and has two degrees of freedom (five for a symmetric traceless 3×3 matrix, less three from the condition $\gamma^{jk} \nabla_k S_{ij}^{T} = 0$). Physically it represents gravitational radiation; the two degrees of freedom correspond to the two polarizations of gravitational radiation. Gravitational radiation is transverse: a wave propagating in the z-direction can have nonzero components $h_{xx} - h_{yy}$ and $h_{xy} = h_{yx}$ but no others. The tensor mode S_{ij}^{T} behaves like a spin-2 field under spatial rotations.

The 'vector mode' behaves like a spin-1 field under spatial rotations. It corresponds to the transverse vector parts of the metric, which are found in $w_i^{\perp}$ and $S_{ij}^{\perp}$. Each part has two degrees of freedom. Although we will not prove it here (see [3] for the details), it is possible to eliminate two of these degrees of freedom by imposing gauge conditions (coordinate conditions). The synchronous gauge of [5] is one popular choice, with $w_i^{\perp} = w_i^{\parallel} = 0$. Another choice is the 'Poisson' or transverse gauge [3] which sets $S_{ij}^{\perp} = 0$. In either case, there are two physical degrees of freedom and they correspond physically to gravitomagnetism. Although this effect is less well known than gravitational radiation or Newtonian gravity, it produces magnetic-like effects on moving and spinning masses, such as the precession of a gyroscope in the gravitational field of a spinning mass (Lense-Thirring precession).

The 'scalar mode' is spin-0 under spatial rotations and corresponds physically to Newtonian gravitation with relativistic modifications. The scalar parts of the metric are given by ϕ, ψ, $w_i^{\parallel}$, and $S_{ij}^{\parallel}$. Any two of these may be set to zero by means of a gauge transformation. One popular choice is $w_i^{\parallel} = S_{ij}^{\parallel} = 0$, also known as the conformal Newtonian gauge. It corresponds to the scalar mode in the transverse gauge, defined by the gauge conditions

$$\gamma^{ij} \nabla_i w_j = 0 \quad , \quad \gamma^{jk} \nabla_k S_{ij} = 0. \tag{1.25}$$

This gauge in linearized general relativity is the gravitational analogue of Coulomb gauge in electromagnetism, where the magnetic vector potential is transverse, $\nabla_i A^i = 0$. In the gravitational transverse gauge, w_i is transverse and S_{ij} is doubly transverse. This gauge is convenient for developing intuition although not necessarily the best for computation. The variables $(\phi, \psi, w_i^\perp, S_{ij}^T)$ correspond to gauge-invariant variables introduced by [6] as linear combinations of metric variables in other gauges.

In linear perturbation theory, the scalar, vector, and tensor modes evolve independently. The vector and tensor modes produce no density perturbations and therefore are unimportant for structure formation, although they do perturb the microwave background. Therefore, only the scalar mode will be considered here.

The Einstein equations give the equations of motion for the metric perturbations in terms of the energy-momentum tensor, the source of relativistic gravity. Here we consider the case of a perfect fluid (or several perfect fluid components combined), for which

$$T^{\mu\nu} = (\rho + p)V^\mu V^\nu + p g^{\mu\nu}, \tag{1.26}$$

where ρ and p are the proper energy density and pressure in the fluid rest frame and V^μ is the fluid 4-velocity.

As with the metric, $T^{\mu\nu}$ is split into time and space components. The conformal scale factor a^2 cancels using mixed components, giving

$$T^0_0 = -\rho(\vec{x}, \tau) = -[\bar{\rho}(\tau) + \delta\rho(\vec{x}, \tau)], \tag{1.27}$$

$$T^0_i = [\bar{\rho}(\tau) + \bar{p}(\tau)]v_i(\vec{x}, \tau) = -[\bar{\rho}(\tau) + \bar{p}(\tau)]\nabla_i W, \tag{1.28}$$

$$T^i_j = [\bar{p}(\tau) + \delta p(\vec{x}, \tau)]\delta^i_j, \tag{1.29}$$

where $\bar{\rho}(\tau)$ and $\bar{p}(\tau)$ are respectively the energy (or mass) density and pressure of the FRW background spacetime, $v_i = \gamma_{ij} dx^j/d\tau$ is the fluid 3-velocity (assumed nonrelativistic), and W is a velocity potential. It is also assumed that the velocity field is irrotational or, if it is not, that the matter fluctuations are linear so that the longitudinal and transverse velocity components evolve independently. This is a good approximation prior to the epoch of galaxy formation. It is also assumed that the shear stress (the non-diagonal part of T^i_j) is negligible compared with the pressure.

When the stress tensor is isotropic, the Einstein equations in transverse gauge imply that the two scalar potentials ϕ and ψ are equal [3] and the metric takes the simple form

$$ds^2 = a^2(\tau)[-(1 + 2\phi)d\tau^2 + (1 - 2\phi)\gamma_{ij}dx^i dx^j]. \tag{1.30}$$

This is a simple cosmological generalization of the standard weak-field limit of general relativity, which is recovered by setting $a = 1$ and $\gamma_{ij} = \delta_{ij}$.

Given the stress-energy tensor, we can now obtain field equations for $\phi(\vec{x}, \tau)$ using the Einstein equations. For the perturbations, we obtain

$$(\nabla^2 + 3k)\phi = 4\pi G a^2[\delta\rho + 3H(\bar{\rho} + \bar{p})W], \tag{1.31}$$

$$\partial_\tau \phi + H\phi = 4\pi G a^2(\bar{\rho} + \bar{p})W, \tag{1.32}$$

$$\partial_\tau^2 \phi + 3H\partial_\tau \phi - (8\pi G a^2 \bar{p} + 2k)\phi = 4\pi G a^2 \delta p, \tag{1.33}$$

where k is the curvature constant. There are more equations than in Newtonian gravity because the Einstein equations have local energy-momentum conservation built into them.

1.2.2   PERFECT FLUID MODEL

Here we present a simple model for understanding CMB anisotropy and large-scale structure. The matter and energy content of the Universe is reduced to a vacuum energy (with $\rho_\nu = \Lambda/8\pi G$ contributing to the mean expansion rate but not to the fluctuations) and two fluctuating components, Cold Dark Matter (CDM) and radiation (photons and neutrinos, the former coupled to baryons by electron scattering until

recombination). The CDM and radiation are treated as perfect fluids, ignoring the free-streaming of neutrinos and the diffusion and streaming of photons during and after recombination.

The fluid equations follow from local energy-momentum conservation, $\nabla_\mu T^{\mu\nu} = 0$. For a perfect fluid, with the scalar mode only (no vorticity and no gravitational radiation), the fluid equations in the metric of equation (1.30) are

$$\partial_\tau \rho + 3(H - \partial_\tau \phi)(\rho + p) + \nabla_i[(\rho + p)v^i] = 0 \tag{1.34}$$

and

$$\partial_\tau[(\rho + p)v^i] + 4H(\rho + p)v^i + \nabla_i p + (\rho + p)\nabla_i \phi = 0. \tag{1.35}$$

These are familiar from Newtonian fluid dynamics, with some extra terms. The damping H terms arise from Hubble expansion and the use of comoving coordinates. The $\partial_\tau(\phi)$ term in the continuity equation (1.34) arises from the deformation of the spatial coordinates, i.e. the $\phi\delta_{ij}$ contribution to the metric. The flux term in (1.34) describes transport relative to the comoving coordinate grid, which is deforming when $\partial_\tau(\phi) \neq 0$. The energy flux (or momentum density, they are equal) includes pressure in relativity because of the pdV work done by compression. Equations (1.34) and (1.35) apply separately to each perfect fluid component.

1.2.3   ADIABATIC AND ISOCURVATURE MODES

This section discusses the evolution of perturbations from the end of inflation (taken to be at $\tau = 0$ for all practical purposes) through recombination using a two-fluid approximation. We approximate the matter and energy content in the Universe as being two perfect fluids: CDM (a zero-temperature gas) and radiation (photons coupled to electrons and baryons before recombination, plus neutrinos which are approximated as behaving like photons). The net energy density perturbation is thus

$$\delta\rho(\vec{x}, \tau) = \bar{\rho}_c(a)\delta_c(\vec{x}, \tau) + \bar{\rho}_r(a)\delta_r(\vec{x}, \tau), \tag{1.36}$$

where $\bar{\rho}_c \propto a^{-3}$ and, if we neglect the contribution of baryons, $\bar{\rho}_r \propto a^{-4}$. We neglect baryons in the interest of economy, since this complicates the presentation without adding any essential new behaviour. The relative density contrasts are defined as $\delta_c \equiv \delta\rho_c/\bar{\rho}_c$ and $\delta_r \equiv \delta\rho_r/\bar{\rho}_r$.

The total pressure is

$$p(\vec{x}, \tau) = \frac{1}{3}\bar{\rho}_r(a)(1 + \delta_r) + p_\nu, \tag{1.37}$$

where $p_\nu = -\rho_\nu$ is the spatially constant negative pressure of vacuum energy (cosmological constant), should any be present.

As we noted in the previous section, density perturbations couple gravitationally only to the scalar mode of metric perturbations, and the scalar mode cannot generate transverse vector fields. As a result, the peculiar velocity fields of CDM and radiation are longitudinal and are fully characterized by their potentials W_c and W_r for CDM and radiation, respectively.

As a final simplifying assumption, we will assume that we are studying effects on distance scales less than the curvature length $|k|^{-1/2} = |\Omega_0 - 1|^{-1/2} H_0^{-1}$, which is at least 5 Gpc and possibly infinitely large.

With these assumptions, we can linearize the fluid equations (1.34) and (1.35) for $\delta_c^2 \ll 1$ and $\delta_r^2 \ll 1$ to obtain

$$\partial_r \delta_r = \frac{4}{3}\nabla^2 W_r + 4\partial_\tau \phi, \tag{1.38}$$

$$\partial_\tau \delta_c = \nabla^2 W_r + 3\partial_\tau \phi, \tag{1.39}$$

$$\partial_\tau W_r = \frac{1}{4}\delta_r + \phi, \tag{1.40}$$

$$\partial_\tau W_c + HW_c = \phi. \tag{1.41}$$

Equations (1.38)-(1.41) are coupled by gravity, which can be determined from the Poisson equation (1.31), which becomes

$$\nabla^2 \phi = 4\pi G a^2[(\bar{\rho}_r \delta_r + \bar{\rho}_c \delta_c) + H(4\bar{\rho}_r W_r + 3\bar{\rho}_c W_c)]. \tag{1.42}$$

9

We can solve equations (1.38)-(1.42) most easily by expanding the spatial dependence in eigenfunctions of the Laplacian ∇^2. In flat space these are plane waves $\exp(i\vec{k}\cdot\vec{x})$, and this is a good approximation even if the background is curved. This approximation is valid for almost all applications except large angular scale CMB anisotropy. Note that $\vec{k}$ is a comoving wavevector; the physical wavelength is $2\pi a/k$.

By expanding the spatial dependence in plane waves, we now have a fourth-order linear system of ordinary differential equations in time. We are free to define linear combinations of the variables $(\delta_c, \delta_r, W_c, W_r)$ as our fundamental variables. In terms of the mechanisms for generating primaeval perturbations, the most natural variables are the metric perturbation ϕ and the specific entropy

$$\eta \equiv \frac{\delta p - c_s^2 \delta\rho}{\bar{\rho}_c c_s^2} = \frac{3}{4}\delta_r - \delta_c, \tag{1.43}$$

where

$$c_s^2 \equiv \frac{d\bar{p}/d\tau}{d\bar{\rho}/d\tau} = \left[3\left(1 + \frac{3\bar{\rho}_c}{4\bar{\rho}_r}\right)\right]^{-1} \tag{1.44}$$

is the effective one-fluid sound speed of the matter and radiation. Acoustic signals actually do not propagate at this speed; they propagate with speed $3^{-1/2}$ through the radiation and they do not propagate at all through CDM.

For a two-component radiation plus CDM universe, the solution of the Friedmann equation gives

$$y \equiv \frac{\bar{\rho}_c}{\bar{\rho}_r} = \frac{\tau}{\tau_e} + \left(\frac{\tau}{2\tau_e}\right)^2, \tag{1.45}$$

$$\tau_e \equiv \left(\frac{a_{eq}}{\Omega_c}\right)^{1/2} H_0^{-1} = \frac{19\text{Mpc}}{\Omega_c h^2}. \tag{1.46}$$

The radiation-dominated era ends and matter-dominated era begins at redshift $1 + z_{eq} = a_{eq}^{-1} = 2.5 \times 10^4 \Omega_m h^2$. A cosmological constant has no significant effect on $y(\tau)$ provided that, during the times of interest, the vacuum energy density is much less than the radiation or cold dark matter density.

The fluid and Poisson equations can now be combined to give a pair of second-order ordinary differential equations,

$$\frac{1}{3c_s^2}\partial_\tau^2\phi + \left(1 + \frac{1}{c_s^2}\right)H\partial_\tau\phi + \left(\frac{k^2}{3} + \frac{1}{4y\tau_e^2}\right)\phi = \frac{\eta}{2y\tau_e^2}, \tag{1.47}$$

$$\frac{1}{3c_s^2}\partial_\tau^2\eta + H\partial_\tau\eta + \frac{k^2 y}{4}\eta = \frac{1}{6}y^2 k^4 \tau_e^2 \phi. \tag{1.48}$$

It is interesting to note that ϕ and η evolve independently aside from the source term each provides to the other. The coupling implies that entropy perturbations are a source for the growth of gravitational perturbations and vice versa.

For a given wavenumber k, there are two key times in the evolution of ϕ and η: the sound-crossing time $\tau \approx \pi/(kc_s)$ and the time of matter-radiation equality at $\tau \approx \tau_e$. For $\tau \ll \tau_e$, ϕ and η decouple and they both have solutions that decay rapidly with τ as well as solutions that are finite as $\tau \longrightarrow 0$. The latter are conventionally called 'growing modes' while the former are called decaying. The growing mode solution in the radiation era $\tau \ll \tau_e$ is

$$\phi(\vec{k},\tau) = \frac{3}{(\omega\tau)^3}(\sin\omega\tau - \omega\tau\cos\omega\tau)A(\vec{k}) + \frac{\tau}{\tau_e}\left[\frac{1}{(\omega\tau)^4}(1 - \cos\omega\tau - \omega\tau\sin\omega\tau) + \frac{1}{2(\omega\tau)^2}\right]I(\vec{k}), \tag{1.49}$$

$$\eta(\vec{k},\tau) = I(\vec{k}) + 9\left[\ln\omega\tau + \mathcal{C} - Ci(\omega\tau) + \frac{1}{2}(\cos\omega\tau - 1)\right]A(\vec{k}), \tag{1.50}$$

where $\omega \equiv k/\sqrt{3}$ is the phase of acoustic waves in the radiation fluid, $\mathcal{C} = 0.5772\ldots$ is the Euler constant, and $Ci(x)$ is the cosine integral defined by

$$Ci(x) = \mathcal{C} + \ln x + \int_0^x \frac{\cos t - 1}{t}dt. \tag{1.51}$$

10

In equation (1.49) we have neglected all terms $\mathcal{O}(\tau/\tau_e)$ aside from the lowest-order contribution of $I(\vec{k})$ to ϕ.

The general growing-mode solution contains two k-dependent integration constants, $A(\vec{k})$ and $I(\vec{k})$, which represent the initial ($\tau \to 0$) amplitude of ϕ and η respectively. Also note that $\phi(\tau \to 0) \neq 0$ only for $A \neq 0$ and $\eta(\tau \to 0) \neq 0$ only if $I \neq 0$. These solutions are called, respectively, the 'adiabatic' (so-called because the entropy perturbation $\eta = 0$ at $\tau = 0$, although 'isentropic' would be more appropriate) and 'isocurvature' (so-called because $\phi = 0$ at $\tau = 0$) mode amplitudes. In addition, there are decaying modes whose amplitude at $\tau = \tau_e$ is negligible unless the initial conditions were fine-tuned or there are external sources such as topological defects to continually regenerate the decaying mode. The solution of equations (1.49) and (1.50) is valid only for inflation or other mechanisms that generate fluctuations exclusively in the early universe, but not for topological defects.

As a result of reheating, inflation produces fluctuations with spatially constant ratios of the number densities of all particle species. For CDM and radiation, for example, $\rho_r^{3/4}/\rho_c = $ constant hence $I = 0$ and thus $\eta = 0$ until radiation pressure forces begin to separate the radiation from the CDM, which takes a sound-crossing time or $\tau \sim \omega^{-1}$. Thus, although inflation produces the adiabatic mode of initial fluctuations, the differing equations of state $p(\rho)$ for the two-fluid system lead to entropy perturbations proportional to the initial adiabatic mode amplitude $A(\vec{k})$; see (1.50).

Physically, the number density of particles of all species are proportional to each other in the adiabatic mode as long as there has been too little time for particles to travel a significant difference via their thermal speeds. However, the differing thermal speeds of different particle species (e.g. photons and CDM) eventually cause the particle densities to evolve differently, so that the number density ratios are no longer constant and the entropy perturbation is no longer zero.

First-order phase transitions, on the other hand, change the equation of state without moving matter or energy on macroscopic scales, hence $\delta\rho_r + \delta\rho_c = \theta_c = \theta_r = 0$ initially implying $\phi = 0$ initially but $\eta \neq 0$. This isocurvature mode is characterized by the initial entropy perturbation amplitude $I(\vec{k})$. As (1.49) shows, the isocurvature mode generates curvature fluctuations when the universe becomes matter-dominated.

On small scales, $k\tau \gg 1$, (1.47) and (1.48) may be solved using a WKB approximation. For our purposes it suffices to take the $\omega\tau \gg 1$ limit of (1.49) and (1.50):

$$\phi \approx -3\frac{\cos\omega\tau}{(\omega\tau)^2}A(\vec{k}) + \frac{1}{\omega^3\tau_e\tau^2}\left(\frac{\omega\tau}{2} - \sin\omega\tau\right)I(\vec{k}). \tag{1.52}$$

The radiation density fluctuation scales as

$$\delta_r \sim \frac{k^2\phi}{Ga^2\bar{\rho}_r} \sim k^2\tau^2\phi, \tag{1.53}$$

which oscillates in proportion to $\cos\omega\tau$ for the adiabatic mode and grows in proportion to $y \sim \tau/\tau_e$ for the isocurvature mode.

Note from (1.52) that the isocurvature mode induces oscillations in the potential with a $\pi/2$ phase shift relative to the adiabatic mode. This shift translates into a shift in the positions of the acoustic peaks in the CMB angular power spectrum.

1.2.4   CMB ANISOTROPY

This section presents a simplified treatment of CMB anisotropy, with the aim of highlighting the essential physics without getting lost in all of the details. A more complete treatment can be found in [98].

The microwave background radiation is fully described by a set of photon phase space distribution functions. Ignoring polarization (a few percent effect), all the information is included in the intensity or in $f(\vec{x}, \vec{p}, \tau)$, where $f d^3p$ is the number density of photons of conjugate momentum $\vec{p}$ at position and time $(\vec{x}, \tau)$. The conjugate momentum is related to the proper momentum measured by a comoving observer, $\vec{p}/a$, so that $\vec{p} = $ constant along a photon trajectory in the absence of metric perturbations.

Remarkably, despite metric perturbations and scattering with free electrons, the CMB photon phase space distribution remains blackbody (Planckian) to exquisite precision:

$$f(\vec{x}, \vec{p}, \tau) = f_{\text{Planck}}\left(\frac{E}{kT}\right) = f_{\text{Planck}}\left[\frac{p}{kT_0(1 + \Delta)}\right], \tag{1.54}$$

where $T_0 = 2.73\ K$ is the current CMB temperature and $\Delta(\vec{x}, \vec{n}, \tau)$ is the temperature variation at position $(\vec{x}, \tau)$ for photons travelling in direction $\vec{n}$. The phase space density is blackbody but the temperature depends on photon direction as a result of scattering and gravitational processes occurring along the line of sight.

The phase space density may be calculated from initial conditions in the early universe through the Boltzmann equation

$$\frac{Df}{D\tau} \equiv \frac{\partial f}{\partial \tau} + \frac{\partial f}{\partial \vec{x}} \cdot \frac{d\vec{x}}{d\tau} + \frac{\partial f}{\partial \vec{p}} \cdot \frac{d\vec{p}}{d\tau} = \left(\frac{df}{d\tau}\right)_c, \tag{1.55}$$

where the right-hand side is a collision integral coming from nonrelativistic electron-photon elastic scattering. In the absence of scattering, the phase space density is conserved along the trajectories

$$\frac{d\vec{x}}{d\tau} = \vec{n} \equiv \frac{\vec{p}}{p}, \tag{1.56}$$

$$\frac{1}{p}\frac{dp}{d\tau} = -\vec{n} \cdot \vec{\nabla}\phi + \partial_\tau \phi, \tag{1.57}$$

and

$$\frac{d\vec{n}}{d\tau} = -2[\vec{\nabla} - \vec{n}(\vec{n} \cdot \vec{\nabla})]\phi. \tag{1.58}$$

The procedure for computing CMB anisotropy is to linearize the Boltzmann equation assuming $\Delta^2 \ll 1$ [7]. Until recently, the temperature anisotropy Δ was expanded in spherical harmonics and the Boltzmann equation was solved as a hierarchy of coupled equations for the various angular moments [4]. [98] developed a much faster integration method call CMBFAST based on integrating the linearized Boltzmann equation along the observer's line of sight before the angular expansion is made:

$$\Delta(\vec{n}, \tau_0) = \int_0^{\tau_0} d\chi\, e^{-\tau_T(\chi)} \left[-\vec{n} \cdot \vec{\nabla}\phi + \partial_\tau \phi + an_e\sigma_T(\frac{1}{4}\delta_\gamma + \vec{v}_e \cdot \vec{n} + \text{pol.terms})\right]_{\text{ret}}, \tag{1.59}$$

where τ_0 is the present conformal time, χ is the radial comoving coordinate, subscript 'ret' denotes evaluation using retarded time $\tau = \tau_0 - \chi$, δ_γ is the relative density fluctuation in the photon gas ($\delta_\gamma = \delta_r$ in the two-fluid approximation), $\vec{v}_e$ is the mean electron velocity (i.e. the baryon velocity, which equals $\vec{v}_r$ in our two-fluid approximation), σ_T is the Thomson cross section, and the Thomson optical depth is

$$\tau_T(\chi) \equiv \int_0^\chi d\chi\, (an_e\sigma_T)_{\text{ret}}. \tag{1.60}$$

Note that small terms ('pol. term') due to polarization and the anisotropy of Thomson scattering in (1.59) have been left out.

The $e^{-\tau_T}$ factor in (1.59) accounts for the opacity of electron scattering, which prevents us from seeing much beyond a redshift of 1100, where $\tau_T \approx 1$. The CMB anisotropy appears to come from a thin layer called the photosphere, just like the radiation from the surface of a star. The two gravity terms give the effective emissivity due to the photon energy change caused by a varying gravitational potential. For a blackbody distribution, if all photon energies are increased by a factor $1 + \epsilon$, the distribution remains blackbody with a temperature increased by the same factor. Thus, the line-of-sight integration of the fractional energy change of (1.58) translates directly into a temperature variation. The terms proportional to the Thomson opacity $an_e\sigma_T$ are the effective emissivity due to Thomson scattering. Bearing in mind that the photon-baryon plasma is in nearly perfect thermal equilibrium (the temperature variations are

only about 1 part in 10^5), the photons we see scattered into the line of sight from a given fluid element have the blackbody distribution corresponding to the temperature of that element. Recalling that the energy density of blackbody radiation is $\rho_\gamma \propto T^4$, we see that $\frac{1}{4}\delta_\gamma$ is simply the fractional temperature variation of the fluid element. In other words, if we carried a thermometer to the photosphere and measured its reading in direction $-\vec{n}$, it would read a fraction $\frac{1}{4}\delta_\gamma$ different from the mean. Now the energy density is defined in the fluid rest frame, while the fluid is moving with 3-velocity $\frac{1}{4}\delta_\gamma$, so the temperature measured by a stationary thermometer (with fixed x^i) is changed by a Doppler correction $\vec{v}_e \cdot \vec{n}$.

Comparing the CMB with a star, when we look at the surface of a star we see the temperature of the emitting gas, corresponding to the $\frac{1}{4}\delta_\gamma$ term. For ordinary stars the Doppler boosting and gravitational redshift effects are negligible, although they are appreciable for supernovae and white dwarfs, respectively. For the CMB, on the other hand, all four emission terms in (1.59) are comparable in importance.

It is instructive to approximate the photosphere as an infinitely thin layer by adopting the instantaneous recombination approximation, according to which the free electron fraction and hence opacity drops suddenly at τ_{rec}, the conformal time of recombination at $z \approx 1100$:

$$\tau_T(\chi) = \left\{ \begin{array}{ll} \infty & , \quad \chi > \chi_{\text{rec}} = \tau_0 - \tau_{\text{rec}} \\ 0 & , \qquad \chi < \chi_{\text{rec}}. \end{array} \right. \tag{1.61}$$

Substituting into (1.59) and integrating by parts the gravitational redshift term gives the result first obtained in another form by [8]:

$$\Delta(\vec{n}) \approx \left(\frac{1}{4}\delta_\gamma + \phi + \partial_\chi W_\gamma \right)_{\text{rec}} + \int\limits_0^{\chi_{\text{rec}}} (2\partial_\tau \phi)_{\text{ret}} d\chi, \tag{1.62}$$

where the argument τ_0 from Δ has been dropped, $\chi_{\text{rec}} = \tau_0 - \tau_{\text{rec}}$ and W_γ is the velocity potential for the photons ($W_\gamma = W_r$ in the two-fluid model discussed above).

While it is interesting that the primary anisotropy depends on the velocity potential derivative along the line of sight, there appears to be no fundamental significance to the simple dependence in (1.62), aside from the fact that CMB anisotropy is produced by departures from hydrostatic equilibrium (in hydrostatic equilibrium, $\vec{v}_r = 0$). If the radiation gas were in hydrostatic equilibrium in a static gravitational potential, there would be no primary CMB anisotropy. Indeed, it can be shown from purely thermodynamic arguments that $T(\vec{x}) \propto \exp[-\phi(\vec{x})]$ (hence $\frac{1}{4}\delta_\gamma + \phi = $ constant) for a photon gas in equilibrium.

[8] showed that for adiabatic perturbations in the matter dominated era, on scales much larger than the acoustic horizon ($\omega\tau \ll 1$ in (1.49) and (1.50)), the sum of the photospheric terms in (1.62) (the terms evaluated at recombination) is $\frac{1}{3}\phi$. Thus, on angular scales much larger than 1° (roughly the size of the acoustic horizon), the CMB anisotropy is a direct measure of the gravitational potential on the photosphere at recombination.

1.2.5 ANGULAR POWER SPECTRUM

The angular power spectrum gives the mean squared amplitude of the CMB anisotropy per spherical harmonic component. Thus, we expand the anisotropy in spherical harmonic functions of the photon direction:

$$\Delta(\vec{n}) = \sum_{l,m} a_{l,m} Y_{l,m}(\vec{n}). \tag{1.63}$$

Observations of our universe give definite numbers for the a_{lm} (with experimental error bars, of course). Theoretically, however, we can only predict the probability distribution of the a_{lm}. For statistically isotropic fluctuations (i.e. having no preferred direction a priori), the a_{lm} are random variables with covariance

$$\langle a_{lm} a_{l'm'}^* \rangle = C_l \delta_{ll'} \delta_{mm'}, \tag{1.64}$$

where the Kronecker deltas make the a_{lm}s uncorrelated ($\delta_{ll'} = 1$ if $l = l'$ and 0 otherwise). The variance of each harmonic is given by the angular power spectrum C_l; rotational symmetry ensures that, theoretically, it is independent of m.

To calculate the angular power spectrum, we expand $\phi(\vec{x}, \tau)$ (and the other variables) in plane waves (assuming that the background is flat, $k = 0$),

$$\phi(\vec{x}, \tau) = \int e^{-i\mu k\chi}\phi(\vec{k}, \tau)d^3k = \int \sum_{l=0}^{\infty}(-i)^l(2l+1)j_l(k\chi)P_l(\mu)\phi(\vec{k}, \tau)d^3k, \tag{1.65}$$

where $\mu = -\vec{k} \cdot \vec{n}/k$ with a minus sign because $-\vec{n}$ is the radial unit vector at the origin. Note that many cosmologists insert a factor $(2\pi)^3$ in the Fourier integral going from k-space to x-space.

In (1.65) we have used the spherical wave expansion of a plane wave in terms of spherical Bessel functions $j_l(x)$ and Legendre polynomials $P_l(x)$. This gives

$$\Delta(\vec{n}) = \int \sum_{l=0}^{\infty}(-i)^l(2l+1)P_l(\mu)\Delta_l(\vec{k})d^3k, \tag{1.66}$$

where, in the instantaneous recombination approximation,

$$\Delta_l(\vec{k}) = \left[\frac{1}{4}\delta_\gamma(\vec{k}, \tau_{\text{rec}}) + \phi(\vec{k}, \tau_{\text{rec}})\right]j_l(k\chi_{\text{rec}}) + kW_r(\vec{k}, \tau_{\text{rec}})j_l'(k\chi_{\text{rec}}) + \int_0^{\chi_{\text{rec}}} 2\partial_\tau\phi(\vec{k}, \tau_0 - \chi)j_l(k\chi)d\chi. \tag{1.67}$$

The temperature expansion coefficient takes a simple form in terms of Δ_l:

$$a_{lm} = (-i)^l 4\pi \int Y_{lm}^*(\hat{k})\Delta_l(\vec{k})d^3k, \tag{1.68}$$

where $\hat{k}$ is a unit vector in the direction of $\vec{k}$.

To get the angular power spectrum now we must relate $\Delta_l(\vec{k})$ to the initial random field of potential or entropy fluctuations that induced the CMB anisotropy. Let us assume we have adiabatic fluctuations, for which $\phi(\vec{k}, \tau \longrightarrow 0) = A(\vec{k})$. We define the CMB transfer function

$$D_l(k) \equiv \frac{\Delta_l(\vec{k})}{A(\vec{k})}, \tag{1.69}$$

which depends only on the magnitude of $\vec{k}$ because the equations of motion have no preferred direction. To compute ensemble averages of products, we will need the two-point function for a statistically homogeneous and isotropic random field, whose variance defines the power spectrum:

$$\langle A(\vec{k})A^*(\vec{k}')\rangle = P_A(k)\delta_D^3(\vec{k} - \vec{k}'). \tag{1.70}$$

For scale-invariant fluctuations (equal power on all scales, as predicted by the simplest inflationary models), $P_A \propto k^{-3}$.

Combining (1.64), (1.68), and (1.69) gives the formal expression for the angular power spectrum as an integral over the three-dimensional power spectrum:

$$C_l = 4\pi \int P_A(k)D_l^2(k)d^3k. \tag{1.71}$$

It is difficult to get a simple approximation to $D_l(k)$ that makes this analytically tractable, except in the limit of large angular scales where the intrinsic and gravitational contributions to $\Delta(\vec{n})$ dominate, with $\Delta \approx \frac{1}{3}\phi$. Then $D_l = \frac{1}{3}j_l(k\chi_{\text{rec}})$ and the integral may be evaluated analytically for $P_A(k) \propto k^{n-4}$ with fixed n. When $n = 1$ (the scale-invariant spectrum), the result gives $l(l+1)C_l = $ constant or equal power on all angular scales. The phenomenon of acoustic peaks in $l(l+1)C_l$ is due to the acoustic oscillations in ϕ and W_γ which modify the potentials at recombination from their scale-invariant primeval forms.

This presentation has been based on the traditional Fourier space representation of the potential and other fields. The physical interpretation of the CMB two-point function is somewhat clearer in real (position) space, although a more detailed analysis based on Green's functions is needed before one can reap the rewards.

14

1.3 THE CMB: AN OBSERVATIONAL VIEWPOINT

The CMB is comprised of photons which were released from thermal equilibrium at the time of recombination, when the Universe's temperature fell sufficiently so that hydrogen could not remain ionized, and its contribution dominates the radiation content of today's universe. Measurements show that today's CMB spectrum is well described by a blackbody at $T = 2.73\ K$. This does not on its own put any further strong constraints on the evolution of the Universe but it does provide very strong evidence for the hot big bang model. Anisotropies in the CMB, whilst small ($\Delta T/T \approx 10^{-5}$), have, however, the potential to place strong limitations on cosmological parameters. Initially, this was attempted with data from the Cosmic Microwave Background Explorer (COBE) satellite [9] whilst, more recently, tight constraints have been produced by the Wilkinson Microwave Anisotropy Probe (WMAP) satellite [10], especially when taken in conjunction with astrophysical data; mainly from SN 1a luminosity distance studies [11] and galaxy surveys [12], although weak lensing studies [13] can also be employed. Ballon-based and terrestrial experiments have also been successful in constraining the form of the perturbations, although they suffer from severe contamination in the form of ground and atmospheric emissions, together with an inability to achieve full-sky coverage.

In order to analyse robustly the signal from CMB observations one must first remove foreground emission, even from space. The primary unwanted signal arises chiefly from within our own galaxy; particularly from dust, free-free and synchrotron emission. Once the removal or masking of the signal is complete, the observed CMB closely mimics the expected patterns of a homogeneous, isotropic universe with an inflationary origin for density perturbations. With density perturbations of just one part in 10^5 this demonstrates the remarkable near homogeneity and isotropy of the Universe (assuming the Copernican principle). However, the angular distribution of the fluctuations provide clues as to the cosmological parameters of the Universe. After primordial perturbations are generated in the very early Universe (maybe through inflation or some other mechanism) they evolve according to the linearized description of general relativity. One may show that gravitation amplifies the perturbations, but in a way that is scale independent on sub-horizon scales, whilst the pressure from the coupled photon-baryon plasma can oppose gravitational collapse.

At the point of decoupling, after which photons can free stream, the form of the CMB we see today is fixed: temperature differences are imprinted onto the photon distribution function at each point by a combination of effects linked to the strength of the perturbations; gravitational redshifting, intrinsic temperature differences and local peculiar velocities. Hence, within the CMB, we observe a frozen representation of the growth of structure at these extremely early times, including the scale-dependent effects.

By extracting the angular power spectrum the content of the CMB is made most explicit:

$$C_l = \frac{1}{2l+1} \sum_{m=-l}^{l} |a_{lm}|^2, \tag{1.72}$$

where

$$a_{lm} = \int \Delta T(\Omega) Y_{lm}^*(\Omega) d\Omega, \tag{1.73}$$

with Y_{lm} representing spherical harmonics. In the simplest (isotropic and Gaussian) theories, the C_l contain all information available from the observed microwave background. Figure 1.1 shows the spectacular agreement between the latest observed temperature power spectrum C_l (diamonds with error bars) and the best fit model (curve) for the ensemble average $< C_l >$. The simple linear description of the opposition of gravitational collapse by pressure completely determines the characteristic peaks in the spectrum. However, the spacetime through which the photons have free-streamed since recombination will influence their particular angular shape. In this way the angular power spectrum picks up information about the Hubble history of the Universe, leading to degenerate but tighter constraints on various cosmological parameters. Further information on these parameters comes from secondary late-time modifications to the photon distribution function due to reionization-induced scattering and acceleration-induced decay of large-scale gravitational potentials (seen through the integrated Sachs-Wolfe effect).
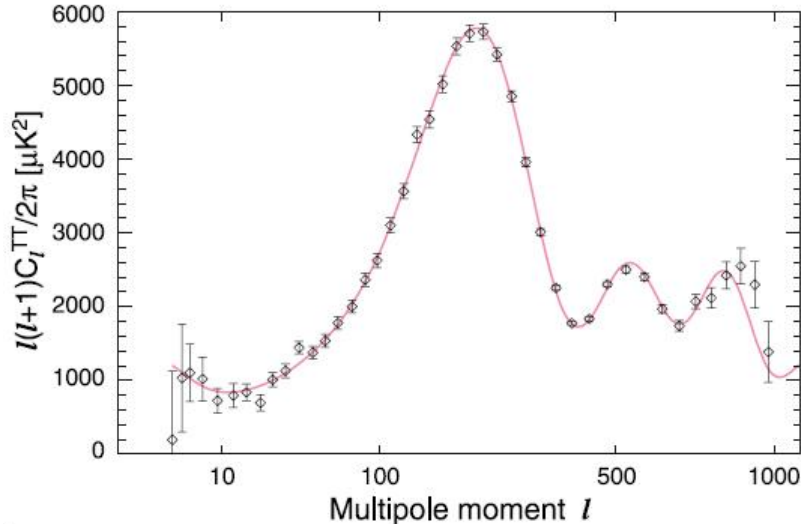
Figure 1.1: The angular power spectrum in the cosmic microwave background temperature anisotropies as measured by the WMAP satellite over five years. Figure taken from Nolta et al., 2009.

Although the WMAP satellite's detailed mapping [14] of the anisotropies in the temperature of the CMB has led us to unprecedented confidence in the applicability of the standard model of cosmology (also known as the concordance model), there are claims that the distribution of temperatures in the CMB are detectably non-Gaussian, thereby putting strain on simple inflationary models [15]. Additionally, there are numerous claims that the assumed isotropy is observationally violated [16], [17].

1.4 WHY ARE INHOMOGENEOUS MODELS OF THE UNIVERSE WORTHY OF STUDY?

A cursory glance at the night sky would suggest that we do not live in a homogeneous Universe. In fact, the distribution of matter in our local vicinity, i.e. within several Mpc, is very far from homogeneous; density contrasts reach huge values not only at the centre of galaxies but also on larger scales like clusters and superclusters, stretching over hundreds of Mpc. So how large does the scale need to be before we reach homogeneity? Certainly, present galaxy catalogues are not there yet. Therefore, how do we interpret the observations we have of objects whose light has travelled a significant fraction of the age of the Universe if we do not live in a homogeneous universe? Presently we assume that, in practice, inhomogeneities average out so that everything functions as if we have homogeneity and this inspired confidence for the construction of the standard model of cosmology. Although this model fits the observations well there is no theoretical understanding of the origin of the cosmological term, inherent in the model and, interestingly, particle physicists have been looking hard to prove that it should be zero. Also, the idea of averaging out inhomogeneities is not without its problems; in general, it is not correct to integrate out constrained degrees of freedom as if they were independent, and the fact that we can make observations only along our past light cone makes the observable Universe a constrained system. Therefore it would be desirable to study how directly observable light is affected by inhomogeneities in an inexact cosmological model. However, in the presence of generic inhomogeneities this would be practically impossible. Instead, we resort to toy models, the simplest of which is the spherically symmetric but inhomogeneous Lemaître-Tolman (L-T), discussed later in this thesis.

Fortunately, with the advent of projects such as WMAP and the Planck satellite, sufficiently good cosmological data is becoming available now and this will enable us to pose the appropriate questions and

hopefully get some definitive answers. The high isotropy of the CMB has often been used to dismiss the issue of inhomogeneity. However, one does not imply the other. Take a spherically symmetric distribution, for example. This is isotropic as seen from its centre, but only if there is isotropy around *every* point is homogeneity implied. An inhomogeneous Universe would suggest that some observers will be near a large concentration of mass whilst others will live in large voids, for example. Certainly what these two observers will experience will differ from what an idealised observer living in a perfectly homogeneous universe would experience. Then a question arises: could the acceleration of the Universe be just a trick of light, a misinterpretation that arises due to an oversimplification of the real, inhomogeneous Universe inherent in the FRW model? Whilst travelling through inhomogeneities, light does not see the average Hubble expansion but rather feels its variations due to the inhomogeneities, and this could sum up to an important correction. Recently, a few researchers have tried to address this point of view: what if the effect of large-scale structure could account for the observed luminosity to redshift behaviour of type Ia supernovae (i.e. give rise to an 'apparent' acceleration of the Universe), without dark energy? This question is important because an affirmative answer might obviate the need for a dark energy component/cosmological constant, which has presented a plethora of unresolved issues. Recent studies of exact solutions to the Einstein equations have, in fact, been able to reproduce the observed luminosity to redshift relation that is usually attributed to acceleration, provided that we live in a large region, or void, that has less density than the spatial average density over the cosmological Horizon [18], [19], [20]; see [60] for a review. One might naively conclude that this result can obviate the need for dark energy. However, in order for the void model to be taken seriously, several key issues have to be addressed. Firstly, the observation of small, nearly scale invariant CMB temperature fluctuations, strongly supports the principle that our universe is homogeneous and isotropic on large scales. In our present Universe non-linear large scale structures exist, marking a deviation from homogeneity. However, according to our current understanding of structure formation, non-linearities are only expected typically at scales $\sim \mathcal{O}(10 \text{ Mpc/h})$. In this case one can again argue that the effect of these inhomogeneities on cosmology, which is governed by the Hubble scale $\sim 3000 \text{ Mpc/h}$, would be too small to be significant. However, there are reasons why one could be wary of such a conclusion. From the theoretical point of view, the non-linear behaviour of structure formation is not a trivial issue. For instance, due to non-linear effects it is known that smaller voids can percolate to form much larger underdense structures which occupy most of the volume of the Universe, forming what is known as a 'cosmic web' of superclusters and voids. Also, we note that non-standard features of the primordial power spectrum, such as a spike at a particular scale, or some non-Gaussianity may enhance the possibility of having larger structures and voids. Observationally speaking, several huge non-linear structures; notably, the Sloan Great Wall has a length of 400/h Mpc [22] have been revealed through surveys like SDSS and 2dF (of course, these data are only tracing the visible matter, so their interpretation in terms of total matter is subject to a bias). It is unclear whether the presence of these large observed objects is consistent with the present understanding of structure formation. For example, [23] claims a discrepancy by a factor of 5 between the observed abundance of such objects (superclusters) and the values obtained using N-body numerical simulations. Peebles has also argued that our understanding of structure formation and observed voids are in apparent contradiction [24] and that this can be classified as a crisis of the ΛCDM model. Further, there has been observational evidence for the presence of local, large underdense ($\sim$25% less dense) region (that extends to $\sim$200 Mpc/h) from number counts of galaxies [25]. This represents a 4 sigma fluctuation, and would be at odds with ΛCDM. More recently, there has been a claim that the presence of a cold spot in the CMB detected in the WMAP sky [26] is also associated with a similar Big Void in the large-scale structure [27]. Intriguingly, the presence of such Big Voids has also been advocated by [28], in order to explain some features of the low-multipole anomalies in the CMB data. Finally, we note that two recent papers [29], [30] claim a significant (95% C.L.) detection of an anisotropy in the local Hubble flow in the Hubble Key Project data [30] and in the SN 1a dataset. This would be a completely natural consequence of being inside a large local void [30], since, of course, we are not expected to be exactly at the centre and the void is not expected to be exactly spherical.

To summarise, the large-scale structure of our Universe might be richer than we thought, which can have far reaching consequences for cosmology. We believe that finding a viable alternative to the presence of dark energy, for example, is a task which is important enough to consider the application of exact inhomogeneous cosmologies, which is already a highly developed branch of relativity. It is time to begin

taking all this knowledge seriously. Assuming that FRW models are everything that relativity has to say about cosmology is counterproductive and contradicts the facts.

1.5   THE STRUCTURE OF THIS THESIS

In the remainder of this thesis we present those elements of exact relativistic cosmology that are directly applicable to the interpretation of observations, with particular emphasis on the interplay between theoretical cosmology and the data obtained from the CMB radiation.

In Chapter 2, we describe the Lemaître-Tolman (L-T) model, which is an exact solution of Einstein's equations with spherical symmetry and a dust source; the simplest generalization of the Friedmann models. Inhomogeneities are naturally generated in an inhomogeneous cosmological model by the form of the arbitrary functions defining it. We investigate the constraints imposed by the measured temperature fluctuations of the CMB and infer the amplitude of perturbation at the time of decoupling from these. We use the L-T model to investigate the formation of a galaxy with a central black hole. Since it is impossible to use Newtonian methods or perturbations of a FRW background even to define a black hole in a meaningful way, this is a problem for whose solution exact methods of relativity are essential. However, the spherical symmetry of the L-T model is a disadvantage, since galaxies are not spherically symmetric, and they also rotate. However, this investigation provides a useful qualitative understanding of the process. We consider two possible mechanisms: the gravitational collapse of an ordinary ball of dust, and a condensation forming around a pre-existing wormhole. The aim is to reproduce the density distribution and mass of M87, which is an actually observed galaxy with a central black hole. In order to do this we use the density profile of that galaxy, believed to be known from observations, and for the density profile within the evolving black hole, about which nothing can be known from observations, we choose a simple model, joined onto the galaxy profile. To set realistic initial conditions it is assumed that by the time of decoupling of radiation and matter the condensation that would later grow to become the galaxy had a density contrast consistent with the implications of measurements of temperature anisotropies of the CMB radiation. However, the currently best achieved angular resolution of temperature measurements is $0.1\,^\circ$, whilst a typical proto-galaxy would occupy a region of only $0.004\,^\circ$ on the CMB sky. Consequently, there are at present no adequate observational data to constrain this model, and so, lacking any better choice, limits known for the $0.1\,^\circ$ scale are taken to apply to a single galaxy. The results are that the galaxy-black hole structure can be generated by both mechanisms, but the black hole appears after a much shorter time for the condensation around a wormhole, almost immediately after the Big Bang. We emphasise in that section that the horizon whose position can be approximately determined from observations is the apparent horizon, not the event horizon.

We also consider in Chapter 2 the formation and evolution of galaxy clusters and cosmic voids. Here, we infer the amplitude of perturbations at the time of decoupling from the constraints imposed by the measured temperature fluctuations of the CMB radiation. It is shown that perturbations at decoupling that are consistent with observational constraints can generate a galaxy cluster whose calculated parameters corresponding to the present epoch agree with the observed parameters at random from the Abell catalogue. However, similar problems were encountered to that mentioned above in that the observational upper limit on the temperature anisotropy of the CMB radiation is determined at angular scales about twenty times larger than the angular diameter that an Abell proto-cluster would occupy on the CMB sky. However, these constraints will be re-evaluated using better resolutions that are sure to be achieved in the future. Using the same method for voids we saw qualitative agreement with observations, but for the density within a void we saw values several times larger than those observed. We argue that the presence of non-baryonic matter, which does not interact with photons, would solve this discrepancy, because the amplitude of dark matter fluctuations at the instant of last scattering could be larger than temperature fluctuations. It could, however, be removed by more conventional methods, which do not require large fluctuations at last scattering. These investigations demonstrate that density perturbations are considerably less efficient in generating structures than are velocity perturbations. Consequently, since the long-standing structure formation paradigm relies on the belief that density perturbations alone are responsible for the origin of structures, our findings suggest a need for a revision of this assumption. For todays typical void, matter at the edge should occupy a region of angular diameter $0.1\,^\circ$ on the CMB sky, which is comparable to the

current best resolution achieved in observations, at least until we have further higher resolution data from the Planck spacecraft. Hence we are on the verge of being able to test void models against observations.

We then discuss a more precise description of the formation of voids. The Lemaître model describing a mixture of inhomogeneous dust and inhomogeneous radiation is used in order to solve the problem of insufficiently low densities within voids in the approach discussed above. Here we assume that the comoving spatial extent of the perturbations of radiation density does not change with time, due to the fact that, without this assumption, the number of unknown functions in the Einstein equations is larger by one than the number of equations and is therefore indeterminate. Proceeding from this, the current density distribution in voids is reproduced with arbitrary precision. The assumption made will probably have to be modified in the future, but the results demonstrate that this is a workable approach to the problem of void formation. This investigation highlights the fact that the decoupling of matter and radiation is not a single instant, as is usually assumed for simplicity, but a process extended in time.

Further, since the available observations are made on our past light cone we discuss light propagation in L-T models. These analyses imply the use of differential equations determining the null geodesics and generally also the redshift. We give the sets of differential equations in the cases of both a central and an off-centre observer. We also consider some examples of exact inhomogeneous models which can be found in the recent literature, and which fit with cosmological observations such as $H(z)$ measurements, baryon acoustic oscillations and supernovae observations, and in addition recover the position of the CMB power spectrum peaks. It was thus shown that evolving inhomogeneities can mimic, partly or totally, the effects of the dark energy component of the standard cosmological model, with universal acceleration due to the presence of dark energy as a specific example. We also investigate whether part of the dipole moment of the CMB might be cosmological in nature and not just due to our motion with respect to the rest frame of the CMB. We do this by putting the observer at the centre of a particular class of L-T models. Although moments beyond the quadrupole are not calculated we do obtain the geodesic equations for non-radial photons and formulae for the dipole and quadrupole are established for these L-T models.

We also investigate the possibility of solving the 'horizon problem' without the use of inflationary models. It is shown that this supposed problem can be solved using the L-T model with appropriately chosen arbitrary functions. This could be preferable to the use of inflationary models, which makes assumptions about the physical conditions in the Universe at such early times that any kind of direct verification is currently impossible. Moreover the solution proposed solves the problem whatever the location of the observer in spacetime, whilst inflation solves it only temporarily. Alternatives to inflation deserve at least to be considered, but, unfortunately, they tend to be suppressed in the noise of lobbying that has surrounded the inflationary paradigm from the very beginning.

In Chapter 3, we relax the assumption of perfect spherical symmetry that we have in the L-T models and describe the Szekeres solutions. In addition to being dust gravitational source solutions, they have no symmetry, i.e. no Killing vectors, and are therefore well-suited to describe a lumpy universe. We begin with a description of the Lemaître model and explain how this is connected with the Szekeres solution. The definition and metric of the Szekeres solution is then described, together with a description of possible geometries and types of evolution associated with each one. We explain the importance of reparametrising the arbitrary functions in the Szekeres metric and how this leads to a transformation called a stereographic projection. We also consider the more specific case of the quasi-spherical Szekeres model, and discuss in some depth the properties of this model. We also discuss the usefulness of stereographic projection and how this kind of analysis leads to the discovery that this model possesses an inherent dipole nature. Also, we describe how the analysis of null geodesics needs to be modified as compared to the L-T models. We show that such a model can describe the evolution of double structures (cluster-void pairs). This model helps us to understand some actually observed facts, such as a faster evolution of larger voids at larger distances from condensations as compared to voids in the proximity of condensations. An additional bonus in this investigation is a physical interpretation of the arbitrary functions in the Szekeres model, since they define the direction of the dipole component of the density distribution. For further investigation, we use the quasi-spherical Szekeres model to describe voids or localized condensations, matched into the homogeneous Friedmann background. This is known as the Swiss-cheese Szekeres model. Here, different arrangements of underdense and overdense quasi-spherical Szekeres regions are matched into a Friedmann background. This leads to the issue of matching junctions of null geodesics in this model. We also include a discussion

of apparent horizons in this model, and describe how this analysis needs to be modified as compared to the L-T models, for example. The light ray under investigation in the Szekeres Swiss-cheese model proceeds from an emitting source during the decoupling epoch. We find that the temperature anisotropies caused by the structures are smaller than those generated by the Sachs-Wolfe effect, unless the observer is situated inside one of the structures.

Chapter 2

The Lemaître-Tolman model and its applications in cosmology

2.1 BASIC PROPERTIES

The Lemaître-Tolman (L-T) model is a spherically symmetric non-static solution of the Einstein equations with a dust source, i.e. the matter tensor is

$$T^{\alpha\beta} = \rho u^\alpha u^\beta. \tag{2.1}$$

The coordinates are assumed to be comoving, so that the 4-velocity is $u^\alpha = \delta_t^\alpha$. See [2] and [31] for an extensive list of properties and other work on this model. Its metric is, in the synchronous time gauge and in units in which $c = 1$

$$ds^2 = dt^2 - \frac{R_{,r}^2}{1 + 2E(r)} dr^2 - R^2(t,r)(d\theta^2 + \sin^2\theta d\phi^2), \tag{2.2}$$

where E(r) is an arbitrary function, $R_{,r} = \partial R/\partial r$, and $R(r,t)$ obeys

$$R_{,t}^2 = 2E + \frac{2M}{R} + \frac{\Lambda}{3}R^2, \tag{2.3}$$

where $R_{,t} = \partial R/\partial t$ and Λ is the cosmological constant. $M = M(r)$ is another arbitrary function of integration and equation (2.3) is a first integral of the Einstein equations. The mass density in energy units is given by

$$\kappa\rho = \frac{2M_{,r}}{R^2 R_{,r}}, \tag{2.4}$$

where

$$\kappa = \frac{8\pi G}{c^4}. \tag{2.5}$$

If $E(r)$ is set to zero the metric of the space $t = $ constant would be flat, therefore E determines the curvature of space at each value of r. Note that we recover the FRW metric (1.5) by imposing the extra inhomogeneity conditions

$$R(t,r) = a(t)r \quad , \quad E(r) = -\tfrac{1}{2}kr^2 \tag{2.6}$$

to (2.2). Furthermore, equation (2.3) is similar to its Newtonian counterpart for a spherical dust distribution:

$$\frac{1}{2}\mathcal{R}_{,t}^2 = \frac{\mathcal{E}}{m} + \frac{G\mathcal{M}}{\mathcal{R}}, \tag{2.7}$$

where $\mathcal{R}$, $\mathcal{E}$ and $\mathcal{M}$ are respectively the radial coordinate, the energy of the particles, and the mass within radius $\mathcal{R}$ (in Newtonian mechanics, the cosmological constant is not considered). Therefore, $M(r)$ is the

gravitational mass inside the comoving spherical shell of the radial coordinate r, and $E(r)$ is the energy per unit mass in that shell.

Equation (2.3) can be solved by simple integration:

$$\int_0^R \frac{d\tilde{R}}{\sqrt{2E + 2\frac{M}{\tilde{R}} + \frac{1}{3}\Lambda\tilde{R}^2}} = t - t_B(r), \tag{2.8}$$

where t_B appears as an integration constant, and is an arbitrary function of r. This means that the Big Bang is not a single event as in the Friedmann models, but occurs at different times for different distances from the origin.

Initially we assume $\Lambda = 0$. Then (2.3) can be solved explicitly:

- When $E < 0$ (elliptic evolution):

$$R(t, r) = -\frac{M}{2E}(1 - \cos\eta), \tag{2.9}$$

$$\eta - \sin\eta = \frac{(-2E)^{3/2}}{M}(t - t_B(r)), \tag{2.10}$$

where η is a parameter. Eliminating η one can recast this as

$$t = t_B + \frac{M}{(-2E)^{3/2}}\left\{\arccos\left(1 + \frac{2ER}{M}\right) - 2\sqrt{-\frac{ER}{M}\left(1 + \frac{ER}{M}\right)}\right\}, \quad 0 \le \eta \le \pi, \tag{2.11}$$

$$t = t_B + \frac{M}{(-2E)^{3/2}}\left\{\pi + \arccos\left(-1 - \frac{2ER}{M}\right) - 2\sqrt{-\frac{ER}{M}\left(1 + \frac{ER}{M}\right)}\right\}, \quad \pi \le \eta \le 2\pi \tag{2.12}$$

for the expanding and collapsing case respectively.

- When $E = 0$ (parabolic evolution):

$$R(t, r) = \left[\frac{9}{2}M(t - t_B(r))^2\right]^{1/3}. \tag{2.13}$$

- When $E > 0$ (hyperbolic evolution):

$$R(t, r) = \frac{M}{2E}(\cosh\eta - 1), \tag{2.14}$$

$$\sinh\eta - \eta = \frac{(2E)^{3/2}}{M}(t - t_B(r)), \tag{2.15}$$

or equivalently,

$$t = t_B - \frac{M}{(2E)^{3/2}}\left\{\operatorname{arccosh}\left(1 + \frac{2ER}{M}\right) - 2\sqrt{-\frac{ER}{M}\left(1 + \frac{ER}{M}\right)}\right\}. \tag{2.16}$$

Note that these formulae are invariant under coordinate transformations of the form $\tilde{r} = g(r)$ and so $t_B(r)$, $M(r)$ and $E(r)$ can be fixed for a convenient choice of g. We can define a scale time and a scale radius for each worldline:

$$T(r) = \frac{2\pi M}{|2E|^{3/2}} \quad , \quad P(r) = \frac{2M}{|2E|}. \tag{2.17}$$

It is apparent from (2.14) and (2.15) that, in the elliptic case, these are the maximum lifetime and R value. The crunch time t_C in the elliptic case is then

$$t_C(r) = T(r) + t_B(r). \tag{2.18}$$

Hence we can rewrite (2.10) and (2.15) respectively as

$$\eta - \sin\eta = \frac{2\pi(t - t_B)}{t_C - t_B}, \tag{2.19}$$

$$\sinh\eta - \eta = \frac{2\pi(t - t_B)}{T}. \qquad (2.20)$$

Consequently, in hyperbolic models, η increases with the number of scale times completed and in elliptic models, larger η means that the dust worldline has completed a larger fraction of its lifetime between the bang and the crunch.

2.2 SHELL CROSSINGS

From a consideration of equation (2.4), the mass density becomes infinite when $M_{,r} \neq 0$ and $R_{,r} = 0$. This singularity is called a shell crossing and physically it corresponds to a location where the radial distance between two adjacent shells that have different values of r becomes zero. If $R_{,r}$ changes sign there, then the mass density on the other side of the shell crossing becomes negative. They are loci of $R_{,r} = 0$ that are not regular minima or maxima of R. They create unwanted singularities where the density diverges and changes sign. The conditions on the three arbitrary functions that ensure none be present anywhere in the L-T model, as well as those for regular minima and maxima, will be used below [32].

Since the signature adopted in this thesis is $(+ - - -)$ we observe that the condition $E \geq -1/2$ must be fulfilled in a physical L-T spacetime, as seen from (2.2). The equality $E = -1/2$ must occur at minima and maxima, but these locations are either at very large cosmological distances from the origin, or inside wormholes.

2.3 L-T MODELS OF COSMIC STRUCTURE

Using exact solutions of Einsteins equations we can follow the evolution of structures up to the present, irrespective of whether they are linear or nonlinear regimes, since in exact models there are no regimes at all. Obviously, the choice of such simple inhomogeneous models to represent large-scale structures in the Universe should be questioned. Generally, assumptions of spherical symmetry and a central observer are made for simplicity, but they are grounded on the observed quasi-isotropy of the CMB temperature. Having relaxed one degree of symmetry relative to the assumption of homogeneity, they are less restricted than the Friedmann models, and they provide a reasonable working approximation in which the Universe has no radial smoothing and is averaged only over the angular coordinates surrounding the observer.

The L-T model does, however, have some disadvantages. For example, we cannot take rotation into account because of the assumption of spherical symmetry. Hence, although the model represents a rough approximation to galaxy clusters, it does not apply to single galaxies. The objects to which the model can best be applied are voids because for them it has been shown by Newtonian methods that spherical symmetry is a stable property [33]. We can, however, avoid possible misleading features of spherical symmetry by assuming an off-centre observer, and some attempts to do this will be discussed later in this thesis. Another disadvantage is that due to the assumption of zero pressure, the model is unable to describe any thermo- or hydrodynamics, and so it is not applicable to the late stages of the collapse of matter or to the early Universe. Other methods of dealing with some of the disadvantages will also be presented later in this thesis; for example, in the Szekeres model [34], one can consider more general shapes of the voids and galaxy clusters, and also solve numerically the Einstein equations for a spherically symmetric distribution of dust with inhomogeneous radiation, and hence partially overcome the disadvantage of zero pressure. The results reproduce the real density profile of voids rather well.

2.3.1 MODEL DEFINED BY INITIAL AND FINAL PROFILES WITH $\Lambda = 0$

Refomulating the evolution equations

In cosmology, the initial state at t_1 (taken, for example, to be the last scattering surface) is accessible with rather imperfect precision and only indirectly. Of all the observational data collected at some final instant t_2, only some of it can be projected back to t_1. Usually, one assumes various data at t_1 and to 'shoot' into the observed final state at t_2.

The evolution equations can be reformulated so that information from both t_1 and t_2 can be fed into the models. We present such an approach to the L-T model [35], [36]. We present numerical examples of evolution of small initial density or velocity perturbations at t_1, the epoch of last scattering to modern structures such as voids at $t_2 = $ now.

Later in this chapter we will use the L-T model to connect an initial state of the Universe, defined by a velocity or mass-density distribution, to a final state also defined by one of these distributions. Numerical examples will be given in which we will incorporate actual astronomical data on the distribution of temperature of the CMB radiation and on the mass distribution in currently existing voids. The L-T model will also be used to interpret observational data on type Ia supernovae.

In constructing the models of voids, it will be convenient to use $M(r)$ as the radial coordinate, i.e. $\tilde{r} = M(r)$, since in most cases we will not need to pass through any bellies or necks. Consequently, in the whole region under consideration $M(r)$ will be a strictly growing function. Then with $R = R(t, M)$

$$\kappa\rho = \frac{2}{R^2 \partial R/\partial M} \equiv \frac{6}{\partial R^3/\partial M} \tag{2.21}$$

and so $R(t,r)$ is defined by a given $\rho(t,r)$:

$$R^3 = \int_0^M \frac{3c^4}{4\pi G\rho(t,x)} dx. \tag{2.22}$$

The last equation results with the initial condition $R = 0$ at $M = 0$ which we will assume in nearly all cases.

For clarity of calculations, we introduce the following quantities:

$$a = \frac{R}{M^{1/3}}, \tag{2.23}$$

$$b = \frac{R_{,t}}{M^{1/3}}, \tag{2.24}$$

$$x = \frac{|2E|}{M^{2/3}}. \tag{2.25}$$

Part I: density to density perturbations

We specify the density distributions at the instants $t = t_i, \ \ i = 1, 2$:

$$\rho(t_i, M) = \rho_i(M) \tag{2.26}$$

and calculate the corresponding $R(t_i, M)$ using (2.22). Throughout, we assume $R_{,t}(t_1, M) > 0$. This assumption is dictated by the intended application of our results, structure formation in the Universe. However, a similar investigation could be done for collapsing matter. For definiteness, we assume also that $t_2 > t_1$ and that the final density $\rho(t_2, M)$ is smaller than the initial density $\rho(t_1, M)$, at the same M. Therefore, the assumption is that matter has expanded along every world line, but the proof of this can be adapted to the collapse situation.

Hyperbolic evolution, $E > 0$

We write the initial and final density distributions at $t = t_1$ and $t = t_2$ as

$$\rho(t_1, M) = \rho_1(M) \quad , \quad \rho(t_2, M) = \rho_2(M). \tag{2.27}$$

Then from (2.21) we have, for each t_1 and t_2

$$R^3(t_i, M) - R^3_{min\ i} = \int_{M_{min}}^M \frac{6}{\kappa\rho_i(M')} dM' := R_i^3(M) \quad , \quad i = 1, 2. \tag{2.28}$$

24

$R_2(M) > R_1(M)$ since $\rho(t_2, M) < \rho(t_1, M)$. We will assume that there is an origin where $M = 0$ and $R(t_i, 0) = 0$, so that $R_{min\ i} = 0 = M_{min}$ is valid. Solving (2.14) and (2.15) for $t(R, r)$ and writing it out for each (t_1, R_1) and (t_2, R_2) leads to

$$t_B = t_i - \frac{M}{(2E)^{3/2}} \left[\sqrt{\left(1 + \frac{2ER_i}{M}\right)^2 - 1} - \text{arccosh}\left(1 + \frac{2ER_i}{M}\right) \right] \quad, \quad i = 1, 2. \tag{2.29}$$

Then eliminating t_B between the two versions of (2.29) yields

$$\frac{(2E)^{3/2}}{M}(t_2 - t_1) = \text{arccosh}\left(1 + \frac{2ER_1}{M}\right) - \text{arccosh}\left(1 + \frac{2ER_2}{M}\right)$$

$$+ \sqrt{\left(1 + \frac{2ER_2}{M}\right)^2 - 1} - \sqrt{\left(1 + \frac{2ER_1}{M}\right)^2 - 1}. \tag{2.30}$$

This equation defines $E(M)$ and (2.29) defines $t_B(M)$, and these two functions completely specify the L-T evolution from $\rho(t_1, M)$ to $\rho(t_2, M)$. For ease of calculations, let us use (2.23) and (2.25) to denote

$$\Psi_H(x) := \text{arccosh}(1 + a_1 x) - \text{arccosh}(1 + a_2 x)$$

$$+ \sqrt{(1 + a_2 x)^2 - 1} - \sqrt{(1 + a_1 x)^2 - 1} - (t_2 - t_1) x^{3/2}. \tag{2.31}$$

Now we have to answer the question: for what values of $a_2 > a_1$ and $t_2 > t_1$, does the equation $\Psi_H(x) = 0$ have a solution $x \neq 0$? An elementary reasoning [35] leads to the conclusion that the equation has a solution if and only if the following inequality is fulfilled:

$$t_2 - t_1 < \frac{\sqrt{2}}{3}\left(a_2^{3/2} - a_1^{3/2}\right). \tag{2.32}$$

Then the solution is unique. This inequality means that the expansion between t_1 and t_2 must have been faster than in the $E = 0$ model. Note that for a given value of M the result above shows only the existence of a solution. Shell crossings are not excluded by (2.32) and some initial conditions may lead to this, but the criteria for the occurrence of shell crossings are well investigated [32].

Elliptic evolution, $E < 0$

In this case we must consider the evolution separately for the final state expanding (for which $\eta \in [0, \pi]$ in (2.9) and (2.10)) and for the final state recollapsing ($\eta \in [\pi, 2\pi]$ in (2.9) and (2.10)). For the still-expanding final state, the Ψ function is, using the definitions given in (2.23) and (2.25)

$$\Psi_X(x) := \arccos(1 - a_2 x) - \arccos(1 - a_1 x)$$

$$+ \sqrt{1 - (1 - a_1 x)^2} - \sqrt{1 - (1 - a_2 x)^2} - (t_2 - t_1) x^{3/2}. \tag{2.33}$$

Using analogous reasoning to that given for (2.31), and taking into account that the arguments of arccos must have absolute values ≤ 1, this yields

$$0 \leq x \leq \frac{2}{a_i} \tag{2.34}$$

for both i, and since $a_2 > a_1$, then

$$0 \leq x \leq \frac{2}{a_2}. \tag{2.35}$$

This means that if there is any solution of $\Psi_X(x) = 0$, then it will have the property (2.29). Using an elementary reasoning [35], this leads to the conclusion that $\Psi_X(x) = 0$ has a solution if and only if two inequalities are fulfilled simultaneously:

$$\frac{\sqrt{2}}{3}\left(a_2^{3/2} - a_1^{3/2}\right) < t_2 - t_1 \leq \left(\frac{a_2}{2}\right)^{3/2} \left[\pi - \arccos\left(1 - \frac{2a_1}{a_2}\right) + 2\sqrt{\frac{a_1}{a_2} - \left(\frac{a_1}{a_2}\right)^2}\right]. \tag{2.36}$$

25

With the above fulfilled, the solution is unique. The first inequality tells us that the model must have expanded between t_1 and t_2 slower than the $E = 0$ would have, whilst the second means that the final state is still earlier than the instant of maximal expansion.

For the recollapsing final state, the Ψ-function is

$$\Psi_C(x) \quad := \quad \pi + \arccos(1 - a_2x) - \arccos(1 - a_1x)$$

$$+ \quad \sqrt{1 - (1 - a_1x)^2} + \sqrt{1 + (1 - a_2x)^2} - (t_2 - t_1)x^{3/2}. \tag{2.37}$$

The solution $\Psi_C(x) = 0$ if and only if [35]

$$t_2 - t_1 \geq \left(\frac{a_2}{2}\right)^{3/2}\left[\pi - \arccos\left(1 - \frac{2a_1}{a_2}\right) + 2\sqrt{\frac{a_1}{a_2} - \left(\frac{a_1}{a_2}\right)^2}\right] \tag{2.38}$$

and then the solution is unique.

Part II: velocity to density evolution

A useful measure of velocity is

$$b_i(M) := \frac{R_{,t}(t, M)}{M^{1/3}}\bigg|_{t=t_i}. \tag{2.39}$$

We suppose that the initial state is specified by a velocity profile $b_1(M)$, whilst the final state is specified by a density distribution $\rho(t_2, M)$. This section will follow a similar scheme to that used in the last.

Hyperbolic evolution, $E > 0$

Using the variables defined in (2.23), (2.24) and (2.25), the equation to be solved is $\Phi_H(x) = 0$, where [36]

$$\Phi_H(x) \quad := \quad \text{arccosh}\left(\frac{b_1^2 + x}{b_1^2 - x}\right) - \text{arccosh}(1 + a_2x)$$

$$+ \quad \sqrt{(1 + a_2x)^2 - 1} - \sqrt{\left(\frac{b_1^2 + x}{b_1^2 - x}\right)^2 - 1} - x^{3/2}(t_2 - t_1). \tag{2.40}$$

Here, the necessary and sufficient condition to solve $\Phi_H(x) = 0$ is

$$t_2 - t_1 < \frac{\sqrt{2}}{3}a_2^{3/2} - \frac{4}{3b_1^3}, \tag{2.41}$$

$$\frac{2}{a_2} < b_1^2. \tag{2.42}$$

The first of these is equivalent to (2.32), whilst the second is a necessary condition for the existence of a $t_2 > t_1$ obeying (2.41), and is equivalent to $R_2 > R_1$. With both inequalities fulfilled, the solution of $\Phi_H(x) = 0$ is unique [36].

Elliptic evolution, $E < 0$

When the final state is still expanding, the equation to be solved is $\Phi_X(x) = 0$, where

$$\Phi_X(x) \quad := \quad \arccos(1 - a_2x) - \arccos\left(\frac{b_1^2 - x}{b_1^2 + x}\right)$$

$$+ \quad \sqrt{\left(\frac{b_1^2 - x}{b_1^2 + x}\right)^2 - 1} - \sqrt{1 - (1 - a_2x)^2} - x^{3/2}(t_2 - t_1) \tag{2.43}$$

26

and the necessary and sufficient condition for the existence of an L-T solution between the two given states is:

$$\frac{\sqrt{2}}{3}a_2^{3/2} - \frac{4}{3b_1^3} < t_2 - t_1 \leq \left(\frac{a_2}{2}\right)^{3/2} \left[\pi - \arccos\left(\frac{\frac{a_2 b_1^2}{2} - 1}{\frac{a_2 b_1^2}{2} + 1}\right) + \frac{b_1\sqrt{2a_2}}{\frac{a_2 b_1^2}{2} + 1}\right]. \tag{2.44}$$

This set of inequalities is equivalent to (2.36), and when these inequalities are fulfilled, the solution of the corresponding equation is unique [36].

When the final state is recollapsing, the $E < 0$ evolution exists if and only if

$$t_2 - t_1 \geq \left(\frac{a_2}{2}\right)^{3/2} \left[\pi - \arccos\left(\frac{\frac{a_2 b_1^2}{2} - 1}{\frac{a_2 b_1^2}{2} + 1}\right) + \frac{b_1\sqrt{2a_2}}{\frac{a_2 b_1^2}{2} + 1}\right] \tag{2.45}$$

and x is the solution of $\Phi_H(x) = 0$ where

$$\Phi_C(x) \quad := \quad \pi + \arccos(a_2 x - 1) - \arccos\left(\frac{b_1^2 - x}{b_1^2 + x}\right)$$

$$+ \quad \sqrt{1 - \left(\frac{b_1^2 - x}{b_1^2 + x}\right)^2} + \sqrt{1 - (1 - a_2 x)^2} - x^{3/2}(t_2 - t_1). \tag{2.46}$$

Part III: velocity to velocity evolution

The given quantities now are an initial and final velocity distribution given by $b_1(M)$ and $b_2(M)$ respectively. We assume $b_1 > 0$ and $t_1 > t_2$.

Hyperbolic evolution, $E > 0$

In this case, we must solve $\Phi_H(x) = 0$, where

$$\Phi_H(x) \quad := \quad \text{arccosh}\left(\frac{b_1^2 + x}{b_1^2 - x}\right) - \text{arccosh}\left(\frac{b_2^2 + x}{b_2^2 - x}\right)$$

$$+ \quad \sqrt{\left(\frac{b_2^2 + x}{b_2^2 - x}\right)^2 - 1} - \sqrt{\left(\frac{b_1^2 + x}{b_1^2 - x}\right)^2 - 1} - x^{3/2}(t_2 - t_1) \tag{2.47}$$

and the necessary and sufficient condition for the existence of an $E > 0$ evolution between the states is

$$0 < b_1 < b_2 \quad, \quad t_2 - t_1 > \frac{4}{3}\left(\frac{1}{b_2^3 - b_1^3}\right). \tag{2.48}$$

The second inequality becomes clearer when it is written in the form

$$b_2^3 > \frac{b_1^3}{1 + \frac{3}{4}b_1^3(t_2 - t_1)}, \tag{2.49}$$

which means that an $E > 0$ evolution between the two states will exist provided the velocity of expansion at t_2 is greater than the velocity of expansion of the $E = 0$ model.

Elliptic evolution, $E < 0$

When the final state is still expanding, x is found by $\chi_X(x) = 0$ where

$$\chi_X(x) \quad := \quad \arccos\left(\frac{b_2^2 - x}{b_2^2 + x}\right) - \arccos\left(\frac{b_1^2 - x}{b_1^2 + x}\right)$$

$$+ \quad \sqrt{\left(1 - \frac{b_1^2 - x}{b_1^2 + x}\right)^2} - \sqrt{\left(1 - \frac{b_2^2 - x}{b_2^2 + x}\right)^2} - x^{3/2}(t_2 - t_1). \tag{2.50}$$

27

The necessary and sufficient condition for the existence of this evolution is the set consisting of the first inequality in (2.48) and

$$t_2 - t_1 < \frac{4}{3}\left(\frac{1}{b_2^3 - b_1^3}\right) \tag{2.51}$$

and now this implies that the expansion between t_1 and t_2 must have been slower for the $E = 0$ model.

When the final state is already recollapsing, we have $b_2 < 0$. Then the evolution exists for

$$b_2 < 0 < b_1 \tag{2.52}$$

and x is the root of

$$\chi_C(x) \quad := \quad \pi + \arccos\left(\frac{x - b_2^2}{x + b_2^2}\right) - \arccos\left(\frac{b_1^2 - x}{b_1^2 + x}\right)$$

$$+ \quad \sqrt{1 - \left(\frac{b_1^2 - x}{b_1^2 + x}\right)^2} - \sqrt{1 - \left(\frac{x - b_2^2}{x + b_2^2}\right)^2} - x^{3/2}(t_2 - t_1). \tag{2.53}$$

2.4 LIGHT PROPAGATION IN L-T MODELS

Since available observations are made on our past light cone, then analyses of cosmological problems imply the use of differential equations determining the null geodesics and generally also the redshift. Therefore, we give below the sets of differential equations, both in the case of a central observer [19], [31] and an off-centre observer, where the method described can be found in [37]. The results of this section will prove useful later in this thesis.

2.4.1 CENTRAL OBSERVER

We describe the Universe by the $t > t_B(r)$ part of the (r,t) plane, increasing t corresponding to going from the past to the future. Light travels on a light cone from a source to the observer in the geometric optics approximation. Consequently, by (2.2), a light ray travelling from a source of radiation with coordinates (t, r, θ, ϕ) and radially directed toward an observer located at the centre of symmetry of the model satisfies

$$\frac{dt}{dr} = -\frac{R_{,r}(t,r)}{\sqrt{1 + 2E(r)}}. \tag{2.54}$$

The solution of this equation will be denoted by $t_n(r)$. We can calculate the redshift along a radial ray to be [19], [31]

$$\ln|1 + z| = \int_0^r \frac{R_{,tr'}(t,r')}{\sqrt{1 + 2E}} dr'. \tag{2.55}$$

Now, we can choose z to be a parameter along the rays to obtain

$$\frac{dr}{dz} = \frac{\sqrt{1 + 2E(r)}}{(1 + z)R_{,tr}[t_n(r), r]}. \tag{2.56}$$

Equation (2.54) becomes therefore

$$\frac{dt}{dz} = -\frac{R_{,r}[t_n(r),r]}{(1 + z)R_{,tr}[t_n(r),r]} \tag{2.57}$$

Therefore, each null geodesic is a solution of (2.55) and (2.56), beginning with z at the source and finishing at $z = 0$, the observer.

2.4.2 OFF-CENTRE OBSERVER

For an observer located off-centre, a possible singularity at the centre does not alter the validity of such a model. Although the calculations are more involved in this case, they can be done numerically and we give below one method allowing us to deal with this issue.

This method was developed by [37] to study the dipole and quadrupole moments of the CMB in their Delayed Big-Bang model (see Section 2.10) and were used by [38] to solve the horizon problem within a class of models with an off-centre observer.

An observer located at a distance r_p from the centre sees an axially symmetric universe with the symmetry axis passing through the observer and the centre because of the spherical symmetry of the model. Therefore, it is allowable to simplify the problem by integrating the geodesics in the meridional plane. The angle α between the direction from which the light ray comes and the direction to the centre, together with the observers position (t_p, r_p), uniquely define the photon path. For the metric given in (2.2), the meridional plane is defined as $\theta = \pi/2$ ($\Longrightarrow k^\theta = 0$), k^θ being the θ component of the photon wave-vector and $k^\mu \equiv dx^\mu/d\lambda$, where λ is an affine parameter along the null geodesics. For $\mu = t, r, \phi$, we obtain, respectively,

$$\frac{dt}{d\lambda} = k^t, \tag{2.58}$$

$$\frac{dr}{d\lambda} = k^r = g^{rr} k_r = -\frac{k_r}{R_{,r}^2}, \tag{2.59}$$

$$\frac{d\phi}{d\lambda} = k^\phi = g^{\phi\phi} k_\phi = -\frac{k_\phi}{R^2}. \tag{2.60}$$

Now, the geodesic equations of light are given by

$$\frac{d^2 x^\mu}{d\lambda^2} + \Gamma^\mu_{\nu\rho} \frac{dx^\nu}{d\lambda} \frac{dx^\rho}{d\lambda} = 0 \tag{2.61}$$

and these allow us to obtain, after some calculations,

$$\frac{dk^t}{d\lambda} = -\frac{R_{,tr}}{R_{,r}^3} (k_r)^2 - \frac{R_{,t}}{R^3} (k_\phi)^2, \tag{2.62}$$

$$\frac{dk_r}{d\lambda} = -\frac{R_{,rr}}{R_{,r}^3} (k_r)^2 - \frac{R_{,r}}{R^3} (k_\phi)^2, \tag{2.63}$$

$$k_\phi = \text{constant}. \tag{2.64}$$

For photons, $ds^2 = 0$, together with (2.58)-(2.60) gives

$$(k^t)^2 = \left(\frac{k_r}{R_{,r}}\right)^2 + \left(\frac{k_\phi}{R}\right)^2. \tag{2.65}$$

The equation for the redshift z of the source, in comoving coordinates is [31]

$$1 + z = \frac{k^t}{(k^t)_p}, \tag{2.66}$$

k^t and $(k^t)_p$ being the time component of the photon wave-vector at the source and at the observer, respectively.

The set of differential equations (2.58)-(2.63) can be integrated with the following initial conditions at the observer:

$$t = t_p, \quad r = r_p, \quad (k^t)_p = 1. \tag{2.67}$$

With these conditions, the redshift of the source reads

$$1 + z = k^t. \tag{2.68}$$

We denote

$$R_p \equiv R(t_p, r_p), \quad R'_p \equiv R_{,r}(t_p, r_p) \tag{2.69}$$

and so forth. The observer at (t_p, r_p) sees the photon trajectory making an angle α with the direction toward the centre of the Universe. Consequently, we can write

$$(k_r)_p = a \cos \alpha, \quad (k_\phi)_p = b \sin \alpha. \tag{2.70}$$

Substituting the former values of the component of $(k_\mu)_p$ into (2.65), written at (t_p, r_p), we find

$$a = R'_p, \quad b = R_p \tag{2.71}$$

and (2.64) becomes

$$k_\phi = R_p \sin \alpha. \tag{2.72}$$

Now, inserting this expression into (2.65), we get an expression for k_r which can be substituted into the set of differential equations and, after some calculations, yields the reduced system of three differential equations for three unknowns, t, r and k^t, which represents the null geodesics defining the past light cone of the observer:

$$\frac{dt}{d\lambda} = k^t, \tag{2.73}$$

$$\frac{dr}{d\lambda} = \pm \frac{1}{R_{,r}} \left[(k^t)^2 - \left(\frac{R_p \sin \alpha}{R} \right)^2 \right]^{1/2}, \tag{2.74}$$

$$\frac{dk^t}{d\lambda} = -\frac{R_{,tr}}{R_{,r}} (k^t)^2 + \left(\frac{R_{,tr}}{R_{,r}} - \frac{R_{,t}}{R} \right) \left(\frac{R_p \sin \alpha}{R} \right)^2, \tag{2.75}$$

with plus and minus signs in (2.74) representing an observer looking inwards and outwards, respectively, provided that the affine parameter λ is chosen to increase from $\lambda = 0$ at (t_p, r_p) to λ at the source (t, r). The redshift follows from (2.68).

2.5 MODELLING A GALAXY PLUS BLACK HOLE FORMA- TION

The aim here is to model the formation of a galaxy with a central black hole, starting from an initial fluctuation at recombination. The model consists of two parts connected across a comoving boundary $M = M_{BH}$, with M_{BH} the estimated present-day mass inside the black hole horizon. In the exterior part, we take existing observational data for the present-day density profile, and the initial fluctuation is made compatible with CMB observations. No observational constraints exist for the interior, so we propose two possible solutions. These are both L-T models, one represents a collapsing body, and the second represents a dense Kruskal-Szekeres wormhole in the sense of [39].

2.5.1 A GALAXY WITH A CENTRAL BLACK HOLE

This is a summary of research carried out by [40]. It has become generally accepted that most large galaxies contain central black holes, e.g. [41]. We will show how such a galaxy formation can be described by an L-T model. Such a model may be an acceptable first approximation since, although spiral galaxies are not spherically symmetric, both the core and the halo (together containing more mass than the disc) are quite close to it. Also, real galaxies rotate and so we would need to use a non-stationary solution with rotating matter in order to investigate the dynamical process of a rotating black hole. However, as yet there are no such solutions and so for the moment we must be satisfied with simpler solutions. M87 will provide the data for a real galaxy-plus-black-hole.

The present state of the galaxy is defined by a mass distribution that consists of two parts:

- The part inside the apparent horizon at t_2. Based on fundamental reasons, apart from the value of M_{BH}, no observational data exist for this region, and so we are free to choose any geometry. Hence, we choose two examples. The first is a simple sub-case of the L-T model in which the black hole does not exist initially but is formed in the course of evolution, whilst the second is a pre-existing wormhole, chosen arbitrarily for simplicity of the calculations.

- The part outside the apparent horizon at t_2. Here we use an approximation to the observationally determined density profile of the M87 galaxy. This part extends inwards to a sphere of mass M_{BH}, the observationally determined mass of the black hole: we shall choose M_{BH} to mean $M_{BH}(t2)$.

The boundary between the inside and outside at times other than t_2 goes along a comoving mass shell, so that at $t < t_2$ the apparent horizon resides in the inside part.

It would be natural to use the last scattering epoch for the initial time t_1, and this is attempted. However, no usable observational data exist for amplitudes of the temperature fluctuations of the CMB at such small scales. The expected angular scale on the CMB sky of a perturbation that will develop into a single galaxy ($0.004°$) is much smaller than the current best resolution of around $0.1°$. Consequently, an exactly homogeneous initial density is tried in one numerical experiment, and a homogeneous initial velocity in a second. Since the first approach led to an unacceptable configuration at t_2, a homogeneous initial velocity was used, which then implied an initial density perturbation with an amplitude of order 10^{-3}.

2.5.2 A COLLAPSED BODY

We take an $E < 0$ L-T model, with a regular centre, whose Bang function $t_B(M)$ is

$$t_B(M) = -bM^2 + t_{B0} \tag{2.76}$$

and whose Big Crunch function is

$$t_C(M) = aM^3 + T_0 + t_{B0}, \tag{2.77}$$

where the parameter T_0 is the lifetime of the central worldline $M = 0$, and a, b and t_{B0} are parameters. Since $t = t_C$ at $\eta = 2\pi$, we find from (2.9) and (2.10) that

$$E(M) = -\frac{1}{2}\left(\frac{2\pi M}{t_C - t_B}\right)^{2/3} = -\left(\frac{\pi^2}{2}\right)^{1/3}\frac{M^{2/3}}{(aM^3 + bM^2 + T_0)^{2/3}}. \tag{2.78}$$

As $M \to \infty$, we have $t_B \to -\infty$, $t_C \to +\infty$ and $E \to 0$. Hence, the space contains infinite mass and has infinite volume.

We require the continuity of the L-T arbitrary functions and their derivatives at $M = M_{BH}$ in order to assure a smooth match between the interior and the exterior modelling, so taking the form of $t_B(M)$ and $E(M)$ given by (2.76) and (2.78), we solve for the constants t_{B0}, T_0, a and b, so that E, t_B, dE/dM and dt_B/dM are matched at the boundary:

$$t_{B0} = \left[t_B - \frac{M}{2}\frac{dt_B}{dM}\right]_{M=M_{BH}}, \tag{2.79}$$

$$T_0 = \left[\frac{M}{6}\frac{dt_B}{dM} + \frac{4\pi M}{3(-2E)^{3/2}} + \frac{2\pi M^2}{(-2E)^{5/2}}\frac{dE}{dM}\right]_{M=M_{BH}}, \tag{2.80}$$

$$a = \left[\frac{1}{3M^2}\frac{dt_B}{dM} + \frac{2\pi}{3M^2(-2E)^{3/2}} + \frac{2\pi}{M(-2E)^{5/2}}\frac{dE}{dM}\right]_{M=M_{BH}}, \tag{2.81}$$

$$b = -\left[\frac{1}{2M}\frac{dt_B}{dM}\right]_{M=M_{BH}}. \tag{2.82}$$

2.5.3   A WORMHOLE

We have no way of knowing anything about the spacetime and matter interior to M_{BH}, and so we can equally well fit in a dust-filled wormhole of the Kruskal-Szekeres type, constructed with the L-T metric. The essential requirement is that, at the centre of the wormhole, M must have the minimum value M_{min}, and $E(M_{min}) = -1/2$. The minimum lifetime (time from past to future singularity) of the wormhole is then $2\pi M_{min}$. The following two functions are chosen:

$$t_B = t_{B0} - b(M - M_{min})^2, \tag{2.83}$$

$$E = -\frac{M_{min}}{2M} + a(M - M_{min}). \tag{2.84}$$

From these, the conditions for matching to an exterior at some M are

$$t_{B0} = \left[t_B + \frac{M}{2}\frac{dt_B}{dM}\left(M\frac{dE}{dM} \pm \sqrt{1 + 2E + M^2\left(\frac{dE}{dM}\right)^2} \right) \right]_{M=M_{BH}}, \tag{2.85}$$

$$M_{min} = \left[M^2\frac{dE}{dM} + M\left(1 \pm \sqrt{1 + 2E + M^2\left(\frac{dE}{dM}\right)^2} \right) \right]_{M=M_{BH}}, \tag{2.86}$$

$$a = \left[\frac{1}{2}\frac{dE}{dM} - \frac{1}{2M}\left(1 \pm \sqrt{1 + 2E + M^2\left(\frac{dE}{dM}\right)^2} \right) \right]_{M=M_{BH}}, \tag{2.87}$$

$$b = \left[\frac{dt_B}{dM} \Big/ \left\{ 2M\left(M\frac{dE}{dM} + \pm\sqrt{1 + 2E + M^2\left(\frac{dE}{dM}\right)^2} \right) \right\} \right]_{M=M_{BH}}. \tag{2.88}$$

This model is not very flexible, it was chosen for simplicity. The lifetime of the wormhole is determined by the matching, thereby fixing the value of M_{min}. The wormhole lifetime could be a free parameter in a different model.

2.5.4   THE EXTERIOR GALAXY MODEL

Since M87 is assumed to contain a large black hole, we choose it as the density profile of the final state. The density profile for its outer part had been proposed some time ago [42]:

$$\rho(s) = \frac{\rho_0}{(1 + bs^2 + cs^4 + ds^6)^n}, \tag{2.89}$$

where $\rho_0 = 1.0 \times 10^{-3}$ g/cm^3, b=0.9724, $c = 3.810 \times 10^{-3}$, $d = 2.753 \times 10^{-8}$ and $n = 0.59$. The distance from the centre, s, measured in arc minutes, is related to the actual distance r by

$$s = \frac{r}{D}\frac{10800}{\pi} := r\delta, \tag{2.90}$$

where D is the distance from the Sun to the galaxy. In this case we require a profile that goes to infinity at $r \to 0$, to allow for the black hole singularity, and a density expressed as a function of mass. Now, the mass profile corresponding to (2.89) is not an elementary function, but the following simple profile (with the same value of ρ_0) is a close approximation to (2.90), in the region considered by [42]:

$$\rho(r) = \frac{\rho_0}{(\delta r)^{4/3}}. \tag{2.91}$$

The corresponding mass distribution is

$$\tilde{M}(r) = \frac{12}{5}\pi\rho_0 r^{5/3}\delta^{-4/3} + M_S, \tag{2.92}$$

where a constant M_S has been added to $\tilde{M}(r)$ to make it singular at $r = 0$. Hence,

$$r = \left[\frac{5(M - M_S)\delta^{4/3}}{12\pi\rho_0} \right]^{3/5} \tag{2.93}$$

and

$$\rho(M) = \frac{12\pi}{5}^{4/5} \rho_0^{9/5} \delta^{-12/5} (M - M_S)^{-4/5}. \tag{2.94}$$

From (2.21), we determine the corresponding $R(M)$ using

$$R^3 = \frac{3}{4\pi} \int\limits_{M_S}^{M} \frac{dx}{\rho(x)}, \tag{2.95}$$

which gives

$$R(M) = \left(\frac{5}{12\pi\rho_0} \right)^{3/5} \delta^{4/5} (M - M_S)^{3/5}. \tag{2.96}$$

Using the requirement that $R = 2M$ at $M = M_{BH}$, we can now determine M_S, i.e.

$$M_{BH} = \frac{1}{2} \left[\left(\frac{5}{12\pi\rho_0} \right)^{3/5} \delta^{4/5} (M - M_S)^{3/5} \right]. \tag{2.97}$$

Hence we find

$$M_S = M_{BH} - \frac{12\pi\rho_0}{5\delta^{4/3}} (2M_{BH})^{5/3}. \tag{2.98}$$

It follows that $M_S < M_{BH}$, as it should.

2.5.5 NUMERICAL EVOLUTION OF THE MODELS

This two-step model construction uses an adaptation of programs written for the papers by Krasińsky and Hellaby. First, the exterior profiles are used as input to the methods of Section 2.3.1, solving numerically for $E(M)$ and $t_B(M)$ for $M_{BH} \leq M \leq M_{galaxy}$. The values of E and t_B and their derivatives at M_{BH} are extracted, and the parameters of the interior model calculated from them. Then, the functions E and t_B are numerically extended into the interior model down to $M = 0$ or $M = M_{min}$. From these data, existing programs are used to reconstruct the model evolution.

The first model uses a flat initial profile at time $t_1 = 10^5$ yr, and the final density profile of Section 2.5.4 is used for the galaxy at time $t_2 = 14$ Gyr, both of which are exterior to M_{BH}. The interior of M_{BH} is a black hole formed by collapse, as described by (2.76) and (2.78), with parameters determined by the matching (2.79)-(2.82). Geometric units are chosen so that 10^{11} $M_\odot$ is the unit mass. In these units, the parameters are:

$$a = 2.5 \times 10^{14}, \quad b = 41525.5859, \quad t_{B0} = 8043.214, \quad T_0 = 8.901 \times 10^{11}. \tag{2.99}$$

It is found that the density fluctuations at recombination are of the order of 10^{-5} (consistent with CMB limits), and the black hole singularity forms at time $T_0 = 13.894$ Gyr, so it is 106 million years old by today.

The second model uses the identical exterior, but the interior is a full Kruskal-Szekeres type black hole containing a temporary wormhole, as described by (2.83) and (2.84), with parameters determined by the matching (2.85)-(2.88). The same geometric units are used, and using the minus sign in (2.85)-(2.88), the parameters are:

$$a = -4.8597 \times 10^{-8}, \quad b = 41525.5859, \quad t_{B0} = 8043.214, \quad M_{min} = 1.8571 \times 10^{-11}. \tag{2.100}$$

Using the plus sign gives $M_{min} = 0.06 > M_{BH} = 0.03$, which is not acceptable.

Since the exteriors are identical, the fluctuations of density at recombination (t_1) outside M_{BH} are well within CMB limits. The wormhole mass (minimum in M) is $M_{min} = 1.8571\ M_\odot$, and the future singularity first forms at $T_0 = 5.7476 \times 10^{-5}s$ after the past singularity (the future and past black hole singularities are the extension of the crunch and bang into the middle of the wormhole). The very short lifetime of the wormhole is a consequence of the need for E to go from $-1/2$ all the way up to -1.3435×10^{-9} and arrive there with a negative gradient. By (2.17), a comparison of the lifetime at the neck, where $T = T_0$, $M = M_{min}$ and $E = -1/2$, and the boundary gives

$$\frac{T_0}{T(M_{BH})} = \frac{M_{min}}{M_{BH}} \times (2 \times 1.3435 \times 10^{-9})^{3/2} < 8.6 \times 10^{-23}, \tag{2.101}$$

since $M_{min} < M_{BH}$, which shows that the wormhole lifetime must be an extremely small fraction of the galaxy lifetime.

This example effectively highlights the fact that the age of the central black hole may be impossible to determine observationally, and that the two kinds of black holes are observationally indistinguishable. By recombination (t_1), this black hole has accreted $8150917\ M_\odot$ within the apparent horizon, which is only 0.161AU across. It will be a long time before any effect this might have on the CMB becomes observable.

In view of the paucity of data, this approach was the first exploratory step into an uncharted territory rather than an actual model to be compared with observations. The main limitation of the spherically symmetric L-T model is a lack of rotation, which slows collapse and stabilises structures. Thus the model is good for much of the evolution into the non-linear regime, but becomes less realistic as collapse sets in.

The results show that the L-T model is a very useful tool for this kind of investigation. However, for its parameters to be fine-tuned to results of observations, the observational data would have to be re-interpreted against the background of the L-T geometries.

2.6 MODELLING A RICH GALAXY CLUSTER

2.6.1 THE MOST REALISTIC MODEL

Here we choose the mass unit $1\ M_G = 10^{15}\ M_\odot$, and we choose units in which $c = 1$ and $G = 1$. The gravitational units of time and distance are $1\ T_G = 156$ yr and $1\ L_G = 47.84$ pc.

The galaxy cluster A2199, from the Abell cluster, is one of the objects that we choose to model. The following (Newtonian!) 'universal profile' is in use in astronomy [43]:

$$\rho(R) = \rho_b \frac{\delta}{(R/R_S)(1 + R/R_S)^2}, \tag{2.102}$$

where $\rho_b = 8 \times 10^{-30}$ g/cm^3 is the average density in the Universe, $\delta = 77440$ is a dimensionless factor and $R_S = 3457\ L_G = 1.65 \times 10^5$ pc $= 5.11 \times 10^{18}$ km is a scale distance. The profile is said to apply for R changing by two orders of magnitude [43].

For this procedure, we need the density as a function of mass. The calculation $\rho(R) \to M(R) \to R(M) \to \rho(M)$ can always be done numerically, but it is more important to have an exact explicit formula. Therefore, the 'universal profile' is approximated by the following $\rho(M)$ profile:

$$\rho(M) = \rho_b \frac{B_2}{1 + e^{\sqrt{M}/\mu_2}}, \tag{2.103}$$

where $B_2 = 498500$ and $\mu_2 = 0.07144\ M_G$.

It is assumed that the initial density perturbation contained a mass of about 0.01 of the final mass, so for the initial profile at t_1 we choose

$$\frac{\rho}{\rho_b} = \begin{cases} 1 + A_1[1 + \cos\frac{100\pi M}{M_C}] & \text{for} \quad M < \frac{M_C}{100} \\ 1 & \text{for} \quad M > \frac{M_C}{100}. \end{cases} \tag{2.104}$$

Here, $A_1 = 1.5 \times 10^{-5}$ and $M_C = 1.182 M_G$ is the mass within the compensation radius (a compensated void is one where the mass within it is the same as the mass of the background that would occupy the same space).

34

It is found that $E(M)$ is everywhere negative, which means that all matter within the model will eventually collapse. Also, it is found that the difference in age between the outer part of the cluster and its central part is approximately $0.1\, T_G \approx 15.6$ years, i.e. this Big Bang is almost simultaneous. However, since $t_B(M)$ is an increasing function, this implies a shell crossing, but this would occur before t_1, where the model does not apply anyway.

Now, we can calculate the associated velocity distribution $b_1(M) = R_{,t}(t_1, M)$ at t_1, since we are given $t_B(M)$ and $E(M)$. It is found that the relative amplitude at the centre of the cluster is about 5×10^{-4}, which is within observational limits.

2.6.2   RESULTS OF SOME OTHER NUMERICAL EXPERIMENTS

For the evolution from a homogeneous initial density to a galaxy cluster (another profile approximating the 'universal profile' [36]) another velocity amplitude at t_1 is obtained,

$$(\Delta b/b)(t_1)|_{max} = 5.2 \times 10^{-4}, \tag{2.105}$$

which is on the border of the observationally implied range. This means that a pure velocity perturbation can very nearly produce a galaxy cluster.

For the evolution from a homogeneous initial velocity to a galaxy cluster, with the same final profile as above, the following density amplitude at t_1 is obtained,

$$(\Delta \rho/\rho)(t_1)|_{max} = 12 \times 10^{-3}, \tag{2.106}$$

which differs from the observationally allowed value by three orders of magnitude. Consequently, density perturbations generate structures far less efficiently than velocity perturbations.

[44] demonstrate that a smooth evolution can take an initial condensation to a void. Hence, the final structure that will emerge is not determined by the initial density distribution; the velocity distribution can obliterate the final step. The proponents of the classical structure formation paradigm should take this very seriously, since they assume that density fluctuations alone are responsible for the creation of structure.

In conclusion, L-T models can be very effective at producing present day galaxy clusters provided we take the contribution of velocity perturbations very seriously.

2.7   MODELLING A VOID

In this section, we check whether it is possible to evolve a void from small initial velocity and density perturbations imposed on a homogeneous background [46]. We will also check what is the influence on the structure formation of the following factors:

- The shape and the amplitude of the initial perturbations.

- The evolution time.

- The expansion rate.

- The outflow of mass from the central part of the void.

Voids are vast regions where only a few instead of thousands of galaxies are observed. From astronomical observations, about 40% of the volume of the Universe is taken up by voids [45]. Therefore, void formation is a very probable process and not an isolated event. It is quite easy to reproduce high-density regions when dealing with gravity, for example, by setting the initial conditions so that collapse or shell crossings occur. However, this cannot be done in the case of low-density regions. Consequently, the study of void formation gives us a better understanding of the Universe in its early stages of evolution.

All models in this section are specified by the initial velocity and density distributions and the work and results presented in [46], are used throughout this section.

The evolution of the void will be calculated using six different background models, which have the following parameters: **1** $\Omega_{mat} = 0.27$, $\Omega_\Lambda = 0$, **2** $\Omega_{mat} = 0.39$, $\Omega_\Lambda = 0$, **3** $\Omega_{mat} = 0.27$, $\Omega_\Lambda = 0.73$, **4** $\Omega_{mat} = 1$, $\Omega_\Lambda = 0$, **5** $\Omega_{mat} = 11$, $\Omega_\Lambda = 0$, **6** $\Omega_{mat} = 0.27$, $\Omega_\Lambda = 1.64$. Some of these models, especially the elliptic ones without cosmological constant, are inconsistent with the observations. These are used to check which of the four factors listed above are more important in the process of void formation, and are not used in order to obtain a model of the observed Universe. In order to compare the various models, let us assume that the initial conditions are independent of the background model.

In order to determine the evolution of the L-T model, one needs two functions, and in this section these will be the initial density and velocity distributions. However, this is not the only method; the evolution can also be determined by specifying the initial and final density profile [35], or the initial velocity and final density distributions [36].

2.7.1 THE ALGORITHM

Numerical methods used in this section are taken from [47] and [48].

1. The initial time t_1 is chosen to be the time of last scattering, and is calculated from the following formula for a background FRW universe:

$$t(z) = \frac{1}{H_0} \int\limits_z^\infty \frac{d\tilde{z}}{(1+\tilde{z})\sqrt{D(\tilde{z})}}, \tag{2.107}$$

where

$$D(z) = \Omega_\Lambda + \Omega_K(1+z)^2 + \Omega_m(1+z)^3 + \Omega_\gamma(1+z)^4. \tag{2.108}$$

H_0 is the present Hubble constant, and:

$$\Omega_\Lambda = \frac{1}{3}\frac{c^2\Lambda}{H_0^2}, \tag{2.109}$$

$$\Omega_K = 1 - \Omega_\gamma - \Omega_m - \Omega_\Lambda, \tag{2.110}$$

$$\Omega_\gamma = \frac{8\pi aGT_{CMB}^2}{3H_0^2}, \tag{2.111}$$

where T_{CMB} is the current temperature of the CMB (2.73 K), $a = 4\sigma/c$ and σ is the Stefan-Boltzmann constant. For the lower limit, $z = 1089$ [49] is used as the redshift at last scattering.

2. The initial density and velocity fluctuations, imposed on this homogeneous background, are defined by $\delta(l)$ and $\nu(l)$ of radius l, as listed in Tables 2.1 and 2.2 respectively, and the actual density and velocity follow from

$$\rho_i(l) = \rho_b(1 + \delta_i(l)) \tag{2.112}$$

$$u_i(l) = u_b(1 + \nu_i(l)) \tag{2.113}$$

The parameter l is defined as the areal radius at the moment of last scattering, measured in kiloparsecs, and is also used for the radial coordinate, i.e.

$$r = l = \frac{R_i}{d} = \frac{R(r, t_i)}{d}, \tag{2.114}$$

where $d = 1$ kpc. Background values are calculated as follows:

$$\rho_b = \rho_0(1 + z_1)^3, \tag{2.115}$$

$$u_b = lH_0\sqrt{D(z_1)}, \tag{2.116}$$

36

where ρ_0 and H_0 are the current values of the average matter density in the Universe and of the Hubble constant, respectively.

3. Then the mass inside a shell of radius R_i, measured in kiloparsecs, is calculated by integrating (2.4):

$$M(l) - M(0) = \frac{\kappa c^2}{2} \int_{l_{min}}^{l} \rho_i(l') l'^2 dl' \big|_{t=t_1}.$$

(2.117)

Since the density distribution has no singularities or zeros over extended regions, it is assumed that $l_{min} = 0$ and $M = 0$ at $l = 0$. This integration was done using Bode's rule, with step size 2.5 pc.

4. The function E is calculated from R_i, $V = (R_{,t})_i$, M and a chosen Λ value, using (2.3).

5. Then t_B is calculated from (2.8) using Simpson's integration, with step size 10^{-5} l.

6. Once M, E and t_B are known, the L-T model can be calculated for any instant. Solving (2.3) with the second-order Runge-Kutta method for $R(t,l)$ along each constant l worldline, the value of $R(t,l)$ and $R_{,t}(t,l)$ are calculated up to the present epoch. The time step is 5×10^5 yr.

7. The density $\rho(t,l)$ is then found from (2.4), using the five-point differentiating formula. The adjusted differences between adjacent worldlines, used in estimating derivatives is 10 pc.

8. For the purpose of comparing the results with observational data, the real density is not presented but, instead, the average one, i.e.

$$\delta = \frac{\langle \rho \rangle}{\bar{\rho}} - 1,$$

(2.118)

where $\bar{\rho}$ is the present background density

$$\bar{\rho} = \frac{3Mc^2}{4\pi G R^2}.$$

(2.119)

9. The current expansion rate inside voids is represented by the equivalent of the Hubble parameter, which is defined as 1/3 of the expansion scalar:

$$H = \frac{1}{3}\theta = 2\frac{R_{,t}}{R} + \frac{R_{,rt}}{R_{,r}}.$$

(2.120)

2.7.2 THE VOID MODELS

2.7.2a Initial perturbations of homogeneity

Due to a lack of precise observational data, it is not possible to calculate the exact profile of the initial density and velocity perturbations. From measurements of CMB radiation, one can estimate only the amplitudes of these profiles. Intuitively, it can be expected that the region which in the future would become a void should have, at the initial instant, a minimum of density and a maximum of velocity at the centre. The chosen initial density and velocity distributions fulfilling the above conditions are presented in Figure 2.1. From this, some initial conclusions can be made: we can say that the amount of mass

re-distribution determines the current depth of the void, i.e. the mass outflow. This outflow depends on the age of the void and on the expansion rate, with the major influence on the structure formation coming from the shell expansion.

The final density contrast in models **4** and **5** is much more negative than in models **1-3**, and in models **4** and **5** the expansion rate is bigger than in models **1-3**, even though the age of the Universe in these models is much lower.

Models **1-5** cannot, unfortunately, recover the observed density contrasts of today's voids. The proper depth can only be obtained in model **6**, where the age of the Universe is significantly larger. Physically this makes sense in that we require a density contrast close to -1, so the void really is $\sim$ empty.

The expansion rate of the void, in limits estimated by the various astronomical observations, is of greater importance, compared to its age. In models **2** and **3**, the expansion rate of shells is similar, and the final density contrast in model **3** is lower due to the available time for evolution being 2 billion years longer.

We now check how big the influence of the initial shape of the density and velocity perturbations is.
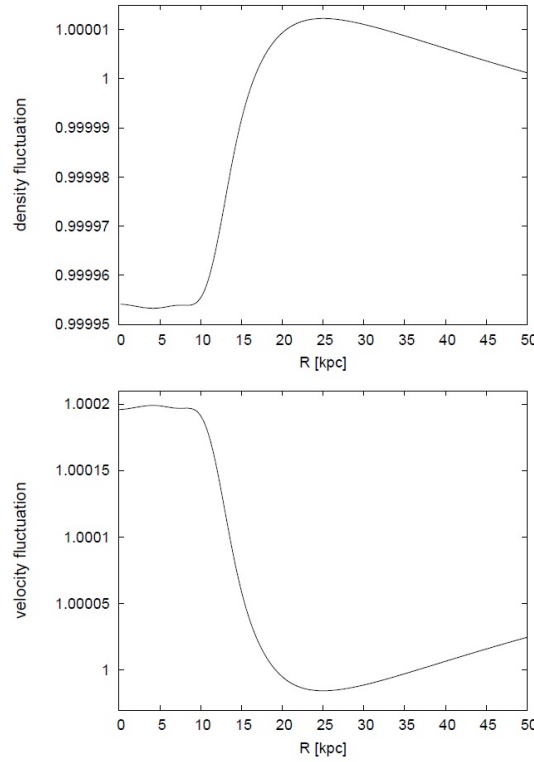
Figure 2.1: The initial density (upper) and velocity (lower) perturbations, as discussed in Section 2.7.2a. Figure taken from [46].

2.7.2b Homogeneous velocity profile

For this case, the initial density profile δ is as in Figure 2.1, while the initial velocity profile is $\nu = 0$. The explicit formulae for these profiles are presented in Tables 2.1 and 2.2. The results shown in Figure 2.4 seem to be surprising. The mass re-distribution is almost the same (with the exeption of model **6**), and the diameters are similar, but the current density profiles are different. In this case, an additional factor responsible for the void formation is seen; a faster expansion rate. This faster expansion compared to the homogeneous background makes the difference between the density in the central regions of the void density in the background increase with time, even when the mass of the shell inside the region of $R(t, r)$

Section	Model	Density Perturbation	Parameters	Graph	Output
2.7.2a	1-6	$\delta_{INIT}(l) = A(b\tan^{-1}c - dl - fe^{-g^2} - e^{-h^2} - ie^{-j^2})k$	$A = 1.1 \times 10^{-5}, b = 4, c = 0.16l - 2.2, d = \frac{1}{7}, f = 0.5, g = \frac{l-7}{6}, h = \frac{l-9}{7}, i = 1.4, j = \frac{l-11}{3}, k = \frac{1}{1+0.03l}$	Fig. 2.1	Figs. 2.2 & 2.3
2.7.2b	1-6	$\delta = \delta_{INIT}(l)$		Fig. 2.1	Fig. 2.4
2.7.2c	1-6	$\delta = 0$			Similar to Figs. 2.2 & 2.3
2.7.2d	1-6	$\delta_{AMP} = A(b\tan^{-1}c - dl - fe^{-g^2} - e^{-h^2} - e^{-j^2})k$	$A = 7.5 \times 10^{-4}, b = 4, c = 0.08l - 1.1, d = \frac{1}{11}, f = 0.4, g = 0.25, h = \frac{l-2}{7}, j = \frac{l-4}{3}, k = \frac{1}{1+0.03l}$		Fig. 2.5
2.7.2e	1,2,3	$\delta_{1,2,3}(l) = 100 \times \delta_{INIT}(l)$		Fig. 2.6	Figs. 2.7 & 2.8
2.7.2e	4	$\delta_4(l) = 2 \times \delta_{1,2,3}(l)$		Fig. 2.6	Figs. 2.7 & 2.8

Table 2.1: The initial density perturbations used in the runs. All the values in the table are dimensionless, and the distance parameter is the areal radius in kiloparsecs $l = R_i/1$ kpc. Note that the output figures depend on the initial perturbation in both density and velocity. Table taken from [46].

is not changing very much. Therefore, in the models with greater expansion rate, the density contrast is most negative.

2.7.2c Homogeneous density profile

In contrast to the above, the initial density profile is $\delta = 0$, while the initial velocity profile, ν, is as in Figure 2.1. The explicit formulae for these profiles are presented in Tables 2.1 and 2.2.

The final results are not very different from the ones shown in Figure 2.2. This demonstrates that the velocity distribution in void formation is very significant, while the density distribution is of lesser significance.

2.7.2d Amplitude

Here, the amplitude of the initial fluctuations is increased as compared to the one used in Section 2.7.2a, and is 7.5×10^{-4}. The profiles of the initial perturbations are presented in Tables 2.1 and 2.2, and the final results in Figure 2.5.

The increased amplitude of the initial perturbations results in a void with a higher negative density contrast. Compared to the values estimated from CMB fluctuations, in order to obtain a density contrast near $\delta \sim -0.9$, the amplitude of the initial density profile needed to be increased by more than 70 times, and the amplitude of the velocity profile 20 times. Even so, the value $\delta \sim -0.94$ of the density contrast was not reached, except in the two non-realistic background models. In model 3, the minimum value is -0.873, and in model 4 it is -0.908. Unfortunately, increasing the amplitude leads to a shell crossing in some models.

2.7.2e Observation and a model - a cross check

There were problems in the previous sections generating voids from small initial density and velocity fluctuations, and the only alternative was to use a background model with an extremely large age of the Universe (inconsistent with limits estimated by the various astronomical observations).

In this section, initial profiles that lead to the best fit with observational data are chosen. Only one background model (preferred by astronomical observations) is focused upon, which is $\Omega_{mat} = 0.27$ and $\Omega_\Lambda = 0.73$.

The initial fluctuations are presented in Figure 2.6, and the profiles are presented in Tables 2.1 and 2.2. The results are shown in Figures 2.7 and 2.8. Model **2** has both proper density contrast and smooth edges. The conclusion from numerical experiments with different shapes of the initial profiles is that a

Section	Model	Velocity Perturbation	Parameters	Graph	Output
2.7.2a	1-6	$\nu_{INIT}(l) = A(b\tan^{-1}c - dl - fe^{-g^2} - e^{-h^2} - ie^{-j^2})k$	$A = -4 \times 10^{-5}, b = 4, c = 0.16l - 2.2, d = \frac{1}{7}, f = 0.5, g = \frac{l-7}{6}, h = \frac{l-9}{7}, i = 1.4, j = \frac{l-11}{3}, k = \frac{1}{1+0.03l}$	Fig. 2.1	Figs. 2.2 & 2.3
2.7.2b	1-6	$\nu = 0$			Fig. 2.4
2.7.2c	1-6	$\nu = \nu_{INIT}(l)$		Fig. 2.1	Similar to Figs. 2.2 & 2.3
2.7.2d	1-6	$\nu_{AMP}(l) = A(b\tan^{-1}c - dl - fe^{-g^2} - e^{-h^2} - e^{-j^2})k$	$A = -7.5 \times 10^{-4}, b = 4, c = 0.08l - 1.1, d = \frac{1}{11}, f = 0.4, g = 0.25, h = \frac{l-2}{7}, j = \frac{l-4}{3}, k = \frac{1}{1+0.03l}$		Fig. 2.5
2.7.2e	1	$\nu_1(l) = 37.5 \times \nu_{INIT}(l)$		Fig. 2.6	Figs. 2.6, 2.7 & 2.8
2.7.2e	2,4	$\nu_{2,4}(l) = A(b\tan^{-1}c - dl - fe^{-g^2} - e^{-h^2} - e^{-j^2} - me^{-n^2})(k + p)$	$A = -3.5 \times 10^{-3}, b = 4, c = 0.02l - 0.02, d = \frac{1}{11}, f = 0.7, g = l, h = \frac{l-1}{7}, j = \frac{l-3}{3}, k = \frac{1}{1+0.03l}, m = 1.225, n = \frac{l-39}{12}, p = 5 \times 10^{-4}$	Fig. 2.6	Figs. 2.7 & 2.8
2.7.2e	3	$\nu_3(l) = A(b\tan^{-1}c - dl - fe^{-g^2} - e^{-h^2} - e^{-j^2} - me^{-n^2})(k + p)$	$A = -3.5 \times 10^{-3}, b = 4, c = 0.02l - 0.02, d = \frac{1}{11}, f = 0.7, g = l, h = \frac{l-1}{7}, j = \frac{l-3}{3}, k = \frac{1}{1+0.03l}, m = 0.7, n = \frac{l-39}{12}, p = 5 \times 10^{-4}$	Fig. 2.6	Figs. 2.7 & 2.8

Table 2.2: The initial velocity perturbations used in the runs. All the values in the table are dimensionless, and the distance parameter is the areal radius in kiloparsecs $l = R_i/1$ kpc. Note that the output figures depend on the initial perturbation in both density and velocity. Table is taken from [46].

model of a void consistent with observational data (with the density contrast less than $\delta \sim -0.94$, smooth edges and high density in the surrounding regions) is very hard to obtain within the L-T model, without the occurrence of a shell crossing singularity. The final state of model **2** was very close to this singularity and in model **4** a shell crossing occurred.

The main factor responsible for void formation is the velocity perturbation, with an amplitude of ~ 0.008 near the centre, and dropping below zero in the outer regions (model **3** did not fulfil this condition). The density fluctuation is of less importance. Models **1** and **3** had the same initial density fluctuations, and in model **4**, the the amplitude was two times greater. In spite of these differences, the final results differ only in shape, and not in the depth of the final density contrast.

2.7.3 VOID EVOLUTION CONCLUSIONS

There are five main conclusions to be drawn from the above analysis:

- It was found that velocity perturbations are of greater significance than density perturbations in the process of void formation.

- In the expanding void, mass moves outwards.

- In the numerical experiments that were carried out, the perturbations that were needed to form a realistic present day void had to have a density amplitude of $\delta\rho/\rho \approx 5 \times 10^{-3}$ and a velocity amplitude $\delta V/V \approx 8 \times 10^{-3}$ (in the model with $\Omega_{mat} = 0.27$ and $\Omega_\Lambda = 0.73$).

- There was no significant difference between the evolution of the void in the model with and without
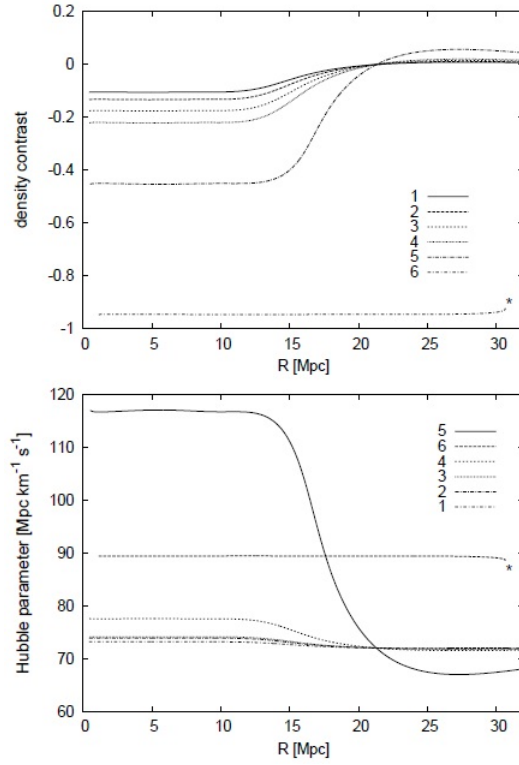
Figure 2.2: The current density contrast and the Hubble parameter for data discussed in Section 2.7.2a, in six different backgrounds, with parameters given in Section 2.7. * - shell crossing. Figure taken from [46].
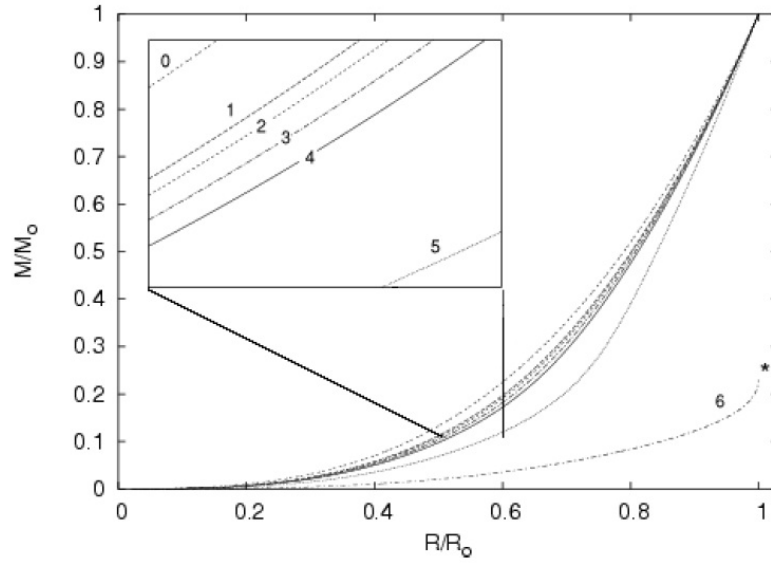
Figure 2.3: The mass re-distribution for data discussed in Section 2.7.2a. R_0 is the smallest R value at which the density takes the background value. The denominator on the y-axis is the mass inside the shell of the areal radius, given by the denominator on the x-axis. **0** - the initial condition; other labels as in Figure 2.2. Figure taken from [46].
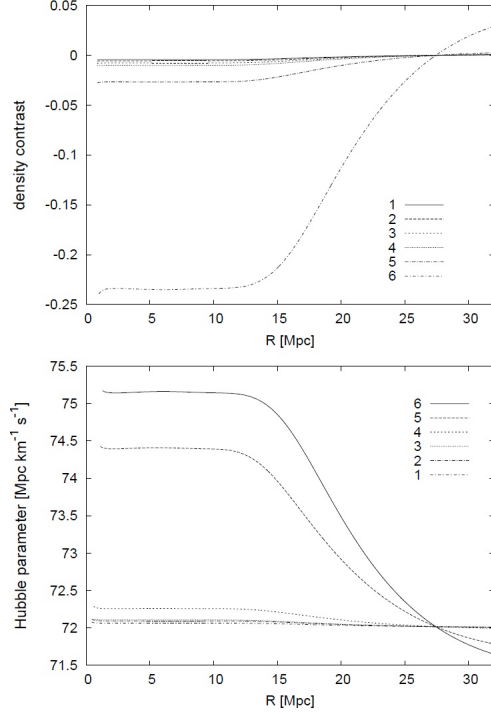
Figure 2.4: The current density contrast and the Hubble parameter for the flat initial velocity profile in six different background models, outlined in Section 2.7. Labels as in Figure 2.2. Figure taken from [46].
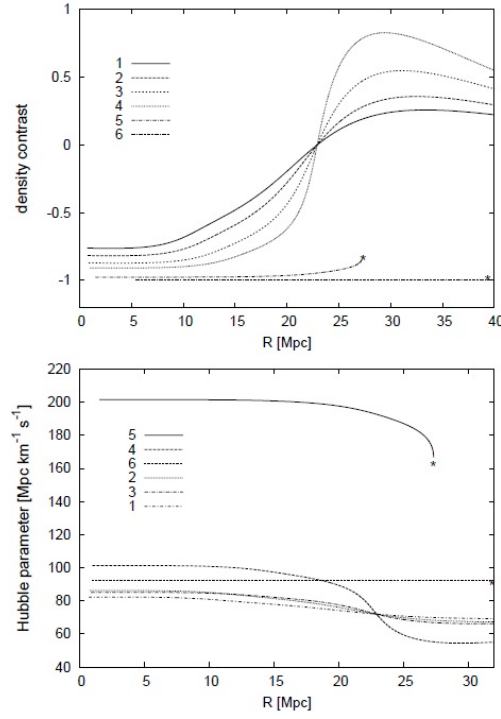
Figure 2.5: The current density contrast and the Hubble parameter for the initial data with higher amplitude of density and velocity perturbations in six different background models, outlined in Section 2.7. Labels as in Figure 2.2. Figure taken from [46].
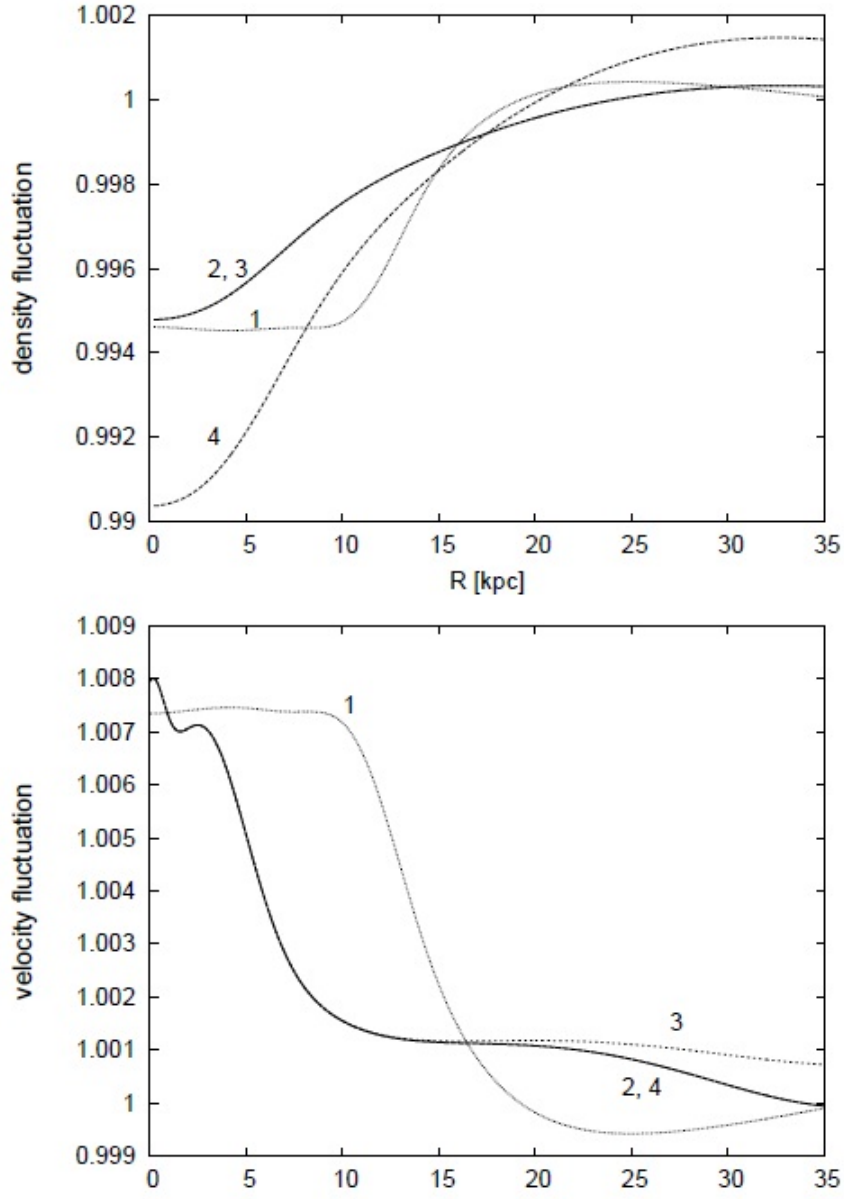
Figure 2.6: The initial density (upper) and velocity (lower) perturbations for the results presented in Figures 2.7 and 2.8. Figure taken from [46].
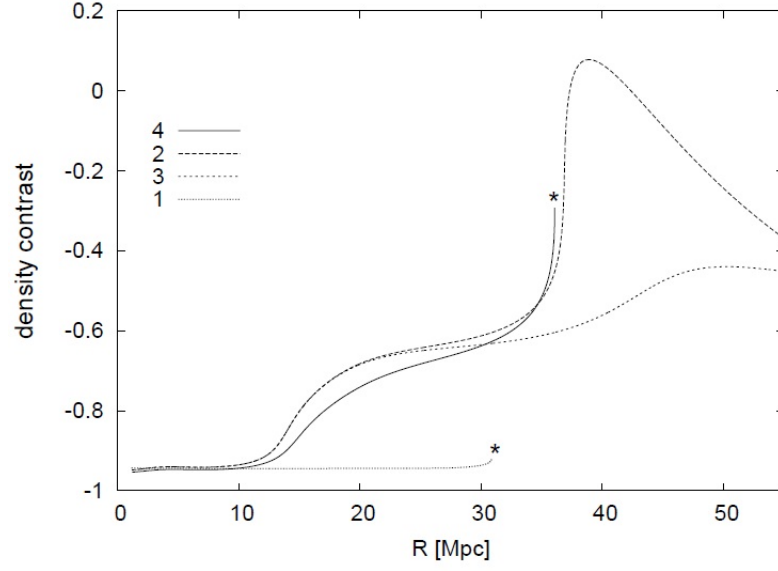
Figure 2.7: The current density contrast for the models discussed in Section 2.7.2e. Figure taken from [46].
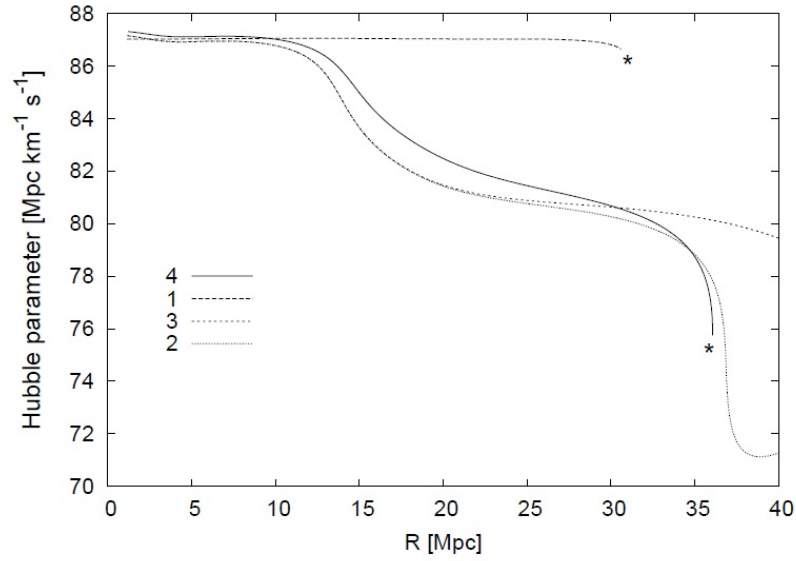
Figure 2.8: The Hubble parameter for the models discussed in Section 2.7.2e. Figure taken from [46].

the cosmological constant. In this latter case, the amplitude of the initial velocity fluctuation needed for this purpose was a little smaller.

- The existence of voids is closely related to the existence of regions of higher density surrounding the voids. In the simulations, there were problems obtaining reasonable profiles for these high density regions, since shell crossing singularities tended to occur. The L-T model breaks down at shell crossings, so to trace the further evolution of the void, focus had to be placed on the central regions of the void. In reality, as density increases, a gradient of pressure would appear, which cannot be described in the L-T model. Since superclusters are observed on the edges of the voids, this singularity is interpreted as an indicator of the presence of a supercluster.

2.8 THE IMPACT OF RADIATION ON VOID FORMATION

In the previous section we found that the initial amplitudes of density and velocity fluctuations needed to generate a void in an L-T model are $\sim 10^{-3}$, whereas the amplitude of baryon density fluctuations estimated from the CMB temperature fluctuations is $\sim 10^{-5}$. Consequently, these L-T model fluctuations are too large to be realistic. Now we examine if this disproportion is due to matter being mostly of non-baryonic nature or to some other physical effects, like the presence of radiation. This issue was first studied by [50] with the Lemaître model discussed in Section 3.1 and the L-T class of models described earlier in this chapter.

The observed redshift of the CMB is $z \approx 1090$, and the pressure of matter at this redshift can be estimated from the perfect gas equation of state:

$$\frac{p}{\rho c^2} = \frac{k_B T}{\mu m_H c^2} \approx 10^{-10}. \tag{2.121}$$

This shows that the pressure of normal matter at last scattering is negligible.

The contribution of radiation to the energy density, however, cannot be neglected, and the ratio of radiation energy density to matter energy density at last scattering is

$$\frac{\rho_{rad}}{\rho_b} = \frac{aT^4}{\rho c^2} = \frac{\Omega_\gamma}{\Omega_m}(1+z), \tag{2.122}$$

which for $\Omega_m = 0.3$ gives

$$\frac{\rho_{rad}}{\rho_b} \approx 0.2. \tag{2.123}$$

As can be seen, this ratio decreases for low redshifts. But, at the early stage of evolution at last scattering, the radiation should have an influence on the evolution of structures. This will be considered further.

2.8.1 THE ALGORITHM

In order to calculate the evolution of a mixture of radiation and matter within the L-T model we first need to specify initial conditions. They consist of velocity fields of both fluids (it is assumed that matter is comoving with radiation, so that radiation contributes only to the energy-density and pressure, where the contributions obey $p_{rad} = \rho_{rad}/3$), initial fluctuations of matter density, expansion rate and radiation.

Time instants

Since it is required that at large distances from the origin the model of a void becomes the Friedmann model, these functions are presented in the form of given fluctuations imposed on a homogeneous background. All background values are calculated for the instant of decoupling (t_1) using (2.107).

The initial density perturbations

The radial coordinate was defined as the areal radius at the moment of last scattering, measured in kiloparsecs:

$$r = l = R(r, t_1)/d, \tag{2.124}$$

where $d = 1$ kpc. The initial density fluctuations, imposed on the homogeneous background, were defined by functions of the radius l, as listed in Tables 2.3 and 2.4, and the actual density fluctuations followed from:

$$\rho_0(l) = \rho_{b0} \times \delta l, \tag{2.125}$$

where ρ_{b0} is the density of the homogeneous background and at the initial instant, and can be expressed as:

$$\rho_{b0} = \Omega_{mat} \rho_{cr} (1 + z)^3. \tag{2.126}$$

The mass inside the shell of radius $R(r, t_1)$ at the initial instant, measured in kiloparsecs, is again calculated from (2.117).

The initial velocity perturbations

The initial velocity fluctuations, imposed on the homogeneous background, were defined by functions of the radius l, as listed in Tables 2.3 and 2.4, and the actual velocity fluctuations followed from:

$$U(l) = U_{b0} \times \nu(l), \tag{2.127}$$

where U_{b0} is the velocity of the homogeneous background at the initial instant, and can be expressed as:

$$U_{b0} = \frac{R_{,t}}{c} = \frac{r a_{,t}}{c}. \tag{2.128}$$

In the FLRW models the time derivative of the scale factor is given by the formula [51]:

$$a_{,t} = a H_0 \sqrt{\mathcal{D}}, \tag{2.129}$$

where $\mathcal{D}$ is given by (2.108). Consequently, the perturbed velocity is

$$U = \frac{(1 + \nu) R H_0 \sqrt{\mathcal{D}}}{c}. \tag{2.130}$$

In the Lemaître models the proper time derivative of the areal radius R, U is just equal to $R_{,t}/c$ in our case, in consequence of the metric of equation 3.1:

$$U = \frac{e^{-A/2} R_{,t}}{c}, \tag{2.131}$$

from which we obtain $R_{,t}$ for a given $\nu(l)$.

The radiation perturbations

In general, the energy density of radiation can be written in the following form:

$$\rho_{rad}(r, t) = \rho_{rad,b} \zeta(r, t), \tag{2.132}$$

where $\rho_{rad,b}$ is the radiation energy density of a homogeneous background. Since from the last scattering instant the radiation fluctuations have always been of small amplitude, let us assume that the time dependence can be separated from the spatial dependence:

$$\zeta(r, t) = \phi(t)[1 + \gamma(r)]. \tag{2.133}$$

Profile	Parameters
$\mathcal{F}(l) = af^{db}e^{df} + g$	$a = (A-g)(-b)^{-db}e^{db}, f = l-b, h = (R-b)^{db}e^{d(b-R)}, g = [1-(-b)^{db}e^{-db}h]^{-1}, d = -0.2, b = -4.6, R_1 = 40, A = 6 \times 10^{-5}$
$\mathcal{G}(l) = A(b\tan^{-1}c - dl - fe^{-g^2} - e^{-h^2} - e^{-j^2} - me^{-n^2})k + p$	$A = -1 \times 10^{-4}, b = 4, c = 0.02(l-1), d = \frac{1}{11}, f = 0.7, g = l, h = \frac{l-1}{7}, j = \frac{l-3}{3}, m = 1.225, n = \frac{l-39}{12}, k = \frac{1}{1+0.03l}, p = -2 \times 10^{-5}$

Table 2.3: Detailed descriptions of the initial fluctuations of Fig. 2.9. All the values in the table are dimensionless, and the distance parameter is the areal radius in kiloparsecs, $l = R_1/1$ kpc. See Table 2.4 and Figs. 2.10 and 2.11.

Let us further assume that the time-dependence amplitude of the radiation is the same as in the homogeneous background, so

$$\phi = 1. \tag{2.134}$$

However, this assumption may have to be modified in the future if observational data on the distribution of radiation become more detailed.

The radiation energy density of a homogeneous background is calculated in the usual way:

$$\rho_{rad,b} = \rho_{rad,b,0}\left(\frac{a_0}{a}\right)^4 = \rho_{rad,b,0}(1+z)^4, \tag{2.135}$$

where $\rho_{rad,b,0}$ is the present value of the radiation energy density and is equal to $4(\sigma/c)T_{CMB}^4$.

Recapitulating we have:

$$\rho_{rad} = 4\frac{\sigma}{c}T_{CMB}^4(1+z)^4(1+\gamma). \tag{2.136}$$

For an exact form of γ see Tables 2.3 and 2.4.

Computing the evolution

The algorithm for computing the evolution consists of the following steps:

- From (2.130), (2.131) and (3.6) the value of $R_{,t}$ and from (3.3) the value of $M_{,t}$ can be calculated. Then, using the predictor-corrector method, the value of $R(t+\tau,r)$ and $M(t+\tau,r)$ in the time step τ can be found. We further denote all the quantities found in this time step by the subscript τ.

- Once R_τ and M_τ are known, we can derive ρ_τ from (3.2).

- Then from (2.136) and the equation of state for radiation $p = 1/3\rho_{rad}$ we derive p_τ.

- From ρ_τ and p_τ we can calculate A_τ by integrating (3.6).

- U_τ can be calculated as follows: From (3.4) and (3.9) we obtain:

$$U^2(t,r) = \frac{2M(t,r)}{R(t,r)} + \frac{1}{3}\Lambda R^2(t,r) - 1 + e^{-B(t_0,r)}\exp\left(\int_{t_0}^{t} \frac{A_{,r}(\tilde{t},r)e^{A(\tilde{t},r)/2}U(\tilde{t},r)}{R_{,r}(\tilde{t},r)}d\tilde{t}\right). \tag{2.137}$$

By solving this equation using the bisection method, for the time $t = t_1 + \tau$, we can calculate U_τ.

- Once U_τ and A_τ are known, $R_{,t}(t,r)$ and then $M_{,t}(t,r)$ can be calculated.

- We repeat these steps until t becomes the current instant.

Results

Measurements of the density contrast inside voids are based on observations of galaxies inside them [45]. However, because in central regions no galaxies are observed, the real density distribution is unknown. Assuming that luminous matter is a good tracer of the total matter distribution, and extrapolating the value of the density contrast measured on the edges of voids (where galaxies are observed) into the central regions, we can conclude that the density inside voids is below $0.06\rho_b$, which is called the limiting value. It is expected that the model will predict a present-day density inside the voids below this value.

A flat Friedmann model with $\Omega_m = 0.27$ and $\Omega_\Lambda = 0.73$ was chosen as a background model. However, in order to check how a choice of background model affects the evolution of voids, at the end of this section three other background models will be also considered.

Figure 2.9 shows the shape of the initial perturbations, and their explicit forms are presented in Tables 2.3 and 2.4. The results plotted in Fig. 2.10 show that four out of seven models voids are formed. As can be seen, models with an inhomogeneous distribution of radiation have no difficulty reproducing regions with density below the limiting value.

To compare the results with the observational data, Fig. 2.11 presents the average density contrast inside the voids as a function of the relative distance from the origin. The average density contrast is given by (2.118). Curve 1 presents the results of run 1, as listed in Table 2.4. Curves NGP and SGP present density contrasts of voids in the 2dFGRS data estimated by [45]. Although the profiles match at the centre, they do not fit accurately at the edge of voids. In this model the density contrast tends to increase faster than is observed, which could be due to assumptions (2.134) and (2.135) about the evolution of radiation, and would suggest that the distribution of radiation did evolve after last scattering. There is another possibility that could explain the difference between these two profiles. The density contrast estimated in [45] is based on observations of galaxies. It is possible that there is non-luminous matter within the walls, and so this procedure does not reproduce the total matter density profile sufficiently well.

Introducing radiation into the calculation we need to know the relation between matter and radiation perturbations. In linear theory there are three concepts of these relations:

1. Adiabatic perturbations, where $\gamma = 4\delta/3$,
2. Isothermal perturbations, where $\gamma = 0$,
3. Isocurvature perturbations, where $\gamma = 4(\delta - \delta_0)/3$. Here δ_0 is some initial value of δ.

It should be stressed that in realistic conditions there are no pure adiabatic, isocurvature or isothermal perturbations and the relations between density and radiation perturbations are more complicated. However, it is instructive to know what kind of relation is more suitable for the process of void formation.

The results presented in Fig. 2.10 imply that voids can be formed out of adiabatic or isocurvature perturbations and there is no significant difference between these two forms of perturbations, as long as the gradient of the radiation is negative. With an isothermal perturbation low density regions cannot be formed as the gradient of radiation is important in the process of void formation.

Finally, let us notice that, in the present-day profiles of Fig. 2.11, the density gradient at the edges of voids is steeper in the models than is observed. There could be several explanations:

1. The shapes of the initial perturbations are not quite correct.
2. The assumption that the radiation distribution did not evolve from last scattering is not fulfilled.
3. Matter around voids can distinctly depart from spherical symmetry.
4. The real density contrast increases faster than the density contrast of luminous matter.
5. Describing radiation as comoving with dust, with the equation of state $p_{rad} = \rho_{rad}/3$ is too crude.

These points must be taken into account in future examinations. However, at this stage we can conclude that, until several million years after last scattering, radiation cannot be neglected in models of structure formation,and that the negative gradient of radiation causes faster expansion of the space inside the void, hence the density contrast decreases faster there. The excess of radiation pressure simply drives matter out of the region destined to be a void and piles it up on the edges. As a result, to evolve structures like voids the amplitude of density fluctuations at last scattering does not have to be larger than 10^{-5}. Therefore, the fluctuations of any non-luminous component at last scattering can be of the same amplitude as the

Run	Profile	Description
1	$\delta_- = -\mathcal{F}, \gamma_+ = +\frac{4}{3}\mathcal{F}, \nu = 1 + \mathcal{G}$	Isocurvature-like perturbations. Reconstructs present-day voids.
2	$\delta_- = -\mathcal{F}, \gamma_- = -\frac{4}{3}\mathcal{F}, \nu = +\mathcal{G}$	Adiabatic perturbations. Collapses after 20 million years. Leads to high density region.
3	$\delta_- = -\mathcal{F}, \gamma_0 = 0, \nu = +\mathcal{G}$	Isothermal perturbations. Does not lead to low-density region.
4	$\delta_+ = +\mathcal{F}, \gamma_+ = +\frac{4}{3}\mathcal{F}, \nu = +\mathcal{G}$	Adiabatic perturbations. Reconstructs the present-day voids.
5	$\delta_+ = +\mathcal{F}, \gamma_+ = +\frac{4}{3}\mathcal{F}, \nu_- = -\mathcal{G}$	Reconstructs present-day voids, but density fluctuations are positive, with velocity perturbations negative.
6	$\delta_0 = 0, \gamma_+ = +\frac{4}{3}\mathcal{F}, \nu_0 = 0$	Reconstructs present-day voids.
7	$\delta_- = -\mathcal{F}, \gamma_- = \delta_- = -\mathcal{F}, \nu = +\mathcal{G}$	Leads to cluster formation with central density $2.1 \times 10^3 \rho_b$

Table 2.4: Summary of run results for models of void formation with inhomogeneous radiation. See Table 2.3 and Figs. 2.9, 2.10 and 2.11.

fluctuations of baryonic matter.

Constraints on background models

Figure (2.10) presents the evolution of voids (the initial conditions like in runs 1 and 3) in four different background models:

(a) $\Omega_m = 1$, $\Omega_\Lambda = 0$, $\Omega_\gamma = 4.77 \times 10^{-5}$,
(b) $\Omega_m = 0.4$, $\Omega_\Lambda = 0$, $\Omega_\gamma = 4.77 \times 10^{-5}$,
(c) $\Omega_m = 0.27$, $\Omega_\Lambda = 0$, $\Omega_\gamma = 4.77 \times 10^{-5}$,
(d) $\Omega_m = 0.27$, $\Omega_\Lambda = 0.73$, $\Omega_\gamma = 4.77 \times 10^{-5}$.

These results imply that in the absence of radiation, or of the gradient of radiation, the structure formation goes on faster in the models which are filled with a greater amount of matter (curves 3a, 3b, 3c and 3d - for more details see [46]). Voids cannot be formed within this kind of radiation perturbations.

The results in Fig. 2.12 imply that the presence of a realistic distribution of radiation is important for void formation - see models 1(c)-(d). Further, the contribution of radiation to the evolution of the system is more significant in models with smaller values of Ω_m. Therefore, the modelling of void formation can put some limits on the values of cosmological parameters. As can be seen, models with $\Omega_m \approx 0.3$ describe observed voids best. However, we cannot constrain the value of the cosmological constant in a similar manner.

2.9 THE COSMOLOGICAL CONSTANT AND THE COINCIDENCE PROBLEM

Since its discovery during the late 1990s [52], [53], the dimming of distant SN Ia has been mostly ascribed to the influence of a mysterious dark energy component. Formulated in a Friedmannian framework, based upon the cosmological principle, this interpretation has given rise to the 'Concordance model'. However, a caveat of such reasoning is that the cosmological principle is derived from the philosophical Copernican assumption and has never been proven.

Moreover, it is well known, since the work of [54], that the inhomogeneities observed in our Universe can have an effect upon the values of the cosmological parameters derived for a smoothed-out or averaged Friedmannian model. A tentative estimate of such an effect was calculated by [55]. He found that the error obtained when using averaging procedures compared to the volume matching, i.e. the procedure proposed by [54] of Friedmann models to inhomogeneous L-T solutions with realistic density profiles implies that
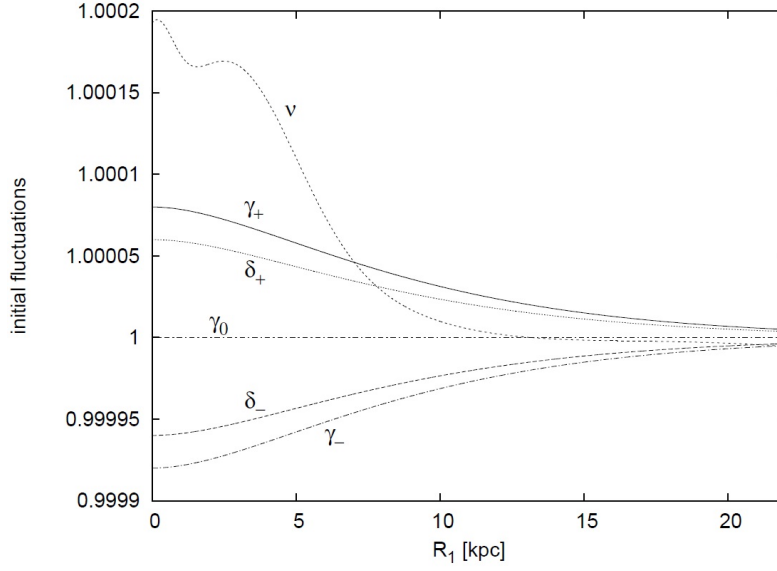
Figure 2.9: The shape of the initial density and velocity fluctuations for void formation with inhomogeneous radiation. See Tables 2.3, 2.4 and Fig. 2.10. Figure taken from [127].
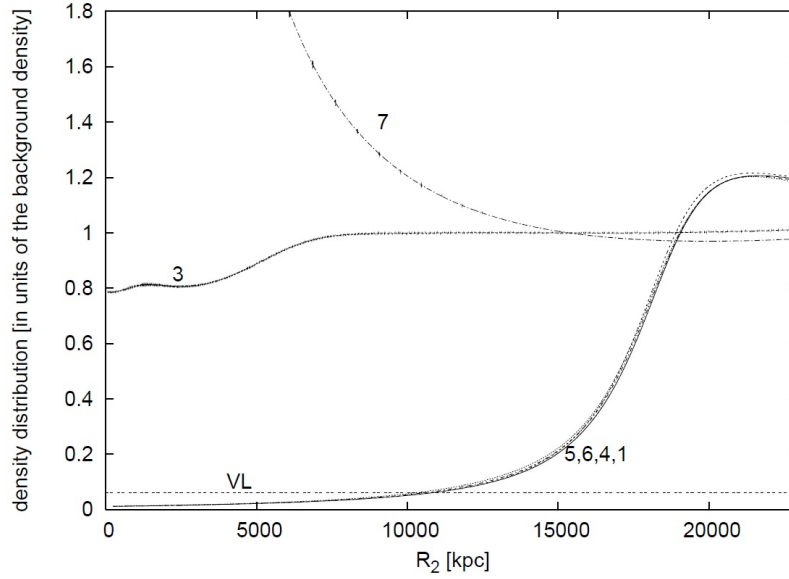
Figure 2.10: The present-day density distribution inside voids when inhomogeneous radiation is included. The curve numbers correspond to the run numbers, as described in Table 2.4. The curve for model 2 is omitted since by t_2 it diverges near the origin. The line denoted by VL (void limit) refers to the measured density inside the voids. Figure taken from [127].
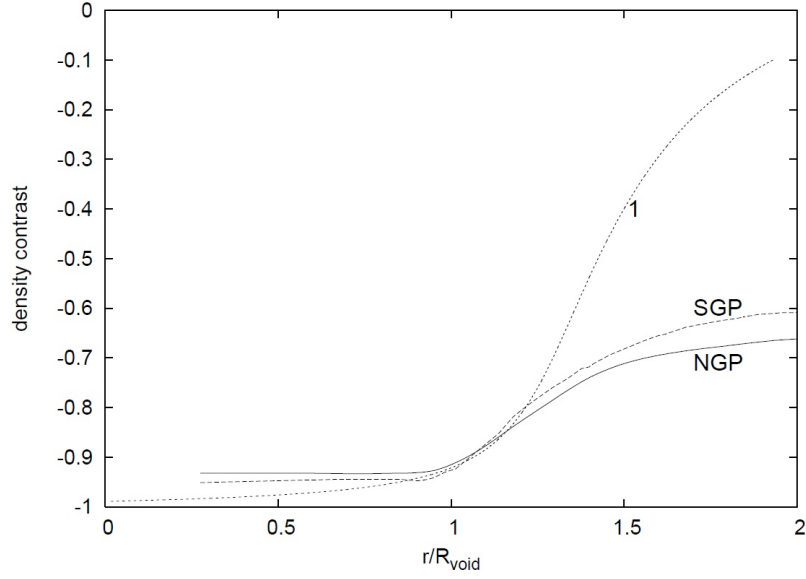
Figure 2.11: Comparison of the present-day density contrast obtained in run 1 (curve 1) with the observed density contrast from [45] (SGP and NGP). Figure taken from [127].
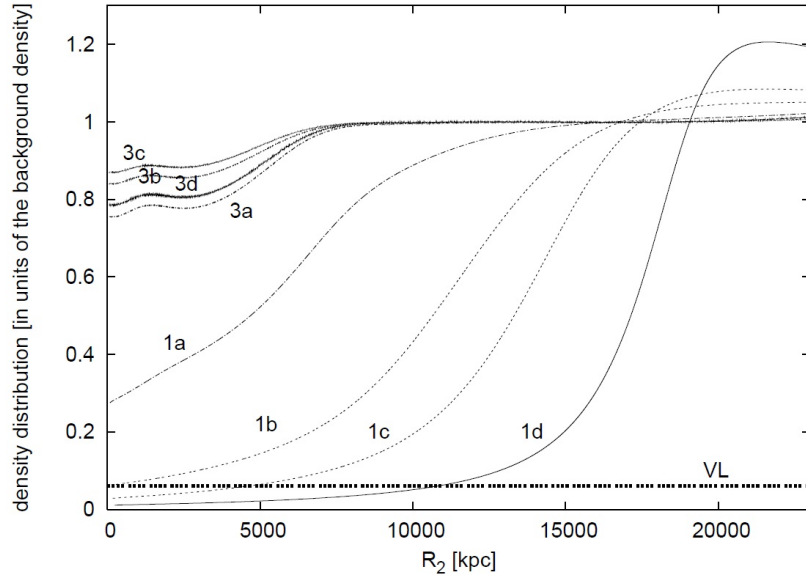
Figure 2.12: The density distribution inside the void with three different background models. The curve numbers correspond to the run numbers (description in Table 2.4) and to the background models (listed on page 48). The curve denoted by VL (void limit) refers to the measured density inside voids. Figure taken from [127].

the mean density and pressure of the averaged Friedmann models are 10-30% underestimated as regards the volume-matched ones. Therefore, even if the cosmological constant is the only component in the Einstein equations beyond ordinary matter, the estimate of its actual value is less straightforward than the conventional wisdom has it.

As regards dark energy, i.e. a negative pressure fluid with an equation of state parameter $\omega \neq -1$, ($\omega = -1$ being the signature of the pure geometric cosmological constant), it remains a phenomenon which cannot be explained in terms of the framework of current physics. This is known as the 'cosmological constant problem'.

Another feature of the luminosity distance-redshift relation inferred from the supernova data when they are analysed in a Friedmannian framework is that it yields a late-time acceleration of the expansion rate, beginning close to the epoch when structure formation enters the non-linear regime. This would imply that we live at a time when the matter-energy density and the dark energy are of the same order of magnitude. This is known as the 'coincidence problem'.

In order to deal with these problems some authors have proposed a modification to the general relativity theory at large distance scales (see, for example, [56]). However, our current purpose is to describe work dedicated to a simpler and more natural proposal, which only makes use of known physics and phenomena. Since it appears that the onset of apparent acceleration and the beginning of structure formation are concomitant, the idea that the SN Ia observations could be reproduced totally or partially by the effect of large-scale inhomogeneities was put forward. This interpretation was first proposed independently by a few authors [57],[58], [19], [59], shortly after the release of the data. Then, after a period of relative disaffection, it experienced a renewed interest.

Three different methods have been used to deal with this proposal: two back-reaction computations, one using an averaging procedure, the other within a perturbative scheme, and the use of exact inhomogeneous models, in particular those involving L-T solutions (see [60] for a review). Since the purpose of this thesis is to investigate how relativistic cosmology can be done using exact methods, we shall focus our attention on the analyses completed within the L-T framework.

2.9.1 CONSTRAINTS ON MODEL PARAMETERS FROM SN Ia DATA

This section summarises work done by [19] proposing a test of the cosmological principle with the SN Ia observations and studying the possibility of explaining the cosmological constant problem as an effect of large-scale inhomogeneities.

The luminosity distance D_L of a source is defined as the distance from which the radiating body, if in a Euclidean space and motionless, would produce an energy flux equal to the one measured by the observer. It follows therefore that

$$l = \frac{L}{4\pi D_L{}^2}, \tag{2.138}$$

L being the absolute luminosity, i.e. the emitted power in the rest frame of the source, and l, the measured bolometric flux, i.e. integrated over all frequencies by the observer.

For a given isotropic cosmological model the distance at redshift z is a function of z and of the model parameters. The apparent bolometric magnitude m of a standard candle of absolute bolometric magnitude M is also a function of z and of the parameters of the model. It can be written, for D_L in megaparsecs, as

$$m = M + 5\text{log}D_L(z; cp) + 25, \tag{2.139}$$

where M is measured at $D_{10} = 10$ pc,

$$M = 2.5\text{log}\frac{L}{4\pi D_{10}{}^2}. \tag{2.140}$$

Here, cp denotes the set of cosmological parameters pertaining to the given model, which can be either constants, as in FRW models, or functions of z, as in L-T ones. Then, the diameter or area distance D_A is also defined by the formula one would use in Euclidean space,

$$D_A = \frac{D}{\alpha}, \tag{2.141}$$

where α is the measured angular diameter of a source, and D is its physical diameter. The reciprocity theorem then relates these two distances,

$$D_L = (1+z)^2 D_A. \tag{2.142}$$

If one considers any cosmological model for which the luminosity distance D_L is a function of the cosmological parameters cp and of the redshift z, and if this function is Taylor expanded near the observer, i.e. for $z < 1$, then

$$D_L(z; cp) = \left(\frac{dD_L}{dz}\right)_{z=0} z + \frac{1}{2}\left(\frac{d^2 D_L}{dz^2}\right)_{z=0} z^2 + \frac{1}{6}\left(\frac{d^3 D_L}{dz^3}\right)_{z=0} z^3 + \frac{1}{24}\left(\frac{d^4 D_L}{dz^4}\right)_{z=0} z^4 + \mathcal{O}(z^5), \tag{2.143}$$

since $D_L(z = 0) = 0$.

Luminosity distance measurements of sources at different redshifts $z < 1$ yield values for the different coefficients in the above expansion. Going to higher redshifts amounts to measuring the coefficients of higher powers of z, whilst for very low redshifts the leading term is first order, and second order for intermediate ones.

Consequently, for cosmological models with a very large number of free parameters, or with parameters which are not constants but, for example, function of the redshift, such measurements only provide constraints upon the values of the parameters near the observer. However, for cosmological models with few parameters, giving independent contributions to each coefficient in the expansion, the method not only provides a way to evaluate these parameters, but, in most cases, to test the validity of the model itself by checking the constraints on the Taylor coefficients. These can be derived with methods such as the one below, developed for FRW cosmologies.

2.9.2   THE ΛCDM COSMOLOGICAL MODEL

For FRW models with a cosmological constant, the luminosity distance is [62]

$$D_L = \frac{c(1+z)}{H_0 \sqrt{|k|}} \mathcal{S}\left(\sqrt{|k|}\int_0^z \left[(1+z')^2(1+\Omega_m z') - z'(2+z')\Omega_\Lambda\right]^{-1/2} dz'\right), \tag{2.144}$$

H_0 being the current Hubble constant, Ω_m is the total mass density, Ω_Λ is the cosmological constant parameter, and

$$\mathcal{S} = \sin \quad \text{and} \quad k = 1 - \Omega_m - \Omega_\Lambda \quad \text{for} \quad \Omega_m + \Omega_\Lambda > 1, \tag{2.145}$$

$$\mathcal{S} = \sinh \quad \text{and} \quad k = 1 - \Omega_m - \Omega_\Lambda \quad \text{for} \quad \Omega_m + \Omega_\Lambda < 1, \tag{2.146}$$

$$\mathcal{S} = I \quad \text{and} \quad k = 1 \quad \text{for} \quad \Omega_m + \Omega_\Lambda = 1, \tag{2.147}$$

I being the identity operator.

The Taylor expansion of (2.143) applied to this expression for the FRW luminosity distance yields

$$D_L^{(1)} \equiv \left(\frac{dD_L}{dz}\right)_{z=0} = \frac{c}{H_0}, \tag{2.148}$$

$$D_L^{(2)} \equiv \frac{1}{2}\left(\frac{d^2 D_L}{dz^2}\right)_{z=0} = \frac{c}{4H_0}(2 - \Omega_m + 2\Omega_\Lambda), \tag{2.149}$$

$$D_L^{(3)} \equiv \frac{1}{6}\left(\frac{d^3 D_L}{dz^3}\right)_{z=0} = \frac{c}{8H_0}(-2\Omega_m - 4\Omega_\Lambda - 4\Omega_m\Omega_\Lambda + \Omega_m^2 + 4\Omega_\Lambda^2), \tag{2.150}$$

$$D_L^{(4)} \equiv \frac{1}{24}\left(\frac{d^4 D_L}{dz^4}\right)_{z=0} = \frac{5c}{72H_0}(8\Omega_\Lambda + 4\Omega_m\Omega_\Lambda + 2\Omega_m^2 - 16\Omega_\Lambda^2 - 12\Omega_m\Omega_\Lambda^2 + 6\Omega_m^2\Omega_\Lambda - \Omega_m^3 + 8\Omega_\Lambda^3). \tag{2.151}$$

These coefficients are independent functions of the three parameters of this class of models, H_0, Ω_m and Ω_Λ.

Now, a simplified way of dealing with the SN Ia data in the framework of a Friedmannian cosmology is to use the magnitude zero-point method. The magnitude zero-point $\mathcal{M} \equiv M5\log H_0 + 25$ can be measured from the apparent magnitude and redshift of low-redshift examples of the standard candles, without knowing H_0, since, in this representation, the apparent magnitude is

$$m \equiv \mathcal{M} + 5\log \mathcal{D}_L(z; \Omega_m, \Omega_\Lambda). \tag{2.152}$$

Since $\mathcal{D}_L(z; \Omega_m, \Omega_\Lambda) \equiv H_0 D_L(z; \Omega_m, \Omega_\Lambda, H_0)$, it depends upon Ω_m and Ω_Λ alone and such is the case for its expansion coefficients $D_L^{(i)}$. We can therefore derive conditions which must be fulfilled by these coefficients when fitting them to the data. These conditions are mandatory for any ΛCDM model to represent the observed Universe.

In the standard CDM model, i.e. for $\Omega_\Lambda = 0$,

$$\mathcal{D}_L^{(2)} = \frac{c}{4}(2 - \Omega_m). \tag{2.153}$$

If the analysis of the measurements gives $D_L^{(1)} < D_L^{(2)}$, it implies $\Omega_m < 0$, which is physically irrelevant, and the model is therefore ruled out. This is what happens with the SN Ia data, and what induced the postulate of a strictly positive cosmological constant, to counteract the $-\Omega_m$ term.

To test FRW models with Ω_Λ, one has to go to at least the third order to have any chance of obtaining a result, and a ruling out of these models at the third-order level, i.e. due to a negative value for Ω_m, would occur if it were found, using (2.148)-(2.150), that:

$$1 - \frac{\mathcal{D}_L^{(3)}}{\mathcal{D}_L^{(1)}} - 3\frac{\mathcal{D}_L^{(2)}}{\mathcal{D}_L^{(1)}} + 2\left(\frac{\mathcal{D}_L^{(2)}}{\mathcal{D}_L^{(1)}}\right)^2 < 0. \tag{2.154}$$

It should be stressed, however, that this test is only valid for data from $z \leq 1$ supernovae. It could be argued that one way of dealing with this problem would be to use best-fit confidence regions in parameter space; if these regions were located in physically irrelevant domains of the parameter space, e.g. $\Omega_m < 0$, this would rule out the Friedmannian models as able to reproduce the geometry of our local Universe. However, the computation of these best-fit confidence regions proceeds from a Bayesian data analysis, for which a prior probability distribution accounting for the physically (in Friedmannian cosmology) allowed part of the parameter space is assumed. The results are therefore distorted by an a priori homogeneity assumption, which would have to be discarded for the completion of any robust test of this hypothesis.

2.9.3   L-T MODELS WITH ZERO COSMOLOGICAL CONSTANT

In this section we examine the possibility of reproducing the SN Ia data in an L-T model with no cosmological constant. In this case the observer is assumed to be located near the symmetry centre of the model.

Since the L-T solution appears to be a good tool for the study of the observed Universe in the matter dominated era, it is used here as an example showing that a non-vanishing cosmological constant in a Friedmann universe can be replaced, under some conditions upon the functions of r defining each model, by inhomogeneity with a zero cosmological constant, and is able to fit the SN Ia data just as well.

In the following, we set $t_B(0) = 0$ at the symmetry centre ($r = 0$) by an appropriate translation of the $t = $ constant surfaces, and describe the Universe by the $t > t_B(r)$ part of the (r, t) plane, increasing t corresponding to going from the past to the future.

When evaluated on the past null cone of a central observer, the areal radius $R_n = R(t_n(r), r)$ is precisely the diameter distance

$$D_A = R_n. \tag{2.155}$$

From the reciprocity theorem, (2.142) and (2.155) yield

$$D_L = (1 + z)^2 R_n, \tag{2.156}$$

and we see that the luminosity distance D_L is a function of redshift z and, through R_n, of the parameter functions of the model: $M(r)$, $E(r)$, and $t_B(r)$. Successive partial derivatives of R with respect to r and t, and derivatives of $E(r)$ with respect to r, evaluated at the observer, contribute to the expressions for the coefficients of the luminosity distance expansion (2.156) in powers of z. It is therefore interesting to note the behaviour of $R(t,r)$ and $E(r)$ near the symmetry centre of the model, i.e. near the observer, which takes the form [85]:

$$R(t,r) = R_{,r}(t,0)r + \mathcal{O}(r^2), \tag{2.157}$$

$$E(r) = \frac{1}{2}E_{,rr}(0) + \mathcal{O}(r^3), \tag{2.158}$$

due to the regularity conditions at the centre which imply $R(t,0) = R_{,t}(t,0) = E(0) = E_{,r}(0) = 0$, as well as the vanishing of higher-order derivatives of R with respect to t alone at $r = 0$.

The expressions for the coefficients of the luminosity distance expansion naturally follow. After some calculations one obtains

$$D_L^{(1)} = \frac{R_{,r}}{R_{,tr}}, \tag{2.159}$$

$$D_L^{(2)} = \frac{1}{2}\frac{R_{,r}}{R_{,tr}}\left(1 + \frac{R_{,r}}{R_{,tr}^2} + \frac{R_{,rr}}{R_{,r}R_{,tr}} - \frac{R_{,trr}}{R_{,tr}^2}\right), \tag{2.160}$$

$$
\begin{aligned}
D_L^{(3)} &= \frac{1}{6}\frac{R_{,r}}{R_{,tr}}\left(-1 + \frac{R_{,r}R_{,ttr}}{R_{,tr}^2} + 3\frac{R_{,r}^2R_{,ttr}^2}{R_{,tr}^4} - \frac{R_{,r}^2R_{,tttr}}{R_{,tr}^3} - 6\frac{R_{,r}R_{,ttr}R_{,trr}}{R_{,tr}^4} + \frac{R_{,rr}R_{,ttr}}{R_{,tr}^3}\right. \\
&\left. + 2\frac{R_{,r}R_{,ttrr}}{R_{,tr}^3} - 3\frac{R_{,rr}R_{,trr}}{R_{,r}R_{,tr}^3} + 3\frac{R_{,trr}^2}{R_{,tr}^4} + \frac{R_{,rrr}}{R_{,r}R_{,tr}^2} - \frac{R_{,trrr}}{R_{,tr}^3} + \frac{E_{,rr}}{R_{,tr}^2}\right), \tag{2.161}
\end{aligned}
$$

with implicit evaluation of the partial derivatives at the observer.

To compare the expansions of D_L in the FRW and in the L-T cases, we recall that the expressions for the Hubble parameter H_0, and of the deceleration parameter, q_0, at the observer in the FRW model are given, in units in which $c = 1$, by

$$H_0 = \frac{1}{D_L^{(1)}}, \tag{2.162}$$

$$q_0 = 1 - 2H_0 D_L^{(2)}. \tag{2.163}$$

The SN Ia data show that the q_0 of (2.146) is negative, and it is claimed that this supports the Concordance model.

Substituting these formulae as well as (2.148)-(2.150) into (2.159)-(2.161), we see that the expressions for the FRW coefficients in the expansion of D_L in powers of z can mimic L-T ($\Lambda = 0$) ones, at least to third order. This is straightforward for $D_L^{(1)}$. The case of $D_L^{(2)}$ is discussed at length in [61]. For higher-order terms, it implies constraints on the L-T parameters, which will be illustrated below with the particular example of flat models. In fact, owing to the appearance of higher-order derivatives of the functions of the parameter ν in each higher-order coefficient, L-T models are completely degenerate with respect to any given magnitude-redshift relation in the sense that one of its arbitrary functions remains unspecified. In contrast, FRW models with constant parameters, including the equation of state parameter ω, are more rapidly constrained and therefore cannot fit any given relation when tested at sufficiently high order in the expansion.

2.9.4 EXAMPLE: FLAT L-T ($\Lambda = 0$) MODELS

To illustrate the kinds of constraints that can be imposed on L-T parameters by observational data, the particular case of spatially flat L-T ($E = \Lambda = 0$) models is analysed here.

In this case, the expression for R is given by (2.13) and the calculation of its successive derivatives, contributing to the expressions of the expansion coefficients, is straightforward.

The mass function M(r) can be used to define the radial coordinate $r : M(r) \equiv M_0 r^3$, where M_0 is a constant.

With the covariant definition of H_0 mentioned in (2.162), the $D_L^{(i)}$ s, as derived from (2.159)-(2.161), can be written, in units in which $c = 1$, as

$$D_L^{(1)} = \frac{1}{H_0}, \tag{2.164}$$

$$D_L^{(2)} = \frac{1}{4H_0}\left(1 - 6\frac{t_{B,r}(0)}{(9GM_0/2)^{1/3}t_p^{2/3}}\right), \tag{2.165}$$

$$D_L^{(3)} = \frac{1}{8H_0}\left(-1 + 4\frac{t_{B,r}(0)}{(9GM_0/2)^{1/3}t_p^{2/3}} + 6\frac{t_{B,r}^2(0)}{(9GM_0/2)^{2/3}t_p^{4/3}} - 9\frac{t_{B,rr}(0)}{(9GM_0/2)^{2/3}t_p^{1/3}}\right), \tag{2.166}$$

with the previously indicated choice $t_B(0)$, and where t_p is the time coordinate at the observer. It is convenient to note that t_p is not a free parameter of the model, since its value follows from the currently measured temperature at 2.73K .

A comparison with the corresponding FRW coefficients (2.148)-(2.150) yields the following relations [63]:

$$\Omega_m \longleftrightarrow 1 + 5\frac{t_{B,r}(0)}{(9GM_0/2)^{1/3}t_p^{2/3}} + \frac{15}{2}\frac{t_{B,r}^2(0)}{(9GM_0/2)^{2/3}t_p^{4/3}} + \frac{9}{4}\frac{t_{B,rr}(0)}{(9GM_0/2)^{2/3}t_p^{1/3}}, \tag{2.167}$$

$$\Omega_\Lambda \longleftrightarrow -\frac{1}{2}\frac{t_{B,r}(0)}{(9GM_0/2)^{1/3}t_p^{2/3}} + \frac{15}{4}\frac{t_{B,r}^2(0)}{(9GM_0/2)^{2/3}t_p^{4/3}} + \frac{9}{8}\frac{t_{B,rr}(0)}{(9GM_0/2)^{2/3}t_p^{1/3}}. \tag{2.168}$$

Equation (2.168) implies that a non-vanishing cosmological constant in an FRW interpretation of the data at $z < 1$ corresponds to a mere constraint on the model parameters in a flat L-T ($\Lambda = 0$) interpretation.

Therefore, any magnitude-redshift relation established up to the third-order level, can be interpreted in either model. For example, the results published in [53] under the following form pertaining to a FRW interpretation

$$0.8\Omega_m - 0.6\Omega_\Lambda \approx -0.2 \pm 0.1, \tag{2.169}$$

should be written, with no model dependent a priori assumption, as

$$2\left(\frac{D_L^{(2)}}{D_L^{(1)}}\right)^2 - 4.2\frac{D_L^{(2)}}{D_L^{(1)}} - \frac{D_L^{(3)}}{D_L^{(1)}} \approx -1.8 \pm 0.1, \tag{2.170}$$

and it would correspond, in a flat ($\Lambda = 0$) interpretation, to

$$4.3\frac{t_{B,r}(0)}{(9GM_0/2)^{1/3}t_p^{2/3}} + 3.75\frac{t_{B,r}^2(0)}{(9GM_0/2)^{2/3}t_p^{4/3}} + 1.125\frac{t_{B,rr}(0)}{(9GM_0/2)^{2/3}t_p^{1/3}} \approx -1 \pm 0.1. \tag{2.171}$$

Such a result would imply a negative value for at least one of the two quantities $t_{(B,r)}(0)$ or $t_{(B,rr)}(0)$, which would be an interesting constraint on the bang time function in the observers neighbourhood. For instance, a function $t_B(r)$ decreasing near the observer would imply, for a source at a given $z < 1$, an elapsed time from the initial singularity that is longer in an L-T model than in the corresponding Friedmann one, i.e. an older Universe. Consequently, a decreasing $t_B(r)$ has, in an L-T universe, an effect analogous to that of a positive cosmological constant in a Friedmann cosmology. They both make the Universe look older.

2.9.5 APPARENT ACCELERATION

When examining the magnitude-redshift relation obtained from the SN Ia with no a priori idea about which model would best describe our Universe, a straight reading of the data does not exclude the possibility of challenging the cosmological principle, i.e. these data can fit other models than the FRW ones with cosmological constant or dark energy.

As an example, it has been shown that any magnitude-redshift relation can be reproduced by L-T models with no cosmological constant, provided the parameter functions defining these models satisfy the constraints issuing from observations. However, such simple models have been given as an illustration and this does not preclude the more general conclusion stated above, i.e. that many other non-Friedmannian models might reproduce the effect of a dark energy component.

When reasoning in the framework of Friedmannian cosmology, the supernovae dimming is associated with an acceleration of the Universe expansion. This is why a number of authors have focussed on the issue of either demonstrating or ruling out an acceleration of the expansion rate in inhomogeneous cosmologies.

Some of them tried to derive [64], [65] or rule out [66], [67] no-go theorems, stating that a locally defined expansion can never be accelerating in models where the cosmological fluid satisfies the strong energy condition.

However, when spatially averaged so as to produce a Friedmann-like behaviour, a physical quantity associated with the expansion rate behaves quite differently [68]. Now, [69] argued that the averaged quantity representing the scale factor or the deceleration parameter may accelerate without there being any observable consequence. Moreover, one can find realistic inhomogeneous models which fit with the supernova observations and have positive values of volume deceleration [70], [71]. Therefore, it is very difficult to deduce general rules from such theorems.

Another pitfall of this method was pointed out by [72]. He showed that an L-T model with a positive averaged acceleration can require averaging on scales beyond the event horizon of a central observer. In such cases, the averaging procedure does not preserve the causal structure of spacetime and can lead to the definition of locally unobservable average quantities. [73] proved that the necessary condition to obtain volume acceleration in the L-T model is $E > 0$. When averaging on Mpc scales with inhomogeneities of realistic features, a large-amplitude function E which is required to obtain volume deceleration leads to a very large amplitude of the bang time function, making the age of the Universe unrealistically small [71].

This reinforces the statement that a positive averaged acceleration of an underlying inhomogeneous Universe is in general not equivalent to a positive acceleration inferred from observations analysed within a Friedmannian scheme.

The idea of a deceleration parameter is not uniquely defined in an inhomogeneous scheme. [65] proposed four different definitions of such a parameter. [66], examining the effect of a mass located at the centre of a spherically symmetric configuration on the dynamics of a dust cosmological fluid, showed that, for an observer located away from the centre, (i) a central overdensity leads to acceleration along the radial direction and deceleration perpendicular to it, (ii) a central underdensity leads to deceleration along and perpendicular to the radial direction. This demonstrates that, even locally, the effect of inhomogeneities on the dynamics of the Universe is not trivial.

To understand intuitively how inhomogeneities can mimic an accelerated expansion, it is interesting to follow [59], [74], [75] who considered a cosmological model composed of a low density inner homogeneous region connected at some redshift to an outer homogeneous region of higher density. Both regions decelerate, but, since the void expands faster than the outer region, an apparent acceleration is experienced by the observer located inside the void.

We therefore conclude that the computation of some local quantity such as the deceleration parameter (possibly subsequently averaged) behaving the same way as in FRW models with dark energy can lead to spurious results, and must therefore be avoided. Actually, what we observe is the dimming of the SN Ia accounted for by the magnitude-redshift relation. 'Acceleration' is a mere consequence of the homogeneity assumption. This is the reason why we shall only consider, in the following, works aimed at studying the magnitude-redshift relation.

2.9.6   CONSTRAINTS ON INHOMOGENEOUS MODELS FROM CMB DATA

In the standard approach, the CMB temperature fluctuations are analysed by solving the Boltzmann equation within linear perturbation around a homogeneous and isotropic FRW model. In an inhomogeneous background, one can do a similar analysis employing the L-T model instead of an FRW model. Alternatively, if it is assumed that the early Universe (before and up to the last scattering instant) is well

described by an FRW model, then the power spectrum can be parametrized [76] by

$$l_m = l_a(m - \phi_m), \tag{2.172}$$

where l_1, l_2 and l_3 are the position of the first, second and third peaks respectively, and

$$l_a = \pi \frac{R}{r_s}, \tag{2.173}$$

where R is the comoving distance to the last scattering surface and r_s is the size of the sound horizon at the last scattering instant. The sound horizon depends on Ω_b, Ω_m, Ω_γ and h. The size of the sound horizon can be calculated by the formulae given in [77]. The function Ω_m depends on Ω_b, Ω_m, h, n_s and the energy density of dark energy (n_s is the spectral index). The exact form of ϕ_m was given by [76]. The Ω_m and h are given by the ratio ρ/ρ_{cr} and $H/(100\text{km s}^{-1}\text{Mpc}^{-1})$ at the last scattering surface (evaluated for the current instant).

Here we present a fit to the CMB data using the above formula. Let us consider four LT models [78]:

Model A1

$$\rho(t_0, r) = \rho_b \left[2.45 - 1.45 e^{-\left(\frac{l}{0.75}\right)^2} \right], \tag{2.174}$$

$$t_B = 0 \quad, \quad \Omega_b = 0.0445 \quad, \quad n_s = 1, \tag{2.175}$$

where $l = r/\text{Gpc}$.

Model A1 + ring

$$\rho(t_0, r) = \rho_b \left[2.45 - 1.45 e^{-\left(\frac{l}{0.75}\right)^2} - 1.75 e^{-\left(\frac{l-5.64}{0.926}\right)^2} \right], \tag{2.176}$$

$$t_B = 0 \quad, \quad \Omega_b = 0.08 \quad, \quad n_s = 0.963. \tag{2.177}$$

Model A2

$$\rho(t_0, r) = \rho_b \left[3.33 + 1.4 e^{-\left(\frac{l}{0.75}\right)^2} \right], \tag{2.178}$$

$$t_B = 0 \quad, \quad \Omega_b = 0.0445 \quad, \quad n_s = 1. \tag{2.179}$$

Model A2 + ring

$$\rho(t_0, r) = \rho_b \left[3.33 + 1.4 e^{-\left(\frac{l}{0.75}\right)^2} + 0.08 e^{-\left(\frac{l-5.64}{0.926}\right)^2} \right], \tag{2.180}$$

$$t_B = 0 \quad, \quad \Omega_b = 0.08 \quad, \quad n_s = 0.963. \tag{2.181}$$

The best fit to the positions of the CMB peaks is presented in Table 2.5. As can be seen, model A1 does not fit the observed CMB power spectrum. However, by adding an underdense ring, we can modify the density distribution in such a way that the CMB peaks can be reproduced - this is done in model A1 + ring. From these results we can see why the model of [79], discussed below, has a larger radius for the local Gpc-scale void. In models where density increases up to some distance from the origin, a satisfactory fit to the first peak of the CMB power spectrum, i.e. the distance to the last scattering instant, can be obtained if the mass of the Universe is decreased. This decrease can be obtained either by having an additional underdense ring between the local void and the last scattering surface, or by having a local void of larger radius (as in [79], where $R \approx 2.5$ Gpc).

On the other hand, it is not only the mass that is important. To show this let us consider model A2. In it, the density increases up to some distance from the origin. In this configuration we can also obtain a good fit to the position of the first peak if we increase the mass of the Universe.

The positions of the other peaks depend strongly upon Ω_b. In order to obtain a good fit to their positions in the model we need to increase the value of Ω_b beyond the value that is consistent with

Model	First peak	Second peak	Third peak
A1	177.34	414.08	627.19
A2	216.59	503.37	754.28
A1 + ring	220.46	530.38	800.19
A2 + ring	220.43	530.51	779.76
WMAP	220.8 ± 0.7	530.9 ± 3.8	700-1000

Table 2.5: The position of the peaks (values of the multipole moment l) of the CMB power spectrum.

observation of light elements in the local Universe to $\Omega_b = 0.08$. However, due to the lower expansion rate at large distances, the physical baryon density $\Omega_b h^2$ remains close to the observed value, i.e. 0.0198 and 0.0212 for models A1 + ring and A2 + ring respectively.

The above results suggest that almost any model can be modified in such a way that a good fit to the CMB data can be obtained. Both models A1 and A2, although very different, can be modified to fit the CMB data. Therefore, the CMB data do not strongly constrain the properties of the local Gpc void. Each model of the local void considered in the previous section can be modified in such a way, by adding one or two rings between the local void and the last scattering surface, so that the CMB power spectrum is recovered.

2.9.7   ALNES, AMARZGUIOUI AND GRØN'S PROPOSAL

In a series of three papers [80], [81], [82], a class of Universe models was studied where the inhomogeneities take the form of a spherically symmetric under-dense bubble, represented by a particular class of L-T models with $E(r) > 0$, which matches smoothly to a flat inhomogeneous Einstein-de Sitter background. In [80], the observer is assumed to be at the centre of the inhomogeneity and the aim is to reproduce both the SN Ia observations and the location of the first acoustic peak in the observed CMB temperature power spectrum. In [81], it is investigated how far away from the centre the observer can be located to explain the magnitude and alignment of the lowest multipoles in the CMB map. This work is described in Section 2.10.5. In another paper [82], they investigate whether such an off-centre position of the observer might yield a better fit of the model to the SN Ia data than in [80]. We present the results of this work in the present section.

First we summarise the presentation of the model as it is given in [80]. The Einstein equations for the L-T solutions can be put in the form

$$\kappa \rho = H_\perp^2 + 2H_r H_\perp - \frac{\beta}{R^2} - \frac{\beta_{,r}}{RR_{,r}}, \tag{2.182}$$

$$-\kappa \rho = 2H_\perp^2 - 2H_r H_\perp - 2\frac{\beta}{R^2} - 6H_\perp^2 q_\perp + \frac{\beta_{,r}}{RR_{,r}}, \tag{2.183}$$

where $H_\perp \equiv R_{,t}/R$, $H_r \equiv R_{,tr}/R_{,r}$ and $q_\perp \equiv -RR_{,tt}/R_{,t}^2$.

The L-T region of the model is described by two functions renamed $\alpha(r) \equiv 2GM(r)$ and $\beta(r) \equiv 2E(r)$. Since the late-time behaviour of the model is of interest, $t = 0$ is defined as the time when the photons decoupled from the matter, i.e. the time of last scattering. Also, $R(t = 0, r) \equiv R_0(r)$ is defined, and a conformal time η is introduced by $\beta^{1/2}dt = Rd\eta$. To represent an underdensity, i.e. a L-T model with negative spatial curvature, the Einstein equations for $\beta > 0$ are integrated to give

$$R = \frac{\alpha}{2\beta}(\cosh\eta - 1) + R_0 \left[\cosh\eta + \sqrt{\frac{\alpha + \beta R_0}{\beta R_0}}\sinh\eta\right], \tag{2.184}$$

$$\sqrt{\beta}t = \frac{\alpha}{2\beta}(\sinh\eta - \eta) + R_0 \left[\sinh\eta + \sqrt{\frac{\alpha + \beta R_0}{\beta R_0}}(\cosh\eta - 1)\right]. \tag{2.185}$$

59

The α and β functions are chosen so that they correspond to a smooth interpolation between two homogeneous regions where the inner region has a lower matter density than the outer region, thus describing a spherical bubble in an otherwise homogeneous universe. They are written as

$$\alpha(r) = H_0^2 r^3 \left[\alpha_0 - \frac{1}{2} \Delta\alpha \left(1 - \tanh\frac{r - r_0}{2\Delta r} \right) \right], \tag{2.186}$$

$$\beta(r) = H_0^2 r^2 \left[\beta_0 - \frac{1}{2} \Delta\beta \left(1 - \tanh\frac{r - r_0}{2\Delta r} \right) \right], \tag{2.187}$$

where H_0 is the value of the Hubble parameter in the outer homogeneous region today, while α_0 and β_0 are the relative densities of matter and curvature in this region. Furthermore, $\Delta\alpha$ and $\Delta\beta$ represent the differences for α and β between the central and homogeneous regions, and r_0 and Δr specify the position and the width of the transition zone.

Since the function $R_0(r)$ can be chosen at will using the freedom of coordinate choice in L-T solutions, $R_0 = a_* r$, where a_* is the scale factor of the FRW model at recombination, in order to match the L-T solution to the homogeneous one at that epoch.

To reduce the number of degrees of freedom of the model and make the problem tractable, a very simple toy model is chosen: an underdense spherically symmetric region surrounded by a flat, matter-dominated universe. To implement this, $\alpha_0 = 1$ and $\beta_0 = 0$ is chosen, with $\Delta\alpha = -\Delta\beta$. This leaves four parameters $\Delta\alpha$, r_0, Δr and the Hubble parameter at the origin, $H_r(0, t_0) = 100h$ kms^{-1}Mpc^{-1}, to be fitted to the observations.

To relate the α and β functions to observable quantities, relative matter and curvature densities are defined from the generalized Friedmann equation (2.182) to be

$$\Omega_m = \frac{\kappa\rho}{H_\perp^2 + 2H_r H_\perp} \quad , \quad \Omega_k = 1 - \Omega_m. \tag{2.188}$$

Central observer

In [80], the observer is located at the centre of the underdensity. We give below a short overview of this analysis since it takes into account some interesting cosmological features seldom found in such studies and since its results will be used in the off-centre observer case [81], [82] which will be described later.

Equations (2.56) and (2.57), which define the path of the photon, can be recast into equations (19) and (20) of [80]. Then, to determine the luminosity distance-redshift relation to be compared with the SN Ia observations, these equations are numerically integrated, with the initial conditions: $T(0) = t_0 \equiv t(r = 0)$ and $z(0) = 0$. The location of the last scattering surface, i.e. the position of the CMB photons we observe today at the time of last scattering, is given by $T(r_*) = 0$ and t_0 is defined by $z(r_*) = z_* \cong 1100$. The luminosity distance follows from (2.142) and the angular diameter distance is

$$D_A(z) = R(t(z), r(z)). \tag{2.189}$$

Now, to confront the model with CMB observations, it would, in principle, require a study of perturbations in an inhomogeneous universe. However, since this model is homogeneous outside a limited region at the centre, it is assumed that the evolution of the perturbations is identical to that in a homogeneous universe until the time of recombination. The standard results for the scale of acoustic oscillations on the last scattering surface can then be used.

The position of the first Doppler peak of the power spectrum is also calculated, and it is shown that agreement with observations is not hard to produce. However, there are a lot of possible choices for the parameters of the model that give a very good fit to both the supernovae data and the position of the first acoustic peak in the CMB temperature power spectrum. Since the problem consisting of deriving an L-T model from the SN Ia data is degenerate, it is not very surprising that the addition of such a slight constraint from the CMB spectrum is insufficient to remove this degeneracy. For this reason another constraint is introduced: that the model be able to reproduce the mass density parameter at the origin, Ω_{m0}, measured from observations of galaxies with redshifts $z < 0.12$. It is proposed as the 'standard model', a solution which gives an underdensity at the centre $\Omega_{m0} = 0.2$, compatible with the results of the 2dF survey, $\Omega_{m0} = 0.24 \pm 0.05$.

Parameter or feature	Symbol	Value
Density contrast	$\Delta\alpha$	0.90
Transition point	r_0	1.35Gpc
Transition width	$\Delta r/r_0$	0.40
Fit to supernova data	χ^2_{SN}	176.5
Position of the first CMB peak	$\mathcal{S}$	1.006
Age of the Universe	t_0	12.8Gyr
Relative density inside underdensity	$\Omega_{m,in}$	0.20
Relative density outside underdensity	$\Omega_{m,out}$	1.00
Hubble parameter inside underdensity	h_{in}	0.65
Hubble parameter outside underdensity	h_{out}	0.51
Physical distance to the last scattering	D_{LSS}	11.3Gyr

Table 2.6: Parameters and features of the best-fit model of [80] with a central observer.

Also, the scale of the baryon oscillations detected in the SDSS galaxy power spectrum [83] is used to try to constrain the model even further. The physical length scale associated with these oscillations is fixed by the sound horizon at recombination. Therefore, measuring how large this length scale appears at some redshift in the galaxy power spectrum might allow one to constrain the time evolution of the Universe from recombination to the time corresponding to this redshift. Anyway, it is unclear how to use the values calculated by [83], since these authors derived their results in the framework of a ΛCDM model.

The results of the analysis of such a class of models with a central observer are that the underdensity might extend about 1.35Gpc outwards. A very good fit to the supernovae data is obtained if the transverse Hubble parameter $H_\perp$ is allowed to decrease with distance from the observer, and this fit is even better than for the ΛCDM model. On the other hand, a good fit to the location of the CMB power spectrum is reached if the Universe is assumed to be flat with a value 0.51 for the Hubble parameter outside the inhomogeneity. Therefore, interpolating between these two limiting behaviours might provide a good model to account for both the SN Ia data and the location of the first CMB peak. The values of the parameters for the best-fit model are given in Table 2.6.

This model yields a better fit to the Riess data set of supernovae than the ΛCDM model. However, for the CMB fit only the location of the first peak was tested. Although the model yields a good fit to this, it does not necessarily mean that it matches the whole CMB spectrum. Indeed, since the physics responsible for the acoustic peaks is determined by the pre-recombination era, it would be expected that the peaks should look more or less the same for a flat, homogeneous model with $h = 0.51$. This suggests that this model might fail to explain the third peak. Furthermore, the model does not appear to explain the observed length scale of the baryon oscillations in the SDSS matter power spectrum either.

Off-centre observer

[81] and [82] consider the best-fit model of [80], but now they put the observer away from the centre.

In their first paper they investigate the influence of such an observer location on the CMB temperature power spectrum (we will come back to this in Section 2.11.3), and in the second paper they try to improve the fit of their model to the SN Ia data by moving the observer off centre, and also to see how these data constrain such a location.

By moving the observer off-centre, one adds three new degrees of freedom as regards the model with a central observer; the distance from the centre r_0, and the two angles which specify the displacement direction. Since the explicit angular dependence of the observed supernovae is available in the data, the most appropriate way to do the analysis is to minimise the χ^2 values with respect to the two angles for each r_0.

The consequence of such an observer location is that the distance measures become anisotropic. The explicit effect on the expression for the angular diameter distance was analysed by [84] and [85]. The

expression, as given in the paper by [85], is

$$D_A^4 \sin^2\gamma = \tilde{g}_{\gamma\gamma}\tilde{g}_{\xi\xi} - \tilde{g}_{\gamma\xi}^2, \tag{2.190}$$

where the $\tilde{g}_{\mu\nu}$ are the metric coefficients in the observer rest frame, and the γ and ξ correspond to the polar and azimuthal angles in this frame.

After integrating the geodesic equations [82], which determine the trajectories of the infalling photons toward the off-centre observer, one proceeds with the diameter distance calculation. The metric $\tilde{g}_{\mu\nu}$ in the observers local coordinates is obtained by the coordinate transformation

$$\tilde{g}_{\mu\nu} = g_{\rho\sigma}\frac{\partial x^\rho}{\partial \tilde{x}^\mu}\frac{\partial x^\sigma}{\partial \tilde{x}^\nu}, \tag{2.191}$$

which yields the following components,

$$\tilde{g}_{\gamma\gamma} = g_{rr}\left(\frac{\partial \hat{r}}{\partial \gamma}\right)^2 + g_{\theta\theta}\left(\frac{\partial \hat{\theta}}{\partial \gamma}\right)^2, \tag{2.192}$$

$$\tilde{g}_{\xi\xi} = g_{\phi\phi} = R^2\sin^2\theta, \tag{2.193}$$

$$\tilde{g}_{\gamma\xi} = 0. \tag{2.194}$$

Substituting these equations into (2.190) yields the expression for the angular diameter distance, which reads

$$D_A^4 = \frac{R^4\sin^2\theta}{\sin^2\gamma}\left[\frac{R_{;r}^2}{R^2(1+2E)}\left(\frac{\partial \hat{r}}{\partial \gamma}\right)^2 + \left(\frac{\partial \hat{\theta}}{\partial \gamma}\right)^2\right]. \tag{2.195}$$

Now, using the reciprocity theorem (2.142) it is straightforward to obtain the luminosity distance D_L.

The results are compared with the data points and error bars from the [86] Gold Set. For the best-fit model of [80], it is found that the minimised χ^2 value is smallest for an observer located at a physical distance of around 94 Mpc from the centre of the inhomogeneity in the direction $(l,b) = (271, 21)$ in galactic coordinates. This improvement, however, turns out to be small compared to the fit with the central observer model (the minimal χ^2 is only reduced from 176.2 to 174.9). Consequently, the current data do not offer any substantial evidence for an off-centre observer in this model. Also, it is found that the χ^2 is lower for off-centre observers with radial distances out to around 225 Mpc, and it is concluded from this that anisotropies in the SN Ia data do not strongly constrain the observers distance from the centre. It is suggested that this is partly due to the fact that there are too few supernovae in the studied sample, with the hope that the future will provide larger and better samples, thus allowing stronger conclusions to be drawn from the anisotropy of the local Universe.

2.9.8   THE GBH MODEL

In [79] a new class of L-T models, the GBH models, is considered. These models describe a local void in an otherwise spatially asymptotically flat universe, and are completely specified by their matter content $\Omega_m(r)$ and their rate of expansion $H(r)$,

$$\Omega_m(r) = \Omega_{out} + (\Omega_{in} - \Omega_{out})\left(\frac{1 - \tanh[(r - r_0)/2\Delta r]}{1 + \tanh[r_0/2\Delta r]}\right), \tag{2.196}$$

$$H(r) = H_{out} + (H_{in} - H_{out})\left(\frac{1 - \tanh[(r - r_0)/2\Delta r]}{1 + \tanh[r_0/2\Delta r]}\right). \tag{2.197}$$

It is governed by six parameters:

- Ω_{in} determined by Large-Scale Structure observations,

- Ω_{out} determined by asymptotic spatial flatness,

- H_{in} determined by Hubble Space Telescope observations,

- H_{out} determined by CMB observations,

- r_0 characterises the size of the void,

- Δr characterises the transition to uniformity.

One parameter is fixed, $\Omega_{out} = 1$, the other five are left to vary freely in the parameter scans.

The authors also consider a more constrained model, in which the Big Bang is simultaneous. This can be obtained by a suitable choice of $H(r)$:

$$H(r) = -H_0 \left[\frac{\Omega_m(r)}{\sqrt{\Omega_K^3(r)}} \text{arcsinh} \sqrt{\frac{\Omega_K(r)}{\Omega_m(r)}} - \frac{1}{\Omega_K(r)} \right], \tag{2.198}$$

so that $t_B = cH_0^{-1}$ is universal, for all observers, irrespective of their spatial location. Note that in this case one has less freedom than in the previous one, since now there is only one arbitrary function, $\Omega_m(r)$, and there is one free parameter less.

The goal is to confront this model with the largest series of currently available observations: supernova data, cosmic microwave background, baryon acoustic oscillations; also requiring it to obey three additional priors: the observed lower age limit on globular clusters in the Milky Way (11.2 Gyr), the HST key project measure of the local value of the Hubble parameter ($H_{in} = 72 \pm 8$) and the gas fraction as observed in galaxy clusters. Here, the observer is located at the centre of the model.

It is proposed that the Hubble parameter $H(z)$ is one of the main observables that will in future help to decide between the different possible scenarios (modifications of gravity, extra energy component, cosmological constant, or non-homogeneous cosmological model). Assuming that the background is a flat FRW cosmology, the authors write it as

$$\frac{H_{T,L}^2}{H_{in}^2} = (1+z)^3 \Omega_{in} + (1 - \Omega_{in}) \exp \left[3 \int_1^{1+z} d\log(1+z')(1 + \omega_{eff}^{T,L}(z')) \right], \tag{2.199}$$

where H_{in} and Ω_{in} are the expansion rate and matter density as observed at $z = 0$, the labels T and L denote the transverse and longitudinal expansion rates, defined as $H_T = R_{,t}/R$ and $H_L = R_{,tr}/R_{,r}$, and the $\omega_{eff}^{T,L}$ are defined in terms of the derivatives of (2.199),

$$\omega_{eff}^{T,L} = -1 + \frac{1}{3} \frac{d\log \left[\frac{H_{T,L}^2(z)}{H_{in}^2} - (1+z)^3 \Omega_{in} \right]}{d\log[1+z]}, \tag{2.200}$$

where it has been assumed that

$$\frac{H_{T,L}^2(z)}{H_{in}^2} - (1+z)^3 \Omega_{in} > 0. \tag{2.201}$$

It is pointed out that $\omega_{eff}^{T,L}(z)$ is the equation of state parameter in the dark energy interpretation, while in the L-T or modified gravity interpretations it is an empirical observational signature that expresses the difference between the measured expansion rate and the expansion rate we ascribe to the observed matter.

Another key outcome of this work is that the acoustic oscillation signal depends partly on H_L , while supernova observations are only related to H_T through its dependence upon D_L. Interestingly, the variation and derivative of $\omega_{eff}^{T,L}(z)$ is quite large in the best-fit L-T models, showing that a precise low-redshift supernova survey sensitive to H_T or a fine-grained BAO survey sensitive to H_L could rule out or reinforce the model in the near future. Conversely, if a disagreement between ω as observed by supernovae and ω as observed through the BAOs is found, this could be a hint of inhomogeneous expansion rates.

One can directly compute $\omega_{eff}^{T,L}(z)$ in the limiting cases $z = 0$ and $z \gg 1$ for asymptotically flat L-T models:

$$\omega_{eff}^{T,L}(z) = \begin{cases} -\frac{1}{3} + \frac{2}{3} \frac{cH_{,r}(0)}{(1-\Omega_{in})H_{in}^2} & \text{for} \quad z = 0, \quad \text{and} \quad H = H_T \\ -\frac{1}{3} + \frac{4}{3} \frac{cH_{,r}(0)}{(1-\Omega_{in})H_{in}^2} & \text{for} \quad z = 0, \quad \text{and} \quad H = H_L \\ 0 & \text{for} \quad z \gg 1 \end{cases} \tag{2.202}$$

where the asymptotic convergence of the L-T metric to a Friedmann metric giving $dz = -da/a$ has been used (here a denotes the scale factor of the Friedmann background). It appears that to have $\omega \ll -1/3$ at low redshifts requires either a significant negative gradient in $H(r)$, or $\Omega_{in} \sim 1$.

In a subsequent work [87], the kinematic Sunyaev-Zel'dovich (kSZ) effect observed for nine distant galaxy clusters was studied. Assuming that we are located at the centre of a constrained GBH model, the large CMB dipole which should be observed in the reference frame of such off-centre clusters would actually manifest itself as a kSZ effect. The authors show that the kSZ observations give far stronger constraints on their model than other observational probes and infer that the void permitted by the existing data cannot be larger than ∼1.5 Gpc. They stress that kSZ surveys to be completed in the near future will place more stringent constraints on the size of the void in their model. On the other hand, if this class of models were to appear to be compatible with observations, future kSZ surveys give a unique possibility of directly reconstructing the expansion rate and the underdensity profile of the void.

The general conclusion of their work is that the current observations do not exclude the possibility that we live close to the centre of a large void with size of order of a few Gpc, with matter density well below the average, and a local expansion rate of 71 km s^{-1} Mpc^{-1}.

2.9.9   L-T SWISS-CHEESE MODELS

The first Swiss-cheese model found in the literature was designed by [88], to study the gravitational fields around stars. The vacuoles, cut out from the Friedmanian background, were modelled by a static Schwarzschild solution. Such models were subsequently used to study, among other effects, the influence of inhomogeneities on the magnitude-redshift relation (see, for example, [89]). However, since Schwarzschild's is a static solution, any influence of the vacuole expansion remained unseen in such models, and the magnitude of the reported effects was very low.

The recent appearance in the literature of Universe models constructed as L-T Swiss-cheese models, where the inhomogeneities are represented by L-T spherical regions within a homogeneous background where the matter is assumed continuously distributed with densities both below and above the average, allows us to account for this vacuole expansion. These local L-T bubbles exactly match to the Friedmann background. The main shortcoming of such models, as regards the issue of solving the cosmological constant problem, is that they can produce surprising cancellations. It is well known that when the two models, L-T and Friedmann, are properly matched together, the metric outside the patch is insensitive to the details of what happens inside. This feature suppresses any backreaction on the homogeneous region which still evolves exactly as a Friedmann universe. For this reason, such models exhibit only corrections due to light propagation inside the patches, usually called the Rees-Sciama effect.

Note however that, at variance with what is claimed in [90], such a drawback is not due to spherical symmetry but to the fact that the inhomogeneous patches are exactly matched to the background. It can be shown that within such Swiss-cheese models in which the inserted inhomogeneous patches were not L-T bubbles but parts of the Szekeres spacetime, with no symmetry, there was still no influence on the outside region. Moreover, one can have a sort of backreaction with both spherical and non-spherical inhomogeneity, provided an ordinary matching with the metric and second form being continuous is not required, but only the continuity of the metric. Then the boundary of the inhomogeneous island does not comove with the Friedmann background, giving rise to interesting phenomena. This was first found by [91].

Brouzakis *et al.*'s model

Brouzakis et al., [92], [93], studied a model where the L-T patches consist of collapsing or expanding regions matched to a Friedmann background. Since they intended that the observer and the sources do not occupy special positions, they placed both within the Friedmann domain. Therefore, light is emitted and received within homogeneous regions, while it crosses several inhomogeneous bubbles, with size of order $10h^{-1}$ Mpc or more, along its path.

In [92], the studied L-T models were of the constant bang time type, i.e. $t_B(r) = 0$. Central overdense regions become denser with time, with underdense spherical shells surrounding them. Central underdense regions turn into voids, surrounded by massive shells. The authors recalled the derivation of the optical

beam equations, as given by [94], which determine the evolution of the beam expansion θ and shear σ as light propagates and derived their specific form for L-T models, which reads

$$\frac{d\theta}{d\lambda} = -4\pi G\rho(k^t)^2 - \theta^2 - \sigma^2,$$

(2.203)

$$\frac{d\sigma}{d\lambda} + 2\theta\sigma = -4\pi G\rho(k^\phi)^2 R^2 \left(\rho - \frac{3M(r)}{4\pi R^3}\right),$$

(2.204)

while the equation for the area A can be written as

$$\frac{1}{\sqrt{A}}\frac{d^2\sqrt{A}}{d\lambda^2} = -4\pi G\rho(k^t)^2 - \sigma^2.$$

(2.205)

They derived a simple model of spherical collapse for the cases of overdense and underdense regions, which gave the evolution of both density profiles. Then, the influence of light propagation toward the centre of such collapsing regions upon the luminosity distance was calculated by numerically integrating the geodesic and optical equations. The results are that the presence of underdense central regions, consistent with the observation of large, approximately spherical voids in the matter distribution of the Universe, is expected to lead to an increase of the luminosity distance relative to the homogeneous case. The opposite is expected if the central regions are overdense.

It is therefore very reasonable to suggest that the dominance of voids, as deduced from observations, can yield increased luminosity distances. The question is whether this can induce an effect which might explain the observed luminosity curves for supernovae. However, a description of the Universe as composed of large voids surrounded by matter concentrated in thin shells implies, in this L-T Swiss-cheese model, a relative increase in the luminosity distance at redshifts of order unity of only a few percent. The deviation of the luminosity distance from its value in a homogeneous universe was estimated in the extreme case where light travels through the centres of the encountered inhomogeneities. An absolute upper bound upon this increase can be derived from (2.205). The focussing of a beam is minimised if the shear is negligible and the energy density is set to zero in this equation. In this L-T Swiss-cheese model, this idealised situation can be achieved if the central underdense regions of the inhomogeneities become totally empty after a long evolution, while overdense thin shells develop around them. To derive the upper bound, one can set the energy density arbitrarily to zero in the optical equation only, since it still drives the cosmological expansion through (2.3), with $\Lambda = 0$. Neglecting the shear, the luminosity distance as a function of redshift can be obtained analytically, assuming that the background expansion is given by the standard Friedmann equation involving the average density. When comparing it to the luminosity distance in the corresponding Friedmann model, one finds

$$\frac{D_L}{D_{L,F}} = \frac{1}{5}\frac{(1+z)^2 - (1+z)^{-3/2}}{1+z - (1+z)^{1/2}}.$$

(2.206)

For redshifts near one, this expression gives a maximum increase in the luminosity distance of around 22%, to be compared to the measured increase which is around 30%. The open question is whether an alternative model of large-scale structures could result in a larger effect. This is discussed in the conclusions of [92].

In [93], the matter distribution, even though inhomogeneous, is more evenly distributed than in the above case. In particular, each spherical region has a central underdensity surrounded by an overdense shell. The densities of the voids and the background are comparable at early times and differ by a factor of order one during the later stages of evolution. The beam shear is negligible in the calculations, and the main effect arises from the variations of the beam expansion due to the inhomogeneities. Also, more general beam geometries are considered, in which the light paths have random impact parameters relative to the centres. In this work, a more detailed statistical analysis is performed and, for a given redshift, the width of the distribution of luminosity distances is evaluated.

The form of this distribution is quantified in terms of two parameters: the width δ_d and the location of the maximum $\delta_m > 0$. The first one characterises the error induced to cosmological parameters derived in the standard way, while the second one determines the bias in such determinations . However, the values of these parameters are very small for the considered inhomogeneity scales. Furthermore, the shift in the

average value δ_m is always smaller than the standard deviation δ_d. Both increase with the inhomogeneity scale and the redshift. But, even for homogeneities with large length scales, comparable to the horizon scale, and redshift $z = 2$, the shift and distribution width are only of the order of a few percent. They can be compared to those generated by gravitational lensing at scales typical of galaxies or galaxy clusters in a standard Swiss-cheese model where the mass of each inhomogeneity is concentrated in a very dense object located at its centre and where the inhomogeneous patch is modelled by a Schwarzschild metric. Here, the typical values of δ_m and δ_d are larger by at least an order of magnitude than in this L-T Swiss-cheese model. The reason is that, in this last model, the density contrast is only of order one.

The conclusion is that, within this L-T Swiss-cheese model, the presence of large length scale inhomogeneities and density contrast of order one does not influence significantly the propagation of light if the source and the observer possess random locations.

Biswas and Notari's model

An analogous L-T Swiss-cheese model has been studied by Biswas and Notari [90]. It consists of blobs of the void type, where the L-T metric satisfies $E(r) > 0$ and $t_B(r) = 0$, cut out from a flat Einstein-de Sitter universe. The photon propagation is studied in the cases when the curvature of the patches is either small or large. In both cases the effects are very small if the observer sits outside the void, strengthening therefore Brouzakis et al.'s results, while they are larger if the observer sits inside. This is a property of Swiss-cheese models: effects are always larger inside the inhomogeneous patch than outside it.

Marra et al.'s model

Another Swiss-cheese model, where L-T bubbles with radius 350 Mpc (roughly 25 times smaller than the radius of the visible Universe) are also inserted into an Einstein-de Sitter background, was studied by Marra et al. [95]. In their main model the bubbles are adjoining and laid out on a cubic lattice, as sketched in Figure 3 of [95].

The initial conditions for each sphere are specified for every shell at the same moment of time $\bar{t}$. The initial density, $\rho(r, \bar{t})$, is chosen to be

$$\rho(r, \bar{t}) = Ae^{[-(r-r_M)^2/2\sigma^2]} + \epsilon \quad \text{for} \quad r < r_n, \tag{2.207}$$

$$\rho(r, \bar{t}) = \rho_{ES}(\bar{t}) \quad \text{for} \quad r > r_n, \tag{2.208}$$

where $\epsilon = 0.0025$, $r_n = 0.042$, $\sigma = r_h/10$, $r_M = 0.037$, $A = 50.59$ and $\rho_{ES}(\bar{t}) = 25$. It exhibits a low-density interior, surrounded by a Gaussian density peak near the boundary, that matches smoothly to the exterior Friedmann density, and such that the matter density ϵ in the centre is roughly 10^4 times smaller than in the Friedmann cheese. To have a realistic evolution, it is also demanded that there are no initial peculiar velocities. This fixes the arbitrary curvature function $E(r)$ to a positive value small compared to unity. Evolving this model from $t = \bar{t} = -0.8$ to $t = 0$ (with the Big Bang time $t_B = 1$ and $t = 0$ being today), one can see that the inner almost empty region expands faster than the outer (cheese) one. The density ratio between the cheese and the interior of the hole increases by a factor of 2. The evolution is realistic. Matter is falling toward the peaks in density. Overdense regions start contracting and become thin shells , mimicking structures, while underdense regions become larger, mimicking voids, and eventually they occupy most of the volume. Because of the distribution of matter, the inner part of each hole is expanding faster than the cheese and the interpolating overdense region is squeezed by it. A shell crossing eventually happens when shells are so squeezed that they occupy the same physical position, i.e. when $R_{,r} = 0$.

Since the aim of this work is to calculate the luminosity-redshift relation $D_L(z)$ in order to understand the effects of inhomogeneities on observables, the next step is to study the propagation of photons in this model. Three cases are considered: the observer is just outside the last hole, in the Friedmannian cheese, looking at photons passing through the holes; the observer is in a hole on a high-density shell; the observer is in the centre of a hole.

Since the photons subtend an angle α at the observer after passing through the centres of all the holes, the equations describing the photon paths are analogous to those established in Section 2.4.2, with the

value of the affine parameter set to zero at the border of the last hole. Given an angle α, the equations can be solved, matching together the solutions between one hole and the other, which generates the solution $t(\lambda)$, $r(\lambda)$, $\phi(\lambda)$ and $z(\lambda)$, from which the observables of interest can be calculated.

The difference for the photon paths between the cases 'observer on the border' and 'observer in the hole' is that in the second case the observer has a peculiar velocity with respect to a Friedmann observer passing by the same point, which is not the case for the observer on the border who is comoving with the cheese. This makes the inside observer see an anisotropic CMB. However, this effect is taken into account in the solution to be found. There remains the effect of light aberration which changes the angle α seen by the inside observer with respect to the angle α_{ES} seen by a Friedmann observer. The relation between α and α_{ES} is given by the relativistic aberration formula:

$$\cos\alpha_{ES} = \frac{\cos\alpha + \frac{v}{c}}{1 + \frac{v}{c}\cos\alpha},\tag{2.209}$$

the angular diameter and luminosity distance follow.

The results are given for different cases and compared with respect to the EdS and the CDM one. For the observer on the border, one model exhibits five holes and the other only one hole five times bigger in size than each of the previous holes. For the observer in the hole, only the five hole case is considered. The observables studied are the redshift $z(\lambda)$, the angular diameter distance $D_A(z)$, the luminosity distance $D_L(z)$ and the corresponding distance modulus $\Delta m(z)$.

The conclusions are that photon physics seems to be affected by the evolution of the inhomogeneities more than by the inhomogeneities themselves. For an observer in the cheese, redshift effects are suppressed when the hole is small because of a compensating effect acting on the scale of half a hole due to spherical symmetry and to the fact that the density profile was chosen in order to have $\langle\delta\rho\rangle = 0$. This is not the case when the hole is bigger since the evolution has more time to change the hole while the photon is going through. As we shall see in Chapter 3, with Szekeres models (of which L-T models are subclasses), small voids among overdense regions evolve more slowly than large voids do. The calculation of the angular diameter distance shows that the evolution of the inhomogeneities bends the photon paths as compared to the Friedmann case. Inhomogeneities should therefore be able, at least partly, to mimic the effects of the so-called 'dark energy'. The Friedmann model best fitting the one big-hole Swiss-cheese universe is ΛCDM with $\Omega_m = 0.95$ and $\Omega_\Lambda = 0.05$, which is very near Einstein-de Sitter. The Friedmann model best fitting the five-small hole Swiss-cheese model is also ΛCDM with $\Omega_m = 0.6$ and $\Omega_\Lambda = 0.4$, which still exhibits a non-negligible 'dark-energy' component.

However, the effects of the inhomogeneities found for this model are bigger than those found by [92], [93] and by [90]. This might be due to the fact that these authors used smaller holes with a different initial density/initial velocity profile.

In a subsequent paper, [96] used the same Swiss-cheese toy model in order to better understand how a clumpy universe can be renormalized by a fitting procedure to give an effective ΛCDM model. The basic idea is that the observational evidences for dark energy come from the possibility that our inhomogeneous universe can be described by means of a homogeneous solution fitting the observations on our past light cone beyond some averaging scale. However, this does not imply that a primary source of dark energy exists, but only that it emerges from a phenomenological fit. If it does exist, the observational evidence encapsulated in the Concordance model would tell us nothing else than the pure-matter inhomogeneous Universe has been merely renormalized into a ΛCDM one.

The procedure employed here to fit a phenomenological FRW model to a Swiss-cheese model is intermediate between the fitting method of [54] and an averaging approach. It is implemented on the past light cone of the observer. The physical quantities studied are the expansion and the density. The expansion behaves as in an FRW case because of the compensation effect already found by [95]. The density behaves quite differently thanks to its sensitivity to the fact that a photon spends more and more time in the expanding large voids than in the collapsing thin high-density structures. Note, however, that this effect is independent of the one found to act on the angular diameter distance [95]. The best fit to an effective dark energy equation of state, quantitatively similar to the one of the Concordance model, is obtained for holes with radius 250 Mpc.

Knowing the behaviour of the density, it is possible to derive the behaviour of the Hubble parameter characterising the FRW solution exhibiting a phenomenological source with the fitted equation of state.

Now, the sensitivity of the density to any compensation effect can yield the possibility that a Swiss-cheese made of spherically symmetric holes and one where the holes differ slightly from spherical symmetry would share the same light-cone average density, thus the same redshift history for the photons and therefore the same fitted FRW model. In this way it could be possible to go beyond the main limitation of the model studied, i.e. the assumption of spherical symmetry for the holes.

2.10 SOLVING THE HORIZON PROBLEM USING THE DE-LAYED BIG BANG MODEL

In hot Big Bang models, the comoving regions over which the CMB is observed to be homogeneous to better than one part in 10^5 at the last-scattering surface is much larger than the intersection of this surface with the future light cone from any point p_B of the Big Bang. Since this light can provide the maximal distance over which causal processes could have propagated from p_B, the observed quasi-isotropy of the CMB remains unexplained. As shown by [38], this 'horizon problem' develops sooner or later in any cosmological model exhibiting a spacelike singularity such as that occurring in the standard FRW universes.

Even inflation, which was put forward in order to remove this drawback in the framework of standard homogeneous cosmology, only postpones the occurrence of the horizon problem, since it does not change the spacelike character of the singularity and is insufficient to solve it permanently.

A proposal at variance with inflation was put forward, solving the horizon problem by means of a shell-crossing singularity in a spherically symmetric inhomogeneous model (see [63], for example). This allows a permanent solution to the problem for all observers regardless of their spacetime location. Now, it can be shown that a property of a large class of shell crossings, valid for general spherically symmetric models, is that they are timelike [97]. Further, in order to solve the horizon problem, we need a cosmological model which exhibits a non-spacelike singularity that is encountered when travelling backward on the observers light cone. For simplicity, we employ L-T models, because they exhibit the needed symmetry and allow a fully analytical exact reasoning [63].

To deal with the horizon problem, one has to consider light cones. As was shown by [63], a large class of L-T models can be found for which the horizon problem is solved by means of light cones never leaving the matter-dominated era. This validates the use of such models. Moreover, since there is evidence that the observed Universe does not present appreciable spatial curvature on very large cosmological scales, it will be here approximated by the flat $E(r) = 0$ L-T model.

The function $M(r)$ is used to define the radial component $r : M(r) \equiv M_0 r^3$, where M_0 is a constant. With the above definition for r, the analytical expression for $R(t,r)$ given by (2.7) becomes

$$R(t,r) = \left(\frac{9GM_0}{2}\right)^{1/3} r[t - t_B(r)]^{2/3}. \tag{2.210}$$

In this case, the g_{rr} component of the metric tensor is

$$R_{,r}(t,r) = \left(\frac{9GM_0}{2}\right)^{1/3} [t - t_B(r)]^{-1/3} \left[t - t_B(r) - \frac{2}{3}rt_{B,r}(r)\right]. \tag{2.211}$$

From reasoning given in [97], we see that the shell-crossing surface

$$t - t_B(r) - \frac{2}{3}rt_{B,r}(r) = 0 \tag{2.212}$$

is timelike.

On the other hand, one can always choose $t_B = 0$ at the centre ($r = 0$) of symmetry by an appropriate choice of t.

Equation (2.211), substituted into (2.3) gives

$$\rho(t,r) = \frac{1}{2}\pi G[3t - 3t_B(r) - 2rt_{B,r}(r)]^{-1}[t - t_B(r)]^{-1}. \tag{2.213}$$

This expression leads to two undesirable consequences:

- The energy density goes to infinity on the Big Bang surface, $t = t_B(r)$, and on the shell-crossing surface (2.212).

- This energy density presents negative values in the region of the Universe located between the shell crossing surface (2.212) and the Big Bang singularity, and corresponding to

$$3t - 3t_B(r) - 2rt_{B,r}(r) < 0 \tag{2.214}$$

$$t - t_B(r) > 0. \tag{2.215}$$

Of course, a negative energy is unphysical for dust.

Since a shell crossing is usually considered to be a deficiency of L-T models one generally tries to avoid it by setting, for our $E(r) = 0$ case: $t_{B,r}(r) \leq 0$ and $M_{,r}(r) \geq 0$ in the region where $R_{,r} > 0$ [32].

However, in order to solve the horizon problem we need an increasing Big Bang function $t_B(r)$. It is possible to circumvent this difficulty. One way out of the shell-crossing surface problem might be to consider that, as the energy density increases while reaching its neighbourhood from higher values of t, radiation becomes the dominant component of the Universe, pressure can no more be neglected and the L-T model no longer holds. However, since the light cones of interest, which are null surfaces, never leave the region situated above the timelike shell-crossing surface, where $3t - 3t_B(r) - 2rt_{B,r}(r)$ remains always positive, and $t - t_B(r) > 0$ by construction, therefore the energy density of (2.213) remains positive.

One of the key points of the reasoning here proposed is a shell-crossing surface situated above the Big Bang surface, its time coordinate monotonically increasing with r to let the light cones remain in the matter-dominated domain. This is always the case if

$$t_B(r = 0) = 0, \tag{2.216}$$

$$t_{B,r}(r) > 0 \quad , \quad \text{for all} \quad r \neq 0, \tag{2.217}$$

$$t_{B,r}(r = 0) = 0, \tag{2.218}$$

$$5t_{B,r}(r) + 2rt_{B,rr}(r) > 0 \quad , \quad \text{for all} \quad r \neq 0, \tag{2.219}$$

$$rt_{B,r}(r)|_{r=0} = 0. \tag{2.220}$$

Now, (2.219) implies $A_{,r} \neq 0$ and therefore a timelike shell crossing. Note that we have added to the specifications of [63], and [38], the constraint that $t_{B,r}$ should vanish at $r = 0$ to allow the model to satisfy the no-central-singularity conditions in order to get a well behaved model whatever the observer's position. With these specifications, the physical singularity of the model - i.e. the first surface encountered on a backward path from the observer where the energy density and the curvature scalar go to infinity is the shell-crossing surface. Therefore, the region between the Big Bang $t = t_B(r)$ and the shell-crossing surface, constraining the unwanted negative energy density, is excluded from the part of the model intended to describe the matter-dominated region of the Universe.

A class of models permanently solving the horizon problem has therefore been constructed with no need for any inflationary phase. A $t_B(r)$ function increasing with r implies that the Big Bang occurred at later cosmic time for larger r, hence the evocative 'Delayed Big Bang' chosen to qualify this singularity.

2.11 THE L-T MODEL AND CMB TEMPERATURE FLUC-TUATIONS

2.11.1 LIGHT PROPAGATION EFFECTS

The last-scattering surface is the most remote region which is observable using electromagnetic radiation. Since photons on their way pass through large-scale inhomogeneities such as voids, clusters and superclusters, it is important to know how the light propagation phenomena affect the CMB radiation. In the standard approach the CMB temperature fluctuations are analysed by solving the Boltzmann equation within linear perturbations around the homogeneous and isotropic FRW model [98], [99]. The use of the FRW metric for the background model results in a remarkably good fit to the CMB data [14]. However, the assumption of homogeneity, which is also consistent with other types of cosmological observations, is not a direct consequence of them [100]. It is often said that such theorems as the Ehlers-Geren-Sachs theorem (1968) and the 'almost EGS theorem' [134], justify the application of the FRW models. These theorems state that if anisotropies in the CMB radiation are small for all fundamental observers, then locally the Universe is almost spatially homogeneous and isotropic. The founding assumption of these theorems, namely the local Copernican principle applied to the 'U region', i.e. the region within and near our past light cone from decoupling to the present day, is not mandatory and we have already stressed it needs still to be tested. Moreover, as shown by [102], it is possible that the CMB temperature fluctuations are small but the Weyl curvature is large.

In such a case the geometry of the Universe is far from Robertson-Walker geometry, and the applicability of the FRW models is not justified. Moreover, the applicability of the linear approach can be questionable, since the density within cosmic structures is much larger than unity. Therefore, there is a need for the application of exact inhomogeneous cosmological models to a study of light propagation and its impact on CMB temperature fluctuations. This issue has been extensively studied within spherically symmetric models: within the thin shell approximation [103], [28],[104] and within the L-T model [105], [106], [107], [108], [109], [110], [111]. However, cosmic structures are not spherically symmetric.

2.11.2 TEMPERATURE FLUCTUATIONS

Assuming that the black body spectrum is conserved during the evolution of the Universe, the temperature must be proportional to $1 + z$:

$$\frac{T_e}{T_0} = 1 + z. \tag{2.221}$$

Then, from (2.221), the temperature fluctuations measured by a comoving observer are:

$$\left(\frac{\Delta T}{T}\right)_0 = \frac{\frac{T_e}{1+z} - \frac{\bar{T}_e}{1+\bar{z}}}{\frac{\bar{T}_e}{1+\bar{z}}}, \tag{2.222}$$

where quantities with overbars refer to the average quantities, i.e the quantities obtained in the homogeneous Friedmann model.

Let us write the temperature at emission as $T_e = \bar{T}_e + \Delta T_e$. Then (2.222) becomes

$$\left(\frac{\Delta T}{T}\right)_0 = \frac{\bar{z} - z}{1 + z} + \left(\frac{\Delta T}{T}\right)_e \frac{1 + \bar{z}}{1 + z}. \tag{2.223}$$

As can be seen from (2.223), the observed temperature fluctuations on the CMB sky are caused by the light propagation effect (first term) and by the temperature fluctuation at the decoupling instant (the second term).

To calculate the light propagation accurately, without assumptions such as small density contrast and linear evolution, a model of cosmic structures based on exact solutions of the Einstein field equations is needed. Unfortunately, there are only a few exact inhomogeneous cosmological models, and in none of them can the cosmic web-like structures be described. In Chapter 3 we discuss how this problem can be overcome by using many inhomogeneous models of cosmic structures and joining them in an inhomogeneous patchwork model of the Universe.

2.11.3 CMB DIPOLE AND QUADRUPOLE IN THE DBB MODEL WITH AN OFF-CENTRE OBSERVER

The dipole moment in the CMB anisotropy is the most prominent feature in the observational data. Its value being of order 10^{-3}, it exceeds the quadrupole, of order 5×10^{-6}, by more than two orders of magnitude [9], [112]; [113].

The dipole is usually considered as resulting from a Doppler effect produced by our motion with respect to the CMB rest frame [114]. A few authors [115], [116]; [117], [118] intended however to show that its origin could be in the large-scale features of the Universe In particular, [115], using an ad hoc toy model, emphasised the possibility that the dipole might be generated by an entropy gradient in an L-T universe. In the model they studied, they assumed that the Big Bang time was the same for all observers, i.e. $t_B(r) =$ constant.

Working in the framework of the Delayed Big Bang (DBB) class of L-T models described in Section 6.3 of [37], they showed that the dipole and quadrupole anisotropy, or parts of them, could be viewed as the outcome of a conic Big Bang surface when the observer is located off the symmetry centre. We sum up their contribution below.

Definition of temperature

The specific entropy S is usually defined as the ratio of the number density of photons to the number density of baryons, i.e.

$$S \equiv \frac{k_B n_\gamma(t,r) m_b}{\rho(t,r)}. \tag{2.224}$$

In order to decouple the effect of an inhomogeneous entropy distribution (as already studied by [115]) from that of an inhomogeneous singularity surface, we set S = constant.

The observed deviation of the CMB from perfect isotropy being very small, we can assume, as a reasonable approximation, the thermodynamic equilibrium for the photons, so at the ultra-relativistic limit for bosons,

$$n_\gamma = a_n T^3, \tag{2.225}$$

T being the radiation temperature, and

$$a_n = \frac{2\zeta(3)k_B^3}{\pi^2(\hbar c)^3}, \tag{2.226}$$

where ζ is the Riemann zeta function.

Letting, with no loss of generality, $S = $ constant $= k_B \eta_0$, and taking the present photon to baryon ratio to be $10^8/(2.66\Omega_b h_0^2)$, we obtain the following expression for T:

$$T(t,r) = \left(\frac{10^8}{5.32 h_0^2 \pi G a_n m_b (3t - 5t_B(r))(t - t_B(r))} \right)^{1/3}, \tag{2.227}$$

where h_0 is the Hubble constant in units 100 kms^{-1}Mpc^{-1}. Hereafter, for numerical applications, the value $h_0 = 0.75$ will be assumed.

Integration of the null geodesics and determination of the dipole and quadrupole moments

Light travels on the past light cone from an emission 2-surface (t_{ls}, r_{ls}) at last scattering, to the observer at (t_0, r_0). The optical depth of the Universe to Thomson scattering is approximated by a step function. The last-scattering surface is therefore defined, in the local thermodynamic equilibrium approximation discussed above, by its temperature, $T = 4000\ K$, as is the now-surface, $T = 2.73\ K$, where the observer is located. The equal-temperature surfaces obey (2.227).

Since the value of the entropy function $S(r)$ is assumed to be constant, the constant T curves are monotonically increasing with r, and they asymptotically approach the shell-crossing surface (2.212).

An observer O located at a distance r_0 from the centre sees an axially symmetric universe, with the axis passing through the observer and the centre of symmetry C. The photon path is uniquely defined by

the observers position (t_0, r_0) and the angle α between the direction from which the light ray comes and the direction of the centre.

Figure 2.13 shows the geometry of incoming light rays. If observed at an angle $\alpha \leq \pi/2$, a light ray emitted from a point A on the last scattering surface approaches C to a comoving distance r_{min}, then proceeds toward O. From the opposite direction, the ray follows the geodesic BO.

The system of three differential equations which specifies the null geodesics is given by (2.73)-(2.75). Provided one chooses the affine parameter λ increasing from $\lambda = 0$ at (t_0, r_0) to $\lambda = \lambda_{ls}$ at (t_{ls}, r_{ls}) on the last scattering surface, one has to consider two cases:

- the 'out-case': the observer looks in a direction away from the centre of symmetry ($\alpha > \pi/2$). The null geodesics are therefore integrated from (t_0, r_0) to (t_{ls}, r_{ls}) with an always increasing r. Equation (2.74) is written with a plus sign.

- the 'in-case': the observer observes a light ray that first approaches the centre of symmetry then moves away from it, before reaching the observers telescope ($\alpha < \pi/2$). Equation (2.74) with the minus sign first obtains until $dr/d\lambda = 0$, then changes to a plus sign.

A number of 'in' and 'out' null geodesics, each characterised by a value for α between zero and $\pi/2$, are integrated back in time from the observer at $[t_0, r_0, (k^t)_0, T_0]$ until the temperature, as given by (2.227), reaches $T_{ls} = (4/2.7) \times 10^3 T_0$, which defines approximately the last-scattering surface.

At this temperature, the redshift with respect to the observer is given by (2.68), is $z_{ls}^{in,out}(\alpha)$, which varies somewhat with α and with the 'in' and 'out' direction, about an average z_{ls}^{av}. Now, the apparent temperature of the CMB as measured in the α in-out direction is:

$$T_{CMB}^{in,out}(\alpha) = \frac{T_{ls}}{1 + z_{ls}^{in,out}(\alpha)}, \tag{2.228}$$

where the averages for T and z are calculated over the whole sky, and in simplified notation this is

$$\frac{T_{CMB}}{T^{av}} = \frac{1 + z^{av}}{1 + z_{ls}}. \tag{2.229}$$

The large-scale CMB temperature inhomogeneities are expanded in spherical harmonics as

$$\frac{T_{CMB}(\alpha, \phi)}{T^{av}} = \Sigma_{l=1}^{\infty} \Sigma_{m=-1}^{+1} a_{lm} Y_{lm}(\alpha, \phi), \tag{2.230}$$

with

$$a_{lm} = \int \frac{T_{CMB}(\alpha, \phi)}{T^{av}} Y_{lm}^*(\alpha, \phi) \sin(\alpha) d\alpha d\phi. \tag{2.231}$$

The dipole and quadrupole moments are defined as

$$D = \left(|a_{1-1}|^2 + |a_{10}|^2 + |a_{11}|^2 \right)^{1/2} \tag{2.232}$$

and

$$Q = \left(|a_{2-2}|^2 + |a_{2-1}|^2 + |a_{20}|^2 + |a_{21}|^2 + |a_{22}|^2 \right)^{1/2}. \tag{2.233}$$

In the special case we are interested in, the large-scale inhomogeneities depend only upon the angle α, so that all of the a_{lm} with $m \neq 0$ are zero. Therefore, the dipole and quadrupole moments reduce to

$$D = a_{10} \quad , \quad Q = a_{20}, \tag{2.234}$$

so that

$$D = (1 + z^{av}) \int_0^{\pi} \frac{Y_{10}(\alpha)}{1 + z_{ls}(\alpha)} \sin\alpha d\alpha, \tag{2.235}$$

$$Q = (1 + z^{av}) \int\limits_0^\pi \frac{Y_{20}(\alpha)}{1 + z_{ls}(\alpha)} \sin\alpha \, d\alpha. \tag{2.236}$$

Taking into account (2.68) and the spherical symmetry of the model, one obtains

$$D = \left| \frac{1}{2}\sqrt{\frac{3}{\pi}} k_{av}^t \left[\int\limits_0^{\pi/2} \frac{2\sin\alpha\cos\alpha}{k_{in}^t(\alpha)} d\alpha - \int\limits_0^{\pi/2} \frac{2\sin\alpha\cos\alpha}{k_{out}^t(\alpha)} d\alpha \right] \right|, \tag{2.237}$$

$$Q = \frac{1}{4}\sqrt{\frac{5}{\pi}} k_{av}^t \left[\int\limits_0^{\pi/2} \frac{\sin\alpha(3\cos^2\alpha - 1)}{k_{in}^t(\alpha)} d\alpha - \int\limits_0^{\pi/2} \frac{\sin\alpha(3\cos^2\alpha - 1)}{k_{out}^t(\alpha)} d\alpha \right]. \tag{2.238}$$
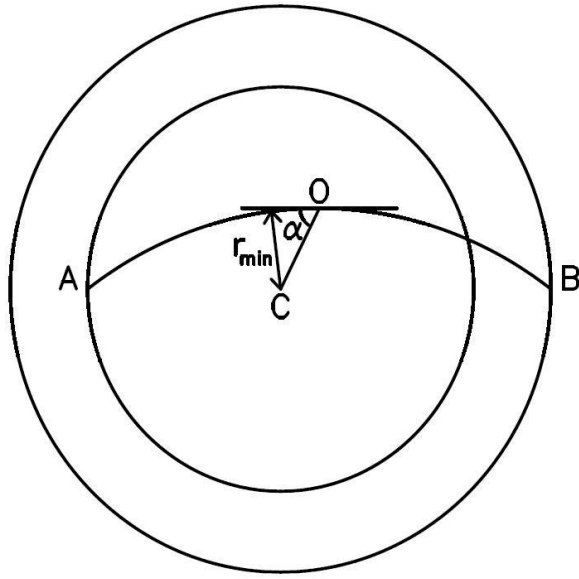

Figure 2.13: The CMB observed from O at an angle α. Systematic illustration of the trajectory of two CMB light beams received by the observer O and making an angle α with the direction of the symmetry centre C of the universe. The two-dimensional projection of the last-scattering surface seen by O is approximately a circle centred on O and passing through A and B. In general, it will intersect many comoving shells of constant r. Points A and B are seen at antipodal points by O, and their comoving shells are solid lines. Note that OB is not a continuation of AO, since O is the vertex of the light cone. Figure taken from [38].

Results and discussion

A class of DBB models exhibiting a Big Bang function of the form

$$t_B(r) = br^n \quad , \quad b > 0 \quad , \quad n > 0, \tag{2.239}$$

was identified by [63] as solving the horizon problem. In a later paper [37], the subclass chosen to be investigated was, for simplicity,

$$t_B(r) = br \quad , \quad \text{with} \quad , \quad 1/R_H > b > 0. \tag{2.240}$$

This conic surface corresponds to perturbations with low spatial frequencies, $k < 1/R_H$, R_H being the horizon radius.

r_0	b	D	Q
0.02	2×10^{-7}	1.61×10^{-3}	5.27×10^{-5}
0.03	9×10^{-8}	1.11×10^{-3}	3.7×10^{-5}
0.04	7×10^{-8}	1.15×10^{-3}	3.99×10^{-5}
0.05	6×10^{-8}	1.23×10^{-3}	4.57×10^{-5}
0.06	5×10^{-8}	1.23×10^{-3}	5.33×10^{-5}
0.07	4×10^{-8}	1.15×10^{-3}	5.79×10^{-5}

Table 2.7: Best-fit values of r_0 and b for reproducing the CMB dipole and quadrupole values using a DBB model. Table taken from [37].

After having numerically integrated back in time from the observer a number of 'in' and 'out' null geodesics, each characterised by a value of α between zero and $\pi/2$, up to the last-scattering surface, as explained above, the dipole and quadrupole moments D and Q were calculated, according to (2.237) and (2.238).

The best-fit values of the doublets (r_0, b) that lead to D and Q close to the observed values, $D \sim 10^{-3}$, $Q \sim 10^{-5}$, are given in Table 2.7. The variations of the dipole and quadrupole as functions of b for various values of r_0 are given in Figures 2.14 and 2.15, respectively.

Using a toy model, chosen within the class of DBB models, it has been shown that values for the model parameters, i.e. the location of the observer in spacetime and the increasing slope of the bang function, can be found that closely reproduce the observed dipole and quadrupole moments in the CMB anisotropy. This provides a possible cosmological interpretation of the dipole (or part of it, as it is obvious that there is probably a Doppler component due to the local motion of the galaxy with respect to the CMB rest frame).

As has long been stressed by other authors [115], [116], [117], [118], there are various observational methods to discriminate between a local and a cosmological origin for the dipole. If, from future analyses of observational data, part of the dipole appears to be non-Doppler, other work, connected in particular with multipole moments of higher order, would be needed to discriminate between the various cosmological candidate interpretations.

Provided the observations allow such a discrimination to be carried out, any unexplained part of the dipole compatible with the above model might set correlated bounds upon the location of the observer and the slope of the Big Bang function, adding therefore new constraints on the parameters of this type of L-T model.

A step toward such a goal was made in [81], with the use of another class of L-T models, which we describe in the next section.

2.11.4 CMB IN THE ALNES *ET AL.* MODEL WITH AN OFF-CENTRE OBSERVER

[81] concentrated on the study of the anisotropies arising in the CMB temperature if the observer is shifted to an off-centre location, analysing two specific realisations of the model of [80]. One of these realisations is the model best fitting the SN Ia data, while the second one is slightly different. To disregard any intrinsic anisotropies on the last-scattering surface, they assumed the temperature to be isotropic there.

Following the line of thought already detailed in the last section, they noted first that the CMB temperature as measured today by the observer is

$$T(\xi) = \frac{T_*}{1 + z(\xi)}, \tag{2.241}$$

where T_* is the temperature at last scattering and ξ the angle denoted α in Section 2.11.3. The average temperature $\hat{T}$, given by the Planck spectrum as seen by the observer, is therefore

$$\hat{T} \equiv \frac{1}{4\pi} \int d\Omega T(\xi) = \frac{T_*}{2} \int_0^\pi \frac{\sin\xi}{1 + z(\xi)} d\xi. \tag{2.242}$$
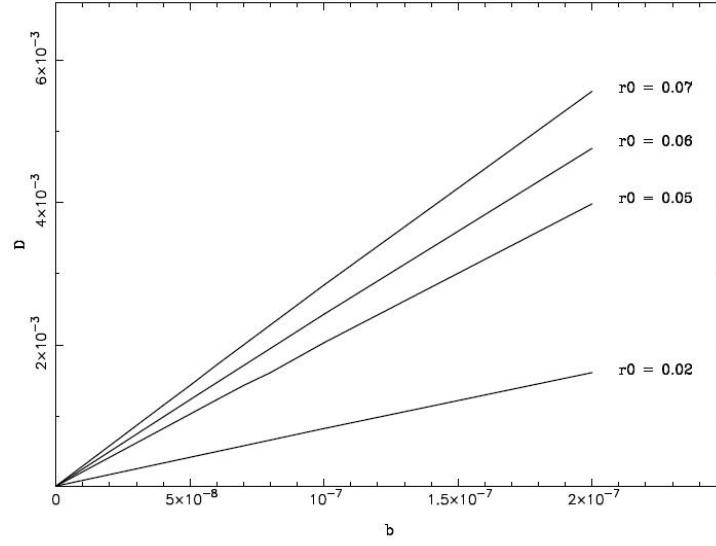
Figure 2.14: The dipole amplitude in a DBB model, as a function of b, for various values of r_0. Figure taken from [37].
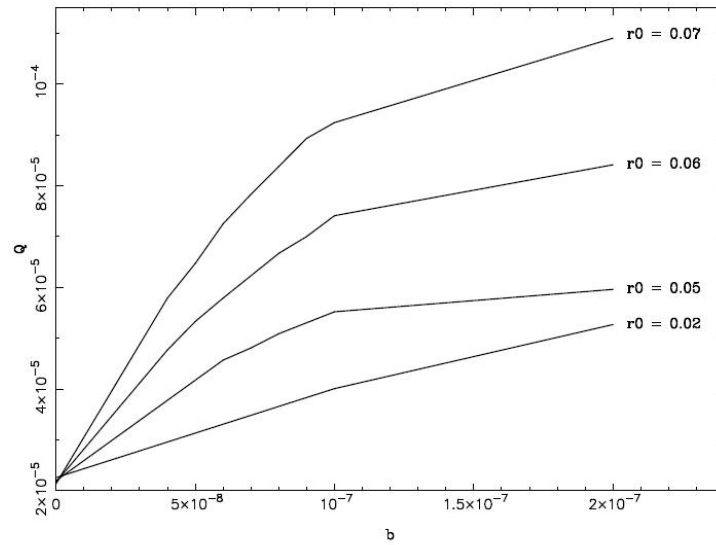

Figure 2.15: The quadrupole amplitude in a DBB model, as a function of b, for various values of r_0. Figure taken from [37].

75

According to [9], this temperature is $\hat{T} = 2.725\ K$. An average redshift for the last-scattering surface can therefore be defined from (2.241) and (2.242) that reads

$$1 + z_* \equiv \frac{T_*}{\hat{T}} = 2 \left[\int_0^\pi \frac{\sin\xi}{1 + z(\xi)} d\xi \right]^{-1} \tag{2.243}$$

This redshift is obtained by integrating the set of differential equations for $(t, r, \theta, p$ and $z)$ given in [81], with the initial conditions $[t_0, r_0, 0, p_0$ and $z_0 = z(\lambda = 0) = 0]$. The relative temperature variation reads thus

$$\theta \equiv \frac{\Delta T}{\hat{T}} = \frac{T(\xi) - \hat{T}}{\hat{T}} = \frac{z_* - z(\xi)}{1 + z(\xi)}. \tag{2.244}$$

Then as in Section 2.10.3, the contributions at different angular scales were considered by decomposing the temperature variation into spherical harmonics. The magnitude of the observed dipole ($\sim 10^{-3}$) was used to put constraints on how far away from the centre the observer may be shifted, since, as shown by [37], a location far off-centre usually yields a larger dipole. Recombination was assumed to occur at $t = 0$ and the present time was defined as the time when the redshift of the photons emitted at $t = 0$ reaches $z_* \cong 1100$.

The geodesic equations were solved for two positions of the observer, 20 Mpc and 200 Mpc from the centre in both models. Then, the coefficients a_{l0} for the dipole ($l = 1$), the quadrupole ($l = 2$) and the octupole ($l = 3$) were calculated as functions of the observer position.

As expected by [37], the induced multipoles become larger the farther away from the centre the observer is located. The distance of the observer from the centre is severely constrained by the dipole value alone. For the induced dipole to be $\leq 10^{-3}$, the physical distance of the observer from the centre should satisfy $d_{obs} \leq 15$ Mpc. When compared to the size of the underdensity in the models, which is around 1500 Mpc, the authors argued that this amounts to a rather strong violation of the Copernican principle, but weaker than in the central observer case. However, if the observer were at a spot with exactly average density, this too would be highly unlikely. Where must one be in a universe full of inhomogeneities in order not to violate the Copernican principle? In the real Universe, there is nowhere that is not in an inhomogeneity. Although finding ourselves exactly at the middle of an inhomogeneity is somewhat non-Copernican, as long as that inhomogeneity is just one of many it is not very strongly non-Copernican. We suggest 5% off-centre is as Copernican as 50% off-centre.

The most striking result is that the quadrupole and the octupole are too small as compared to the dipole. If the induced dipole value is assumed to be around the observed 10^{-3}, the induced quadrupole becomes smaller than $\sim 10^{-7}$ and the induced octupole is less than $\sim 10^{-9}$,their behaviour being similar in both models. This is far less than their measured values $\sim 10^{-5}$. It is thus clear that these models cannot explain the observed alignment of the low-l multipoles in the CMB spectrum.

Even if part of the dipole might be assigned to a nonvanishing peculiar velocity of the observer with respect to the CMB photon flow, which can be fixed to any arbitrary value, the problem would remain, since the multipoles would be expected to keep the hierarchical scaling they exhibit in this particular kind of model. Using a simplified Newtonian framework, it is easy to show that for these models the dipole scales linearly, the quadrupole quadratically and the octupole cubically with the observer location. Therefore, even if one can manage to fit the correct values of the dipole and quadrupole, the octupole would still remain too small.

As a conclusion, the authors claimed that their models are not ruled out by these results, even if they are unable to explain the low multipole anomaly. We want however to stress that the models studied in this work are only special cases of L-T models from which it might be premature to draw general conclusions. Nevertheless, the features thus exhibited are striking, and, given that there is plenty of structure in our local Universe, these effects must play some role.

Chapter 3

The Szekeres model and its applications in cosmology

In this chapter we present a study of structure formation in different environments using the Szekeres model. Additionally, since in this chapter we are considering more general solutions of the Einstein field equations, we initially present a very brief description of the Lemaître model, from which the Lemaître-Tolman (L-T) model is a special case. There then follows a description of the Szekeres model and some of its main properties. After this, since we want to explore types of structure formation that possess at least some spherical symmetry and the Szekeres model is an inhomogeneous model with no symmetries, we therefore consider in detail a subclass of the Szekeres model, namely the quasi-spherical Szekeres model. After exploring in detail the properties of this model and their physical consequences for structure formation, we first present a study of the evolution of pairs of voids and superclusters. We then present a study of the application of the so-called Szekeres Swiss-cheese model to the analysis of observations of the cosmic microwave background (CMB) radiation. In such mode a model, light propagation can be calculated exactly, without such approximations as small amplitude as a small amplitude of the density, which would be required in cosmological perturbation theory.

3.1   THE LEMAÎTRE MODEL

The evolution of a spherically symmetric perfect fluid was first modelled by [119]. The metric, in comoving coordinates, is of the form:

$$ds^2 = e^{A(t,r)}dt^2 - e^{B(t,r)}dr^2 - R^2(t,r)(d\theta^2 + \sin^2\theta d\phi^2). \tag{3.1}$$

The Einstein equations reduce to

$$\kappa R^2 R_{,r}\rho = 2M_{,r}, \tag{3.2}$$

$$\kappa R^2 R_{,t}p = -2M_{,t}, \tag{3.3}$$

where M is defined by

$$2M(t,r) = R(t,r) + R(t,r)e^{-A(t,r)}R_{,t}^2(t,r) - R(t,r)e^{-B(t,r)}R_{,r}^2(t,r) - \Lambda R^3(t,r). \tag{3.4}$$

In the Newtonian limit, GM/c^2 is equal to the mass inside the shell of radial coordinate r, but it is the active gravitational mass which generates the gravitational field, and not an integrated rest mass. From (3.4), we see that the mass is not constant in time, and from (3.3), we see that in the expanding Universe it decreases.

From the equations of motion, $T^{\alpha\beta}_{;\beta} = 0$ we obtain:

$$T^{0\alpha}_{;\alpha} = 0 \implies B_{,t} + 4\frac{R_{,t}}{R} = -\frac{2\rho_{,t}}{\rho + p}, \tag{3.5}$$

$$T^{1\alpha}_{;\alpha} = 0 \implies A_{,r} = -\frac{2p_{,r}}{\rho + p}, \tag{3.6}$$

$$T^{2\alpha}_{;\alpha} = T^{3\alpha}_{;\alpha} = 0 \implies \frac{\partial p}{\partial \theta} = 0 \quad , \quad \frac{\partial p}{\partial \phi} = 0. \tag{3.7}$$

Equation (3.7) states that the perfect fluid energy-momentum tensor inherits the symmetries of the metric of the spacetime.

The function B can be written in the following form:

$$B(t,r) = B(t_0, r) + \ln R^2_{,r} - \int_{t_0}^{t} \frac{A_{,r} R_{,t}}{R_{,r}} d\tilde{t}. \tag{3.8}$$

Now using (3.6) we obtain

$$e^{B(t,r)} = \frac{R^2_{,r}(t,r)}{1 + 2E(r)} \exp\left(\int_{t_0}^{t} \frac{2R_{,t}(\tilde{t}, r)}{[\rho(\tilde{t}, r) + p(\tilde{t}, r)]R_{,r}(\tilde{t}, r)} p_{,r}(\tilde{t}, r) d\tilde{t} \right), \tag{3.9}$$

where $E(r)$ is an arbitrary function.

In the special case of dust, the above equations reproduce the L-T model. As follows from (3.6) and (3.9), if $p_{,r} = 0$ then $e^A = 1$, $e^B = R^2_{,r}/(1 + 2E)$. Then the metric (3.1) becomes (2.2).

3.2 THE SZEKERES SOLUTION

3.2.1 DEFINITION AND METRIC

In the following, the Szekeres solution will be used to describe the formation and evolution of galaxy clusters and voids and to study light propagation effects acting on the CMB photons in a lumpy Universe. We begin by presenting the most basic properties of this solution those that will prove useful later in this chapter. A more extended account can be found in [31], [120] and [121].

The metric of the Szekeres solution is

$$ds^2 = dt^2 - e^{2\alpha} dr^2 - e^{2\beta}(dx^2 + dy^2), \tag{3.10}$$

where α and β are functions of (t, x, y, r), to be determined from the Einstein equations with a dust source. The coordinates of (3.10) are comoving so that $u^\mu = \delta^\mu_0$. Note that x and y play the role of angular coordinates here.

There are two families of Szekeres solutions, depending on whether $\beta_{,r} = 0$ or $\beta_{,r} \neq 0$. The first family is a simultaneous generalisation of the [122] models and, since it has so far found no useful application in astrophysical cosmology, we shall not discuss it here (see [31]). After the Einstein equations are solved, the metric functions in the second family become

$$e^\alpha = h(r)\Phi(t,r)\beta_{,r} \equiv h(r)(\Phi_{,r} + \Phi\nu_{,r}), \tag{3.11}$$

$$e^\beta = \Phi(t,r)e^{\nu(r,x,y)}, \tag{3.12}$$

$$e^{-\nu} = A(r)(x^2 + y^2) + 2B_1(r)x + 2B_2(r)y + C(r), \tag{3.13}$$

where the function $\Phi(t,r)$ is a solution of the equation

$$\Phi^2_{,t} = -k(r) + \frac{2M(r)}{\Phi} + \frac{1}{3}\Lambda\Phi^2, \tag{3.14}$$

where $h(r)$, $k(r)$, $M(r)$, $A(r)$, $B_1(r)$, $B_2(r)$ and $C(r)$ are arbitrary functions obeying

$$g(r) := 4(AC - B_1^2 - B_2^2) = \frac{1}{h^2(r)} + k(r). \tag{3.15}$$

The mass density in energy units is

$$\kappa \rho = \frac{(2Me^{3\nu})_{,r}}{e^{2\beta}(e^{\beta})_{,r}} \quad , \quad \kappa = \frac{8\pi G}{c^4}. \tag{3.16}$$

In the L-T model, the bang time function follows from (3.14):

$$\int_0^\Phi \frac{d\Phi}{\sqrt{-k + \frac{2M}{\Phi} + \frac{1}{3}\Lambda\Phi^2}} = t - t_B(r). \tag{3.17}$$

In general, the Szekeres metric has no symmetry, but acquires a 3-dimensional symmetry group with 2-dimensional orbits when A, B_1, B_2 and C are all constant (that is, when $\nu_{,r} = 0$).

The sign of $g(r)$ determines the geometry of the constant t, constant r 2-surfaces (and the symmetry of the constant A, B_1, B_2 and C case). The geometry of these surfaces is spherical, planar or hyperbolic when $g > 0$, $g = 0$ or $g < 0$, respectively. With A, B_1, B_2 and C being functions of r, the surfaces $r =$ constant within a single space $t =$ constant may have different geometries, i.e. they can be spheres in one part of the space and surfaces of constant negative curvature elsewhere, the curvature being zero at the boundary.

The sign of $k(r)$ determines the type of evolution: with $k > 0 = \Lambda$, the model expands away from an initial singularity and then recollapses to a final singularity; with $k < 0 = \Lambda$ the model is either ever-expanding or ever-collapsing, depending on the initial conditions; $k = 0$ is the intermediate case corresponding to the 'flat' Friedmann model. The sign of $k(r)$ influences the sign of $g(r)$. Since $1/h^2$ in (3.15) must be non-negative, we have the following: with $g > 0$ (spherical geometry), all three types of evolution are allowed; with $g = 0$ (plane geometry), k must be non-positive (only parabolic or hyperbolic evolutions are allowed); and with $g < 0$ (hyperbolic geometry), k must be strictly negative, so only the hyperbolic evolution is allowed.

The Friedmann limit follows when $\Phi(t,r) = rR(t)$, $k = k_0 r^2$ where $k_0 =$ constant and $B_1 = B_2 = 0$, $C = 4A = 1$. This definition of the Friedmann limit includes the definition of the limiting radial coordinate (the Szekeres model is covariant with the transformations $r = f(r')$, where $f(r')$ is an arbitrary function).

The Szekeres models are subdivided according to the sign of $g(r)$ into the quasi-spherical ones (with $g > 0$), quasi-plane ($g = 0$) and quasi-hyperbolic ($g < 0$). Only the quasi-spherical model has been well investigated and found useful application in astrophysical cosmology, so in this text we limit ourselves to this class. The quasi-spherical model may be imagined as a generalization of the L-T model in which the spheres of constant mass are made non-concentric. The functions $A(r)$, $B_1(r)$ and $B_2(r)$ determines how the centre of a sphere changes its position in a space $t =$ constant when the radius of the sphere is increased or decreased. Still, this is a rather simple geometry because all the arbitrary functions depend on one variable, r.

Often, it is more practical to reparametrise the arbitrary functions in the Szekeres metric as follows (this parametrisation was invented by [123]). Even if $A = 0$ initially, a transformation of the (x,y)-coordinates can restore $A \neq 0$, so we may assume $A \neq 0$ with no loss of generality. Then let $g \neq 0$. Writing $A = \sqrt{|g|}/(2S)$, $B_1 = -\sqrt{|g|}P/(2S)$, $B_2 = -\sqrt{|g|}Q/(2S)$, $\epsilon := g/|g|$, $k = |g|\tilde{k}$ and $\Phi = \sqrt{|g|}\tilde{\Phi}$, we can represent the metric (3.11)-(3.13) as

$$e^{-\nu} = \sqrt{|g|}\mathcal{E} \quad , \quad \mathcal{E} := \frac{S}{2}\left[\left(\frac{x-P}{S}\right)^2 + \left(\frac{y-Q}{S}\right)^2 + \epsilon\right], \tag{3.18}$$

$$ds^2 = dt^2 - \frac{(\Phi_{,r} - \Phi\mathcal{E}_{,r}/\mathcal{E})^2}{\epsilon - k(r)}dr^2 - \frac{\Phi^2}{\mathcal{E}^2}(dx^2 + dy^2), \tag{3.19}$$

where $\epsilon = +1$, for the quasi-spherical model. When $g = 0$, the transition from (3.11)-(3.13) to (3.19) is $A = 1/(2S)$, $B_1 = -P/(2S)$, $B_2 = -Q/(2S)$ and Φ is unchanged. Then (3.19) applies with $\epsilon = 0$, and the resulting model is quasi-plane, which we do not discuss here.

The parametrisation introduced above makes several formulae simpler, mainly because all the functions present in it are independent and the constraint (3.15) is identically satisfied in it. Further, within each

single $t = $ constant, $r = $ constant surface, the transformation from the (θ, ϕ) coordinates of (2.2) to the (x, y) coordinates is

$$\frac{(x - P, y - Q)}{S} = \cot\left(\frac{\theta}{2}\right)(\cos\phi, \sin\phi). \tag{3.20}$$

This transformation is called a stereographic projection.

We have briefly presented the Szekeres metric following the method by which it was originally derived: the form (3.10) was postulated, and then the complete solution of the Einstein equations was found.

3.2.2 GENERAL PROPERTIES OF THE SZEKERES SOLUTIONS

The Szekeres models are solutions of the Einstein equations for an irrotational dust source. In addition the acceleration vanishes, so that $u^\alpha_{;\beta}u^\beta = 0$. The shear tensor is

$$\sigma^\alpha_\beta = \frac{1}{3}\left(\frac{\Phi_{,tr} - \Phi_{,t}\Phi_{,r}/\Phi}{\Phi_{,r} - \Phi\mathcal{E}_{,r}/\mathcal{E}}\right)\mathrm{diag}(0, 2, -1, -1). \tag{3.21}$$

The scalar of expansion is

$$\theta = u^\alpha_{;\alpha} = \frac{\Phi_{,tr} + 2\Phi_{,t}\Phi_{,r}/\Phi - 3\Phi_{,t}\mathcal{E}_{,r}/\mathcal{E}}{\Phi_{,r} - \Phi\mathcal{E}_{,r}/\mathcal{E}}. \tag{3.22}$$

In the Friedmann limit, $R \longrightarrow rR_F$, where R_F is the Friedmann scale factor. Thus $\theta \longrightarrow 3H_0$, where H_0 is the current value of the Hubble parameter and $\sigma^\alpha_\beta \longrightarrow 0$.

The equations of motion $T^{\alpha\beta}_{;\beta} = 0$ reduce to the continuity equation:

$$\rho_{,t} + \rho\theta = 0. \tag{3.23}$$

In the expanding Universe, $\theta > 0$, so the density decreases. The structures which exist in the Universe emerged either due to lower expansion of the space (formation of overdense regions) or due to faster expansion (formation of underdense regions).

The Weyl curvature decomposed into its electric and magnetic parts is of the following form:

$$E^\alpha_\beta = C^\alpha_{\gamma\beta\delta}u^\gamma u^\delta = \frac{M(3\Phi_{,r} - \Phi M_{,r}/M)}{3\Phi^3(\Phi_{,r} - \Phi\mathcal{E}_{,r}/\mathcal{E})}\mathrm{diag}(0, 2, -1, -1), \tag{3.24}$$

$$H_{\alpha\beta} = \frac{1}{2}\sqrt{-g}\epsilon_{\alpha\gamma\mu\nu}C^{\mu\nu}_{\beta\delta} = 0. \tag{3.25}$$

Finally, the $4D$ and $3D$ Ricci scalars are, respectively

$$\mathcal{R}^{4D} = -4\Lambda - 8\pi G\rho, \tag{3.26}$$

$$\mathcal{R}^{3D} = 2\frac{k}{\Phi^2}\left(\frac{\Phi k_{,r}/k - 2\Phi\mathcal{E}_{,r}/\mathcal{E}}{\Phi_{,r} - \Phi\mathcal{E}_{,r}/\mathcal{E}} + 1\right). \tag{3.27}$$

3.2.3 PROPERTIES OF THE QUASI-SPHERICAL SZEKERES SOLUTION

When $\Lambda \neq 0$, the solutions of (3.14) involve elliptic functions. A general formal integral of (3.14) was found by [124]. Any solution of (3.14) will contain one more arbitrary function of r, denoted $t_B(r)$, which will enter the solution in the combination $(t - t_B(r))$. The instant $t = t_B(r)$ defines the initial moment of evolution; when $\Lambda = 0$ it is necessarily a singularity corresponding to $\Phi = 0$, and it goes over into the Big Bang singularity in the Friedmann limit. When $t_{B,r} \neq 0$ (that is, in general) the instant of singularity is position-dependent, just as it is in the L-T model.

As for the L-T model, another singularity may occur where $(e^\beta)_{,r} = 0$ (if this equation has solutions). This is a shell crossing, but now it is qualitatively different from that in the L-T model. If this singularity is present in the L-T model, then whole spherical shells collide there. Here, as can be seen by (3.11)-(3.13), the equation $(e^\beta)_{,r} = 0$ may define a subset of the x, y surface at each r. When a shell crossing exists, its

intersection with a $t =$ constant space will be a circle, or in exceptional cases, a single point, in each of a set of constant r 2-surfaces, and not a sphere.

Equation (3.14) is formally identical to the Friedmann equation, but with k and M depending on r, so each surface $r =$ constant evolves independently of the others. The solutions $\Phi(t, r)$ are the same as the L-T solutions $R(t, r)$ of (2.3), and are unaffected by the dependence of the Szekeres solutions on the (x, y) coordinates.

As defined by (3.11)-(3.14), the Szekeres models contain eight functions of r, of which only seven are arbitrary because they must obey (3.15). Further, the parametrisation of (3.18)-(3.19) turns the function $g(r)$ to a constant parameter ϵ, thus reducing the number to six. By a choice of r (still arbitrary up to now), we can fix one more function (for example, by defining $r' = M(r)$), thereby reducing the physical degrees of freedom to five.

In the following, we will represent the quasi-spherical Szekeres solution with $\beta_{,r} \neq 0$ in the parametrisation introduced in (3.18)-(3.19). The formula for density in these variables is

$$\kappa\rho = \frac{2(M_{,r} - 3M\mathcal{E}_{,r}/\mathcal{E})}{\Phi^2(\Phi_{,r} - \Phi\mathcal{E}_{,r}/\mathcal{E})}. \tag{3.28}$$

Basic physical restrictions

We choose $\Phi \geq 0$ ($\Phi = 0$ is an origin, the bang or the crunch; in no case is a continuation to negative Φ possible) and $M(r) \geq 0$, so that any vacuum exterior has positive Schwarzschild mass.

For a well-behaved r-coordinate we require

$$\infty > \frac{(\Phi_{,r} - \Phi\mathcal{E}_{,r}/\mathcal{E})^2}{1 - k} > 0, \tag{3.29}$$

i.e. $1 - k > 0$, except where $(\Phi_{,r} - \Phi\mathcal{E}_{,r}/\mathcal{E})^2 = 0$.

The density must be positive, and the Kretschmann scalar $R_{\alpha\beta\gamma\delta}R^{\alpha\beta\gamma\delta}$ must be finite, which adds either

$$M_{,r} - \frac{3M\mathcal{E}_{,r}}{\mathcal{E}} \geq 0 \quad \text{and} \quad \Phi_{,r} - \frac{\Phi\mathcal{E}_{,r}}{\mathcal{E}} \geq 0, \tag{3.30}$$

or

$$M_{,r} - \frac{3M\mathcal{E}_{,r}}{\mathcal{E}} \leq 0 \quad \text{and} \quad \Phi_{,r} - \frac{\Phi\mathcal{E}_{,r}}{\mathcal{E}} \leq 0. \tag{3.31}$$

If $\left(\Phi_{,r} - \frac{\Phi\mathcal{E}_{,r}}{\mathcal{E}}\right)$ passes through zero anywhere other than at a regular extremum, we have a shell crossing.

The significance of $\mathcal{E}$

As seen from (3.18), with $\epsilon = +1$ and $S > 0$, we always have $\mathcal{E} > 0$. Can $\mathcal{E}_{,r}$ change sign?

We will consider the variation of $\mathcal{E}(r, x, y)$ around the spheres of constant t and r. Setting $\epsilon = +1$ and applying the transformation (3.20) to $\mathcal{E}$ in (3.18) and to its derivative we see that the locus of $\mathcal{E}_{,r} = 0$ is

$$S_{,r}\cos\theta + P_{,r}\sin\theta\cos\phi + Q_{,r}\sin\theta\sin\phi = 0. \tag{3.32}$$

Writing

$$Z = \cos\theta \quad , \quad Y = \sin\theta\cos\phi \quad , \quad X = \sin\theta\sin\phi, \tag{3.33}$$

we see that (X, Y, Z) is on a unit sphere through $(0,0,0)$, and (3.32) becomes $S_{,r}Z + P_{,r}X + Q_{,r}Y = 0$ which is the equation of an arbitrary plane through $(0,0,0)$. Such planes all intersect the unit sphere along great circles, with locus

$$\tan\theta = \frac{-S_{,r}}{P_{,r}\cos\phi + Q_{,r}\sin\phi}. \tag{3.34}$$

With $S_{,r} = 0$, the function $\mathcal{E}_{,r}$ is negative on one side of the circle, zero on the circle and positive on the other side.

As seen from (3.34), with $S_{,r} = 0$ we have $\theta = 0$, which means that the great circle defined by $\mathcal{E}_{,r} = 0$ passes through the pole of stereographic projection. In this case, the image of the circle $\mathcal{E}_{,r} = 0$ on the

(x, y) plane is a straight line passing through $(x, y) = (P, Q)$. $\mathcal{E}_{,r}$ has a different sign on each side of the straight line. From the definition of $\mathcal{E}$ we find

$$\frac{\mathcal{E}_{,r}}{\mathcal{E}} = \frac{-[S_{,r}\cos\theta + \sin\theta(P_{,r}\cos\phi + Q_{,r}\sin\phi)]}{S}. \tag{3.35}$$

Thus

$$\frac{\mathcal{E}_{,r}}{\mathcal{E}} = \text{constant} \implies S_{,r}Z + P_{,r}X + Q_{,r}Y = S \times \text{constant}, \tag{3.36}$$

which is a plane parallel to the $\mathcal{E}_{,r} = 0$ plane, implying that all loci of $\mathcal{E}_{,r}/\mathcal{E} = $ constant are circles parallel to the $\mathcal{E}_{,r} = 0$ great circle.

The extrema of $\mathcal{E}_{,r}/\mathcal{E}$ are located at

$$\tan\phi_e = \frac{Q_{,r}}{P_{,r}}, \tag{3.37}$$

$$\tan\theta_e = \frac{P_{,r}\cos\phi_e + Q_{,r}\sin\phi_e}{S_{,r}} = \epsilon_1 \frac{\sqrt{P_{,r}^2 + Q_{,r}^2}}{S_{,r}}, \tag{3.38}$$

$$\cos\theta_e = \epsilon_2 \frac{S_{,r}}{\sqrt{S_{,r}^2 + P_{,r}^2 + Q_{,r}^2}} \quad, \quad \epsilon_1, \epsilon_2 = \pm 1. \tag{3.39}$$

The extreme value is then

$$\left(\frac{\mathcal{E}_{,r}}{\mathcal{E}}\right)_{\text{extreme}} = -\epsilon_2 \frac{\sqrt{S_{,r}^2 + P_{,r}^2 + Q_{,r}^2}}{S}. \tag{3.40}$$

Since

$$(\sin\theta_e\cos\phi_e, \sin\theta_e\sin\phi_e, \cos\theta_e) = \frac{\epsilon_2(P_{,r}, Q_{,r}, S_{,r})}{\sqrt{S_{,r}^2 + P_{,r}^2 + Q_{,r}^2}}, \tag{3.41}$$

the extreme values of $\mathcal{E}_{,r}/\mathcal{E}$ are poles to the great circles of $\mathcal{E}_{,r} = 0$.

Clearly $\mathcal{E}_{,r}/\mathcal{E}$ has a dipole variation around each constant-r sphere, changing sign when we go over to the antipodal point: $(\theta, \phi) \longrightarrow (\pi - \theta, \phi + \pi)$. Writing

$$\Phi_{,r} - \frac{\Phi\mathcal{E}_{,r}}{\mathcal{E}} = \Phi_{,r} + \frac{\Phi[S_{,r}\cos\theta + \sin\theta(P_{,r}\cos\phi + Q_{,r}\sin\phi)]}{S}, \tag{3.42}$$

we see that $\Phi\mathcal{E}_{,r}/\mathcal{E}$ is the correction to the radial separation $\Phi_{,r}$ of constant-r shells, due to their not being concentric. In particular, $\Phi S_{,r}/S$ is the forward ($\theta = 0$) displacement, and $\Phi P_{,r}/S$ and $\Phi Q_{,r}/S$ are the two sideways displacements ($\theta = \pi/2, \phi = 0$) and ($\theta = \pi/2, \phi = \pi/2$). The shortest radial distance is where $\mathcal{E}_{,r}/\mathcal{E}$ is a maximum.

It will be shown later that, where $\Phi_{,r} > 0$, $\mathcal{E}_{,r}/\mathcal{E} \leq M_{,r}/(3M)$ and $\mathcal{E}_{,r}/\mathcal{E} \leq \Phi_{,r}/\Phi$ are required to avoid shell crossings, and also $\Phi_{,r}/\Phi > M_{,r}/(3M)$ in (3.56). These inequalities, together with $M_{,r} > 0$, imply that the density given by (3.28), as a function of $x := \mathcal{E}_{,r}/\mathcal{E}$,

$$\rho = \frac{2M_{,r}}{\Phi^2\Phi_{,r}} \frac{1 - 3Mx/M_{,r}}{1 - \Phi x/\Phi_{,r}}, \tag{3.43}$$

has a negative derivative by x:

$$\rho_{,x} = \frac{\Phi/\Phi_{,r} - 3M/M_{,r}}{(1 - \Phi x/\Phi_{,r})^2} \frac{2M_{,r}}{\Phi^2\Phi_{,r}} < 0, \tag{3.44}$$

so the density is minimum where $\mathcal{E}_{,r}/\mathcal{E}$ is maximum.

Conditions of regularity at the origin

We list here only those conditions of regularity that must be directly taken into account in considering the galaxy cluster and void models. The full list of conditions, with derivations, can be found in [120] and [31].

At the origin of spherical coordinates (which we assume to be at $r = 0$; this can always be satisfied by a transformation of r), we have $\Phi(t, 0) = 0$, $\forall t$ (the 2-spheres have no size). Similarly, $\Phi_{,t}(t, 0) = 0 = \Phi_{,tt}(t, 0)$, etc. $\forall t$. There will be a second origin, at $r = r_0$ say, in any closed, regular, $k > 0$ model. The regularity conditions say that

$$\lim_{r \to 0} M = 0 \quad , \quad \lim_{r \to 0} k = 0, \tag{3.45}$$

$$0 < \lim_{r \to 0} \left(|k|^{3/2} M \right) < \infty \quad , \quad \lim_{r \to 0} [3Mk_{,r}/(2M_{,r}k)] = 1. \tag{3.46}$$

All of the conditions taken together imply that, near an origin

$$M \sim \Phi^3 \quad , \quad k \sim \Phi^2 \quad , \quad S \sim \Phi^n \quad , \quad P \sim \Phi^n \quad , \quad Q \sim \Phi^n \quad , \quad n \geq 0. \tag{3.47}$$

The equation $\mathcal{E}_{,r}/\mathcal{E} \leq M_{,r}/(3M)$ that will be obtained in the next section implies that $n \leq 1$ near an origin.

Shell crossings

A shell crossing, if it exists, is the locus of zeros of the function $\chi := \mathcal{E}\Phi_{,r}/\Phi - \mathcal{E}_{,r}$. Now $\Phi_{,r} > 0$ and $\chi < 0$ cannot hold for all x and y. This would lead to $\mathcal{E}_{,r} > \mathcal{E}\Phi_{,r}/\Phi > 0$, and we know that $\mathcal{E}\Phi_{,r}$ cannot be positive at all x and y (see [120]). Hence, with $\Phi_{,r} > 0$, there must be a region in which $\chi > 0$. By a similar argument, $\Phi_{,r} < 0$ and $\chi > 0$ cannot hold for all x and y, so with $\Phi_{,r} < 0$ there must be a region in which $\chi < 0$.

Assuming $\Phi_{,r} > 0$, can χ be positive for all x and y? A calculation [120] shows that χ will have the same sign for all x and y, i.e. there will be no shell crossings if and only if

$$\frac{\Phi_{,r}^2}{\Phi^2} = \frac{S_{,r}^2 + P_{,r}^2 + Q_{,r}^2}{S^2} := \Psi^2(r). \tag{3.48}$$

If $\Phi_{,r}^2/\Phi^2 = \Psi^2$, then $\chi = 0$ at one x-value, say x_{SS}. In this case, the shell crossing is a single point in the constant-(t, r) surface, i.e. a curve in a space of constant t and a 2-surface in spacetime.

If $\Phi_{,r}^2/\Phi^2 < \Psi^2$, then the locus of $\chi = 0$ is in general a circle with the centre at

$$(x_{SC}, y_{SC}) = \left(P - \frac{P_{,r}}{S_{,r}/S + \Phi_{,r}/\Phi}, Q - \frac{Q_{,r}}{S_{,r}/S + \Phi_{,r}/\Phi} \right), \tag{3.49}$$

and with the radius $L_{SC} = \sqrt{\delta}/(S_{,r}/S + \Phi_{,r}/\Phi)$, where

$$\delta := P_{,r}^2 + Q_{,r}^2 + \epsilon(S_{,r}^2 - S^2\Phi_{,r}^2/\Phi^2). \tag{3.50}$$

This is a general a different circle from the one defined by $\mathcal{E}_{,r} = 0$. The shell-crossing set intersects with the surface of constant t and r along the line $\mathcal{E}_{,r}/\mathcal{E} = \Phi_{,r}/\Phi =$ constant. As noted after (3.36), this is a circle that lies in a plane parallel to the $\mathcal{E}_{,r}$ great circle. It follows that the $\mathcal{E}_{,r}$ and SC circles cannot intersect unless they coincide.

Now we will consider the conditions for avoiding shell crossings. They were worked out by [34], and improved upon by [120]. The account here is based on the latter reference.

For positive density, (3.28) shows that $(M_{,r} - 3M\mathcal{E}_{,r}/\mathcal{E})$ and χ must have the same sign. Consider the case when both are positive. When $(M_{,r} - 3M\mathcal{E}_{,r}/\mathcal{E} \leq 0)$ and $\chi \leq 0$, the inequalities in all of the following should be reversed.

Both $(M_{,r} - 3M\mathcal{E}_{,r}/\mathcal{E})$ and χ can be zero for a particular (x, y) value if $M_{,r}/3M = \Phi_{,r}/\Phi$, but the latter cannot hold for all time. This case can hold for all (x, y) only if $M_{,r} = 0$, $\mathcal{E}_{,r} = 0$ and $\Phi_{,r}/\Phi = 0$, which requires all of $M_{,r}$, $k_{,r}$, $t_{B,r}$, $S_{,r}$, $P_{,r}$ and $Q_{,r}$ to be zero at some r value.

Consider the inequality $M_{,r} - 3M\mathcal{E}_{,r}/\mathcal{E} \geq 0$. It must hold for all values of $\mathcal{E}_{,r}/\mathcal{E}$, including the extreme value (3.40), for which

$$\frac{M_{,r}}{3M} \geq \frac{\mathcal{E}_{,r}}{\mathcal{E}}\Big|_{\max} = \frac{\sqrt{S_{,r}^2 + P_{,r}^2 + Q_{,r}^2}}{S} \qquad \forall r. \tag{3.51}$$

We will now consider $\chi > 0$ for all three types of evolution. We quote the results only. For details see [120].

Hyperbolic evolution, $k < 0$

Here, $\chi > 0$ implies

$$t_{B,r} < 0 \qquad \forall r, \tag{3.52}$$

$$\frac{\Phi_{,r}}{\Phi} - \frac{\mathcal{E}_{,r}}{\mathcal{E}} > 0 \implies \frac{k_{,r}}{2k} - \frac{\mathcal{E}_{,r}}{\mathcal{E}} > 0, \tag{3.53}$$

$$\frac{k_{,r}}{2k} > \frac{\sqrt{S_{,r}^2 + P_{,r}^2 + Q_{,r}^2}}{S} \qquad \forall r, \tag{3.54}$$

which implies $k_{,r} < 0$ $\forall r$. Since we already have $M_{,r} \geq 0$, this is sufficient, and implies $\Phi_{,r} > 0$.

Parabolic evolution, $k = 0$

All terms involving $k_{,r}/k$ cancel out and we retain conditions (3.51) and (3.52). Naturally, (3.54) ceases to impose any limit.

Elliptic evolution, $k > 0$

Here, the conditions are (3.52) and

$$\frac{2\pi M}{k^{3/2}} \left(\frac{M_{,r}}{M} - \frac{3k_{,r}}{2k}\right) + t_{B,r} > 0 \qquad \forall r, \tag{3.55}$$

which says that the crunch time must increase with r. Since we already have $M_{,r} \geq 0$, these conditions are sufficient to keep $\Phi_{,r} > 0$ for all time. Further, it can be shown that

$$\frac{\Phi_{,r}}{\Phi} > \frac{M_{,r}}{3M}, \tag{3.56}$$

so that (3.51) guarantees that for each given r the maximum of $\mathcal{E}_{,r}/\mathcal{E}$ as (x, y) are varied is no more than the minimum of $\Phi_{,r}/\Phi$ as η varies.

The mass-dipole

In the Szekeres solution discussed here, the distribution of mass over each single sphere $\{t = \text{constant}, r = \text{constant}\}$ has the form of a mass dipole superimposed on a monopole. This was first noted by [34], and then explained in much more detail by [126]. The presentation here is based on the latter reference (see also [31]).

The basic idea is to separate the expression for matter density, (3.28), into a spherically symmetric part ρ_s, depending only on t and r, and a nonsymmetric part $\Delta\rho$. Without additional requirements, this can be done in an infinite number of ways. The way to achieve a unique result is as follows. The calculation is simpler in the variables of (3.10)-(3.16), so we do it first in that representation. For better readability, we denote

$$\mathcal{N} = e^{-\nu}. \tag{3.57}$$

Adding and subtracting $H(t, r)/\Phi^2$ on the right-hand side of (3.16), where $H(t, r)$ is an arbitrary function, results in

$$\rho = \rho_s(t, r) + \Delta\rho(t, r, x, y), \tag{3.58}$$

where

$$\kappa\rho_s = \frac{H}{\Phi^2} \quad , \quad \kappa\Delta\rho = \frac{\mathcal{N}(2M_{,r} - H\Phi_{,r}) - \mathcal{N}_{,r}(6M - H\Phi)}{\Phi^2(\mathcal{N}\Phi_{,r} - \Phi\mathcal{N}_{,r})}. \tag{3.59}$$

Now additional requirements on H will make the splitting unique. We transform (x, y) to spherical polar coordinates on a sphere of radius one that is tangent to the (x, y) plane at the point $(x, y) = (0, 0)$. The transformation is as in (3.20), but with $S = 1$ and $P = Q = 0$, viz.

$$x = \cot(\theta/2)\cos\phi \quad , \quad y = \cot(\theta/2)\sin\phi, \tag{3.60}$$

which transforms $\mathcal{N} = e^{-\nu}$, as given by (3.11)-(3.13), to

$$\mathcal{N} = A\cot^2(\theta/2) + 2B_1\cot(\theta/2)\cos\phi + 2B_2\cot(\theta/2)\sin\phi + C. \tag{3.61}$$

We substitute this in (3.59) and consider the equation $\Delta\rho = 0$. We embed the sphere in a Euclidean 3-space, and express (θ, ϕ) through the Cartesian coordinates in the space via (3.33). Using (3.33) and (3.61) in $\Delta\rho = 0$ we obtain

$$[A_{,r}(1 + Z) + 2B_{1,r}X + 2B_{2,r}Y + C_{,r}(1 - Z)](6M - H\Phi)$$

$$= [A(1 + Z) + 2B_1 X + 2B_2 Y + C(1 - Z)](2M_{,r} - H\Phi_{,r}). \tag{3.62}$$

Now we require that the surface of $\Delta\rho = 0$ passes through the centre of the sphere, i.e. that (3.62) is fulfilled at $X = Y = Z = 0$, thus

$$(A + C)(2M_{,r} - H\Phi_{,r}) = (A_{,r} + C_{,r})(6M - H\Phi). \tag{3.63}$$

Since (A, C, M, Φ) depend only on t and r, this can be solved for H:

$$H = \frac{2M_{,r}(A + C) - 6M(A + C)_{,r}}{\Phi_{,r}(A + C) - \Phi(A + C)_{,r}}. \tag{3.64}$$

This solution makes sense except when $[(A + C)/\Phi]_{,r} \cong 0$. But then, the Szekeres model would degenerate into the Friedmann model. Hence, (3.64) applies whenever the Szekeres model is inhomogeneous.

With H given by (3.64), (3.59) becomes

$$\kappa\rho_s = \frac{2M_{,r}(A + C) - 6M(A + C)_{,r}}{\Phi^2[\Phi_{,r}(A + C) - \Phi(A + C)_{,r}]}, \tag{3.65}$$

$$\kappa\Delta\rho = \frac{A_{,r} + C_{,r} - (A + C)\mathcal{N}_{,r}/\mathcal{N}}{\Phi^2(\Phi_{,r} - \mathcal{N}_{,r}/\mathcal{N})} \frac{6M\Phi_{,r} - 2M_{,r}\Phi}{\Phi^2[\Phi_{,r}(A + C) - \Phi(A_{,r} + C_{,r})]}. \tag{3.66}$$

Now, $\Delta\rho = 0$ has two solutions:

$$A_{,r} + C_{,r} - (A + C)\mathcal{N}_{,r}/\mathcal{N} = 0 \tag{3.67}$$

and

$$\left(\frac{2M}{\Phi^3}\right)_{,r} = 0. \tag{3.68}$$

The second one defines a hypersurface that depends on t, that is, it is not comoving except when $(2M/\Phi^3)_{,r} \equiv 0$, but then the matter-density becomes spatially homogeneous. Therefore, we can discard this solution. However, the first solution defines a hypersurface, call it H_1, which is independent of t. Also, $\Delta\rho$ changes sign when H_1 is crossed, and, in the variables (X, Y, Z), $\Delta\rho$ is antisymmetric with respect to H_1. Hence $\Delta\rho$ is a dipole-like contribution to matter density. Although the separation (3.58) is global, the orientation of the dipole axis is different on every sphere $\{t = \text{constant}, r = \text{constant}\}$.

Repeating the calculation in the variables (3.18)-(3.19) we obtain

$$\kappa\Delta\rho = \frac{\chi_{,r} - \chi\mathcal{E}_{,r}/\mathcal{E}}{\Phi^2(\Phi_{,r} - \mathcal{E}_{,r}/\mathcal{E})} \frac{6M\Phi_{,r} - 2M_{,r}\Phi}{\Phi^2(\Phi_{,r}\chi - \Phi\chi_{,r})}, \tag{3.69}$$

$$\chi := \frac{1 + P^2 + Q^2}{2S} + \frac{S}{2}. \tag{3.70}$$

The set H_1 intersects every (t = constant, r = constant) sphere along a circle, unless $P_{,r} = Q_{,r} = S_{,r} = 0 (= A_{,r} = C_{,r})$, in which case the dipole component of density is simply zero. The intersection of H_1 with any sphere of constant r is a circle parallel to the great circle $\mathcal{E}_{,r} = 0$. It will coincide with the $\mathcal{E}_{,r} = 0$ circle at those points where $\chi_{,r} = 0$ (if they exist). The dipole-like component will be antisymmetric with respect to $\mathcal{E}_{,r}/\mathcal{E}$ only at those values of r where $\chi\Phi = 0 = \chi_{,r}\Phi_{,r}$, but such values may exist only at the centre, $\Phi = 0$, because (3.70) clearly implies $\chi > 0$.

3.3   NULL GEODESICS IN THE QUASI-SPHERICAL SZEKERES MODEL

The geodesic equations $k^{\alpha}_{;\beta}k^{\beta} = 0$ (where $k^{\alpha} = dx^{\alpha}/ds$) in the quasi-spherical Szekeres model are [120]

$\alpha = 0$:

$$\frac{d^2 t}{ds^2} + \frac{\Phi_{,tr} - \Phi_{,t}\mathcal{E}_{,r}/\mathcal{E}}{1-k}(\Phi_{,r} - \Phi\mathcal{E}_{,r}/\mathcal{E})\left(\frac{dr}{ds}\right)^2 + \frac{\Phi\Phi_{,t}}{\mathcal{E}^2}\left[\left(\frac{dx}{ds}\right)^2 + \left(\frac{dy}{ds}\right)^2\right] = 0, \qquad (3.71)$$

$\alpha = 1$:

$$\frac{d^2 r}{ds^2} + 2\frac{\Phi_{,tr} - \Phi_{,t}\mathcal{E}_{,r}/\mathcal{E}}{\Phi_{,r} - \Phi\mathcal{E}_{,r}/\mathcal{E}}\frac{dt}{ds}\frac{dr}{ds} + \left(\frac{\Phi_{,rr} - \Phi_{,r}\mathcal{E}_{,r}/\mathcal{E} - \Phi\mathcal{E}_{,rr}/\mathcal{E} + \Phi(\mathcal{E}_{,r}/\mathcal{E})^2}{\Phi_{,r} - \Phi\mathcal{E}_{,r}/\mathcal{E}} + \frac{1}{2}\frac{k_{,r}}{1-k}\right)\left(\frac{dr}{ds}\right)^2$$

$$+2\frac{\Phi}{\mathcal{E}^2}\frac{\mathcal{E}_{,r}\mathcal{E}_{,x} - \mathcal{E}\mathcal{E}_{,xr}}{\Phi_{,r} - \Phi\mathcal{E}_{,r}/\mathcal{E}}\frac{dr}{ds}\frac{dx}{ds} + 2\frac{\Phi}{\mathcal{E}^2}\frac{\mathcal{E}_{,r}\mathcal{E}_{,y} - \mathcal{E}\mathcal{E}_{,yr}}{\Phi_{,r} - \Phi\mathcal{E}_{,r}/\mathcal{E}}\frac{dr}{ds}\frac{dy}{ds}$$

$$-\frac{\Phi}{\mathcal{E}^2}\frac{1-k}{\Phi_{,r} - \Phi\mathcal{E}_{,r}/\mathcal{E}}\left[\left(\frac{dx}{ds}\right)^2 + \left(\frac{dy}{ds}\right)^2\right] = 0, \qquad (3.72)$$

$\alpha = 2$:

$$\frac{d^2 x}{ds^2} + 2\frac{\Phi_{,t}}{\Phi}\frac{dt}{ds}\frac{dx}{ds} - \left(\frac{1}{\Phi}\frac{\Phi_{,r} - \Phi\mathcal{E}_{,r}/\mathcal{E}}{1-k}(\mathcal{E}_{,r}\mathcal{E}_{,x} - \mathcal{E}\mathcal{E}_{,xr})\right)\left(\frac{dr}{ds}\right)^2$$

$$+2\left(\frac{\Phi_{,r}}{\Phi} - \frac{\mathcal{E}_{,r}}{\mathcal{E}}\right)\frac{dr}{ds}\frac{dx}{ds} - \frac{\mathcal{E}_{,x}}{\mathcal{E}}\left(\frac{dx}{ds}\right)^2 - 2\frac{\mathcal{E}_{,y}}{\mathcal{E}}\frac{dx}{ds}\frac{dy}{ds} + \frac{\mathcal{E}_{,x}}{\mathcal{E}}\left(\frac{dy}{ds}\right)^2 = 0, \qquad (3.73)$$

$\alpha = 3$:

$$\frac{d^2 y}{ds^2} + 2\frac{\Phi_{,t}}{\Phi}\frac{dt}{ds}\frac{dy}{ds} - \left(\frac{1}{\Phi}\frac{\Phi_{,r} - \Phi\mathcal{E}_{,r}/\mathcal{E}}{1-k}(\mathcal{E}_{,r}\mathcal{E}_{,y} - \mathcal{E}\mathcal{E}_{,yr})\right)\left(\frac{dr}{ds}\right)^2$$

$$+2\left(\frac{\Phi_{,r}}{\Phi} - \frac{\mathcal{E}_{,r}}{\mathcal{E}}\right)\frac{dr}{ds}\frac{dy}{ds} + \frac{\mathcal{E}_{,y}}{\mathcal{E}}\left(\frac{dx}{ds}\right)^2 - 2\frac{\mathcal{E}_{,x}}{\mathcal{E}}\frac{dx}{ds}\frac{dy}{ds} - \frac{\mathcal{E}_{,y}}{\mathcal{E}}\left(\frac{dy}{ds}\right)^2 = 0. \qquad (3.74)$$

When studying light propagation in the quasi-spherical Szekeres model, these equations, together with the evolution equations and the condition $k_{\alpha}k^{\alpha} = 0$, must be solved. Apart from special cases which will be discussed in the next section, these equations do not reduce to a simpler form. Also, in the general case there is no simple formula for redshift; to find the frequency shift z the general formula $1 + z = k_e^0/k^0$ (where the subscript e refers to the emission instant) must be employed.

3.3.1   CONSTANT (x, y) GEODESICS

When studying light propagated in the Friedmann or L-T models, radial null geodesics are often considered. Along such geodesics only the time and the radial coordinate change, while the other two spatial coordinates remain constant. However, in the Szekeres model, in general it is impossible to define a radial direction.

As follows from (3.71)-(3.74) if initially $k^x = k^y = 0$, then the coordinates x and y will remain constant only if, along the whole geodesic,

$$\Phi_{,r} = \Phi \frac{\mathcal{E}_{,r}}{\mathcal{E}},$$
(3.75)

or

$$\mathcal{E}\mathcal{E}_{,xr} = \mathcal{E}_{,x}\mathcal{E}_{,r} \quad , \quad \mathcal{E}\mathcal{E}_{,yr} = \mathcal{E}_{,y}\mathcal{E}_{,r}.$$
(3.76)

The relation (3.75) holds only at a shell-crossing singularity, which must be eliminated in a physically acceptable model. Let us then focus on condition (3.76). In the quasi-spherical model $\mathcal{E} > 0$ for all r. From the definition of $\mathcal{E}$, (3.18), we have

$$\mathcal{E}_{,x} = \frac{x-P}{S} \quad , \quad \mathcal{E}_{,xr} = -\frac{P_{,r}}{S} - \frac{S_{,r}}{S}\mathcal{E}_{,x},$$
(3.77)

$$\mathcal{E}_{,y} = \frac{y-Q}{S} \quad , \quad \mathcal{E}_{,yr} = -\frac{Q_{,r}}{S} - \frac{S_{,r}}{S}\mathcal{E}_{,y}.$$
(3.78)

Since (3.76) are not functional relations, we have to consider the following cases:

$\mathcal{E}_{,x} \neq 0 \neq \mathcal{E}_{,y}$

From (3.76)

$$\frac{\mathcal{E}_{,xr}}{\mathcal{E}_{,x}} = \frac{\mathcal{E}_{,yr}}{\mathcal{E}_{,y}} \iff \frac{P_{,r}}{x-P} = \frac{Q_{,r}}{y-Q}.$$
(3.79)

This should hold at constant $x = x_0$ and $y = y_0$ along the whole geodesic, i.e. at every r. This equation is fulfilled for any P and Q at $(x_0, y_0) \longrightarrow (\pm\infty, \pm\infty)$. However, $(x_0, y_0) = (\infty, \infty)$ is a singular point of the geodesic equations (3.71)-(3.75) and of the metric (3.19), so this case must be investigated separately, and we will discuss it after dealing with the other cases. In looking for other solutions, we integrate (3.79) with respect to r. One special solution of this equation is $P_{,r} = Q_{,r} = 0$ and we will come back to this case below. The general integral is

$$Q = y_0 + C_0(P - x_0),$$
(3.80)

along the geodesic, where C_0 is an arbitrary constant. However, with $\mathcal{E}_{,x} \neq 0 \neq \mathcal{E}_{,y}$, (3.79) also implies

$$\frac{\mathcal{E}_{,xr}}{\mathcal{E}_{,x}} = \frac{\mathcal{E}_{,r}}{\mathcal{E}},$$
(3.81)

i.e.

$$\frac{P_{,r}}{x_0-P} = \frac{2[(x_0-P)P_{,r} + (y_0-Q)Q_{,r}] - 2SS_{,r}}{(x_0-P)^2 + (y_0-Q)^2 + S^2}.$$
(3.82)

Again, this is fulfilled for any P and Q at $(x_0, y_0) \longrightarrow (\pm\infty, \pm\infty)$, which will be discussed later. If $P_{,r} = 0$ in (3.82), then $Q_{,r} = 0$ from (3.80), and the above implies $S_{,r} = 0$, which reduces the Szekeres model to the L-T model. Apart from this special case, with $P_{,r} \neq 0$, (3.82) is integrated with the result:

$$S^2 = C_1(x_0-P) - (C_0^2+1)(x_0-P)^2,$$
(3.83)

where C_1 is another arbitrary constant $\neq 0$.

$\mathcal{E}_{,y} = 0 \neq \mathcal{E}_{,x}$

With $\mathcal{E}_{,y} = (y-Q)/S = 0$ we have $y_0 = Q$ along the whole geodesic, i.e. $Q_{,r} = 0$. Then the second of (3.78) shows that also $\mathcal{E}_{,yr} = 0$ along this geodesic, and the second of (3.76) is fulfilled. The first of (3.76) then becomes a special case of (3.82):

$$\frac{P_{,r}}{x_0-P} = \frac{2(x_0-P)P_{,r} - 2SS_{,r}}{(x_0-P)^2 + S^2}.$$
(3.84)

This again has the special solution $(x_0, y_0) = (\infty, \infty)$, to be discussed below, and $P_{,r} = S_{,r} = 0$, which is the L-T model. The general integral of (3.84) is the subcase $C_0 = 0$ of (3.83).

$\mathcal{E}_{,y} \neq 0 = \mathcal{E}_{,x}$

The result here follows from the previous case by interchanges of coordinates and functions. The general solution is

$$P = x_0 \implies P_{,r} = 0 \quad , \quad S^2 = C_2(y_0 - Q) - (y_0 - Q)^2. \tag{3.85}$$

$\mathcal{E}_{,y} = 0 = \mathcal{E}_{,x}$

This implies, via (3.77)-(3.78) that

$$(x_0, y_0) = (P, Q) \implies P_{,r} = Q_{,r} = 0 \tag{3.86}$$

and (3.76) is then fulfilled without any further conditions. With $P_{,r} = Q_{,r} = 0$ the model becomes axially symmetric, and $(x_0, y_0) = (P, Q)$ is the axis of symmetry in each 3-space of constant t.

Now it can be verified that all the four cases discussed above are equivalent to each other under coordinate transformations. The general form of the Szekeres metric (3.16) is preserved by the 2-dimensional Haantjes transformations (see pp. 92-93 in [31]). We combine the shift $(x, y) \longrightarrow (x - x_0, y - y_0)$ with a Haanjes transformation:

$$x = x_0 + \frac{x' + D_1(x'^2 + y'^2)}{T}, \tag{3.87}$$

$$y = y_0 + \frac{y' + D_2(x'^2 + y'^2)}{T}, \tag{3.88}$$

$$T := 1 + D_1 x' + 2D_2 y' + (D_1^2 + D_2^2)(x'^2 + y'^2), \tag{3.89}$$

where D_1 and D_2 are arbitrary constants. A characteristic property of this transformation is

$$(x - x_0)^2 + (y - y_0)^2 = \frac{x'^2 + y'^2}{T}, \tag{3.90}$$

$$dx^2 + dy^2 = \frac{dx'^2 + dy'^2}{T^2}. \tag{3.91}$$

Applying the transformation (3.87)-(3.89) to the Szekeres metric whose P, Q and S obey (3.80) and (3.83) we see that if

$$D_1 = -1/C_1 \quad , \quad D_2 = -C_0/C_1, \tag{3.92}$$

then the new $\mathcal{E}$ will be of the form $(x'^2 + y'^2)/(2\tilde{S}) + \tilde{S}/2$, where

$$\tilde{S} = C_1 \sqrt{\frac{x_0 - P}{C_1 - (C_0^2 + 1)(x_0 - P)}}, \tag{3.93}$$

i.e. the resulting metric will be axially symmetric.

Since (3.84) follows from (3.79)-(3.83) as the subcase $C_0 = 0$, this is obviously axially symmetric, too. For (3.85) an explicitly axially symmetric metric is obtained by taking $D_1 = 0$ and $D_2 = -1/C_2$ in (3.89).

The image of the position of the geodesic at $(x, y) = (x_0, y_0)$ is, in each of the above cases, the set $x' = y' = 0$, which is evidently the axis of symmetry in the (x', y')-plane.

Now we deal with the point $(x_0, y_0) = (\infty, \infty)$. To check the behaviour of geodesics passing through this point we transform (3.19) by

$$(x, y) = \frac{(x', y')}{x'^2 + y'^2}. \tag{3.94}$$

The image of the surface $(x, y) = (\infty, \infty)$ under this transformation is the surface $(x', y') = (0, 0)$. Equation (3.94) transforms (3.19) into a Szekeres metric still of the form (3.19), but with $\mathcal{E}$ replaced by

$$\tilde{\mathcal{E}} = \frac{1}{2\tilde{S}} \left[(x' - \tilde{P})^2 + (y' - \tilde{Q})^2 \right], \tag{3.95}$$

where

$$(\tilde{P}, \tilde{Q}, \tilde{S}) = \frac{(P, Q, S)}{P^2 + Q^2 + S^2}.$$ (3.96)

We now verify whether a null geodesic on which initially $(x', y') = (0, 0)$ preserves $(x', y') = (0, 0)$ along it. The investigation above suggests that this should be the case for every form of (P, Q, S). If this were true, then the relations (3.76) would now be identities obeyed by $\tilde{\mathcal{E}}$ at $x' = y' = 0$, for any functions $(\tilde{P}, \tilde{Q}, \tilde{S})$.

However, this cannot be true: equations (3.76) applied to $\tilde{\mathcal{E}}$ at $x' = y' = 0$ are of the same algebraic form as (3.76) applied to $\mathcal{E}(x, y)$ at $x = y = 0$, i.e. they will impose limitations on $(\tilde{P}, \tilde{Q}, \tilde{S})$. We show just one example of this. Equations (3.76) applied to $\tilde{\mathcal{E}}$ imply

$$\tilde{\mathcal{E}}_{,y'}\tilde{\mathcal{E}}_{,x'r} = \tilde{\mathcal{E}}_{,x'}\tilde{\mathcal{E}}_{,y'r}.$$ (3.97)

Substituting for $\tilde{\mathcal{E}}$ from (3.95) at $x' = y' = 0$ we get $\tilde{P}_{,r}\tilde{Q} = \tilde{P}\tilde{Q}_{,r}$. Apart from the special case $\tilde{P}_{,r} = \tilde{Q}_{,r} = 0$ this is integrated with the result $\tilde{Q} = A\tilde{P}$, where A is a constant. From (3.96), this is equivalent to $Q = AP$. This means that (3.97) is not identically obeyed at $x' = y' = 0$. Thus, apart from the special forms of P, Q and S, a null geodesic on which initially $(x, y) = (\infty, \infty)$ is not a constant (x, y) geodesic.

The final conclusion of our considerations is:

Theorem 3.1 *A constant-(x,y) null geodesic with constant x and y exists only in an axially symmetric Szekeres spacetime. Apart from the L-T limit, there is only one such geodesic: the one which stays on the axis of symmetry within each (x,y) surface. Depending on the coordinates, the functions P, Q and S in such a spacetime obey one of the sets of equations:*

- *(3.79) and (3.83)*

- *the subcase $C_0 = 0$ of (3.79), (3.81) and (3.82)*

- *(3.85)*

- *(3.86)*

Although it is possible that there are other geodesics which have a fixed direction, for example geodesics along which x/y is constant, here we only considered geodesics which are axially directed. Let us call this kind of geodesics the axial geodesics.

3.3.2   THE REDSHIFT FORMULA FOR THE AXIAL GEODESICS

In the case of the axial geodesics one can set $dx = 0 = dy$ to obtain the following equation for a null geodesic:

$$\frac{dt}{dr} = \frac{\Phi_{,r} - \Phi \mathcal{E}_{,r}/\mathcal{E}}{\sqrt{1-k}}.$$ (3.98)

We choose the $-$ sign, so the observer is at the origin. Let us choose the following parametrization:

$$k^1 = -1 \quad , \quad k^0 = \frac{\Phi_{,r} - \Phi \mathcal{E}_{,r}/\mathcal{E}}{\sqrt{1-k}}.$$ (3.99)

This is not an affine parametrisation, so the parallel transport does not preserve the tangent vector. Therefore, k^α, after being parallel transported, becomes λk^α (where λ is a scalar coefficient a function of the parameter s along the geodesic). In this case the geodesic equations are of the form [31]:

$$k^\alpha_{;\beta} k^\beta = -\frac{1}{\lambda}\frac{d\lambda}{ds}k^\alpha.$$ (3.100)

The above is equivalent to only one equation:

$$-\frac{1}{\lambda}\frac{d\lambda}{ds} = 2\frac{\Phi_{,tr} - \Phi_{,t}\mathcal{E}_{,r}/\mathcal{E}}{\sqrt{1-k}} - \frac{\Phi_{,rr} - \Phi_{,r}\mathcal{E}_{,r}/\mathcal{E} - \Phi \mathcal{E}_{,rr}/\mathcal{E} + \Phi(\mathcal{E}_{,r}/\mathcal{E})^2}{\Phi_{,r} - \Phi \mathcal{E}_{,r}/\mathcal{E}} - \frac{1}{2}\frac{k_{,r}}{1-k}.$$ (3.101)

89

All the quantities above are evaluated on the geodesic, where t and r are connected with each other via (3.98). Thus we have

$$\Phi_{n,r} = (\Phi_{,t})_n \frac{dt}{dr} + (\Phi_{,r})_n, \tag{3.102}$$

$$(\Phi_{,r})_{n,r} = (\Phi_{,tr})_n \frac{dt}{dr} + (\Phi_{,rr})_n, \tag{3.103}$$

where the subscript n refers to quantities measured on the geodesic.

The second term on the right-hand side of (3.101) looks like a logarithmic derivative. However, because of (3.102)-(3.103) we have

$$\frac{d\ln\left[(\Phi_{,r})_n - \Phi_n(\mathcal{E}_{,r}/\mathcal{E})_n\right]}{dr} = \frac{(\Phi_{,r})_{n,r} - \Phi_{,nr}(\mathcal{E}_{,r}/\mathcal{E})_n - \Phi_n(\mathcal{E}_{,rr}/\mathcal{E})_n + \Phi_n(\mathcal{E}_{,r}/\mathcal{E})_n^2}{(\Phi_{,r})_n - \Phi_n(\mathcal{E}_{,r}/\mathcal{E})_n}$$

$$= \frac{(\Phi_{,rr})_n - (\Phi_{,r})_n(\mathcal{E}_{,r}/\mathcal{E})_n - \Phi_n(\mathcal{E}_{,rr}/\mathcal{E})_n + \Phi_n(\mathcal{E}_{,r}/\mathcal{E})_n^2}{(\Phi_{,r})_n - \Phi_n(\mathcal{E}_{,r}/\mathcal{E})_n}$$

$$+ \frac{(\Phi_{,tr})_n - (\Phi_{,t})_n(\mathcal{E}_{,r}/\mathcal{E})_n}{(\Phi_{,r})_n - \Phi_n(\mathcal{E}_{,r}/\mathcal{E})_n} \frac{dt}{dr}. \tag{3.104}$$

Using the above relation we can integrate equation (3.101):

$$\lambda = C \frac{\sqrt{1 - k_n}}{(\Phi_{,r})_n - \Phi_n(\mathcal{E}_{,r}/\mathcal{E})_n} \exp\left(\int \frac{(\Phi_{,tr})_n - (\Phi_{,t})_n(\mathcal{E}_{,r}/\mathcal{E})_n}{\sqrt{1 - k_n}} dr\right). \tag{3.105}$$

Now we can easily find that k^α in the affine parametrisation is given by $\tilde{k}^\alpha = (\lambda/C)k^\alpha$. Using the general formula for redshift, $1 + z = \tilde{k}_e^0/\tilde{k}_o^0$, we can write an easy-to-use relation for redshift:

$$\ln(1 + z) = l \int_{r_e}^{r_o} \frac{(\Phi_{,tr})_n - (\Phi_{,t})_n(\mathcal{E}_{,r}/\mathcal{E})_n}{\sqrt{1 - k_n}} dr, \tag{3.106}$$

where $l = 1$ for $r_e < r_o$ and $l = -1$ for $r_e > r_o$. This equation is valid only on the axial geodesics, thus one of the conditions listed in Section 3.3.1 must hold. Under such conditions light propagation studies become much simpler. One needs to study only one equation, i.e. (3.98), and the redshift can be directly calculated from (3.106).

3.4   JUNCTIONS OF NULL GEODESICS IN THE SZEKERES SWISS-CHEESE MODEL

The Swiss-cheese models are often used to take into account the inhomogeneous matter distribution observed in our Universe. However, when employing such models to the analysis of astronomical observations, junction conditions must be handled properly. Consequently, this subject in considered in this section.

For a curve $x^\gamma(\lambda)$ with tangent vector $X^\sigma = dx^\sigma/d\lambda$ crossing the junction Σ, the obvious junction conditions are the continuity of its position and its tangent vector, but expressed in a form that makes them invariant with respect to the transformations of the 4D coordinates, x^γ. The two manifolds on either side of Σ are labelled '+' and '−', and the hypersurface Σ is defined on either side by

$$x_\pm^\gamma = x_\pm^\gamma(\xi^k), \tag{3.107}$$

where ξ^k, $k = 1, 2, 3$ are surface coordinates. For the curve to be of class C^0 we need to ensure the curve intersects Σ at the same intrinsic coordinate point, i.e.:

$$[\xi^k(x^\gamma)] = \xi^k(x_+^\gamma(\lambda_\Sigma^+)) - \xi^k(x_-^\gamma(\lambda_\Sigma^-)) = 0. \tag{3.108}$$

For the curve to be of class C^1, the components of the tangent vector, the components of the tangent vector, projected normal to and tangent to Σ, must be continuous:

$$[X^\beta n_\beta] = \frac{dx_+^\beta}{d\lambda^+} n_\beta^+ \bigg|_\Sigma - \frac{dx_-^\beta}{d\lambda^-} n_\beta^- \bigg|_\Sigma = 0, \tag{3.109}$$

$$[X_\alpha e_i^\alpha] = \frac{dx_+^\alpha}{d\lambda^+} g_{\alpha\beta} e_i^\beta \bigg|_\Sigma - \frac{dx_-^\alpha}{d\lambda^-} g_{\alpha\beta} e_i^\beta \bigg|_\Sigma = 0, \tag{3.110}$$

where n^α is the unit normal to Σ, $e_i^\alpha = \partial x^\alpha / \partial \xi^i$ are three orthogonal unit tangent vectors to Σ and square brackets indicate a jump in a quantity across the junction. In fact, the curve should still be C^1 even if we re-parametrise the curve on one side only, $\bar\lambda = \bar\lambda(\lambda)$. This would re-scale all components that matters:

$$[(X_\alpha e_i^\alpha / X^\beta n_\beta)] = 0. \tag{3.111}$$

If the curve is null, then it suffices to set

$$[l_\alpha e_i^\alpha] = \left[\frac{dx^\alpha}{d\lambda} g_{\alpha\beta} e_i^\beta \right] = 0 \tag{3.112}$$

and use $l^\alpha l_\alpha = 0$ to fix the normal component.

For our Swiss-cheese model, let us consider Szekeres spheres matched into a Friedmann background, and let us imagine a light ray passes out of one Szekeres inhomogeneity straight into another one, where the boundary spheres touch. We can compress the double matching into a single junction calculation - Szekeres to Szekeres. Let us denote the null vector in the Szekeres model by $l^\alpha = (l^t, l^r, l^x, l^y)$. Since it is null, one component is set, say l^r:

$$l^r = \frac{\sqrt{(\epsilon - k)[(l^t)^2 - (\Phi/\mathcal{E})^2\{(l^x)^2 + (l^y)^2\}]}}{\Phi_{,r} - \Phi\mathcal{E}_{,r}/\mathcal{E}}. \tag{3.113}$$

A surface of constant r, with surface coordinates (t, x, y), has

$$n_\alpha = \left(0, \frac{\Phi_{,r} - \Phi\mathcal{E}_{,r}/\mathcal{E}}{\sqrt{\epsilon - k}}, 0, 0 \right), \tag{3.114}$$

$$e_i^\alpha = \begin{pmatrix} 1 & 0 & 0 \\ 0 & 0 & 0 \\ 0 & 1 & 0 \\ 0 & 0 & 1 \end{pmatrix}, \tag{3.115}$$

$$g_{ij} = \begin{pmatrix} 1 & 0 & 0 \\ 0 & -\Phi^2/\mathcal{E}^2 & 0 \\ 0 & 0 & -\Phi^2/\mathcal{E}^2 \end{pmatrix}, \tag{3.116}$$

$$K_{ij} = \begin{pmatrix} 0 & 0 & 0 \\ 0 & -\Phi\sqrt{\epsilon - k}/\mathcal{E}^2 & 0 \\ 0 & 0 & -\Phi\sqrt{\epsilon - k}/\mathcal{E}^2 \end{pmatrix}. \tag{3.117}$$

Thus

$$l_\alpha e_i^\alpha = \left(l^t, -\Phi^2 l^x/\mathcal{E}^2, -\Phi^2 l^y/\mathcal{E}^2 \right). \tag{3.118}$$

The components of l^α in the orthonormal tetrad (n^α, e_i^α) are

$$l^{(\alpha)} = \left(l^t, \frac{\Phi_{,r} - \Phi\mathcal{E}_{,r}/\mathcal{E}}{\sqrt{\epsilon - k}} l^r, \frac{\Phi}{\mathcal{E}} l^x, \frac{\Phi}{\mathcal{E}} l^y \right). \tag{3.119}$$

The matching requires that three of the following equations are obeyed:

$$l^t \big|_{\Sigma^+} = l^t \big|_{\Sigma^-}, \tag{3.120}$$

$$\left.\frac{\Phi_{,r} - \Phi\mathcal{E}_{,r}/\mathcal{E}}{\sqrt{\epsilon - k}}l^r\right|_{\Sigma^+} = \left.\frac{\Phi_{,r} - \Phi\mathcal{E}_{,r}/\mathcal{E}}{\sqrt{\epsilon - k}}l^r\right|_{\Sigma^-}, \tag{3.121}$$

$$\left.\frac{\Phi}{\mathcal{E}}l^x\right|_{\Sigma^+} = \left.\frac{\Phi}{\mathcal{E}}l^x\right|_{\Sigma^-}, \tag{3.122}$$

$$\left.\frac{\Phi}{\mathcal{E}}l^y\right|_{\Sigma^+} = \left.\frac{\Phi}{\mathcal{E}}l^y\right|_{\Sigma^-}. \tag{3.123}$$

while the fourth one follows from the null condition.

Now let us notice that when a Szekeres sphere is matched to a Friedmann background, its orientation is completely undetermined. If we fix the point where the light ray exits one Szekeres sphere and where it enters another, then one can still be rotated around the common normal direction relative to the other. This is equivalent to rotating the tangential component of the null vector. Thus we only need to match up the time component and the tangential component:

$$[l^t] = 0 = \left[\frac{\Phi^2}{\mathcal{E}^2}((l^x)^2 + (l^y)^2)\right]. \tag{3.124}$$

3.5   THE APPARENT HORIZONS IN THE SZEKERES MODEL

An apparent horizon (AH) is the boundary of the region of trapped surfaces. A trapped surface is a closed surface on which both the inward- and outward- directed null geodesics converge (i.e. have a negative expansion scalar). Thus, for a trapped surface Σ, if k^μ is any field of vectors tangent to null geodesics that intersect Σ, then

$$k^\mu_{;\mu} < 0 \quad , \quad \text{on} \quad \Sigma. \tag{3.125}$$

Consequently, on an apparent horizon:

$$k^\mu_{;\mu} = 0. \tag{3.126}$$

In the above, k^μ is null and geodesic. Proceeding from this definition, [34] found that in the quasi-spherical Szekeres model the apparent horizon is given by the same equation as in the L-T model:

$$\Phi = 2M. \tag{3.127}$$

On the other hand, [120], while investigating the possibility of traversing through a Szekeres wormhole, defined a related notion, which they also called apparent horizon. Namely, they considered surfaces from which a fastest-moving object could not escape outwards. Thus, they considered the analogue of (3.126), but for non-geodesic null fields. The reasoning was that where a geodesic ray would already be forced inward, an accelerating ray might still escape farther before being turned back, and we name this horizon the 'absolute apparent horizon '(AAH)', in order to avoid confusion.

The reasoning of [120] was as follows. A general null direction $k^\alpha = dx^\alpha/dt$ in the metric of (3.19) with $\epsilon = +1$ obeys

$$0 = k^\alpha k^\beta g_{\alpha\beta} = 1 - \frac{(\Phi_{,r} - \Phi\mathcal{E}_{,r}/\mathcal{E})^2}{1 - k}\left(\frac{dr}{dt}\right)^2 - \frac{\Phi^2}{\mathcal{E}^2}\left[\left(\frac{dx}{dt}\right)^2 + \left(\frac{dy}{dt}\right)^2\right], \tag{3.128}$$

which implies

$$\frac{(\Phi_{,r} - \Phi\mathcal{E}_{,r}/\mathcal{E})^2}{1 - k}\left(\frac{dr}{dt}\right)^2 = 1 - \frac{\Phi^2}{\mathcal{E}^2}\left[\left(\frac{dx}{dt}\right)^2 + \left(\frac{dy}{dt}\right)^2\right]. \tag{3.129}$$

Thus, on a null curve with $dx/dt = 0 = dy/dt$ (which, apart from exceptional cases, will not be a geodesic), the rate of change of r is maximal. One would tend to interpret this to mean that along such a curve the null signal will be able to escape farther than the location of the AH at $\Phi = 2M$. This in fact will not always be the case. A curve (3.129) on which $dx/dt = 0 = dy/dt$ will have the maximal dr/dt compared to curves with nonzero values of dx/dt and dy/dt passing through the point with the same coordinate x

and y. However, going to a different pair of values x and y changes the value of $\mathcal{E}_{,r}/\mathcal{E}$. For some of the (x, y) pairs this will decrease dr/dt compared to the former (x, y) direction, and the curve (3.129) with $dx/dt = 0 = dy/dt$ will not make it to the AH, being turned back at a smaller value of M.

Equation (3.129) implies, along this fastest escape route,

$$\left.\frac{dt}{dr}\right|_n = \frac{j}{\sqrt{1-k}}\left(\Phi_{,r} - \frac{\Phi\mathcal{E}_{,r}}{\mathcal{E}}\right) \quad , \quad j = \pm 1, \tag{3.130}$$

where $j = +1$ for outgoing rays, and $j = -1$ for ingoing rays. The solution of the above, $t = t_n(r)$, is the equation of the 'fastest ray'. The value of the function Φ along this ray, $\Phi_n(r) = \Phi(t_n(r), r)$, which is an analogue of the L-T areal radius, will in general be increasing and decreasing with growing r. The absolute apparent horizon (AAH) is where $\Phi_n(r)$ has an extremum, i.e. it changes from increasing to decreasing or vice-versa. Thus, the AAH is a locus where

$$0 = \frac{d\Phi_n}{dr} \equiv \frac{\partial\Phi}{\partial t}\frac{dt_n}{dr} + \frac{\partial\Phi}{\partial r} = l_j\frac{\sqrt{2M/\Phi - k}}{\sqrt{1-k}}\left(\Phi_{,r} - \frac{\Phi\mathcal{E}_{,r}/\mathcal{E}}{\mathcal{E}}\right) + \Phi_{,r}, \tag{3.131}$$

where $l = +1$ for an expanding model and $l = -1$ for a collapsing model. Explicitly, this reads

$$\Phi_{,r} = (\sqrt{1-k} - \sqrt{2M/\Phi - k}) + \Phi\sqrt{2M/\Phi - k}\mathcal{E}_{,r}/\mathcal{E} = 0. \tag{3.132}$$

Note that the solution of (3.132) is a hypersurface in spacetime determined by the equation $t = t_{AAH}(r, x, y)$. Thus, unlike in the spherically symmetric case or in the case of the ordinary apparent horizon, the function $t_{AAH}(r, x, y)$ essentially depends on three variables and cannot be faithfully represented by a 3D graph.

The equation of the apparent horizon in the (t, M)-coordinates will be the same as in the corresponding L-T model. It is independent of (x, y), and, for the future apparent horizon (in the recollapse phase of evolution of the $k > 0$ model) it is [40]

$$t = t_B + \frac{M}{k^{3/2}}\left[\pi + \arccos(2k - 1) + 2\sqrt{k(1-k)}\right]. \tag{3.133}$$

In order to find the corresponding equation for the AAH from (3.131) we use the following expression for $\Phi_{,r}$ [to be calculated from the evolution equation, see Sec.18.10 in [31], in particular Eq. (18.107)]:

$$\frac{\Phi_{,r}}{\Phi} = \left(\frac{M_{,r}}{M} - \frac{k_{,r}}{k}\right) + \left(\frac{3}{2}\frac{k_{,r}}{k} - \frac{M_{,r}}{M}\right)\frac{\sin\eta(\eta - \sin\eta)}{(1 - \cos\eta)^2} - \frac{k^{3/2}}{M}t_{B,r}\frac{\sin\eta}{(1 - \cos\eta)^2}. \tag{3.134}$$

Before we use this in (3.132) we note that from the evolution equation it follows that with $\pi \leq \eta \leq 2\pi$, where $\sin\eta < 0$, we have

$$\sqrt{\frac{2M}{\Phi} - k} = -\sqrt{k}\frac{\sin\eta}{1 - \cos\eta}. \tag{3.135}$$

We substitute (3.134) and (3.135) into (3.132) and get:

$$\left[\frac{M_{,r}}{M} - \frac{k_{,r}}{k} + \left(\frac{3}{2}\frac{k_{,r}}{k} - \frac{M_{,r}}{M}\right)\frac{\sin\eta(\eta - \sin\eta)}{(1 - \cos\eta)^2} - \frac{k^{3/2}}{M}t_{B,r}\frac{\sin\eta}{(1 - \cos\eta)^2}\right]$$

$$\times \left[\sqrt{1-k} + \frac{\sqrt{k}\sin\eta}{1 - \cos\eta}\right] + \frac{\sqrt{k}\sin\eta}{1 - \cos\eta}\frac{\mathcal{E}_{,r}}{\mathcal{E}} = 0. \tag{3.136}$$

We will use this as an implicit definition of $\eta(M)_{AAH}$,i.e. as the equation of the AAH in the (η, M) variables (η will depend on x and y via $\mathcal{E}$). Then $t(M)$ on the AAH can be found from the evolution equation:

$$t(M)_{AAH} = \left[\frac{M}{k^{3/2}}(\eta - \sin\eta) + t_B\right]_{AAH}. \tag{3.137}$$

Equation (3.136) can be solved only numerically. To verify its solvability, and to find the initial values for the bisection method, we will transform it because in the form (3.136) its left-hand side becomes infinite at $\eta \longrightarrow 2\pi$.

93

We will assume that the shell crossings are absent. Among the conditions for no shell crossings, found by [120], the following are useful here:

$$2\pi \left(\frac{3}{2} \frac{k_{,r}}{k} - \frac{M_{,r}}{M} \right) - \frac{k^{3/2}}{M} t_{B,r} < 0, \tag{3.138}$$

(see Eq. (126) in [120]), and

$$\frac{M_{,r}}{M} - \frac{k_{,r}}{k} > 0, \tag{3.139}$$

which follows from the fact that $\Phi_{,r}/\Phi > 0$ must hold for all (η, r), and from (3.134) taken at $\eta = \pi$ (see [120]).

We observe that

$$\lim_{\eta \to 2\pi} \frac{\sin\eta}{\sqrt{1 - \cos\eta}} = -\sqrt{2} \tag{3.140}$$

and multiply (3.136) by $(1 - \cos\eta)^2$ to obtain:

$$\Psi(\eta) := \left[\left(\frac{M_{,r}}{M} - \frac{k_{,r}}{k} \right) (1 - \cos\eta)^{3/2} \frac{\sin\eta(\eta - \sin\eta)}{\sqrt{1 - \cos\eta}} - \frac{k^{3/2}}{M} t_{B,r} \frac{\sin\eta}{\sqrt{1 - \cos\eta}} \right]$$

$$\left[\sqrt{1 - k} \sqrt{1 - \cos\eta} + \frac{\sqrt{k}\sin\eta}{\sqrt{1 - \cos\eta}} \right] + \sqrt{k}\sin\eta(1 - \cos\eta) \frac{\mathcal{E}_{,r}}{\mathcal{E}} = 0. \tag{3.141}$$

Now we verify that

$$\lim_{\eta \to \pi} \Psi(\eta) = 4\sqrt{1 - k} \left(\frac{M_{,r}}{M} - \frac{k_{,r}}{k} \right) > 0, \tag{3.142}$$

being positive in consequence of (3.139); and

$$\lim_{\eta \to 2\pi} \Psi(\eta) = 2\sqrt{k} \left[2\pi \left(\frac{3}{2} \frac{k_{,r}}{k} + \frac{M_{,r}}{M} \right) - \frac{k^{3/2}}{M} t_{B,r} \right] < 0, \tag{3.143}$$

being negative in consequence of (3.138).

Thus $\Psi(\pi) > 0$ and $\Psi(2\pi) < 0$, so there exists an $\eta_0 \in (\pi, 2\pi)$ at which $\Psi(\eta_0) = 0$. By this we have proved that each particle in a recollapsing quasi-spherical Szekeres model must cross the AAH before it hits the Big Crunch at $\eta = 2\pi$.

We briefly recapitulate some of the properties of the AAH found in [120] and reported in [31]. The AAH may either (1) not intersect a given surface of constant (t, r); or (2) have a single point in common with it; or (3) intersect it along a circle or a straight line. Let

$$D := 1 - \frac{\sqrt{2M/\Phi - k}}{\sqrt{1 - k}}. \tag{3.144}$$

Except for the special case when $S_{,r}/S = D\Phi_{,r}/\Phi$, the circle of intersection in the (x, y) plane has its centre at

$$(x_{AH}, y_{AH}) = \left(P - \frac{P_{,r}}{S_{,r}/S - D\Phi_{,r}/\Phi}, Q - \frac{Q_{,r}}{S_{,r}/S - D\Phi_{,r}/\Phi} \right) \tag{3.145}$$

and the radius

$$L_{AH} = \frac{\sqrt{\lambda}}{S_{,r}/S - D\Phi_{,r}/\Phi}. \tag{3.146}$$

The special case

$$\frac{S_{,r}}{S} = D \frac{\Phi_{,r}}{\Phi}, \tag{3.147}$$

when the locus of the AAH in the (x, y) plane is a straight line, is an artefact of the stereographic projection; this straight line is an image of a circle on the sphere.

From the definition of the AAH, and from $\Phi > 0$, $\mathcal{E} > 0$ and $\Phi_{,r} > 0$, we have

$$(D > 0) \Longrightarrow (\mathcal{E}_{,r} < 0) \quad , \quad (D < 0) \Longrightarrow (\mathcal{E}_{,r} > 0). \tag{3.148}$$

But $D > 0$ and $D < 0$ define regions independent of x and y. Hence, where $D > 0$ (resp. $D < 0$), we have $\mathcal{E}_{,r} < 0$ (resp. $\mathcal{E}_{,r} > 0$) on the whole of the AAH. This implies that the $\mathcal{E}_{,r} = 0$ circle and the AAH cannot intersect unless they coincide. Indeed, these circles lie in parallel planes.

Along $\Phi = 2M$,

$$(\Phi_n)_{,r} = -\Phi \frac{\mathcal{E}_{,r}}{\mathcal{E}}, \tag{3.149}$$

so the apparent horizon, which is at $\Phi = 2M$, does not coincide with the AAH except where $\mathcal{E}_{,r} = 0$.

3.6 EVOLUTION OF COSMIC STRUCTURES IN THE QUASI-SPHERICAL SZEKERES MODEL

In Chapter 2 of this thesis, the spherically symmetric L-T model was used to study structure formation. However, the structures we observe in the Universe are far from being spherical, and we want to refine our analysis by considering a wider variety of astrophysical objects. Therefore, in this section, we investigate the evolution of small voids among compact clusters and large voids surrounded by large walls or filaments within the quasi-spherical Szekeres model.

This analysis is based on the studies by [127] and [128].

3.6.1 THE ALGORITHM

To specify a Szekeres model, 5 functions of the radial coordinate need to be known. The computational algorithm used to specify the model and to calculate its evolution consists of the following steps.

- The chosen background model is the homogeneous Friedmann model with density:

$$\rho_b = \Omega_m \times \rho_{cr} = 0.24 \times \frac{3H_0^2}{8\pi G}, \tag{3.150}$$

  where the Hubble constant is $H_0 = 74 \text{ kms}^{-1}\text{Mpc}^{-1}$. The cosmological constant, Λ, corresponds to $\Omega_\Lambda = 0.76$.

- The cosmic time of last scattering (t_1) is calculated using (2.107).

- The radial coordinate is chosen as the value of Φ at the initial instant $t_1 = 0.5 \times 10^6$ yr after the Big Bang:

$$\tilde{r} := \Phi(t_1, r). \tag{3.151}$$

  For clarity in further use, the new radial coordinate is denoted r.

- The function $M(r)$, which describes the active gravitational mass inside an $r = $ constant sphere, is calculated in the following way:

$$M(r) = M_b(r) + \delta M(r), \tag{3.152}$$

  where M_b is the mass in the corresponding volume of the homogeneous universe as defined by (2.117) with $l = r$ and $\rho = \rho_b$, and δM is a mass correction, which can be either positive or negative. The δM is defined similarly to the spherically symmetric case:

$$\delta M(r) = 4\pi \frac{G}{c^2} \int\limits_0^r \Phi^2(t_1, u) \Phi_{,r}(t_1, u) \delta \bar{\rho}(u) du, \tag{3.153}$$

  where $\delta \bar{\rho}(r)$ is the function chosen to specify δM. Although $\delta \bar{\rho}(r)$ is not the initial density fluctuation (since the latter is a function of all spatial coordinates), it gives some estimate of the initial fluctuation of the monopole density component.

Model	$\delta\bar{\rho}$	S	P	Q
1	$-5\times10^{-3}\exp[-(r/8\text{kpc})^2]$	1	0	$-0.6\ln(1+r/\text{kpc})\exp(-0.003\text{kpc}^{-1}\times r)$
2	$1.14\times10^{-3}\exp[-(r/9\text{kpc})^2]$	1	0	$-1.45\ln(1+0.2r/\text{kpc})\exp(-0.003\text{kpc}^{-1}\times r)$
3	$-5\times10^{-3}\exp[-(r/8\text{kpc})^2]$	$-(r/\text{kpc})^{0.4}$	$0.55(r/\text{kpc})^{0.4}$	$0.33(r/\text{kpc})^{0.4}$
4	$1.14\times10^{-3}\exp[-(r/9\text{kpc})^2]$	$-(r/\text{kpc})^{0.9}$	$0.55(r/\text{kpc})^{0.8}$	$0.33(r/\text{kpc})^{0.8}$
5	$1\times10^{-3}\exp[-(r/20\text{kpc})^2]-6.5\times10^{-4}\exp[-(r-35\text{kpc}/10\text{kpc})^2]$	1	0	$0.33(r/\text{kpc})^{0.8}$

Table 3.1: The set of functions used to specify double structure models. The bang function in the following models is assumed to be zero, $t_B = 0$. Table information is taken from [128].

- The bang time function is assumed to be zero, i.e. $t_B(r) = 0$. Then the function $k(r)$ can be calculated from (3.17).

- The last three functions needed to define the quasi-spherical Szekeres model are $P(r)$, $Q(r)$, $S(r)$. The form of these functions is presented in Table 3.1.

- The evolution of the system is calculated by solving (3.14).

- The evolution of different models is compared by their density contrast evolution. Two different types of density contrast indicators are taken into account. The first one is the usual density contrast defined as follows:

$$\delta = \frac{\rho - \rho_b}{\rho_b}, \tag{3.154}$$

where ρ_b is the background density. However, the density contrast defined as above is a local quantity. We can introduce another indicator of a density contrast in the way proposed by [129]:

$$S_{IK} = \int \left| \frac{h^{\alpha\beta}}{\rho^I} \frac{\partial\rho}{\partial x^\alpha} \frac{\partial\rho}{\partial x^\beta} \right|^K dV, \tag{3.155}$$

where I and K are the set of real numbers, excluding zero. This family of density contrast indicators can be considered as local or global depending on the size of Σ. Such a quantity not only describes the change of density but also the change of gradients and the volume of a perturbed region. So this density indicator describes the evolution of the whole region in a more sophisticated way than δ. Here only the case $I = 2$, $K = 1/2$ is considered.

- The integral given by (3.155) is calculated in the quasi-spherical (θ, ϕ) coordinates of (3.20). This is because the (x, y) coordinates have an infinite range, while in numerical calculations (all the models presented in this section are calculated numerically) it is more convenient to use coordinates that have a finite range.

3.6.2 DOUBLE STRUCTURES

In this section, the evolution of double structures, namely a void with an adjoining galaxy cluster, is investigated. Although sets of more than two structures can be described within the Szekeres model, the investigation of less complex cases are useful because they enable us to draw some general conclusions without going into too much detail. A more complex model is investigated in the next section, and it is found that the conclusions drawn for the double structures are still valid in such situations.

Models with $P_{,r} = 0 = S_{,r}$, $Q_{,r} \neq 0$

As mentioned above, if $P_{,r} = 0 = S_{,r} = Q_{,r}$, then the quasi-spherical Szekeres model becomes the L-T model. Hence, the class of models considered in this section is the simplest generalization of the spherically symmetric models.

The double structure consisting of a void and an adjoining supercluster can be described in the Szekeres model in two different ways: $\delta M < 0$, and with $\delta M > 0$. Both of these possibilities are examined here.

Let us first consider two models: model 1 and 2 (see Table 3.1 for details). The density distribution of models 1 and 2 are given in Figure 3.1. As can be seen, the model with $\delta M < 0$ (model 1) has a void around the centre, and the cluster is described by the high-density side of the dipole component of the matter distribution. It is the opposite in model 2: the overdense region is around the origin and the void is half of the dipole component in the density.

Figure 3.2 shows the evolution of the density contrast of models 1 and 2 in comparison with the corresponding model obtained in the L-T metric, which is specified by assuming the same conditions as the ones in the Szekeres model at the initial instant, namely $t_B = 0$ and the profile of the density distribution. The local density contrast, δ, is compared at the point of maximal and minimal density value. The upper-left panel of Figure 3.2 show the evolution of the density contrast inside the void, and as can be seen, the behaviour of the density contrast in both models is similar. This is a consequence of imposing the origin conditions, where $\Phi(r_0, t) = 0 \ \forall \ t$ and some other functions are also equal to zero. These conditions imply that the origin behaves like the Friedmann model, and this is the reason why the quasi-spherical Szekeres and the L-T models evolve very similarly close to the origin. The lower-left panel of Figure 3.2 compares the evolution of the density contrast at the centre of the overdense region of model 1 with the corresponding L-T model, and shows the growth of the density contrast in the Szekeres model is much faster within a $\delta M < 0$ perturbation, where the mass is below the background value. This indicates that within the perturbed region of mass below the background mass ($\delta M < 0$) the evolution of underdensities does not change, but the evolution of the overdense regions situated at the edge of the underdense regions is much faster than the corresponding evolution of isolated structures.

The evolution of the density contrast of model 2 ($\delta M > 0$) is shown on the right-hand side of Figure 3.2. The density contrast at the point of minimal density is depicted in the upper-right panel of Figure 3.2. As in model 1, the evolutions at the origin in the Szekeres model and the L-T model are very similar. The evolution of the void, however, is slower within the Szekeres model than it is in the L-T model. This implies that single, isolated voids evolve much faster than the ones which are in the neighbourhood of large overdensities where the mass of the perturbed region is above the background mass ($\delta M > 0$).

Now let us compare the evolution of the $S_{2,1/2}$ density indicator of (3.140). As above, two different types of Σ are considered:

- In the case of overdense regions Σ is defined as a region where $\rho > \rho_b$.

- In the case of underdense regions Σ is defined as a region where $\rho < \rho_b$.

Since the value of S_{IK} depends on units, the results shown in Figure 3.3 and Figure 3.6 are normalized so they are now of order unity.

The upper panel of Figure 3.3 presents the evolution of $S_{2,1/2}$ for an underdense region, the lower one for an overdense region. As can be seen $S_{2,1/2}$ for the two Szekeres models are comparable and the growth of $S_{2,1/2}$ for the L-T model is much slower. This is because the volumes of the considered regions are different. In the Szekeres model the volume is larger than that in the L-T model.

Figure 3.1 presents the shape of the structures without corrections for the shell displacement. For example, the void in Figure 3.1 (upper panel) and in Figure 3.5 seems to be almost spherical. In fact this void is squeezed in the $+Y$ direction and elongated in the Y direction [$Q_{,r} \neq 0, P_{,r} = 0 = S_{,r}$ this follows from the metric (3.19) and Eqs. (3.35), (3.20)]. This also leads in some regions to density gradients larger than in the L-T model, which causes such a large disproportion in $S_{2,1/2}$ between the Szekeres and L-T models.

The results indicate that the evolution of a Szekeres model is much more complex than that of an L-T model. The evolution not only depends upon the amplitude of the density contrast, but also on the density gradients and on the volume of the perturbed region. This is the reason why the $S_{2,1/2}$ curve for the void in model 2 is higher than in other models, although the density contrast in this model evolves More slowly than in model 1. Similarly, as can be seen in Figures 3.4 and 3.5, the overdense region in the model with $\delta M < 0$ is much larger than in other models, and as a consequence the $S_{2,1/2}$ value for this model evolves much faster than in other models. The $S_{2,1/2}$ plots give us information about the evolution of the whole perturbed region.
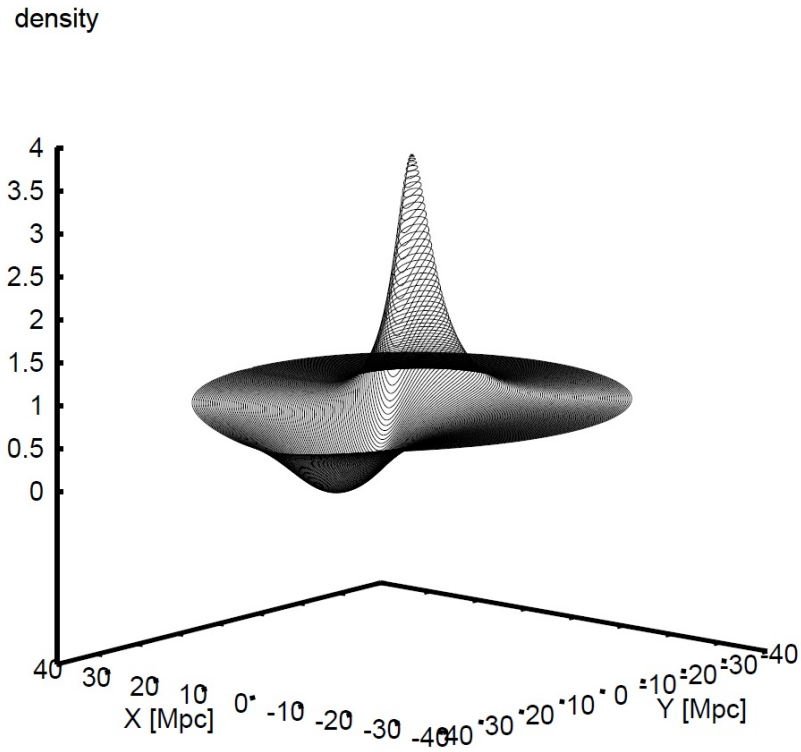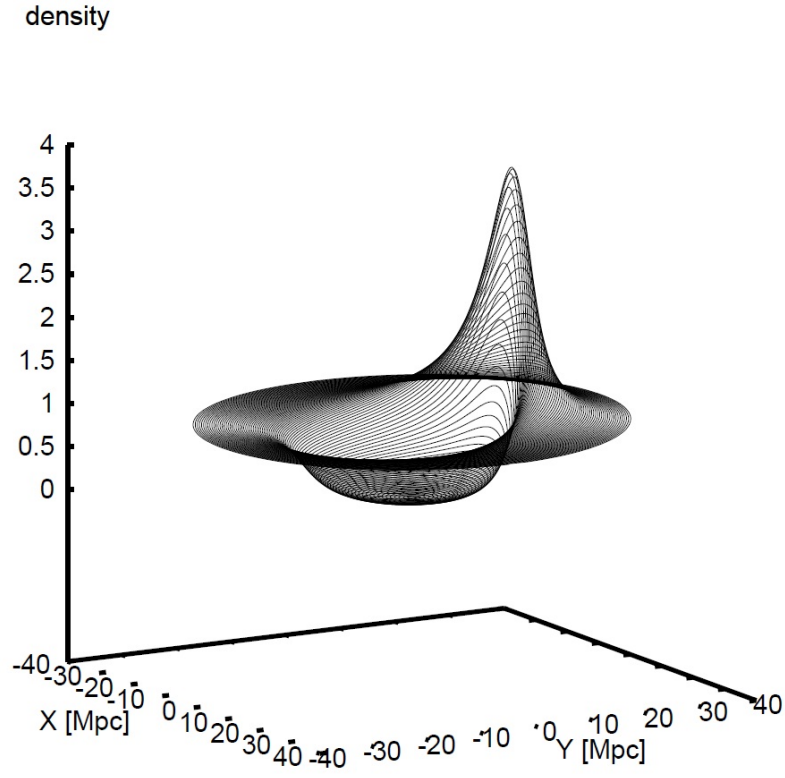
Figure 3.1: The present day density distribution of double structure models. The upper panel represents model 1 and the lower panel model 2. Figure taken from [128].
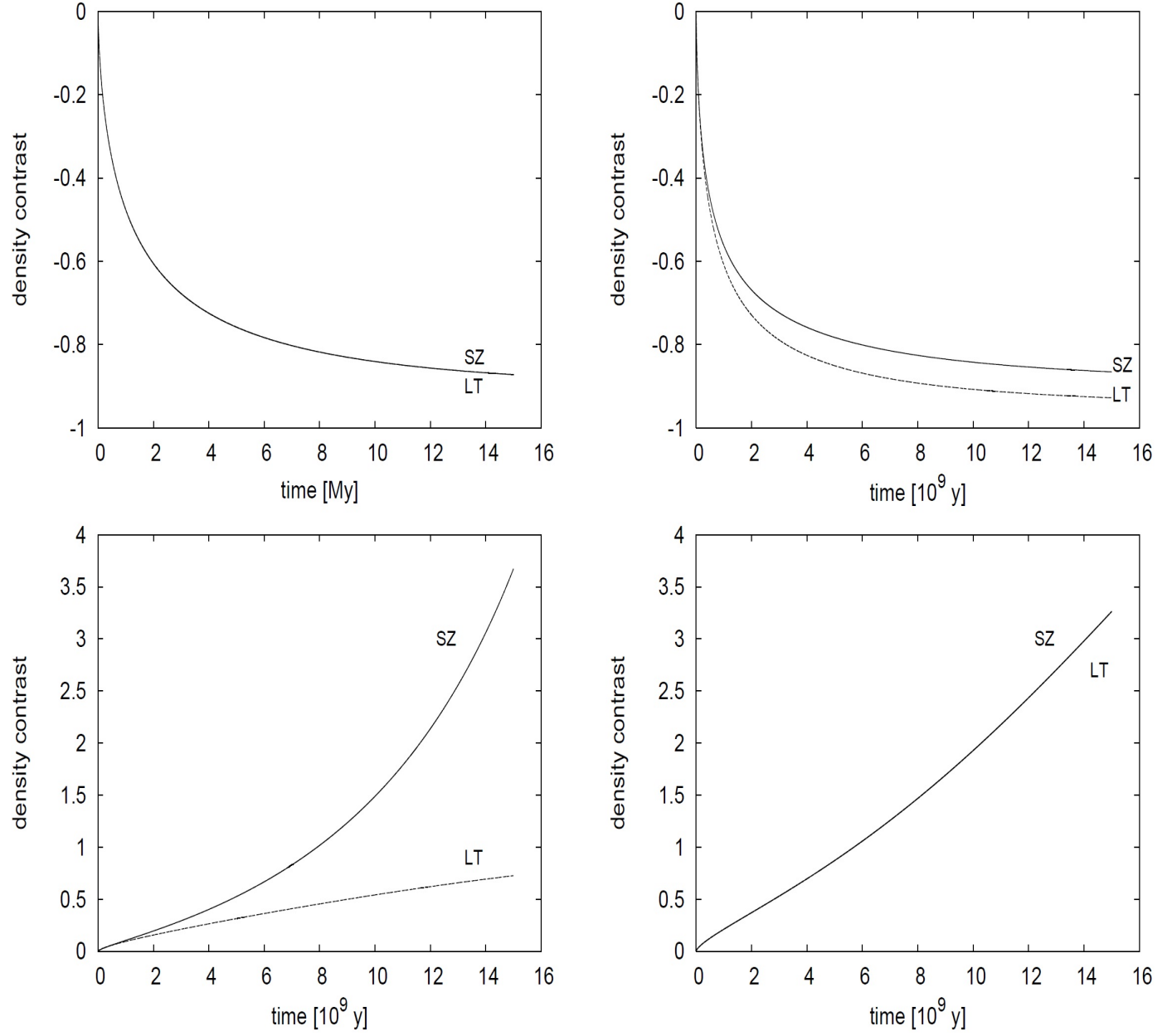
Figure 3.2: The evolution of density contrast, equation (3.154), inside the void (upper panel) and inside the cluster (lower panel) for model 1; SZ and LT curves representing the Szekeres and L-T models respectively. The graphs on the left represent model 1, with model 2 on the right. Figure taken from [128].
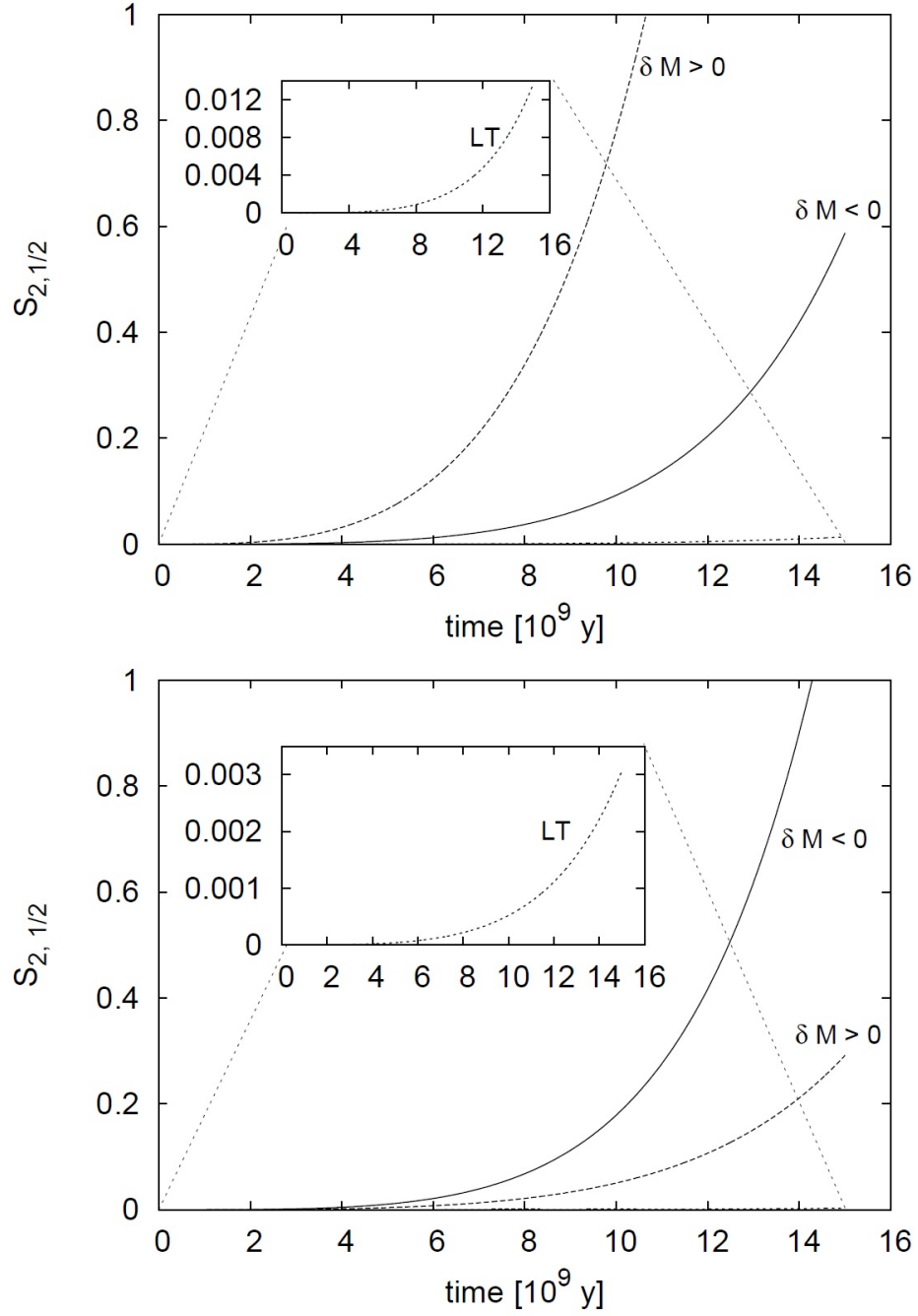
Figure 3.3: Comparison of $S_{2,1/2}$ for models with $\delta M > 0$, $\delta M < 0$ and the corresponding LT model for a void in the upper panel and supercluster in the lower panel. Figure taken from [128].
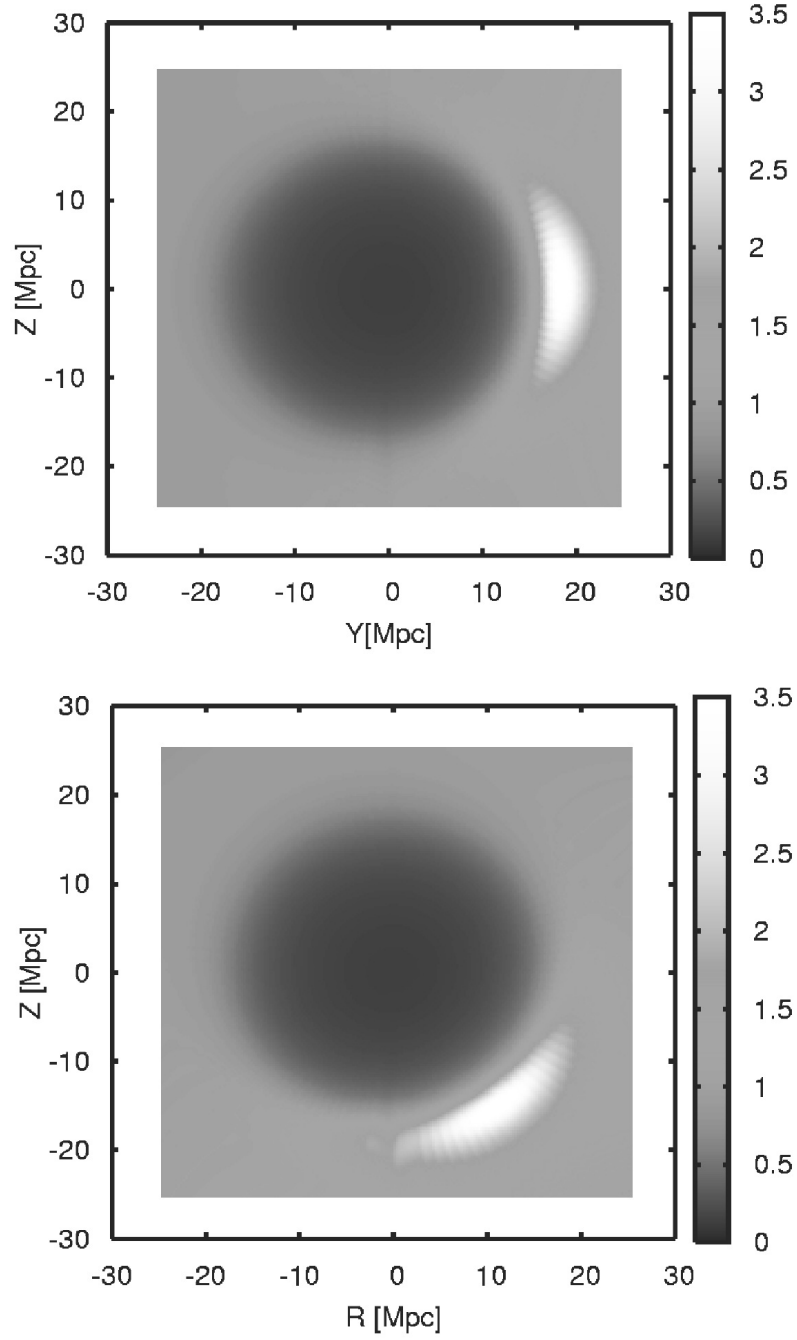
Figure 3.4: The present colour-coded density distribution, ρ/ρ_b, for models with $\delta M < 0$. Upper panel - $P' = S' = 0$ (Model 1). Lower panel - $P' \neq 0 \neq S'$ (Model 3). Figure taken from [128].
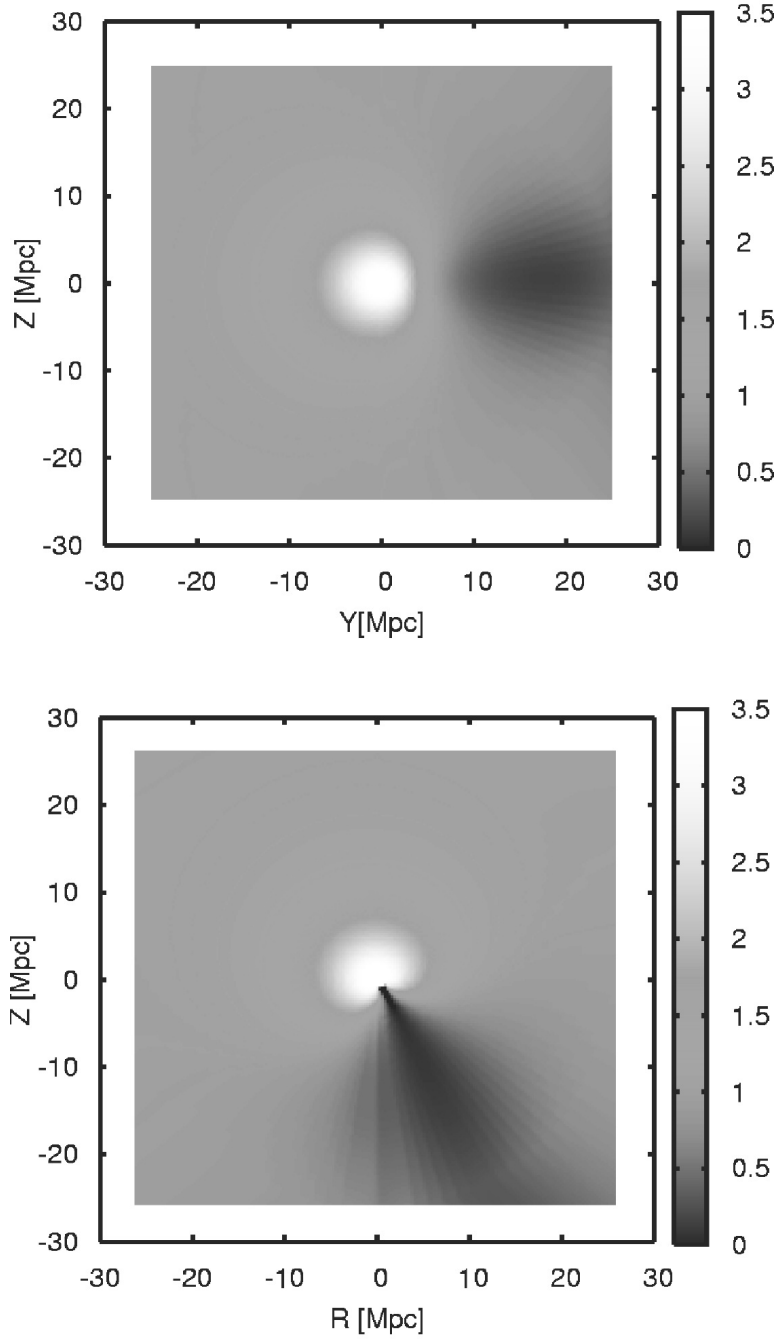
Figure 3.5: The present colour-coded density distribution, ρ/ρ_b, for models with $\delta M > 0$. Upper panel - $P' = S' = 0$ (Model 2). Lower panel - $P' \neq 0 \neq S'$ (Model 4). Figure taken from [128].

The evolution of the density at a single point is described by the local density contrast δ. As can be seen, the evolution of the maximal and minimal density contrast depends on the value of δM in the unperturbed region. The evolution of the density contrast inside large and isolated voids is faster than inside small voids which are surrounded by highly dense regions. On the other hand, the evolution of the density contrast in high-density regions in close neighbourhood of large voids is faster, due to faster mass flow from the voids.

Models with $P_{,r} \neq 0 \neq S_{,r}$, $Q_{,r} \neq 0$

Now let us consider two models non-constant P, Q and S models 3 and 4 (see Table 3.1 for details).

Figure 3.4 presents the comparison of the present-day density distribution in models 1 and 3 in colour-coded diagrams. It presents the cross sections perpendicular to the XY surface of the considered structures. The upper panel of Figure 3.4 presents the cross section through the surface $\phi = \pi/2$ and the lower panel presents the cross section through the surface $\phi \approx \pi/6$. Figure 3.5 presents the cross sections of models 2 and 4. As can be seen, each pair of structures appears to be similar but, in comparison with model 1, the void in model 3 is moved down and right. In model 4, on the other hand, it is the cluster which is moved down and right as compared to model 2.

The evolutions of the density contrasts inside the voids and clusters of models 3 and 1 are very similar, which should not be surprising, as model 3 has the same $\bar{r}$ as model 1. Also, the evolutions of the corresponding density contrasts of models 4 and 2 are similar. The functions (S, P, Q) were chosen so that they reproduce the same shapes of current structures and the same density contrasts inside them. However, it is not clear whether the evolutions of $S_{2,1/2}$ are comparable, too. When the functions (S, P, Q) are not constant, the axis of the mass-dipole changes from one sphere to another.

Also, volumes of the unperturbed regions and the density gradients can be different. So it may be interesting to compare the evolution of the whole perturbed underdense and overdense regions of models 1, 2 3 and 4.

Figure 3.6 presents the comparison of the $S_{2,1/2}$ evolution of models 1-4. The primed letters denote models with $S_{,r} \neq 0 \neq P_{,r}$, $Q_{,r} \neq 0$. As can be seen, the evolution of $S_{2,1/2}$ for all these models is also comparable. These results confirm what might have been intuitively guessed, i.e. that the evolution in the quasi-spherical Szekeres model does not depend on the position of the dipole component. As long as the shape and the density contrast of the models are similar, they evolve in a very similar way.

3.6.3 CONNECTION TO THE LARGE-SCALE STRUCTURE OF THE UNIVERSE

There remains the problem whether the conclusions presented in the previous section are not limited to the class of models considered in this thesis. Are they general? How relevant are they for the real large-scale structure of the Universe? These questions are dealt with in this section.

First of all, let us consider whether the choice of functions used so far does not significantly restrict our analysis. The models presented above are defined by choosing (t_B, M, S, Q, P). As can be seen, the functions (S, Q, P) describe the position of the dipole and even with S and P constant, we are still able to construct the cosmic structures. The other functions which specify the model are t_B and M. It is also possible to choose other sets of functions, such as k and t_B, or any k and M. In practice, however, we cannot take any arbitrary k and M because such arbitrary choices may lead to shell crossings or to fluctuations at last scattering that are too large, and in most cases to both of these. Typically, fluctuations in the bang time t_B, which generate decaying modes [130], should be less than a few thousand years to satisfy CMB constraints, though carefully chosen combinations of large-amplitude fluctuations in these three arbitrary functions may be possible. However, one does not expect large differences in the age of the Universe within the region of size of several to several tens of Mpc. So if t_B is set (say that in the studied region $t_B \approx 0$), then we are left with one function to manipulate. Let it be M, or, more intuitively, δM. As seen from (3.17), if δM increases, then k must decrease in order to preserve the constant age of the Universe. On the other hand, the decrease of k leads to the decrease of the expansion rate, θ (3.22). This, further, via the continuity equation (3.23), influences the evolution. If we look at the distribution of the

expansion rate, which is presented in Figure 3.7, we can see the expansion rate closely follows the pattern of the density distribution (Figures 3.4 and 3.5). Figure 3.7 presents the ratio θ_{SZ}/θ_b of the expansion scalar in the Szekeres models (3.22) to the expansion factor in the homogeneous background.

Now it should be clear why the void in models 1 and 3 ($\delta M < 0$) evolves much faster than in models 2 and 4 ($\delta M > 0$). This is because if the mass of the perturbed region is below the background mass, such a region expands much faster than the background, leading to the formation of large underdense regions. Let us also notice that similar patterns are present in more complicated configurations. Let us now consider model 5 which describes the evolution of a triple structure. All functions used to specify this model are presented in Table 3.1. Figure 3.8 presents the density distribution with two overdense regions, one at the origin, and a small void between them which extends round the centre at large radii. The evolution of model 5 is presented in Figure 3.9 for five different time instants. For clarity, the plotted profiles are those along the line $X = 0$ in Figure 3.8. As can be seen, the part which is between overdensities evolves faster in regions where the void is wider than in regions close to the origin where it is narrower. Another significant fact is that the overdense region, which interfaces with the void across a larger area, evolves much faster than the cluster at the origin, which is more compact. This model exhibits the features of the models previously considered. Thus, it might be speculated that the evolution of real structures follows similar patterns. Namely, small voids in the Universe which are surrounded by large high-density regions evolve more slowly than large isolated voids. From the perspective of the continuity equation the expansion of the space in this region is very slow and this is the reason why the voids do not evolve as fast as they otherwise could. On the other hand, the expansion is much faster inside large voids, where the mass of the perturbed region is below the background mass ($\delta M < 0$). In such structures matter flows from voids towards the dense regions which form at their larger sides and enhance their evolution. In this way, the higher expansion rate inside large voids leads to the formation of large and elongated structures such as walls and filaments which emerge at their edges.

3.7 LIGHT PROPAGATION EFFECTS IN THE SZEKERES SWISS-CHEESE MODEL AND CMB OBSERVATIONS

This section presents the application of the Szekeres Swiss-cheese model to the analysis of observations of the cosmic microwave background (CMB) radiation. The impact of an inhomogeneous matter distribution on the CMB observations is in most cases studied within the linear perturbations of the Friedmann-Robertson-Walker model. However, since the density contrast and the Weyl curvature within cosmic structures are large, this issue is worth studying using a different approach. In the Szekeres model, light propagation and matter evolution can be calculated exactly, without such approximations as small amplitude of the density contrast. This allows us to examine in a more realistic manner the contribution of the light propagation effect to the measured CMB temperature fluctuationa.

The results of such an analysis show that small-scale, non-linear inhomogeneities induce, via the Rees-Sciama effect, temperature fluctuations of amplitude $10^{-7} - 10^{-5}$ on angular scales $\theta < 0.24°$ ($l > 750$). This is still much smaller than the measured temperature fluctuations on this angular scale, i.e $\sim 10^{-3}$. However, local and uncompensated (improperly matched into the Friedmann background and not co-expanding with it) inhomogeneities can induce temperature fluctuations of amplitude as large as 10^{-3}, and therefore can be responsible for the low amplitude multipole anomalies observed in the angular CMB power spectrum.

3.7.1 MODEL SPECIFICATION AND EVALUATION

This Swiss-cheese model consists of a variety of inhomogeneous Szekeres patches or regions in a Friedmann background. In fact, they are arranged so that the light rays followed always pass directly from one inhomogeneous patch to another. The six specific Szekeres regions, A to F defined below, are assembled into different sequences along the light paths, that we call models 1 to 5. The details of this section are taken from [131].

To completely define a Szekeres model, the freedom in the radial coordinate r must be fixed, and five
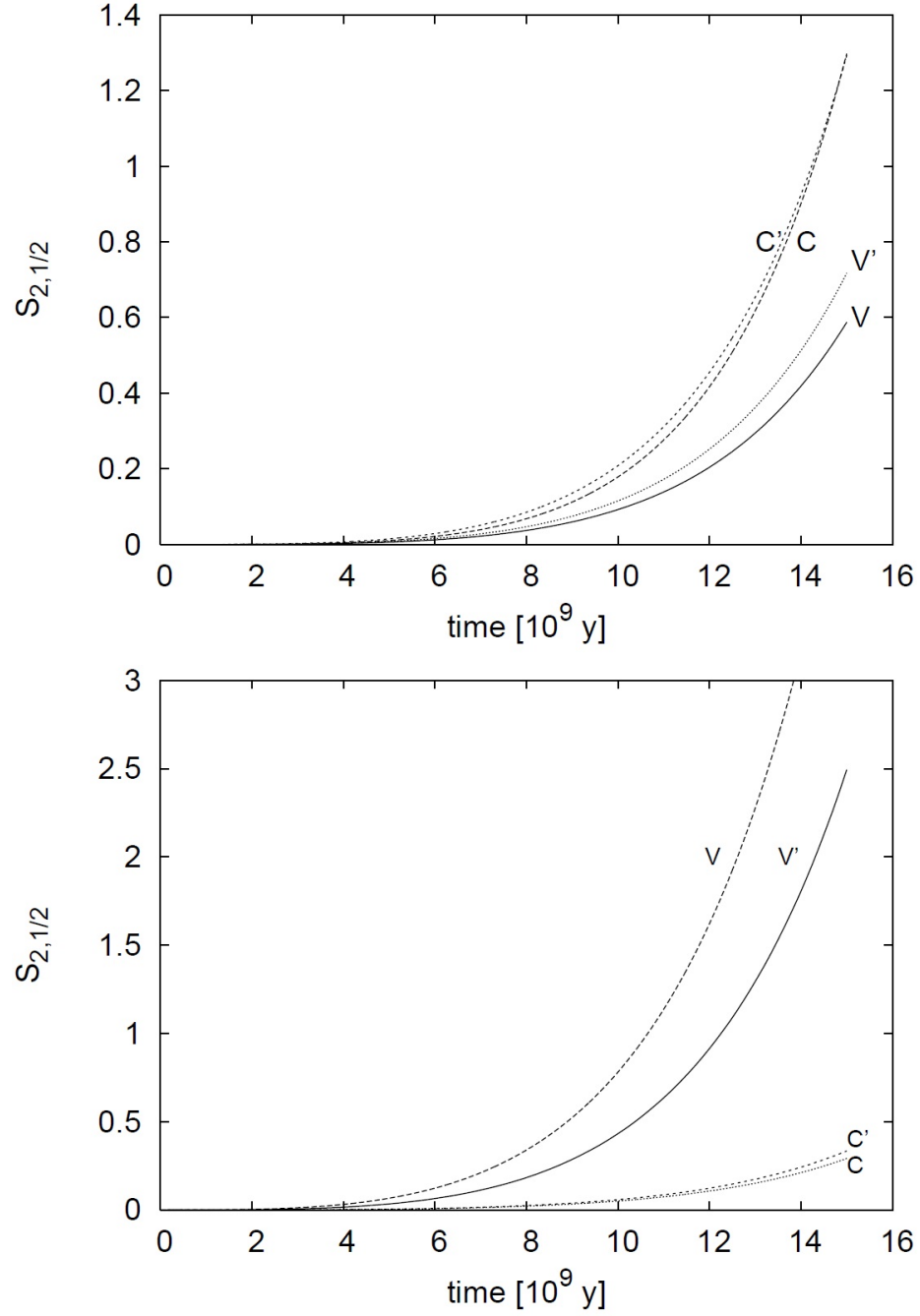
Figure 3.6: Comparison of $S_{2,1/2}$ for models with $\delta M < 0$ (upper panel) and $\delta M > 0$ (lower panel). V corresponds to a void (underdense region), and C corresponds to a supercluster (overdense region). Primes denote models with $P' \neq 0 \neq S'$. Figure taken from [128].
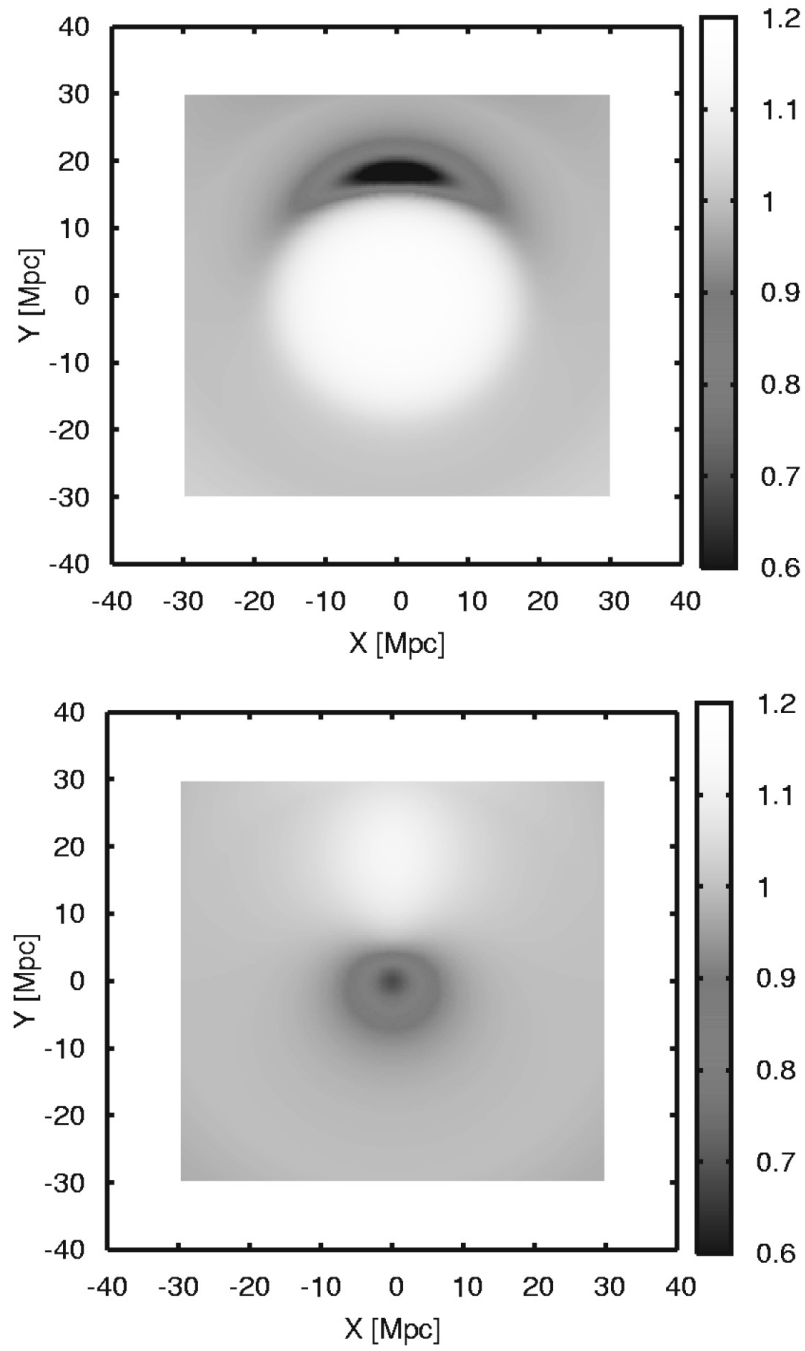
Figure 3.7: The ratio θ_{SZ}/θ_b. Upper panel represents the ratio for model 1, lower panel model 2. Figure taken from [128].
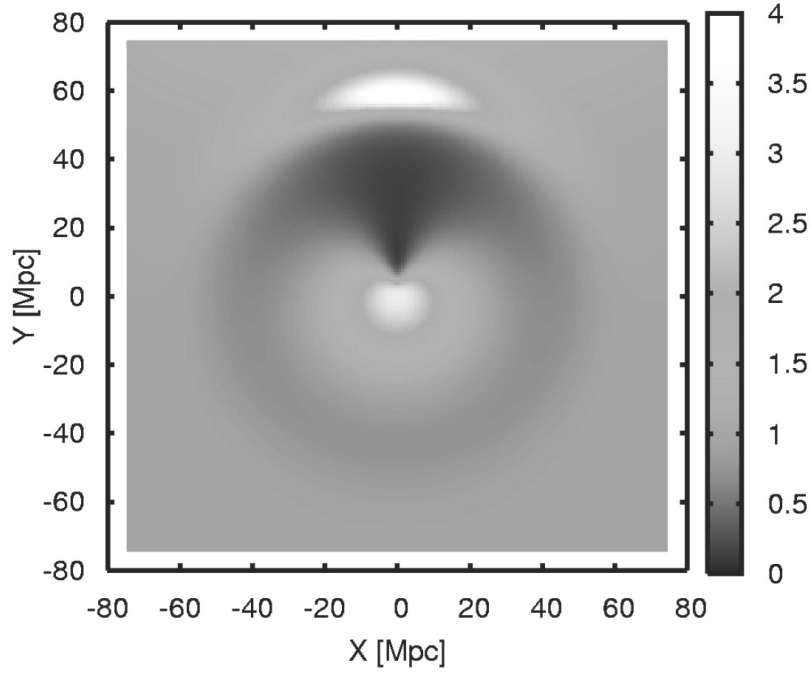
Figure 3.8: The present-day colour-coded density distribution for the triple structure of model 5, showing a slice through the origin. White indicates a high density region. Figure taken from [128].
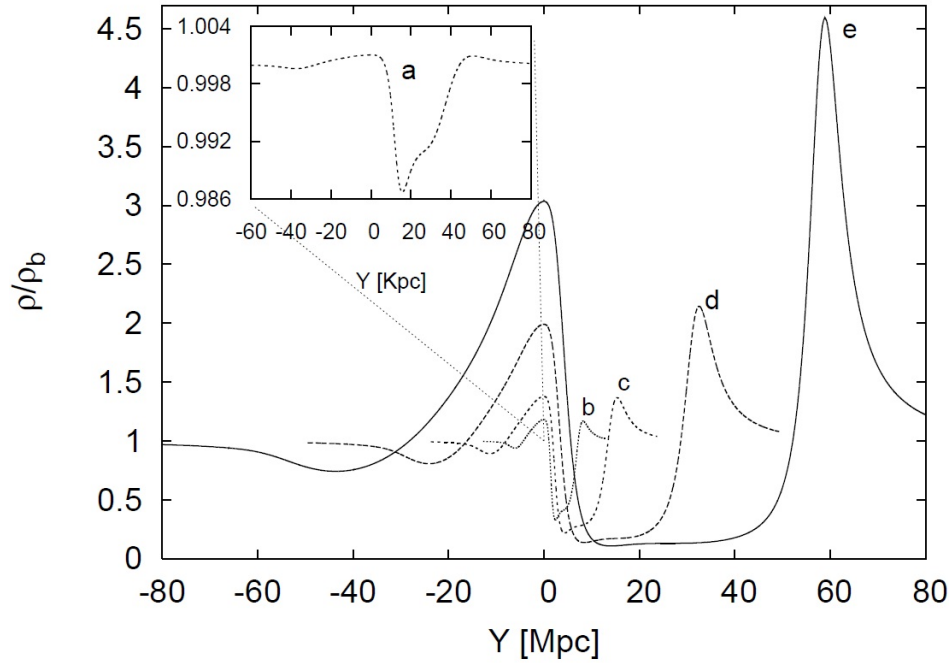

Figure 3.9: The evolution of the density profile of the triple structure in model 5. The profiles correspond to the limit $X = 0$ in Fig. 3.9. Letters correspond to different time instants: a - 500,000 years after the Big Bang; b - 1.5 billion years; c - 5 billion years; d - 10 billion years; e - present instant. Figure taken from [128].

functions of r need to be specified. In this section, all models will be defined by the functions: k, M, S, P and Q. The algorithm used in the calculations can be defined as follows:

- The radial coordinate is chosen to be the areal radius at the last-scattering instant, $t_1 : r' = \Phi(r, t_1)$. For clarity in further use, the prime is omitted.

- The chosen background model is the ΛCDM model, i.e. a flat Friedmann model with $\Lambda \neq 0$. The background density at the current instant is then given by

$$\rho_b = \Omega_m \times \rho_{cr} = 0.27 \times \frac{3H_0^2}{8\pi G}, \tag{3.156}$$

where the Hubble constant is $H_0 = 72 \text{ kms}^{-1}\text{Mpc}^{-1}$. The cosmological constant, Λ, corresponds to $\Omega_\Lambda = 0.73$.

- The initial time, t_1, is chosen to be the time of last scattering, and is calculated using (2.107).

- Six different Szekeres regions are considered here. Let us denote them as regions A, B, C, D, E and F. Regions A, B, C, D and F are overdense, whilst region E is underdense. The functions M, k, Q, P and S in these regions are defined as follows:

Regions A and B

$$M = M_b + \begin{cases} M_1 r^3 & \text{for} & r \leq 0.5a \\ M_2 \exp\left[-12\left(\frac{r-a}{a}\right)^2\right] & \text{for} & 0.5a \leq r \leq 1.5a \\ M_1(2a - r)^3 & \text{for} & 1.5a \leq r \leq 2a \\ 0 & \text{for} & r \geq 2a, \end{cases} \tag{3.157}$$

where M_b is the mass of the corresponding volume of the homogeneous universe,

$$M_b = (4\pi G/3c^2)\rho_{LS}r^3 \quad , \quad \rho_{LS} = (3H_0^2)/(8\pi G)(1 + z_{LS})^3 \quad , \quad M_1 = 8M_2 a^{-3} e^{-3/2} \tag{3.158}$$

and GM_2/c^2 is equal to 0.3 kpc and 0.2 kpc for region A and B respectively, and $a = 12$ kpc.

$$k = -\frac{1}{2} \times \begin{cases} k_1 r^2 & \text{for} & r \leq 0.5b \\ k_2 \exp\left[-4\left(\frac{r-b}{b}\right)^2\right] & \text{for} & 0.5b \leq r \leq 1.5b \\ k_1(2b - r)^2 & \text{for} & 1.5b \leq r \leq 2b \\ 0 & \text{for} & r \geq 2b, \end{cases} \tag{3.159}$$

where $k_1 = 4k_2 a^{-2} e^{-1}$, k_2 is equal to -5.15×10^{-6} and 3.5×10^{-6} for regions A and B respectively, and $b = 10.9$ kpc.

$$S = 1 \quad , \quad P = 0 \quad , \quad Q = Q_1 \ln(1 + Q_2 r) \times \exp(-Q_3 r), \tag{3.160}$$

where, for regions A and B respectively, Q_1 equals 0.72 and 1.45, Q_2 equals 1 kpc^{-1} and 0.4 kpc^{-1}. With these definitions the mass distribution and the curvature are the same as in Friedmann models, for $r > 24$ kpc.

Regions C_1 and C_2

In region C the functions M and k are the same as in region A. The only difference is in the form of functions S, P and Q which are as follows:

$$S = e^{\alpha r} \quad , \quad P = 0 \quad , \quad Q = 0, \tag{3.161}$$

where α is equal to -0.0255 kpc^{-1} and $+0.0255$ kpc^{-1} for regions C_1 and C_2 respectively. Region C_1 is the mirror image of C_2 , where the $Z = 0$ surface is the symmetry plane [$Z := \Phi \cos\theta$ and θ is defined by the stereographic projection (3.20)]. The reason why two mirror-similar regions are employed is

that in the coordinates used here, the axial geodesics can only be studied for propagation along the $Z < 0$ direction, in which $\theta = \pi$. Along the $Z > 0$ direction we have $\theta = 0$, which corresponds to a point at infinity in the stereographic projection. This problem is overcome by matching C_1 with C_2 along the surface $Z = 0$. When calculating propagation toward the origin, model C_1 is employed, and when calculating propagation away from the origin, model C_2 is employed. In both models light propagates along the $Z < 0$ axis.

Regions D_1 and D_2

In regions D the functions M and k are the same as in region B. The only difference is in the form of the functions S, P and Q which are of the following form:

$$S = r^\alpha \quad , \quad P = 0 \quad , \quad Q = 0, \tag{3.162}$$

where α equals -0.97 and $+0.97$ for regions D_1 and D_2 respectively. As above, region D comes from matching D_1 and D_2 along the $Z = 0$ surface.

Regions E and F

$$M = M_b + \begin{cases} M_1 r^3 & \text{for} \quad r \leq 0.5a \\ M_2 \exp\left[-6\left(\frac{r-a}{a}\right)^2\right] & \text{for} \quad r \geq 0.5a, \end{cases} \tag{3.163}$$

$$k = \begin{cases} k_1 r^2 & \text{for} \quad r \leq 0.5b \\ k_2 \exp\left[-4\left(\frac{r-b}{0.5b}\right)^2\right] & \text{for} \quad r \geq 0.5b, \end{cases} \tag{3.164}$$

$$S = 1 \quad , \quad P = 0 \quad , \quad Q = Q_1 - 0.22\ln(1 + Q_2 r) \times \exp(-Q_3 r), \tag{3.165}$$

where

$$M_1 = 8a^{-3} M_2 e^{-1} \quad , \quad k_1 = 4a^{-2} k_2 e^{-1}. \tag{3.166}$$

For region E, $M_2 = -0.75$ kpc, $a = 15.23$ kpc, $k_2 = 1.00173 \times 10^{-5}$, $b = 12.95$ kpc, $Q_1 = 0.22$, $Q_2 = 1$ kpc^{-1}, $Q_3 = 0.1$ kpc^{-1}. For region F, $M_2 = 0.9$ kpc, $a = 23.76$ kpc, $k_2 = 7 \times 10^{-6}$, $b = 19.1$ kpc, $Q_1 = -1.4$, $Q_2 = 0.4$ kpc^{-1}, $Q_3 = 0.005$ kpc^{-1}.

- Light propagation was calculated by solving (3.71)-(3.74) (for models 1 and 3) and (3.98) (for models 2, 4 and 5) simultaneously with the evolution equation (3.14). At each step the null condition, $k_\alpha k^\alpha = 0$, was used to test the precision of calculations. All equations were solved with the fourth-order Runge-Kutta method.

- The temperature fluctuations were calculated from (2.223) (for models 1 and 3) and (3.106) (for models 2, 4 and 5). The mean redshift $\bar{z}$ was calculated using the ΛCDM model.

3.7.2 ARRANGEMENT OF THE SWISS-CHEESE MODEL

The Swiss-cheese models which are employed here are constructed from a Friedmann background and many inhomogeneous Szekeres patches, using six different building blocks: spherical regions A-F. These Szekeres regions are placed so that their boundaries touch wherever a light ray exits one inhomogeneous patch; thus the ray immediately enters another Szekeres inhomogeneity and spends no time in the Friedmann background (except for model 3, where light propagates for a while in the Friedmann region). Five models are constructed, using different sequences of regions A-F.

When constructing a Swiss-cheese model, we need to satisfy the junction conditions for matching the particular inhomogeneous patches to the Friedmann background, and also assure the continuity of the null geodesics. The standard junction conditions are that the 3-D metric of the surface and its extrinsic curvature, the first and second fundamental forms, must be continuous.

For matching a Szekeres patch to a Friedmann background across a comoving spherical surface, $r =$ constant, the conditions are: that the mass inside the junction surface in the Szekeres patch is equal to

the mass that would be inside that surface in the homogeneous background; that the spatial curvature function at the junction surface is the same in both the Szekeres and Friedmann models, $k_{SZ} = k_F r^2$; and the bang time must be continuous across the junction. We have assumed the same value of Λ for both to make the matching possible.

The junction of null geodesics requires the continuity of all components of the null vector. However, let us notice that when one Szekeres sphere is matched to another Szekeres sphere it can be rotated around the normal direction. Thus, we only need to match up the time component k^0 and the tangential component:

$$k^T = \frac{\Phi}{\mathcal{E}} \sqrt{(k^x)^2 + (k^y)^2}\bigg|_{\text{region 1}} = \frac{\Phi}{\mathcal{E}} \sqrt{(k^x)^2 + (k^y)^2}\bigg|_{\text{region 2}}. \qquad (3.167)$$

The radial component is then given by the null condition, $k_\alpha k^\alpha = 0$.

Five different Szekeres Swiss-cheese models are considered here:

Model 1

Model 1 is constructed by alternately matching regions A and B (A + B + A + B ....) into the Friedmann background. When a light ray exits one Szekeres region, it immediately enters another inhomogeneous patch. Each time, the (x, y) position of the point of entry is randomly selected. In addition k^x and k^y are quasi-randomly selected , i.e.

$$(k^y)^2 = \gamma \left(k^T \frac{\mathcal{E}}{\Phi}\right)^2 \quad , \quad (k^x)^2 = (1 - \gamma) \left(k^T \frac{\mathcal{E}}{\Phi}\right)^2, \qquad (3.168)$$

where γ is a random value in the range $0 \leq \gamma \leq 1$. The radial coordinate of the matching point is $r_j = 24$ kpc - the point where the Szekeres region becomes Friedmann.

Model 2

This model is constructed from alternating regions C and D, but only axial null geodesics are considered, i.e. $k^x = 0$ and $k^y = 0, x = y = 0$. The radial component of the matching point is again $r_j = 24$ kpc.

Model 3

The next model consists of regions E and F placed alternately. Null vector components k^x and k^y are chosen in such a way that $10^{-8} \leq k^x \leq 10^{-4}$ and $10^{-8} \leq k^y \leq 10^{-4}$, but are otherwise random. As can be noted, this is not in accordance with condition (3.167). In order to maintain the continuity of the tangential component of the null vector the next Szekeres patch must be oriented with respect to the preceding patch. This however would lead to an overlapping of successive Szekeres regions. To eliminate such an overlap, the Szekeres patches are separated from each other by a distance $\Delta r = 40$ kpc (which corresponds to a current distance of approximately 40 Mpc).

Model 4

Model 4 is constructed using only C regions, with $r_j = 24$ kpc, and only axial geodesics are considered, i.e. $k^x = k^y = x = y = 0$.

Model 5

The last model is also axially symmetric, $k^x = k^y = x = y = 0$, $r_j = 24$ kpc, but uses only D regions.

In a generic cosmological model, as proved by [91], voids are not compensated, i.e. the mass within a void is smaller than the mass of the background that would occupy the same space. Such voids expand faster than the background, and once they begin to collide, they flatten against each other.
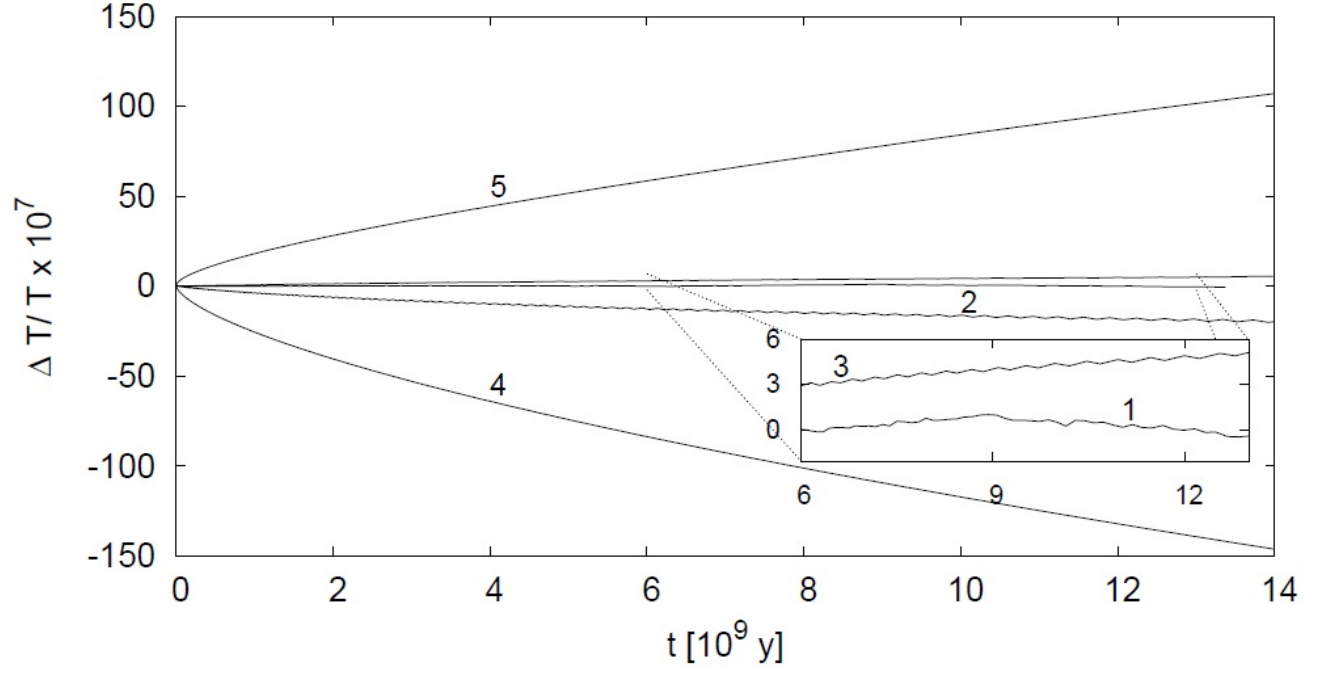
Figure 3.10: The temperature fluctuations caused by light propagation effects in models 1-5. In models 1-3 light propagates alternatively through underdense and overdense regions. In model 4 light propagates only through regions of $\delta M < 0$, $\delta k > 0$, and in model 5 only through regions of $\delta M > 0$, $\delta k < 0$. Figure taken from [131].
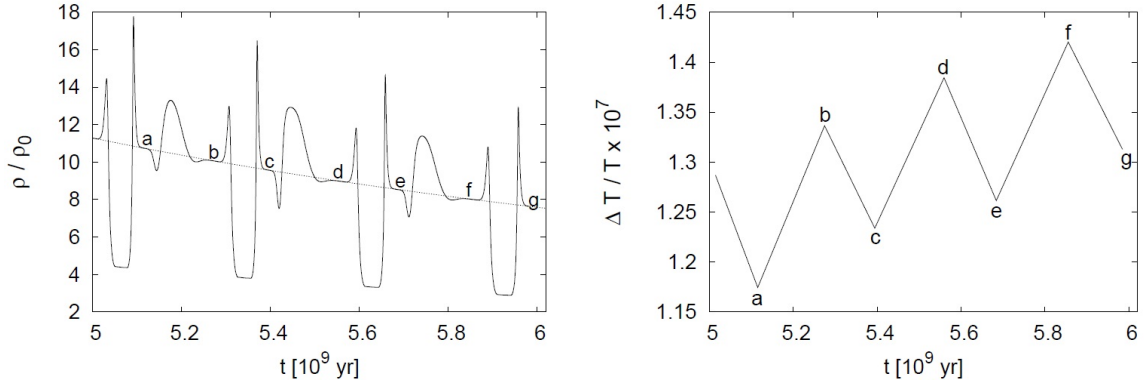

Figure 3.11: A small part of the light propagation in model 3. The left panel shows the density variation that light 'feels' as it propagates. The black thin dotted line shows the density in the background model. The right panel presents the temperature fluctuations as measured by an observer situated outside the structure in the inhomogeneous FRW region. The letters in both panels label corresponding points along the light path. Figure taken from [131].

3.7.3 THE REES-SCIAMA EFFECT

To estimate the temperature fluctuations induced by the light propagation effects, it is assumed that the initial temperature distribution is uniform, $(\Delta T/T)_e = 0$. Then temperature fluctuations are calculated using (2.160) and they are plotted against time of propagation in Figure 3.10. As seen, the final values are small, of amplitude $\Delta T/T \approx 10^{-7}$ (model 3), $\Delta T/T \approx 10^{-6}$ (models 1 and 2), and $\Delta T/T \approx 10^{-5}$ (models 4 and 5). A detailed analysis of how inhomogeneities induce temperature fluctuations is presented in Figure 3.11 (for clarity, only a small fraction of the time is presented). The left panel of Figure 3.11 shows the density of regions through which the light propagates in model 3. The right panel presents the temperature fluctuations as measured by an observer situated at the junction point where the model is that of Friedmann. Letters correspond to each inhomogeneous patch (left panel) and temperature fluctuations caused by them (right panel). Clearly, underdense regions induce negative temperature fluctuations and overdense regions produce positive fluctuations.

Apart from estimating the amplitude of the Rees-Sciama effect, it is also important to estimate the angular scale which is the most affected by this effect. Without going into any complicated analysis, we can estimate the angular scale by employing the following approximation: the correlation between two distant points on the sky is zero: photons which were propagating along two distant paths have the temperature fluctuations uncorrelated. Only when the light paths are near to each other are the temperature fluctuations correlated. Thus the simplest estimation of the angular scale of the Rees-Sciama effect, as seen from the schematic Figure 3.12, is the angular size of the Szekeres patch at the last scattering instant. For the models studied in this section, such approximations lead to an angular scale of $\theta \approx 0.21°$, or alternatively, $l \approx 850$. If the photons are propagating along neighbouring paths for only half the age of the Universe (in such a case, as seen from Figure 3.13, the final temperature fluctuations are two times smaller), then the angular amplitude is smaller, $\theta \approx 0.24°$ ($l \approx 750$). Thus the Rees-Sciama effect of amplitude $\sim 10^{-6}$ contributes to the CMB temperature fluctuations on the angular scale $\theta < 0.25°$ ($l > 700$). This angular scale corresponds to the angular scale at which the third peak of the CMB angular power spectrum is observed. At this scale the measured rms temperature fluctuations are of amplitude $\approx 5 \times 10^{-5}$. This is still several times higher than the results obtained within models 4 and 5. In the case of models 1-3 the measured value is more than one order of magnitude larger than the model estimates.

3.7.4 THE ROLE OF LOCAL STRUCTURES

So far, it has been assumed that each inhomogeneous structure is compensated (i.e. each Szekeres region was matched with the FRW background), so that measurements are carried out away from the inhomogeneities, i.e. where the Universe is homogeneous. However, in the real Universe there is no place where the cosmic structures in the observers vicinity are fully compensated and therefore the Universe should not be treated locally as homogeneous. Since all measurements are always local, let us consider what happens if temperature fluctuations are measured in an uncompensated region. Figure 3.13 presents presents the temperature fluctuations measured by an observer situated at different places within region E. These results are obtained under the assumption that light from last scattering is propagating through homogeneous regions, and currently reaches an observer in an inhomogeneous structure (region E). The light enters and propagates along the bright line shown in the upper right inset of Figure 3.13. The above results show that local structures can significantly contribute to the CMB temperature fluctuations. This indicates that care must be taken when extracting information from the CMB observations. Although it is highly unlikely that the signal caused by the local structures have a signature of acoustic oscillations we should be aware that local structures can have some visible impact on observations. Thus, it is important to test if local structures can cause the observed correlations of the alignment of dipole, quadrupole and octupole axes of the angular power spectrum of the CMB temperature fluctuations or their low amplitude.
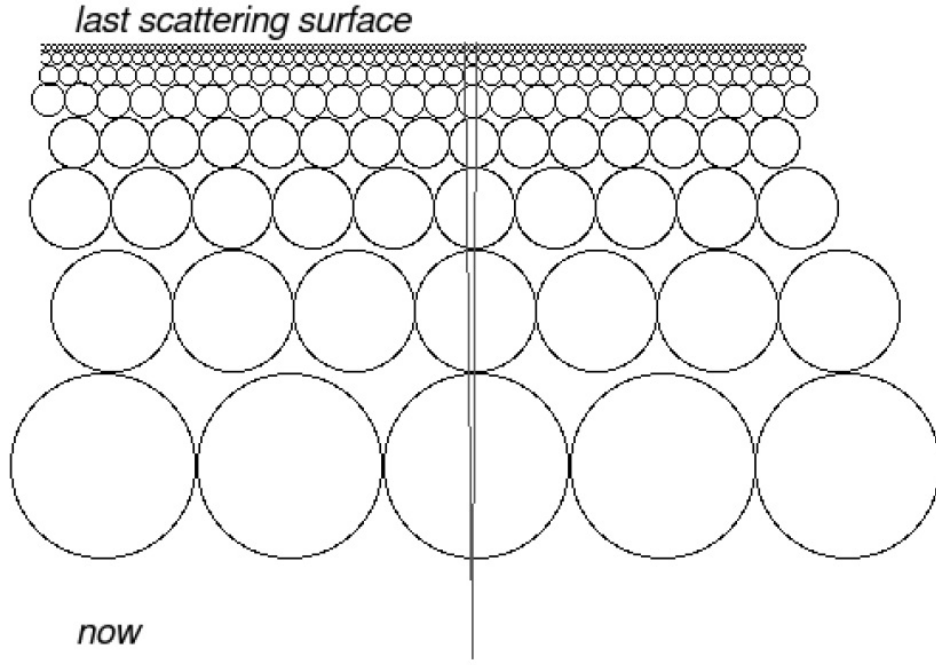
Figure 3.12: The schematic representation of the Swiss-cheese model. When two photons are propagating along a similar path the final temperature fluctuations are similar. If paths are different, then the final temperature fluctuations are also different and hence not correlated. Figure taken from [131].
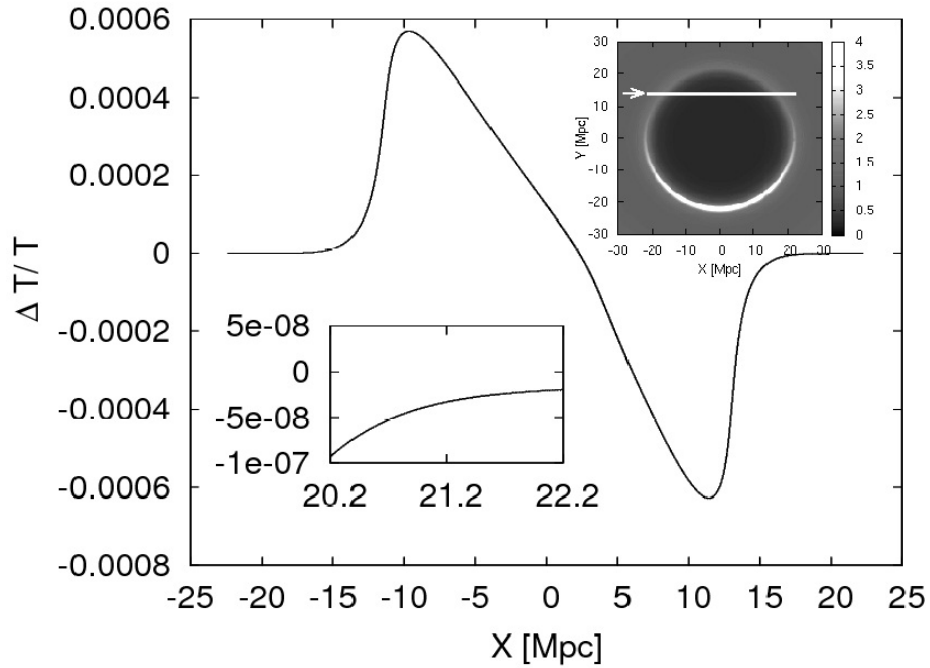

Figure 3.13: Temperature fluctuation amplitude, as measured by observers at different locations in region E, along the path of a light ray. The ray path is shown as the bright line in the upper inset. Figure taken from [131].

Chapter 4

Conclusion

The Universe as we observe it is very inhomogeneous. Its structures include groups and clusters of galaxies, large cosmic voids and very large elongated structures such as filaments and walls. However, homogeneous and isotropic models of the Robertson-Walker class have been used almost exclusively in cosmology and, in these, structure formation is described by an approximate perturbation theory. This cannot be applied once perturbations become large and evolution becomes nonlinear, and only applies as long as the perturbations remain small. This is where the methods of inhomogeneous cosmology are more advantageous. These methods can be employed both to study the evolution of cosmic structure, and to investigate the formation and evolution of black holes, as well as studying the geometry and dynamics of the Universe.

Despite the successes of the Concordance model, based on an FRW metric plus perturbation theory, structure evolution eventually becomes non-linear and non-Newtonian, and our understanding of present day observations will be incomplete without the methods of inhomogeneous cosmology. The phenomena of fully relativistic inhomogeneous evolution must occur and cannot be ignored.

This thesis presents the application of inhomogeneous exact solutions of the Einstein equations in such areas as the evolution of galactic black holes and cosmic structures, and the impact of inhomogeneities on light propagation which allows us to solve the horizon and dark energy problems. The following is a brief summary of its contents and results.

Evolution of galactic black holes

It is commonly assumed that galactic black holes can be described using the Kerr or Schwarzschild metric. However, these black holes do not evolve, and so non-stationary models must be employed. In Section 2.5.1 we have described the nonlinear evolution of an initial density perturbation at recombination into a galaxy with a central black hole at the present day, using the spherically symmetric L-T model. A density profile based on observational data for M87 was taken for the galaxy exterior to the horizon, and a black hole with mass $3 \times 10^9 M_\odot$ was smoothly joined on as the interior.

No observational data concerning the interior of the horizon exists, and so two distinct forms of this central black hole were considered, both of which are L-T models. Firstly, a condensation that collapses to a singularity, and secondly a full Schwarzschild-Kruskal-Szekeres type wormhole with nonzero density. It has been demonstrated that within these two cases it is possible to obtain a realistic model of a galactic black hole. In the collapse case, the black hole forms less than half a billion years before the present. In the wormhole case, the wormhole is only open for a fraction of a second, having minimum mass of only a few $M_\odot$, but has already accreted a quarter of a million $M_\odot$ by recombination. Both models grow to $3 \times 10^9 M_\odot$ by today.

Due to a lack of data, this approach was the first exploratory step into as yet unchartered territory, rather than an actual model to be compared with data.

Evolution of cosmic structures

The linear perturbation formalism or N-body simulations are usually used to describe the evolution of cosmic structures. However, these methods face both problems and limitations; the linear approach is invalid once the density contrast becomes large. Further, in the linear regime one cannot study the impact of shape on evolution since, in this approximation, the shape of a structure does not affect its evolution [132]. The N-body simulations have the following limitations: the assumption of a uniform Hubble expansion, the use of Newtonian mechanics, and the finite number of particles [133]. Consequently, investigations based on exact solutions are mandatory, and we have used exact relativistic models such as the L-T, Lemaître and Szekeres models to reproduce the formation of structures in the Universe.

In Section 2.3.1 methods of generating the L-T models that evolve between given initial and final profiles of either density or velocity were presented. These methods have been used in Section 2.6 to describe the formation and evolution of the Abell cluster A2199. In Section 2.7 we present a model of cosmic voids. In Section 3.6 we show the evolution of pairs consisting of a galaxy supercluster and a void, and of triple structures consisting of a galaxy supercluster, a void and a wall. We have found that density perturbations are less efficient at generating structures than velocity perturbations. The gravitational instability paradigm, which focuses on analysing Fourier modes rather than individual structures, is probably not telling us the whole story. This point is strengthened by the fact that an initial condensation can evolve into a void, and vice-versa.

It has been found that the shape and environment of cosmic structures have an impact on evolution. In particular, large isolated voids evolve faster than small voids among large overdense regions do. This is because the expansion of the space is slower inside smaller voids than inside larger voids. Further, this higher expansion rate inside larger voids leads to the formation of large and elongated structures such as walls and filaments which emerge at the edges of these large voids. These elongated structures evolve much faster than compact overdense regions: the density contrast within these structures increases faster.

The angular distribution of the CMB temperature must be known at much finer scales before any models of structure formation can be truly tested against these observations. At the time of writing this thesis, the best resolution of $0.1°$ is to be compared with the approximate angular size of the portions of matter on the CMB sky that will go into a galaxy cluster, $\sim 0.1°$, and into a single galaxy, $\sim (10^{-3} - 10^{-2})°$.

One unsatisfactory feature of the L-T and Szekeres models used here is that once matter starts collapsing, it will keep collapsing to a singularity. In real objects, rotation, pressure gradients and non-perfect fluid behaviour can prevent collapse so that the object virializes. More general exact cosmological solutions will be needed if we are to create highly accurate models that remain valid as collapse sets in.

The horizon problem

An important application of exact inhomogeneous models is to study the early stages of the Universe and its large-scale homogenisation. The central problem here is whether the Universe started homogeneous (or very close to homogeneous) or the currently observed large-scale homogeneity has developed during its evolution. Currently, this second opinion is in favour among cosmologists, and the mechanism which leads to homogenisation is believed to be inflation. However, inflation does not really solve this problem, but merely explains that regions of the Universe which now enter our horizon were causally connected before the inflation epoch. The inflationary hypothesis only postpones the occurrence of the horizon problem to a later time, after which the observer will be more confronted with it. This raises the question, why are we living at a time when inflation still solves the horizon problem? Moreover, inflation replaces one problem of initial conditions with another, i.e. the specific initial conditions of the Universe (homogeneity) are replaced by mechanisms which are specifically designed to drive inflation and whose natural production has become a major topic in the literature. In Section 2.10 a resolution of the horizon problem was given in the framework of a large class of L-T Delayed Big Bang models, which solves it permanently, unlike the inflation paradigm. The geometry of these L-T models allows our past light cone to bend sufficiently to never cross the Big Bang surface and therefore solves the causality problem at last scattering surface.

Cosmological observations in the inhomogeneous universe

Another aspect of this thesis was to use inhomogeneous models to analyse cosmological observations such as supernovae, the cosmic microwave background, the baryon acoustic oscillation scale, etc., which are usually only analysed against homogeneous models.

In Section 2.9 we demonstrated that the L-T models are able in principle to reproduce the observed dimming of the distant supernovae with no need for a cosmological constant or, in any case, that an effect of inhomogeneities on the determination of the cosmological parameters might not be negligible. However, the luminosity data do not fully specify an L-T model, leaving one arbitrary function undetermined, even in the case of non-spherically symmetric models, e.g. Swiss-cheese models where the holes in a Friedmannian background are represented by L-T solutions. It was emphasised that the correct way of dealing with this issue is to try to reproduce not an accelerating universe but the Hubble diagram of the SN Ia. Actually, an inhomogeneous model can mimic the magnitude-redshift relation of the Concordance model without exhibiting an accelerating expansion.

The CMB temperature fluctuations have been studied in the framework of both L-T (Chapter 2) and Szekeres (Chapter 3) models. The observed values of the dipole, the quadrupole and octupole have been removed by shifting our location away from the centre of particular inhomogeneous cosmological models. However, even if future analyses of observational data show that part of the dipole appears to be of cosmological origin, more work connected with multipole moments of higher order would be needed to discriminate between various cosmological candidate interpretations. The effect of light propagation in a lumpy universe on the CMB temperature fluctuations has been studied in Sections 2.11 and 3.7. The Rees-Sciama effect was analysed in Section 3.7 by propagating light rays through Swiss-cheese models where the holes are Szekeres regions matched into a Friedmann background. When each underdense region is followed by an overdense region the final fluctuations are small, of order 10^{-7}. But when light is propagated only through underdense or overdense regions, the final value is by one order of magnitude higher. Further, the results of Section 3.7 indicate that the Rees-Sciama effect caused by the propagation of light through inhomogeneous but compensated structures do not significantly affect the CMB temperature fluctuations. Some would say that this result is obvious since a similar result is reached when using perturbative methods. However, within real cosmic structures the density contrast and the Weyl curvature are significantly large. Thus, the application of the perturbative methods cannot be justified. It has been shown in this section that the Rees-Sciama effect of amplitude $\sim 10^{-6}$ contributes to the CMB temperature fluctuations on the angular scale $\theta < 0.25°$ ($l > 700$). However, if the structures are not compensated or the measurements are carried out inside inhomogeneous non-compensated structures, the amplitude of measured temperature fluctuations can be slightly higher. Since in reality we cannot separate ourselves from the surroundings and say that all local structures at our positing are 'compensated', thus the local cosmic structures must be taken into account when analysing CMB observations. Especially, it is possible that the local structures can have some impact on low multipole anomalies of the angular CMB power spectrum.

The results show that the L-T and Szekeres models are very useful tools for this kind of investigation. However, for the parameters of the models to be properly fitted to the results of observations, the observational data would have to be re-interpreted against the background of these inhomogeneous geometries. This calls for a thorough revision of the whole existing body of data and literature - a process that will take a long time.

The traditional FRW cosmological models are the simplest solutions of Einstein's equations with nonzero expansion. They were used at the beginning of relativistic cosmology to account for the redshift of the galaxies observed in the 1920s by Hubble and Humason. However, they make use of relativity in a most simplistic way, which is doomed to fail when trying to account for an accurate description of our Universe at all cosmological scales. In the further development of astrophysical cosmology based on these models, the main input from relativity was the assumption that the Universe was hot and dense in the past, and then cooled as it expanded. Everything else is thermodynamics and particle physics. It is usually claimed that the light element abundances confirming the standard picture of nucleosynthesis, the nearly isotropic CMB black body power spectrum and the Hubble law are three observational pillars which sustain the robustness of FRW models. However, even in a Friedmannian framework, observations are not sufficiently precise to define the evolution uniquely, so there is certainly enough room to consider more general models. It is often claimed that the high isotropy of the CMB radiation, combined with the

Copernican principle, proves that our Universe is homogeneous and exhibits therefore a Robertson-Walker geometry; see [134], for example. Such statements often ignore the caveats stated in [134], as well as the smallness of the effect of matter inhomogeneities on the temperature of propagating radiation. Existing estimates show that the interaction is weak, and no temperature anisotropies larger than 10^{-5} should ever be expected.

By considering more general (L-T, Lemaître and Szekeres) cosmological models, one does not in any way deny the confirmed successes of the FRW cosmology. The more general models should fill in many aspects that cannot be captured in the FRW geometries, like structure formation. The FRW models still remain valid as a rough first approximation to a more detailed description.

We do not claim that all solutions to all problems and mysteries of modern cosmology have been found. Further, before we decide that we do indeed have an explanation of a set of observations, we should carefully consider all possible theoretical descriptions, and choose the one that is logically simplest and does without untestable assumptions. We offer this caveat since unverified and often untestable theories have been advanced with certainty to explain some observed phenomena, whilst inhomogeneous alternatives are casually dismissed. Some possible questionable theoretical descriptions are as follows:

- Cold dark matter was introduced in order to allow perturbations to begin growing before re-combination, because otherwise structures would not form soon enough to agree with observations. Its equation of state has been adjusted to improve the properties of the present-day matter distribution. Although astronomers had long mooted the existence of dark matter to account for galaxy rotation curves etc., neither the equation of state nor the amount were at all like current proposals.

- An early example is the inflationary prediction that $\Omega_0 = 1$. In fact, inflation predicts Ω_0 is very close to unity, and it does not increase the probability that Ω_0 is exactly 1, which remains vanishingly small. Whilst calculations in a flat FRW model give good approximations for many purposes, there are qualitative differences between flat and non-flat models. Indeed there are problems for inflation in FRW models with positive spatial curvature, [135]. Despite this, for a long time many advocates stated it is exactly 1.

- Extra-galactic type Ia supernova measurements indicate a decrease of apparent luminosities, relative to expectations in zero pressure, zero Λ Friedmann models. Since these larger than expected luminosity distances dont fit our once preferred model, and since homogeneity is not to be questioned, we force the calculated dimming to agree with our favourite simple cosmological model, by declaring that 70% of the current energy density of the Universe is 'dark energy' whose properties nobody can explain.

- In fact we boldly declare that we know how the scale factor evolved, while freely admitting that we do not know the physical nature of more than 95% of the content of the Universe. Currently there are several tens of different explanations for dark energy and dark matter, starting from brane worlds and ending with aether-like scalar fields or a Chaplygin gas. Although within such a model one obtains concordance, i.e. the right CMB power spectrum, an explanation of the dimming of supernovae and the calculated age of Universe comparable to the age of the oldest stars, it is actually a collection of phenomenological proposals that lack a coherent physical basis. Given these uncertainties, it is far too soon to declare that the Concordance model is a true image of our Universe. It should be noted that there already exist explanations of the CMB power spectrum and other cosmological observations based on general relativity that do not invoke any entities unknown from the laboratory, but simply take into account that inhomogeneities in the matter distribution do exist, and do influence the collection and interpretation of observational results.

The history of science should teach us some caution. It happened before that ad-hoc fixes proposed in order to solve an isolated problem developed into elaborate research paradigms. Well-known examples are the aether hypothesis and the steady-state theory, the first proposed to provide a natural reference frame for electromagnetic waves, the second to solve the 'age problem' of the Universe. In both cases, the solution of the original problem was found by taking the good old theory to farther limits than before, which led to new interesting developments. We propose to do the same with the apparent 'acceleration of

expansion'. We showed in this thesis that very promising attempts at explaining this phenomenon within standard relativity, without invoking 'dark energy', already exist in the literature.

A curious tendency can be observed in cosmology. At the end of the 19th century most scientists firmly believed that Newtonian mechanics can be successfully employed to describe the world. Nowadays, most scientists have no doubts that there is still plenty to discover about the true nature of the Universe. However, many tend to look for new physics rather than to seek an explanation within the current paradigm. The main point of this thesis is a demonstration that a solid part of relativistic cosmology can be done using exact methods of relativity, without applying approximations, heuristic methods of dubious mathematical foundation or by referring to new physics. Additionally, whatever new physics emerges, the methods and results of inhomogeneous cosmology still need to be taken into account. The L-T model has been used many times over the years for a wide variety of applications, yet it continues to generate some interesting results. The Szekeres model on the other hand has only recently been used for modelling, and has a much greater potential for a very broad range of interesting applications and results. The diversity of possible models and uses is essentially unknown, and we can be sure that more useful applications will emerge. Especially with the Szekeres models, there is enormous scope for investigating the formation and evolution of complex structures.

This thesis shows that relativity has a lot more to offer to cosmology than just the standard homogeneous models of the Robertson-Walker class, and it also demonstrates that inhomogeneous metrics can quite easily generate realistic models of cosmic structures and their nonlinear formation and evolution.

To end on an optimistic note, let us observe that in recent years appreciation of inhomogeneous models in the astrophysical community has increased in a dramatic way. In [2], a review of inhomogeneous cosmologies was presented, and it included just all papers in which any aspect of such models had been discussed up until then. Up to that time, papers on such topics had been published predominantly in physical and mathematical journals. By today, there is a regular stream of new publications discussing various astrophysical and observational applications of the L-T model, they are often published in astronomical journals, and the preferred medium for their pre-publication is astro-ph, not gr-qc as before. It would be rather impossible to capture them in a review of reasonable size, and any such review would instantly become outdated. The Szekeres model is slowly making its way into the field. Thus, it seems that we are witnessing the birth of a new-style theoretical astrophysics that will not be slavishly bound to just one class of cosmological models, but will allow general model-fitting as a legitimate activity.

Bibliography

[1] Hawking S.W. and Ellis G.F.R., 1973, *The Large-Scale Structure Of Space-Time*, 1st Edition, Cambridge University Press

[2] Krasińsky A., 1997, *Inhomogeneous Cosmological Models*, 1st Edition, Cambridge University Press

[3] Bertschinger E., 1996, *Proc. Les Houche Summer School*, 273

[4] Ma C.P. and Bertschinger E., 1995, *Astrophys. J.*, 455, 7

[5] Lifshitz E.M., 1946, *J. Phys.*, 10, 116

[6] Bardeen J.M., 1980, *Phys. Rev. D*, 22, 1882

[7] Peebles P.J.E. and Yu J.T., 1970, *Astrophys. J.*, 162, 815

[8] Sachs R.K. and Wolfe A.M., 1967, *Astrophys. J.*, 147, 73

[9] Smoot G.F. *et al.*, 1992, *Astrophys. J.*, 396, L1

[10] Dunkley J., *et al.*, 2009, *Astrophys. J. Suppl.*, 180, 306, arXiv:0803.0586

[11] Kowalski M., *et al.*, 2008, *Astrophys. J.*, 686, 749, arXiv:0804.4142

[12] Padmanabhan N., *et al.*, 2007, *Mon. Not. R. Astron. Soc.*, 378, 852, arXiv:astro-ph/0605302

[13] Fu L., *et al.*, 2008, *Astron. Astrophys.*, 479, 9, arXiv:0712.0884

[14] Hinshaw G., *et al.*, 2009, *Astrophys.J. Suppl. Ser.*, 180, 225, arXiv:0803.0732

[15] Yadav A.P. and Wandelt B.D., 2008, *Phys. Rev. Lett.*, 100, 181301, arXiv:0712.1148

[16] Land K. and Magueigo J., 2005, *Phys. Rev. Lett.*, 95, 071301, arXiv:astro-ph/0502237

[17] de Oliveira-Costa A. and Tegmark M., 2006, *Phys. Rev. D*, 74, 023005, arXiv:astro-ph/0603369

[18] Tomita K., 2001, *Mon. Not. R. Astron. Soc.*, 326, 287, arXiv:astro-ph/9906027

[19] Célérier M.N., 2000a, *Astron. Astrophys.*, 353, 63, arXiv:astro-ph/990726

[20] Biswas T., *et al.*,2006, arXiv:astro-ph/0606703

[21] Célérier M.N., 2007, arXiv:astro-ph/0702416

[22] Gott J.R.I., *et al.*, 2005, *Astrophys. J.*, 624, 463, arXiv:astro-ph/0310571

[23] Einasto J., 2006, arXiv:astro-ph/0609686

[24] Peebles P.J.E., 2001, arXiv:astro-ph/0101127

[25] Frith W.J., *et al.*, 2003, *Mon. Not.R. Astron. Soc.*, 345, 1049, arXiv:astro-ph/0302331

[26] Cruz M., *et al.*, 2006, *Mon. Not. R. Astron. Soc.*, 369, 57, arXiv:astro-ph/0601427

[27] Rudnick L., *et al.*, 2007, arXiv:astro-ph/0704.0908

[28] Inoue K.T. and Silk J., 2006, arXiv:astro-ph/0612347

[29] Schwarz D.J. and Weinhorst B., 2007, arXiv:astro-ph/0706.0165

[30] McClure M.L. and Dyer C.C., 2007, *New Astron.*, 12, 533, arXiv:astro-ph/0703556

[31] Plebański J. and Krasińsky A., 2006, *An Introduction To General Relativity And Cosmology*, Cambridge University Press

[32] Hellaby C. and Lake K., 1985, *Astrophys. J.*, 290, 381

[33] Sato H. and Maeda K., 1983, *Progr. Theor. Phys.*, 70, 119

[34] Szekeres P., 1975, *Commun. Math. Phys.*, 41, 55

[35] Krasińsky A. and Hellaby C., 2002, *Phys. Rev. D*, 65, 023501

[36] Krasińsky A. and Hellaby C., 2004a, *Phys. Rev. D*, 69, 023502

[37] Schneider J. and Célérier M.N., 1999, *Astron. Astrophys.*, 348, 25

[38] Célérier M.N., 2000b, *Astron. Astrophys.*, 362, 840

[39] Hellaby C., 1987, *Class. Quant. Grav.*, 4, 635

[40] Krasińsky A. and Hellaby C., 2004b, *Phys. Rev. D*, 69, 043502

[41] Begelman M.C., 2003, *Science*, 300, 1898

[42] Fabricant D., *et al.*, 1980, *Astrophys. J.*, 241, 552

[43] Navarro J.F., *et al.*, 1995, *Mon. Not. R. Astron. Soc.*, 275, 720

[44] Mustapha N. and Hellaby C., 2001, *Gen. Rel. Grav.*, 33, 455

[45] Hoyle F. and Vogeley M.S., 2004, *Astrophys. J.*, 607, 751

[46] Bolejko K., *et al.*, 2005, *Mon. Not. R. Astron. Soc.*, 362, 213

[47] Press W.H., *et al.*, 1986, *Numerical Recipes. The Art Of Scientific Computing*, Cambridge University Press

[48] Pang T., 1997, *An Introduction To Computational Physics*, Cambridge University Press

[49] Bennett C.L., *et al.*, 2003, *Astrophys. J. Suppl. Ser.*, 148, 1

[50] Bolejko K., 2006a, *Mon. Not. R. Astron. Soc.*, 370, 924

[51] Peebles P. J. E., 1993, *The Large-Scale Structure of the Universe*, Princeton University Press

[52] Riess A.G., *et al.*, 1998, *Astron. J.*, 116, 1009

[53] Perlmutter S., *et. al.*, 1999, *Astrophys. J.*, 517, 565

[54] Ellis G.F.R. and Stoeger W., 1987, *Class. Quant. Grav.*, 4, 1697

[55] Hellaby C., 1988, *Gen. Rel. Grav.*, 20, 1203

[56] Carroll S.M., *et. al.*, 2004, *Phys. Rev. D*, 70, 043528

[57] Dabrowski M.P. and Hendry M.A., 1998, *Astrophys. J.*, 498, 67

[58] Pascual-Sánchez J.F., 1999, *Mod. Phys. Lett. A*, 14, 1539

[59] Tomita K., 2000, *Astrophys. J.*, 529, 38

[60] Célérier M.N., 2007, *New Adv. Phys.*, 1, 29

[61] Partovi H.H. and Mashhoon B., 1984, *Astrophys. J.*, 276, 4

[62] Carroll S.M., *et. al.*, 1992, *Ann. Rev. Astron. Astrophys.*, 30, 499

[63] Célérier M.N. and Schneider J., 1998, *Phys. Lett. A*, 249, 37

[64] Flanagan E.E., 2005, *Phys. Rev. D*, 71, 103521

[65] Hirata C.M. and Seljak U., 2005, *Phys. Rev. D*, 72, 083501

[66] Apostolopolous P.S., *et al.*, 2006, *J. Cosmol. Astropart. Phys.*, 06(2006), 009

[67] Moffat J.W., 2006, *J. Cosmol. Astropart. Phys.*, 05(2006), 001

[68] Kai T., *et al.*, 2007, *Prog. Theor. Phys.*, 117, 229

[69] Ishibashi A. and Wald R., 2006, *Class. Quant. Grav.*, 23, 235

[70] Enqvist K., 2008, *Gen. Rel. Grav.*, 40, 451

[71] Bolejko K. and Andersson L., *J. Cosmol. Astropart. Phys.*, 10(2008), 003

[72] Romano A.E., 2007, *Phys. Rev. D*, 75, 043509

[73] Sussmann R.A., 2008, arXiv:0807:1145

[74] Tomita K., 2001, *Mon. Not. R. Astron. Soc.*, 326, 287

[75] Tomita K., 2003, *Astrophys. J.*, 584, 580

[76] Doran M. and Lilley M., 2002, *Mon. Not. R. Astron. Soc.*, 330, 965

[77] Eisenstein D.J. and Hu W., *Mon. Not. R. Astron. Soc.*, 496, 605

[78] Bolejko K. and Wyithe J.S.B., *J. Cosmol. Astropart. Phys.*, 02(2009), 020

[79] García-Bellido J. and Haugbølle T., 2008a, *J. Cosmol. Astropart. Phys.*, 04(2008), 003

[80] Alnes H., *et al.*, 2006, *Phys. Rev. D*, 73, 083519

[81] Alnes H. and Amarzguioui M., 2006, *Phys. Rev. D*, 74, 103520

[82] Alnes H. and Amarzguioui M., 2007, *Phys. Rev. D*, 75, 023506

[83] Eisenstein D.J., *et al.*, 2005, *Astrophys. J.*, 633, 560

[84] Ellis G.F.R., *el al.*, 1985, *Phys. Rep.*, 124, 315

[85] Humphreys N.P., *et al.*, 1997, *Astrophys. J.*, 477, 47

[86] Reiss A.G., *et al.*, 2004, *Astrophys. J.*, 607, 665

[87] García-Bellido J. and Haugbølle T., 2008b, *J. Cosmol. Astropart. Phys.*, 09(2008), 016

[88] Einstein E. and Straus E.G., 1945, *Rev. Mod. Phys.*, 17, 120

[89] Kantowski R., 1969, *Astrophys. J.*, 155, 89

[90] Biswas T. and Notari A., 2008, *J. Cosmol. Part. Phys.*, 06(2008), 021

[91] Sato H., 1984, *General Relativity and Gravitation*

[92] Brouzakis N., *et al.*, 2007, *J. Cosmol. Astropart. Phys.*, 02(2007), 013

[93] Brouzakis N., *et al.*, 2008, *J. Cosmol. Astropart. Phys.*, 04(2008), 008

[94] Sachs R.K., 1961, Proc. R. Soc., A264, 309

[95] Marra V., *et al.*, 2007, *Phys. Rev. D*, 76, 123004

[96] Marra V., *et al.*, 2008, *Phys. Rev. D*, 77, 023003

[97] Célérier M.N. and Szekeres P., 2002, *Phys. Rev. D*, 65, 123516

[98] Seljak U. and Zaldarriaga M., 1996, *Astrophys. J.*, 469, 437

[99] Seljak U., *et al.*, 2003, *Phys. Rev. D*, 68, 083507

[100] Ellis G.F.R., 2008, *Nature*, 452, 158

[101] Stoeger W.R., *et al.*, 1995, *Astrophys. J.*, 443, 1

[102] Nilsson U.S., *et al.*, 1999, *Astrophys. J.*, 521, L1

[103] Thompson K.L. and Vishniac E.T., 1987, *Astrophys. J.*, 313, 517

[104] Inoue K.T. and Silk J., 2007, *Astrophys. J.*, 664, 650

[105] Panek M., 1992, *Astrophys. J.*, 388, 225

[106] Arnau J.V., *et al.*, 1993, *Astrophys. J.*, 402, 359

[107] Saez D., *et al.*, 1993, *Mon. Not. R. Astron. Soc.*, 263, 681

[108] Arnau J.V., *et al.*, 1994, *Mon. Not. R. Astron. Soc.*, 268, L17

[109] Fullana M.J., *et al.*, 1994, *Astrophys. J. Suppl. Ser.*, 94, 1

[110] Rakić A., *et al.*, 2006, *Mon. Not. R. Astron. Soc.*, 369, L27

[111] Masina I. and Notari A., 2009, *J. Cosmol. Astropart. Phys.*, 02(2009), 019

[112] Kogut A., *et al.*, 1993, *Astrophys. J.*, 419, 1

[113] Hinshaw G., *et al.*, 2007, *Asrophys. J. Suppl.*, 170, 288

[114] Partridge R.B., 1988, *Rep. Progr. Phys.*, 51, 647

[115] Paczyński B. and Piran T., 1990, *Astrophys. J.*, 364, 341

[116] Turner M.S., 1991, *Phys. Rev. D*, 44, 3737

[117] Langlois D., 1996, *Phys. Rev. D*, 54, 2447

[118] Langlois D. and Piran T., 1996, *Phys. Rev. D*, 53, 2908

[119] Lemaítre G., 1933, *Gen. Rel. Grav.*, 29, 637(1997)

[120] Hellaby C. and Krasiński A., 2002, *Phys. Rev. D*, 66, 084011

[121] Hellaby C. and Krasiński A., 2008, *Phys. Rev. D*, 77, 034529

[122] Kantowski R. and Sachs R., 1966, *J. Math. Phys.*, 7, 443

[123] Hellaby C., 1996, *Class. Quant. Grav.*, 13, 2537

[124] Barrow J.D. and Stein-Schabes J., 1984, *Phys. Lett. A*, 103, 315

[125] Bonnor W.B., 1976, *Commun. Math. Phys.*, 51, 191

[126] de Souza M.M., 1985, *Revista Brasileira de Fisica*, 15, 379

[127] Bolejko K., 2006b, *Phys. Rev. D*, 73, 123508

[128] Bolejko K., 2007, *Phys. Rev. D*, 75, 043508

[129] Mena F.C. and Tavakol R., 1999, *Class. Quant. Grav.*, 16, 435

[130] Silk J., 1977, *Astron. Astrphys.*, 59, 53

[131] Bolejko K., 2008, arXiv:0804.1846v2[asro-ph]

[132] Barrow J.D. and Silk J., 1981, *Astrophys. J.*, 250, 432

[133] Joyce M. and Marcos B., 2007, *Phys. Rev. D.*, 75, 063516

[134] Stoeger W.R., *et al.*, 1995, *Astrophys. J.*, 443, 1

[135] Ellis G.F.R., *et al.*, 2002, *Gen. Rel. Grav.*, 34, 1445-9